The Dynamic Character of the Flow over a 3.5 Caliber Tangent-Ogive Cylinder in Steady and Maneuvering States at High Incidence

By
Matthew D. Zeiger

Dissertation submitted to the faculty of the Virginia Polytechnic Institute and State University in partial fulfillment of the requirements for the degree of

Doctor of Philosophy
in
Engineering Mechanics

Demetri P. Telionis, Chair
Scott L. Hendricks
Dean T. Mook
Saad A. Ragab
Roger L. Simpson

17 October 2003
Blacksburg, Virginia

Keywords: Forebody, Vortex, Asymmetry, Axisymmetric, Unsteady, Maneuver

The Dynamic Character of the Flow over a 3.5 Caliber Tangent-Ogive Cylinder in Steady and Maneuvering States at High Incidence

By

Matthew D. Zeiger

Abstract

Although complex, inconsistent and fickle, the time-averaged flow over a stationary slender forebody is generally well-understood. However, the nature of unsteady, time-varying flows over slender forebodies – whether due to the natural unsteadiness or forced maneuvering - is not well-understood. This body of work documents three experimental investigations into the unsteadiness of the flow over a 3.5 caliber tangent-ogive cylinder at high angles of incidence. The goal of the investigations is to characterize the natural and forced flow unsteadiness, using a variety of experimental tools.

In the first investigation, flow data are collected over a stationary model in a water tunnel. Particle-Image Velocimetry (PIV) is employed to acquire time-dependent planes of velocity data with the model at several angles of attack. It is discovered that the asymmetric flow associated with the tangent-ogive forebody exhibits a large degree of unsteadiness, especially for data planes located far from the forebody tip. Vortex shedding of the type exhibited by a circular cylinder in crossflow is observed, but this shedding is skewed by the presence of the tip, the shedding process does not require equal periods of time from each side of the body, and this results in a time-averaged flowfield that is asymmetric, as expected. The rms values of the time-averaged velocity, as well as the turbulent kinetic energy and axial vorticity are calculated.

In the second investigation, surface pressure data are acquired from several circumferential rings of pressure ports located on two models undergoing ramp coning motions in two different wind tunnel facilities. The surface pressure data are integrated to determine the sectional yaw forces. Coning motions were performed at several different reduced frequencies, and pneumatic control actuation from the nose was employed. The chosen control actuation method used a small mass flow rate ejected very close to the forebody tip, so as to leverage the inherent convective instability. The data resulting from these tests were analyzed in order to determine how the coning motions affect the distribution of surface pressure and yaw forces, how quickly the flow reacts to the motion, and the extent of control authority of the pneumatic actuation. It was discovered that the yaw forces increase in the direction of the motion for small reduced frequencies, but in the direction opposite to the motion for large reduced frequencies. The effects of the motion tend to dominate the control method, at least for the reduced frequencies and setup tested in the low-speed wind tunnel. The results from the high-speed testing with transitional separation give a preliminary indication that the control method could have sufficient control authority when the reduced frequencies are low.

The third investigation involves tangent-ogive cylinder undergoing a pitching maneuver in a water tunnel. Laser-Doppler Velocimetry (LDV) is used in order to map out several planes of velocity data as the model is pitched. The LDV data is used to calculate vorticity and turbulent kinetic energy. Variables that are proportional to the flow asymmetry and proximity to the steady-state flow are defined. All of these variables are displayed as a function of time and space (where appropriate). The delay in the development of the asymmetry and the flow progression to the steady state are determined to be a function of pitch-axis location. The propagation velocity of the convective asymmetry is faster than expected, most likely because of the increased axial velocity in the vortex cores. Vortex breakdown of one of the vortices is observed, with loss of axial velocity and dilution of the vorticity over a large area. The cause of this phenomenon is not yet understood, but it is reminiscent of vortex breakdown over delta wings.

Dedication

For Polly, Kelby, Tristan, & Adeline

There is no greater treasure than you.

Acknowledgements

In an individual project of this magnitude, it is almost impossible to finish without support from others. There were many people that contributed in some way to this project, and I am sure that I will forget to mention somebody. I have been blessed to have been able to interact with each one.

First, I would like to thank my advisor, Demetri Telionis. Although we don't always agree on method, we almost always agree on form. I wish that I could have been less stubborn, but he always accommodated my strive for perfection with patience. I can definitely say that I learned from my mistakes, and above everything else, this is what I have kept close. I am fortunate to be able to count Demetri as a mentor and friend.

I would like to thank Professors Roger Simpson, Saad Ragab, Dean Mook and Scott Hendricks, members of my committee. Thank you for allowing me to reap from your expertise, and thank you for being patient with a wayward soul.

Many thanks to Jerry Jenkins and the Design Predictions Group at Wright-Patterson AFB for his intellectual insight and monetary support for the Stability Tunnel testing. I am fortunate to have been able to work with you, if only for a short time.

To Norman Schaeffler, Martin Donnelly, Chris Moore, Othon Rediniotis, Pavlos Vlachos, Sandie Klute, Dmitri Stamos, Ngoc Hoang, Andy Mathes and Luis Chalmeta - my laboratory colleagues: We had some great times in the ESM Fluids Lab, the VT Stability Tunnel and in Blacksburg. I cannot expect to ever again have as much fun doing work, but I am certainly going to try. Thanks for your fellowship, advice and cooperation.

I want to extend many thanks and love to my parents, Jerome and Rozanne. You have always supported me in all of my endeavors. You taught me not only how to be successful, but more importantly how to be a good person and a good parent.

Finally, I want to thank my wife, Polly and my three children Kelby, Tristan and Addie. No matter what the obstacle, you always supported me and believed that I would (eventually) succeed. I am so happy to be able to share life with you.

Contents

Figures

Tables

Nomenclature

Scalar Quantities

t	Time
t^*	Nondimensional Axial Time, $t \cdot U_\infty \cdot \cos\alpha / D$
t_c^*	Nondimensional Crossflow Time, $t \cdot U_\infty \cdot \sin\alpha / D$
t_g^*	Time of Asymmetry Generation at the Forebody Tip
t_{eta}^*	Theoretical Expected Time of Arrival of the Asymmetry
t_{ata}^*	Actual Arrival Time of the Asymmetry
x	Distance Along Body Axis, Measured from the Forebody Tip
x_p	Location of Pitching Axis
x_c	Location of Coning Axis
y	Horizontal Distance from Body Axis or Sectional Yaw Force
z	Vertical Distance from Body Axis
u	X-Component of Velocity
v	Y-Component of Velocity
w	Z-Component of Velocity
u'	Deviation from Mean u
v'	Deviation from Mean v
w'	Deviation from Mean w
σ_u	Standard Deviation in u
σ_v	Standard Deviation in v
σ_w	Standard Deviation in w
D	Base Diameter, Typically the Characteristic Length
d	Local Diameter
k_c	Coning Reduced Frequency, $\dot{\gamma} \cdot D/U_\infty$
k_p	Pitching Reduced Frequency, $\dot{\alpha} \cdot D/U_\infty$
R	Base Radius, D/2; Universal Gas Constant = 287.04 J/(kg K)
r	Local Radius
L	Distance from Pitch Axis to Forebody Tip
L_o	Overall Body Length
L_N	Forebody Length, for a 3.5-Caliber Forebody $L_N = 3.5 \cdot D$

r_N	Radius of the Arc that Defines the Tangent-Ogive Geometry
δ	Included Half-Angle of the Forebody Tip
α	Angle of Attack (Angle of Incidence)
$\dot{\alpha}$	Pitch Rate
β	Angle of Sideslip
ϕ	Roll Angle
γ	Rotation Angle During Coning
$\dot{\gamma}$	Coning Rate
θ	Circumferential Angle, Defines Location Around Body
ρ	Density
μ	Viscosity
ν	Kinematic Viscosity
H	Helicity, $\boldsymbol{\omega \cdot V}$
T	Static Temperature
T_o	Total Temperature
P	Static Pressure
P_o	Total Pressure
Y	Yaw Force
N	Normal Force
n	Sectional Normal Force
C_m	Pitching Moment Coefficient, Mass Flow Coefficient
C_n	Sectional Normal Force Coefficient, N/2qD or Yaw Moment Coefficient
C_y	Sectional Yaw Force Coefficient, y/2qD
C_p	Pressure Coefficient, $(P - P_\infty)/q$
Re_D	Reynolds Number Based on Base Diameter, $U_\infty \cdot D/\nu$
Re_L	Reynolds Number Based on Length, $U_\infty \cdot L/\nu$
Re_t	Tip Reynolds Number, $U_\infty \cdot r_t/\nu$
M	Mach Number
U_∞, U_{Inf}	Freestream Velocity
U_{ac}	Asymmetry Axial Convection Velocity
q	Dynamic Pressure, $\frac{1}{2}\rho U_\infty^2$

$C_{\dot{m}}$	Mass Flow Coefficient, $\frac{\dot{m}}{\rho U_\infty D^2}$
A	Measure of Flow Asymmetry
SS	Measure of Deviation of Flow from Steady State
S	Characteristic Area, Either D^2 or the Planform Area of the Forebody
c	Chord Length
TKE	Turbulent Kinetic Energy, $\frac{1}{2}(u'^2 + v'^2 + w'^2)$

Vector Quantities (Boldface Notation)

V	Velocity, u**i** + v**j** + w**k**
ω	Vorticity, $\nabla \times V$

Subscripts

∞, Inf	Freestream Value
S	Symmetric
A	Asymmetric
U	Unsteady
b	Bottom
s	Side
t	Forebody Tip

Chapter 1 - Introduction and Literature Review

Quotes on the Subject of the Slender Forebody Problem:

"...Infuriating..." - B.L. Hunt, Northrop Corp.

"...Fickle..." - L.E. Ericsson, Lockheed Missile Corp.

"...Numerous inconsistencies and discrepancies between the results of different workers." - P.J. Lamont, NASA Ames

"Experienced experimenters, applying conventional wind-tunnel testing techniques with the greatest of care, found great difficulty in repeating their results and even greater difficulty duplicating the results of others." - B.L. Hunt, Northrop Corp.

"Somebody should have called it nonlinear." - R.L. Simpson, Virginia Tech, Upon Hearing the Above Quotes

1.1 Introduction

From the late 1940's to early 1950's, aircraft design was rapidly evolving due to the radical changes in propulsion systems. First proven by the German Luftwaffe in World War II, the turbojet engine was to quickly drive the piston-driven propeller to extinction as the propulsion means for state-of-the-art fighters and bombers. Although piston-driven P-51 Mustangs and F-4U Corsairs would remain in service through the Korean War, their heyday was decidedly over. Besides the turbojet, the Germans also

made great strides in the development of the rocket engine, which they used with great success. The V1 and V2 rockets showed that explosives mounted on a long-range rocket could be a formidable weapon.

As the amount of thrust available increased, aircraft were able to expand their performance envelope so that velocities greater than the speed of sound were possible. By the early 1960's, most of the world-class fighter aircraft were designed to cruise supersonically. Since slender bodies of revolution have relatively low drag and a predictable conical or near-conical shock pattern in supersonic flow, it is not surprising that axisymmetric bodies were used as forebodies (nose sections) in the high-speed fighter aircraft. In addition, these shapes continued to be used in the design of rockets and missiles.

Three of the most popular axisymmetric shapes in use by researchers are the ogive cylinder, cone cylinder and the hemisphere cylinder. Generic examples of these shapes are shown in Figure 1. The cone and ogive cylinders are classified as slender forebodies because the length of the nose is typically longer than the base diameter. Slender forebodies of the same type (cone, tangent-ogive, etc.) are known to exhibit a wide variety of flows under similar conditions due to variations in the caliber (also known as fineness ratio). The caliber/fineness ratio is defined as the length of the forebody in the axial direction (L_N) divided by the base diameter D (or less often as base diameter R). Ogives are solid bodies of revolution with circular arcs as generators, the radius of these arcs depending on the caliber of the forebody. For instance, the radius of the generating arcs for a 3.5-caliber tangent-ogive body is 12.5•D. Blunt forebodies, such as the hemisphere cylinder and its derivatives, have nose lengths that are less than or equal to the base diameter. All of these generic axisymmetric shapes and their derivatives are still used as forebodies for the majority of modern high-speed aircraft and missiles. In application, the ogival bodies are more commonly used than the conical.

When forebodies are used in missile applications, there will be an afterbody of a more generic type, usually being a cylinder of diameter D abutting the forebody. Where aircraft forebodies are concerned, the afterbody is typically not slender, usually including the canopy.

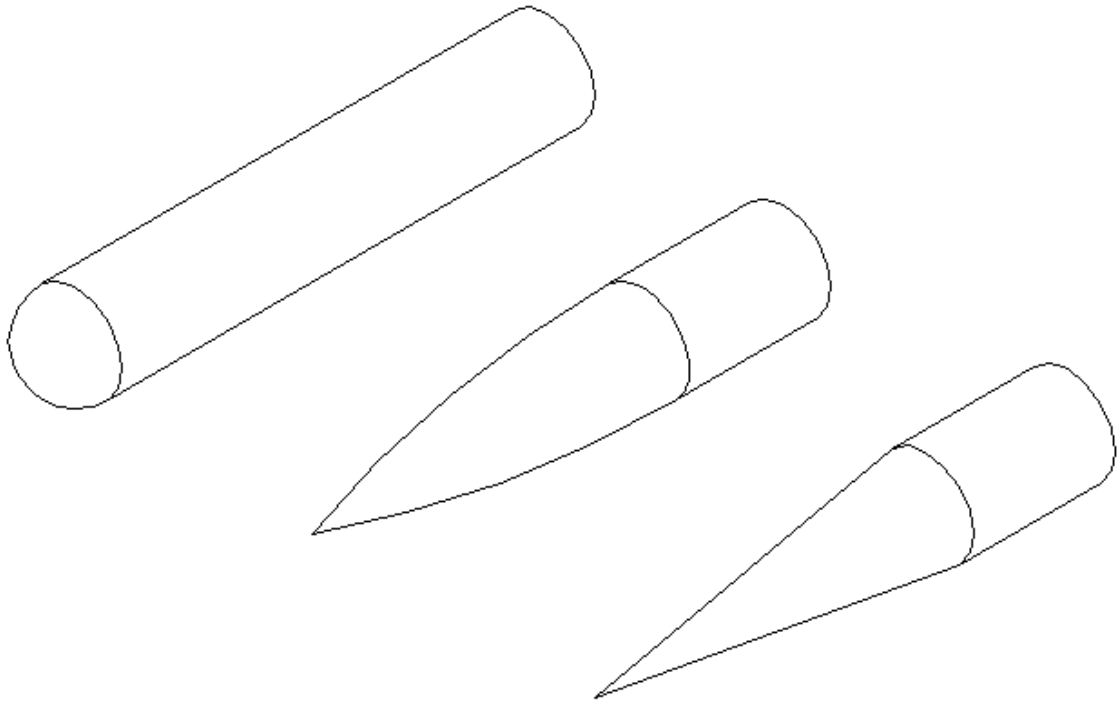

Figure 1.1: Examples of Typical Forebody Geometries: A Hemisphere (Left), Tangent-Ogive (Center) and Cone (Right). Note that the Cylindrical Afterbodies Are Normally Employed in Application in order to Achieve a Desired Fineness Ratio for the Body Combinations.

Because these forebodies were axisymmetric and of a simple geometry, the aircraft and missile industry did not foresee many problems in their implementation. Indeed, during cruise and standard maneuvering, the forebodies performed as expected. However, during the late 1940's, it was discovered that placing axisymmetric slender forebodies at high angles of attack at zero sideslip could result in yaw forces and moments, that is, out-of-plane forces. The first investigations to document this phenomena (Letko, 1953, Dunn, 1954) were performed in the early 1950's. The results were surprising, because it seemed unreasonable that an axisymmetric body could produce yaw forces (those perpendicular to the angle-of-attack plane), no matter the angle of incidence. These investigations were primarily concerned with vortical interaction with control surfaces, and did not explore the character or generation of the forebody vortices. At about the same time, it was noted that blunt bodies such as hemisphere cylinders did not produce the yaw forces and moments seen with the slender forebodies. Thus, the aerodynamics and fluid mechanics of axisymmetric bodies at high angles of attack depends greatly upon their fineness ratio. From this point forward, the discussion shall focus almost solely on slender forebodies.

Researchers and the aircraft and missile industry did not show interest in the slender forebody problem until the mid-1960's, when high-angle-of-attack (high-α) maneuvers became possible due to advances in control technology. Aircraft and missiles that could achieve control at high angles of attack

could expand their performance envelope and score victories over opponents that could not maneuver at such angles. In addition, the designs of high-speed civil transports (such as the Concorde) were being considered. These transports were to be equipped with slender forebodies to be efficient in cruise, and because of lift requirements during landing, they would be placed at high angles of attack at low speed. Due to these applications and others, high-α aerodynamics became a heavily researched topic. With the new effort directed at high-α problems, it did not take long to rediscover the yaw force present on slender bodies at incidence or the fact that the force was accompanied/caused by a profound asymmetry in the vortex wake formation.

The slender forebody placed at a high angle of attack has proven to be one of the most interesting and difficult fluid mechanics problems, as evidenced by the amount of literature produced. The difficulty of the problem can be attested by the fact that the cause of asymmetric forces on slender forebodies and characteristics of the vortex wake is still being researched at the present time, approximately 40 years after first being discovered.

1.2 Basic Slender Forebody Flow and Important Parameters

1.2.1 The Flow as a Function of the Angle of Attack (α)

The flow over a slender forebody of circular cross-section can be separated into four regimes based on α: (1) No separation ($\alpha < \alpha_S$) - At very low angles of attack, the flow does not separate from the body. (2) Symmetric flow ($\alpha_S < \alpha < \alpha_A$) - At low to moderate angles of attack, but below the critical angle for the onset of asymmetry, the flow rolls into two symmetric vortices on the leeside of the forebody. (3) Steady asymmetric flow $\alpha_A < \alpha < \alpha_U$) - At high angles of attack above the critical angle (α_A), the flow over the slender forebody and afterbody exhibit asymmetric lee vortices and a nonzero yaw force. (4) Unsteady asymmetric flow - At very high angles of attack, the vortical flow becomes increasingly unsteady, especially over the afterbody. The mean flow is still asymmetric, but the mean yaw force decreases with α. The onset angle of attack for this flow regime will be designated α_U and is generally between 70° and 80°, depending on the fineness ratio (caliber) of the forebody. At $\alpha = 90°$, the forebody produces the familiar Karman vortex street, except for cross-sections near the tip of the

forebody. Flow visualization of the slender body flow variance with angle of attack which supports the division into four regimes was done by Fiechter (1966).

The boundary angles for each regime (α_S, α_A, α_U) may be functions of Reynolds number, fineness ratio (L_N/D), surface roughness and tip geometry. Tip geometry refers to the shape of the nose tip, and encompasses all relevant tip parameters that affect the flow. Other relevant parameters include, but are not limited to, the included half-angle of the nose tip (δ), the bluntness ratio of the nose ($2R_t/D$), variation in cross-section and any geometric micro-asymmetries present. The various geometric quantities are shown in Figure 1.2 for a generic slender forebody. The micro-asymmetries could be machining asymmetries that cannot be entirely eliminated because of accuracy limits in the machining process. In other words, no matter how carefully the forebody is machined, there will always be very minute geometric flaws. The micro-asymmetries present near the nose tip are very important in the determination of the flow over the entire slender forebody because they introduce disturbances to the flow that can be locally large.

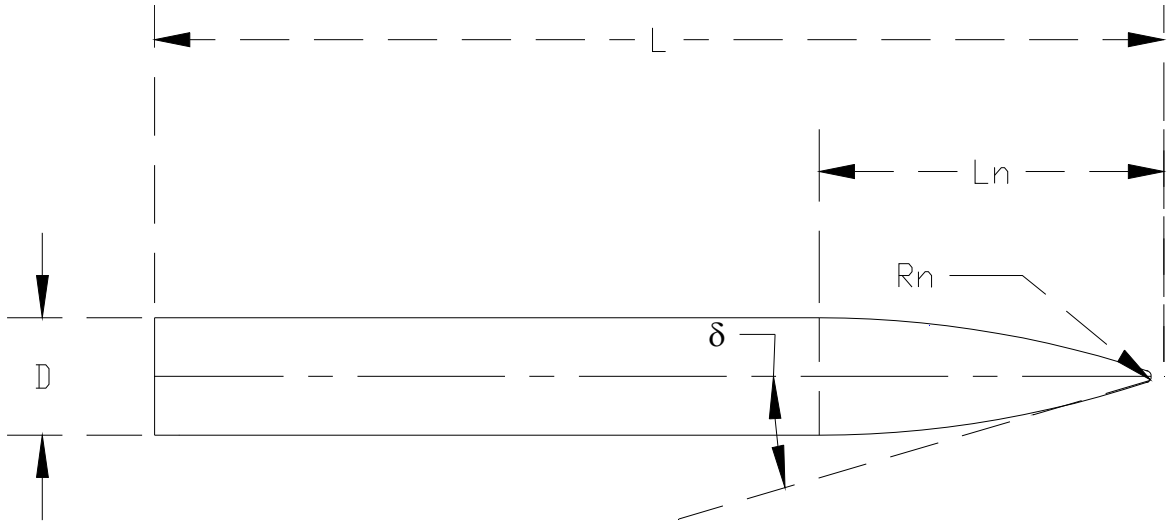

Figure 1.2: Relevant Geometry for a 3.5 Caliber Tangent-Ogive Cylinder, a Typical Slender Forebody. D = Base Diameter, L = Overall Length, L_N = Nose Length (which is 3.5D for this Particular Forebody) , R_N = Tip Radius, δ = Included Half-Angle at Tip.

Figure 1.3 shows the coordinate system and variables that will be used in all subsequent discussions. The coordinate x-axis is coincident with the axis of symmetry of the model and is aligned with the free stream velocity vector when all angles are zero. The coordinate y is in the direction of the starboard wing (pilot's view), and the coordinate z is subsequently given by the right-hand rule. The coordinate system is fixed to the body. The body may be rotated from the flow vector by three angles:

Pitch (α), roll (ϕ) and yaw (β). The normal force N is aligned with the +z-direction, and the normal yaw force Y is aligned with the +y-direction. There is a component of the aerodynamic force in the x-direction, but this is typically small and is not measured in most tests on a slender forebody. Pitch and yaw moments are designated as m and n, respectively. Note that the force and moment coefficients are notated with a "C" and a subscript corresponding to the quantity that is being non-dimensionalized, so that the yaw force coefficient would be designated with the C_Y variable. The circumferential angle is given by the coordinate θ, and this is used to show the location of surface pressure ports and blowing ports, for example.

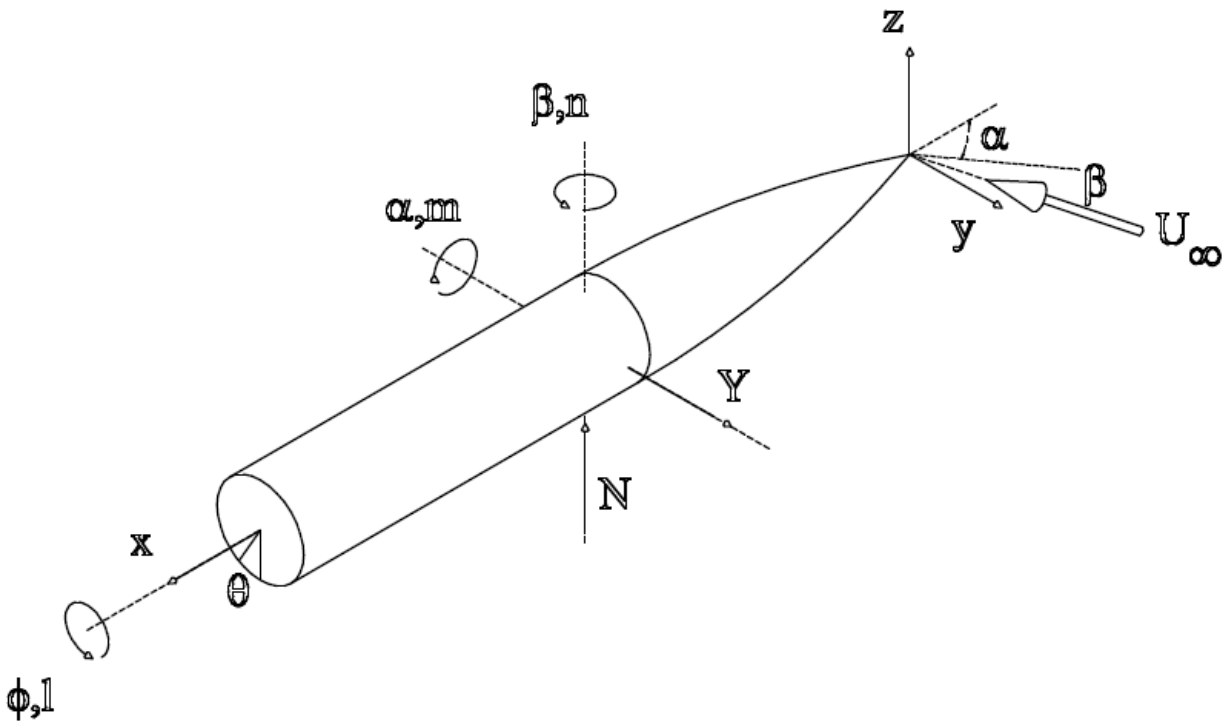

Figure 1.3: Coordinate System for the Slender Forebody. The Coordinate System is Fixed to the Body.

Typical flowfields for each flow regime are shown in Figure 1.4. In the first flow regime, shown in Figure 1.4a, $\alpha < \alpha_S$. In this regime, the flow is entirely attached, and the normal force and pressure distribution can be calculated quite accurately through the application of slender body theory (Munk, 1924), which is based on potential flow theory. The normal force is low, and the yaw forces are nonexistent.

The second flow regime encompasses the angles of attack from α_S to α_A. It has been observed that $\alpha_S \approx \delta$. In this regime, the flow over the slender forebody separates and the wake rolls up into a pair of steady, symmetric vortices as shown in Fig. 1.4b. The normal force increases with α, as expected, and

the yaw force is zero in the mean, although a very small yaw force may appear due to natural unsteady fluctuations in the vortex pattern. The separation point of the vortices is far down the body at lower α, and moves towards the nose tip as α increases.

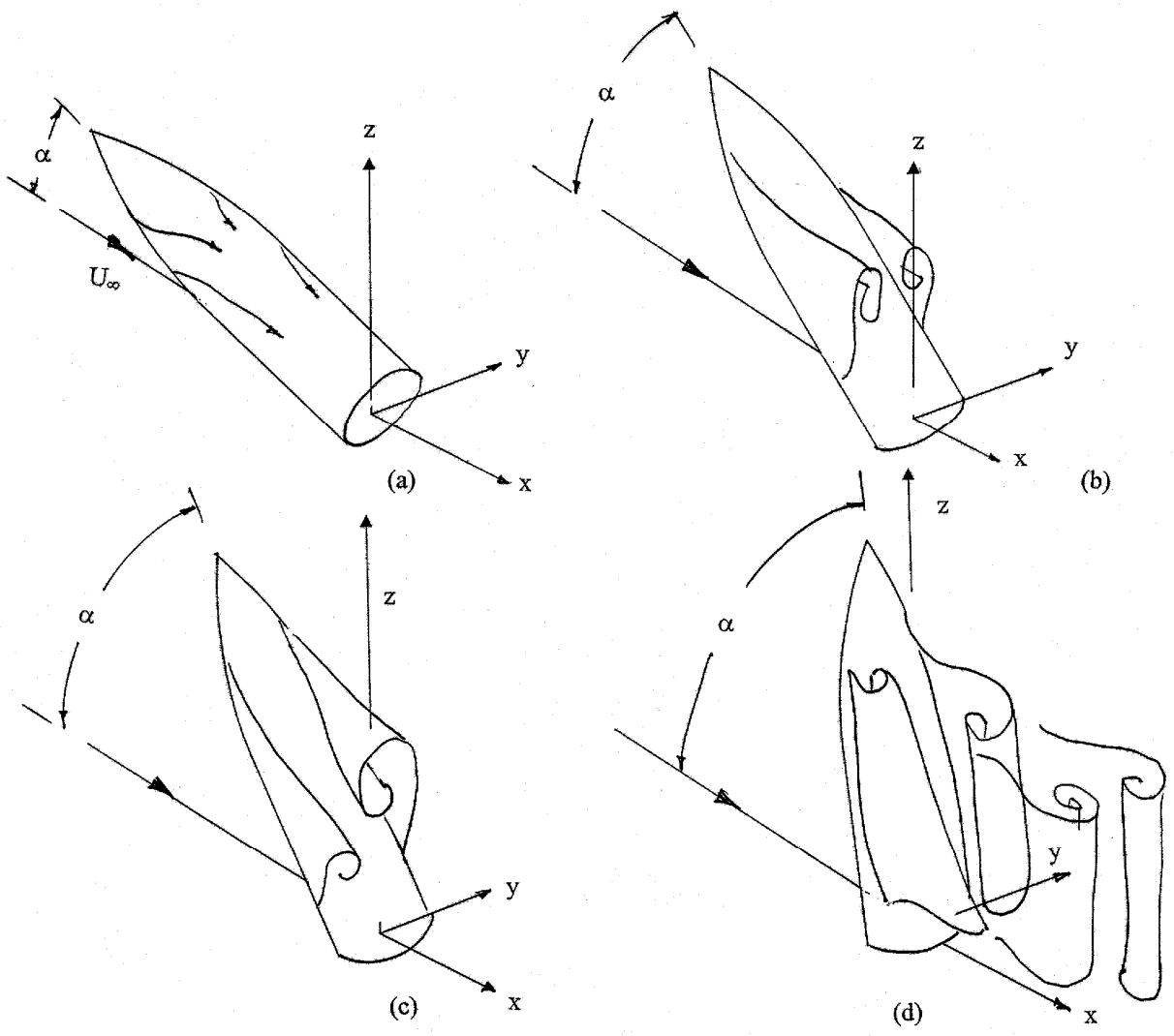

Figure 1.4: Flow Regimes on a Slender Forebody as a Function of the Angle of Attack (α) - (a) Attached Flow (b) Separated Flow with Symmetric Leeside Vortices (c) Separated Flow with Asymmetric Leeside Vortices, Time-Averaged Leeside Flow is Asymmetric (d) Separated Flow with Asymmetric Leeside Vortices with Large Transience Approaching Von Karman Vortex Street, Time-Average Leeside Flow is Symmetric.

At a critical angle of attack, the symmetric formation of vortices is broken and the vortex pattern becomes asymmetric, which is the characteristic phenomenon associated with the third flow regime. The asymmetry onset α_A is approximately 2δ for both tangent-ogive and cone forebodies so it follows that the flow near the tip of the tangent-ogive must be nearly conical (Keener and Chapman, 1974; Keener et al.,

1976; See Review by Hunt, 1982). With a possible exception at very low Mach numbers, α_A is not a function of flow compressibility (Keener 1977).

The root cause of the asymmetry is closely related to the separation point of the vortices being very close to the tip. At the tip, the cross-sections are very small, and the aforementioned micro-asymmetries influence the separation of the vortex pair in an asymmetric fashion. Because the two vortices are in close proximity to one another, their mutual interaction exaggerates the initial asymmetry, and the vortices assume a pattern resembling that of Figure 1.4c, with one vortex very close to the body and the other further away.

A common misconception, especially among those unfamiliar with the slender forebody problem but familiar with the two-dimensional cylinder in crossflow, is that the asymmetry of the wake vortices changes from one side of the body to the other over time (similar to the von Karman vortex street). Actually, the yaw force and moment are nonzero in the mean. In fact, it has been shown that the yaw force can be as much as 1.6 times the normal force (Keener, 1977) and the yaw moment induced by the forebody asymmetry can be several times that which can be produced by an aircraft rudder at high angles of attack. The vast difference between the vortex-induced moment and the rudder capability results because the yaw force on the forebody increases with α, but the rudder becomes increasingly ineffective, because it is buried in the wake of the aircraft.

It should be noted that the third flow regime could technically be split into two subregimes. At approximately $\alpha = 50°$, there may be a change in the nature of hydrodynamic instability which causes the asymmetric flow (see the section Convective and Global Hydrodynamic Instabilities below). Although this has a profound effect on the variation of the vortex pattern and yaw force with changes in the disturbance which causes the asymmetry, it does not effectively alter how the flow varies with angle of attack with the disturbance held constant.

Several investigations by Keener and colleagues (Keener et al. 1976, 1977) provided a fundamental force and moment database for slender bodies at incidence. They indicated that the yaw force reaches a maximum near $\alpha = 55°$. As the angle of attack is increased from α_S, the flow asymmetry becomes more pronounced. The maximum achievable yaw force increases with angle of attack until α_U, at which point the flow becomes dominated by transience as it moves into the fourth flow regime, and the yaw force quickly decreases to zero in the mean. As with the yaw force, the behavior of the normal force at moderate to high α may be counterintuitive, since the maximum normal force occurs at $\alpha = 60°$, rather

than at 90°, where one might expect. The increase in normal force is caused by increased suction on the lee side of the body due to the asymmetric vortex pattern. Wake investigations have shown that in highly asymmetric vortex patterns, the core of the primary vortex nearest to the body lies near the leeward generator.

The flow over the slender forebody in the fourth regime is more complex than in any of the previous regimes, as can be discerned from Fig. 1.4d. In this regime, the flow separates from the nose tip immediately, and the resulting first pair of asymmetric vortices quickly aligns with the freestream. All subsequent vortices, which originate farther down the bluff body, exist in various stages of transience because they are no longer continuously attached to their separation lines but are actually shed into the wake. Since the subsequent vortices are transient, the mean yaw force decreases as α increases in this regime, since only the first pair of vortices continues to contribute to a non-zero mean asymmetry. As a result, the mean yaw force ceases to be a real concern at angles of attack slightly higher than α_U. This behavior could be expected because the flow over an axisymmetric body at high angles of attack should begin to resemble that of a circular cylinder in crossflow. At $\alpha = \alpha_U$, the shedding frequency is small, but as the angle of attack grows, so does the shedding frequency, which reaches the Strouhal frequency at $\alpha = 90°$, if measured at an axial station far from the tip so that end effects are minimized.

1.2.2 Impulsively Started 2-D Cylinder Flow Analogy (IFA)

The asymmetric crossflow (flow in a plane perpendicular to the axis of symmetry) present in the wake of a slender forebody when $\alpha > 2\delta$ immediately sparks the thought of the impulsively started two-dimensional cylinder. Recall that the impulsively started flow consists of an initial symmetric growth of lee vortices, followed by the alternate shedding of the vortices, the Karman vortex street. However, a discrepancy exists between the two problems because the wake and forces on the two-dimensional cylinder vary with time, whereas the wake and forces on a slender forebody are steady phenomena, although some natural unsteadiness exists at high angles of attack.

An interesting analogy, originally suggested by Allen & Perkins (1951), may be made which relates the wake seen over the impulsively started cylinder as a function of time to that seen over a slender axisymmetric body inclined to the freestream as a function of the distance in the axial direction. If the flow over the axisymmetric body is separated into crossflow and an axial flow component, then the analogy states that if a sheet of fluid in the crossflow plane is convected over the body by the axial component, it is influenced by the presence of the body as if it were impulsively started. The flow

development with axial distance (x) over the axisymmetric body may be related to the flow development with time in the two-dimensional case as follows. The nondimensional time for the impulsively started cylinder in crossflow is $t = U_\infty \cdot t^*/D$. For the axisymmetric body at incidence, the crossflow velocity is $U_\infty \sin\alpha$, and the corresponding time would be $t^* = x/(U_\infty \cdot \cos\alpha)$. Substituting into the corresponding equation for the cylinder in crossflow, we see that the nondimensional time becomes $t = (U_\infty \sin\alpha \cdot x)/(U_\infty \cdot \cos\alpha \cdot D) = (x/D) \cdot \tan\alpha$. In using this analogy, it was hoped that the wake pattern over a slender forebody could be established by using the analogy to relate the nondimensional times. Then the corresponding sectional yaw force at each axial location could be calculated or derived from two-dimensional experimental results, giving an estimate of the overall yaw force that would compare well with data obtained experimentally.

There are several assumptions in this analogy that do not reflect the actual forebody flow. First, the flow velocity in the axial direction may vary throughout the crossflow plane, and the average convection rate in the axial direction may not be $U_\infty \cos\alpha$. The second erroneous assumption is that the wake of the 2-D cylinder is like the crossflow in the 3-D case. The flow and boundary layer development over the forebody is strongly three-dimensional, and the crossflow cannot be easily compared to its 2-D counterpart without consideration to the effects of the nose. Flow over a cylindrical afterbody, away from the forebody effects, can be more easily modeled by the impulsive flow analogy.

This analogy has been thoroughly explained by Sarpkaya (1966) and Lamont & Hunt (1976), the latter using the analogy to produce a partial collapse of the yaw force distributions. Other investigators have attempted to use the direct analogy as a basis for determining the wake development and overall yaw force (Atraghji 1976). It was discovered that the normal force could be predicted rather well, but attempted predictions of the yaw force failed to predict the correct magnitude, although they were qualitatively similar. Although it cannot be used for correct quantitative prediction of the yaw forces, the impulsively started cylinder analogy is a powerful tool that can be used to explain, if only qualitatively, the development of asymmetric forces and wakes on an axisymmetric body.

1.2.3 Wake Vortex Flow

The asymmetric vortical structures produced by a slender forebody at moderate to high incidence are the signature of the problem. The vortex interaction with the boundary layer is very complex because it is nonlinear and three-dimensional. The interaction is nonlinear because the vortices emanate from

separation lines on the body, but the angular locations of these lines are affected by the position and strength of the vortices they feed. In addition, the vortices themselves are mutually influenced, affecting the location of the separation lines indirectly. This nonlinear problem is compounded by the fact that the entire flow is strongly three-dimensional, so that two-dimensional analyses, while easier to perform, generally fall short of accurately modeling the problem.

At this point, the wake vortex patterns that exist in the third angle of attack regime will be discussed. An afterbody will be assumed to be present. In the absence of an afterbody, only a single pair of vortices will generally be present. The first pair of vortices to originate from the forebody is shed very near the tip. They develop symmetrically at first, but quickly assume an asymmetric disposition because of their mutual interaction. Because the asymmetry grows with axial distance (due to amplification of the initial disturbance), the flow over the forebody is less asymmetric than the flow over the afterbody (Degani 1991).

Lowson and Ponton (1992) performed flow visualization and discussed the development of the wake flow topology. The following discussion is a parallel. The first pair of vortices will begin to lift off from the body near the shoulder (the juncture of the forebody and afterbody) and begin to align with the freestream. In the asymmetric flow regimes, one vortex will be pushed further away from the body by the other. When the primary vortices begin to lift from the body, the more distant vortex will cease to substantially influence the flow development on the body. When this occurs, a third primary vortex begins to emanate from the side of the body that originated the more distant primary vortex. At this point, the more distant vortex is shed, and ceases to be fed directly by vorticity generated from the body. The physical mechanisms by which initial primary vortices are shed and subsequent primary vortices develop are not well understood. As the axial distance is increased further, the third primary vortex will move the other primary vortices away from the body. This alternating pattern, reminiscent of the Von Karman vortex street, will continue until the afterbody ends.

At any angle of attack, provided that the fineness ratio of the forebody/afterbody combination is sufficiently high, the flow may be separated into three distinct axial regimes, as prescribed by Tobak, Degani & Zilliac (1990) and visualized by Ramberg (1983). The first regime exists at axial locations far from the nose, so that the flow is unaffected by the existence of the forebody. The flow in the first regime is time-dependent vortex shedding over an inclined circular cylinder. The third regime is located near the nose, and is dominated by the vortex pair generated by the forebody. The flow in the third regime is generally steady. The second regime lies between the other two, and the flow is still affected by the

presence of the forebody, so that the vortex shedding in this region is not parallel with the body but inclined to it.

It is possible that vortex heaving can occur at high angles of attack and large axial distances where there are at least three primary vortices in the wake. The following explanation was offered by Lowson & Ponton (1992): Since only the two vortices closest to the body are directly connected to the feeding sheet, other vortices could be "captured and released" by these vortices, causing oscillation that leads to vortex heaving.

Computational investigations using thin-layer compressible and incompressible Navier-Stokes codes have determined forces, surface pressures, streamlines, vortex trajectories and the helicity (scalar product of the velocity and vorticity). Using a thin-layer Navier-Stokes code, Degani and Schiff (1991) introduced a turbulence model, and computed symmetric and asymmetric flows for $\alpha = 40°$ and Reynolds numbers as high as $2 \bullet 10^5$. The computed flow compared well with experimental data. Data presented included normal and yaw force, helicity contours and streamlines. Degani and Schiff also included information about the computational grid and turbulence model.

Degani used a similar thin-layer Navier Stokes code to investigate the effect of minute disturbances on the flow. In general, the computations verified many effects seen experimentally by Moskovitz et al. (1989, 1992), including the saturation of the asymmetry with increasing disturbance size and that the flow is increasingly sensitive the closer the disturbance is placed to the forebody tip.

Hartwich and Hall (1990) have used a thin-layer Navier-Stokes code with a turbulence model that involved the modeling of a laminar separation bubble with transition in the free shear layer for Reynolds numbers from 0.2 - $3.0 \bullet 10^6$. Comparison of the results with experimental was good. The same group showed that the computation of an asymmetric flow was sensitive to grid topology and machine accuracy. The fact that numerical error was sufficient to induce asymmetry of the flow was confirmed by Vanden and Belk (1993). They also analyzed the connection between the section yaw force distribution and the crossflow wake topology, in order to shed more light on the mechanism of vortex shedding. With a theoretical application of classical stability analysis, Hartwich (1994) showed that the attached or separated flow over a cone is neutrally stable in areas of decelerating circumferential flow. The same analysis showed that reducing the slenderness or surface curvature (i.e. blunting the forebody) will reduce the effects of a perturbation on the stability of the flow, giving a theoretical basis for the results seen experimentally and computationally.

Hoang and colleagues (1990, 1991) have investigated the velocity field over a hemisphere cylinder using LDV and seven-hole probes. Some discrepancy was seen between the LDV and probe data, suggesting that perhaps the insertion of a probe into the flow can disturb the vortical flow. This type of interference has been documented in the case of delta wings, and has been shown to produce vortex breakdown in that case. Because the flow over slender bodies produces vortices that are less strong than delta-wing vortices, they are not as susceptible to the drastic and sudden vortex breakdown phenomenon that is inherent in the delta wing problem.

Kegelman & Roos (1991) investigated the velocity fields and forces for three tangent-ogive forebodies of different cross-sections: Circular, elliptical and chined. They discovered that stronger vortices were produced when the separation conditions were laminar, rather than transitional or turbulent (see Flow as a Function of Reynolds Number below for further explanation of separation conditions). The elliptical body produced stronger vortices than the circular, and the chined body produced the strongest vortices, which was expected because separation occurred from a sharp edge. Observed that of the two vortices existing over the forebody, the detaching vortex is initially stronger than the attached, but weakens as it moves further from the body. The attached vortex (closest to the body) strengthens until it bursts. This latter observation confirms those of Keener (1986), who noted the abrupt disappearance of this vortex when performing flow visualization.

Further investigations by Roos and colleagues (1991, 1993, 1997) have resulted in the identification of three types of vortices found in the wake of slender forebody/afterbody combinations. The first type of vortex mimics the classic helical vortex found over a delta wing, and has a high axial velocity along with a large amount of vorticity in the core of the vortex, with these quantities decreasing with distance from the core. The second type of vortex could be construed as a broken-down vortex, because the cross-sectional area of the vortex is large and the axial velocity and vorticity are evenly diffused across the entire area. The third type of vortex is like the classic helical vortex, except that the axial velocity profile is relatively constant across the cross-section of the vortex.

Other investigators have researched the characteristics of the multiple vortex patterns in the wake of slender axisymmetric bodies. Pagan & Molton (1991) used five-hole probes to investigate the velocity field over a tangent-ogive cylinder for angles of attack from 0° - 20°. Thomson & Morrison (1991) described the velocity field and vortex strengths over cone and tangent-ogive cylinders. They noted that the vorticity in the wake became highly diffuse as the axial distance increased. Zilliac (1986) performed

flowfield studies in order to validate computational results. Several planes of velocity data were acquired, but at relatively low Reynolds numbers.

Wardlaw & Yanta (1982) acquired an extensive amount of flowfield data over a tangent-ogive cylinder. The acquired data were among the first to illuminate the position and extent of the secondary vortices. By Simultaneously acquisition of circumferential surface pressures beneath the planes of velocity data resulted in the conclusion that the highest sectional yaw forces were accompanied by high vortex asymmetry. Testing of a blunt model revealed that the vortices generated were just as strong as over the sharp model, but further removed from the model. In a later paper, Wardlaw & Yanta (1984) examined the topology of the flow over a tangent-ogive cylinder at $\alpha = 45°$. They discovered that the flowfield asymmetry originates from the primary saddle point. The primary saddle captures one of the nodes, which then moves leeward from the body. At the point of maximum asymmetry and highest sectional yaw force, the primary saddle and its captured node combine. Although the discussion was very illuminating, the authors noted the possibility that the crossflow streamlines that produced the topology may not be representative of three-dimensional flow.

1.2.4 Cyclical Nature of the Sectional Yaw Force Due to Vortex Shedding

In general, the forebody itself will generate only two primary vortices in the third angle-of-attack regime. Therefore, the distribution of yaw force with axial distance will not change sign on the forebody. If an afterbody is added, the sign of the yaw force may change several times, with the distance between vortex shedding points depending on the afterbody fineness ratio. In addition to fineness ratio, the yaw-force distribution may be affected by α, ϕ, forebody bluntness and Reynolds number.

It is common to refer to the sectional yaw force distribution in terms of cycles of a sine-type wave, because of the resemblance. Each change of sign of the yaw force represents the shedding of a vortex (release from the feeding sheet), as described above, and the start of another half-cycle. Lamont (1985) observed that yaw-force distribution might not be cyclical if transitional boundary layer separation occurs on the forebody. If the distribution is cyclical, the first half-cycle will be low-amplitude and relatively short in axial distance.

Lamont & Hunt (1976) used detailed experimental data to assess the value of the IFA in describing the flow over a tangent-ogive forebody with a cylindrical afterbody. It was discovered that although the IFA was qualitatively correct, there were several major differences that were not correctly predicted: the amplitude of the yaw-force oscillation with axial distance decays to near-zero after three or four half-cycles; the oscillatory period is affected by α; very large yaw forces can occur at moderate α, especially if the forebody has a large fineness ratio. The last discrepancy was attributed to the affect of the forebody on the flow development.

1.2.5 Vortex Interaction

The forebody vortices can remain organized vortical structures for large distances in the axial direction, and can influence and interact with control surfaces in the case of missiles (Kiedaisch 1994), or with the vortices emanating from the leading edge of the wing and from the leading-edge extensions (LEX's) (Skow etal AGARD, 1976). These interactions are another concern for the aircraft designer, necessitating research into the flowfield on the lee side of the forebody to ascertain the strengths and trajectories of the forebody vortices.

1.2.6 Secondary Vortices

The nature and development with axial distance of the secondary vortices is still not well understood. The experimental work of Wardlaw and Yanta (1984) provided some insight, as the positions and strengths of the secondary vortices were presented for several angles of attack. Vanden and Belk (1993) used a thin-layer Navier Stokes code to compute the flowfield over a tangent-ogive forebody/afterbody and reported that the primary vortices interact with the secondary vortices to a greater extent in subsonic flow, as compared to supersonic.

1.2.7 Dominance of the Nose Tip Geometry

The asymmetric flow over a slender forebody has been clearly shown to be dominated by the nose tip geometry (Moskovitz et al. 1989, 1991, Hunt and Dexter, 1979). As discussed previously, micro-asymmetries very near the tip of the slender forebody cause the flow separation pattern to become slightly asymmetric. Asymmetric flow separation that occurs near the tip leads to an globally asymmetric flow pattern. Essentially, the geometric disturbance may be thought of as a small perturbation that

activates the hydrodynamic instability, which exists in the flow at high angles of attack. The forebody cross-sectional diameters grow in the axial direction, and any micro-asymmetries present where the diameters are small can greatly distort the overall shape of the body as far as the flow is concerned, asymmetrically affecting the nature of separation. Thus, it must follow that the critical angle α_A (near $\alpha = 2\delta$) at which the asymmetry is first seen is the angle at which the initial separation occurs at an axial location of sufficiently small diameter so that the existing micro-asymmetries are locally large enough to distort the developing flow. Any asymmetry in the tip flow is amplified by vortex interaction as it convects (the essence of the hydrodynamic stability), so that the tip of the slender forebody dominates the entire flow.

Because minute changes near the tip of a slender forebody can cause large changes in the flow, many investigators have not been able to show repeatability in their own measurements. Examples of this repeatability problem may be found in Lamont & Hunt (1976) and Hunt (1982). Obviously, there also exists a palpable inability to reproduce the results of others, leading to conflicting theories about the nature of the flow and the generation of the asymmetries. The fickle nature of the effects of nose geometry has caused frustration among experienced investigators and is probably the foremost reason the slender forebody problem has been tough to solve.

As might be expected in a situation where such a small portion of the flow has global implications, there are many parameters that can alter the entire flow because they affect the flow in the vicinity of the nose tip. Freestream turbulence (see section on natural unsteadiness below), surface roughness and perturbations, forebody cross-sectional geometry, nose bluntness, the roll angle (ϕ) and the Reynolds number are all known to affect the asymmetry in the vicinity of the tip.

1.2.8 Surface Perturbations

Surface perturbations have been shown to affect the asymmetry because they cause changes in boundary layer transition near the point of initial flow separation, which in turn affects the nature of flow separation. The perturbations are much more effective when placed close to the tip of the forebody, where they act as large versions of micro-asymmetries. They may be used when the investigator wishes to ensure that the flow asymmetry is stable, because the inherent micro-asymmetries produce asymmetric patterns that may have some degree of natural unsteadiness.

Moskovitz et al (1989,1991), performed a detailed investigation into the effects of perturbation size and location on the flow asymmetry. They discovered that small imperfections were, in many cases, as good as or better than large imperfections at producing flow asymmetry. They also noted that for a given body and freestream conditions, there was a maximum amount of vortex asymmetry that could be produced, which did not depend on the bluntness of the forebody. The latter conclusion has been substantially confirmed in experimental investigations by Hoang and Telionis (1990,1991) and Roos (1994, 1996), both of whom showed that surface disturbances (geometric or mass flow) could produce asymmetric flow over hemisphere cylinders. Degani (1991) computationally confirmed the possible saturation of the asymmetry. From a control standpoint, the most important result of Degani (1991) was that perturbations located ±135°-140° from the windward ray produced the largest flow asymmetry. Those investigators applying control techniques quickly realized that actuators positioned near ±135° were most effective.

1.2.9 Surface Roughness

Surface roughness elements applied near the nose can affect transition of the boundary layer, causing it to become turbulent before separation would naturally occur. Because of the premature transition, the flow stays attached longer than it would if it were laminar, affecting the position of the separation line, the resulting vortex, and the degree of asymmetry.

1.2.10 Blunted Slender Forebodies

It has been shown that blunting the nose is a practical method for reducing the asymmetry of the flow, and therefore is considered a passive method of flow control (see Forebody Flow Control). One possible drawback of blunting the nose could be an adverse affect on the aerodynamic qualities of the missile or aircraft (especially during supersonic cruise) due to possible changes in shock attachment and/or orientation.

The effect of blunting the forebody is twofold: First, the amplitude of the first half-cycle of the sectional yaw-force distribution is decreased. Second, the shedding period is usually increased. For the case of the forebody alone, the net result is a decreased yaw force. However, when an afterbody is added, the longer extent of the first half-cycle at reduced amplitude can mean an increase in the overall yaw force.

With respect to the fluid mechanics, two conclusions with respect to nose bluntness can be drawn: Blunting the nose serves to increase the local diameter where separation first occurs, so that any micro-asymmetries present are locally less large in comparison; the blunted nose distances the developing vortices, decreasing their interaction and delaying or eliminating the flow asymmetry.

1.2.11 Forebodies with Non-Circular Cross Sections

Changing the cross-sectional geometry near the tip can affect the asymmetry. In particular, using an elliptical shape with the major axis aligned perpendicular to the cross flow will tend to decrease the asymmetry of the flow. This decrease in asymmetry results from the vortices being distanced from one another by the elongated cross-section, thus decreasing their mutual affect. While the elliptic cross-sections decrease the amount of asymmetry, they also decrease α_S, regardless of the orientation of the major axis (Keener et al. 1977). A chined forebody, where the flow separation is from sharp edges, produces no yaw force at any angle of attack. Many other cross-sectional shapes have also been used, mostly in attempts to decrease or eliminate the asymmetry altogether. Moskovitz et al. (1991) designed a special forebody tip that blended elliptic to circular cross-sections. The effect of this tip was to produce a yaw-force that was nearly sinusoidal with ϕ, the advantage being that the behavior of the yaw force would be easier to predict.

1.2.12 The Flow as a Function of the Roll Angle (ϕ)

It is not surprising, given the dominance of the tip geometry, that changing the roll angle φ of the slender forebody can change the strength of the asymmetry. There is evidence indicating that the oscillatory nature of the yaw force results from the rotation of the forebody, specifically the rotation of the geometric asymmetry present near the nose. An important result of the flow being a function of roll angle is that in order to ensure that all possible flow states have been defined, it is necessary to perform tests where the roll angle is varied. Failing to perform such tests may cause the investigator to misinterpret the results, including possible omission of maxima or minima in the parameters of interest.

Like the yaw force, the normal force is also a function of roll angle, although its variance with ϕ is weaker. This effect is due to the changing position of the wake vortices with ϕ. As the roll angle is varied, these vortices may move closer to body, causing a lower pressure, or they may move farther away from the body, increasing the pressure directly aft.

As α is increased past 50°, the yaw force varies with roll angle in a different manner, which reflects a subtle but important change in the flow state. Evidence again indicates that there is no roll angle for which a zero yaw force exists, and the asymmetry of the flow is restricted to just two states. This peculiar behavior is the result of the change in the type of hydrodynamic instability that causes the asymmetry. These types of instabilities and their effect on the flow over a slender forebody are discussed next.

1.2.13 The Concept of Hydrodynamic Instability and Application to the Slender Forebody Problem

Convective and Global Hydrodynamic Instabilities

The definitions of convective and global hydrodynamic instabilities are taken from the discussion by Tobak, et al. (1990). A convective instability will amplify space-fixed time-fixed disturbances. Temporal disturbances will only be amplified during the time in which they are applied. Once temporal disturbances are removed, flows governed by convective instabilities will return to the undisturbed state. An example of a flow governed by a convective instability is flow over an airfoil, where a surface perturbation could cause massive flow separation. However, removal of the perturbation will return the flow to the undisturbed state. Global instabilities amplify all disturbances, and the flow will remain disturbed even after the removal of a temporal disturbance. An example of a flow produced by a global instability is the von Karman vortex street.

One of the strengths of inviscid vortex-lattice and vortex-filament codes when applied to the slender forebody problem was the ability to show what types of vortex configurations were possible in the absence of viscous effects. Due to the results of several investigations of this type, it became apparent that vortex asymmetry could exist, even with symmetric separation. Evidence of this kind gave strong indications that the vortex asymmetry was most likely due to a hydrodynamic instability of some type that did not seem to depend upon viscosity to exist.

Questions concerning the existence and nature of the instability persisted, and were points of argument for more than a decade. However, several investigations (experimental and computational) by Degani and colleagues gave much-needed insight into the characteristics of the instability. Using a thin-

layer Navier-Stokes code, Degani & Schiff (1991) computed flows over a 3.5 caliber tangent-ogive cylinder at $\alpha = 40°$ and found that the flow was symmetric to 12 orders of magnitude. In order to trigger flow asymmetry, a small perturbation was placed near the nose, and the flow became asymmetric. When the perturbation was removed, the flow returned to the symmetric state, giving strong evidence that the flow asymmetry is governed by a convective instability. An investigation by Degani (1991) into the effect of placing minute disturbances close to the tip of the forebody provided further confirmation.

In experimental work, Degani & Tobak (1991) used a fine wire protruding from the forebody tip to disturb the flow. The length of wire that protruded from the model could be finely controlled. At angles of attack above = 50° where it was previously thought that a true bistable state existed, intermediate states of near-symmetric flow were observed. The conclusion was that although the asymmetry was very sensitive to disturbances and tended toward bistability, the existence of symmetric states showed that the flow was still under the influence of a convective instability. Tobak, Degani & Zilliac (1990) attributed the existence of the nearly bistable states to the fact the forebody vortices were no longer responding to body geometry.

At angles of attack less than 50°, a convective instability is responsible for the asymmetry of the flow over a slender forebody. In this case, the instability is perturbed by the geometric asymmetry near the tip of the forebody. Asymmetrically affected separation lines lead to vortex asymmetry, which in turn affects the separation lines on the body. In this manner, the asymmetry is amplified as the flow convects down the body. The convective instability produces a flow in which the tip geometry itself is truly dominant and governs the flow. The vortices themselves do not generate the asymmetry, but only serve to amplify the flow asymmetry once it is produced by the geometric asymmetry. When under the influence of a convective instability, the yaw force as a function of roll angle is a continuous variation..

When $\alpha > 50°$, there is a possibility that the convective instability will become a global instability. A global instability is present when a flow can induce the instability upon itself. In other words, no external disturbances are required for the instability to occur. In the case of the slender forebody, the asymmetry is caused by a global instability when the vortices shed from the tip induce disturbances in the flow at the tip that can be greater than the geometric disturbance. The vortex asymmetry is then self-induced, and can lock the vortices into a new configuration.

Dependence of the Hydrodynamic Instability Type on Reynolds Number

The reason there is only a possibility of the global instability being present when $\alpha > 50°$ is because the change from one type of instability to the other is dependent on the Reynolds number. Bernhardt and Williams (1990) Have demonstrated the dependence of the maximum yaw force with Reynolds number for a cone-cylinder at $\alpha = 55°$, but it is more illuminating in the definition of the different states of the flow, which are governed by the type of instability that is present. Although the appearance of the asymmetry is an inviscid phenomenon, this dependence of the instability type on the Reynolds number suggests that viscous effects near the tip are in part responsible for specific flow characteristics.

At Reynolds numbers below $1 \cdot 10^4$ a bistable state exists, and it is characterized by two and only two distinct values of the yaw force. No intermediate values of the yaw force exist. The asymmetry will switch sides only if a disturbance of sufficient magnitude is applied. This behavior leads to hysteresis as the disturbance strength and direction are varied. As the Reynolds number is increased beyond $1 \cdot 10^4$, the flow enters a two-state mode. Here, the hysteresis effect disappears, but the asymmetry still locks in one of two possible positions. For Reynolds numbers over $3 \cdot 10^4$, the yaw force is a continuous function of ϕ. In this continuous state, intermediate values of the yaw force are possible, meaning that a variety of vortex positions and strengths exist, depending on the circumferential location of the geometric disturbance. In this state, the flow is influenced by a convective instability.

1.2.14 The Flow as a Function of the Reynolds Number

The Reynolds number for the slender forebody is usually expressed with the forebody base diameter D as the characteristic length. Besides determining the type of instability present in the flow, as discussed previously, the Reynolds number also characterizes the state of the boundary layer before separation. Initially, investigators tried to correlate Reynolds number effects of the slender forebody to the two-dimensional cylinder in crossflow, where the critical Reynolds numbers were well known. Some of the methods are based on a strict application of crossflow theory, where the crossflow velocity, $V \cdot \sin\alpha$ was used in the calculation of the Reynolds number. Other methods make use of a varying characteristic length (such as $D \cdot \csc\alpha$). As might be expected, the complex flow over the slender forebodies did not lend itself easily to such correlation, and no simple theory existed that explained all the forebody effects in terms of crossflow over a two-dimensional cylinder.

Investigations by Lamont (1986) contributed greatly to present knowledge concerning the effect of Reynolds number on the flow over slender axisymmetric bodies. These investigations involved the acquisition of circumferential pressure distributions over a tangent-ogive forebody (fineness ratio 2) with attached afterbody for many angles of attack and Reynolds numbers in laminar, transitional and turbulent regimes. These pressure distributions were acquired at spacing of D/2, allowing the pressure measurements to be integrated along the body to produce overall yaw forces.

Using results from investigations by Poll (1982) to determine the states of the boundary layer based on circumferential pressure distributions, Lamont was able to identify laminar, transitional and turbulent separation on a 3.5 caliber tangent-ogive cylinder. Lamont showed that laminar and turbulent separation produced sectional yaw force distributions that were qualitatively similar in nature, and produced larger maximum yaw forces than transitional separation conditions. In general, this conclusion confirmed the findings of other investigators. However, it seems that under certain circumstances (See Hunt Review), the maximum yaw force may be produced by transitional separation. This has led some researchers to claim that the maximum yaw forces are produced in the transitional regime. Although this point has been hotly disputed, it must be stressed that the majority of the data is in opposition to the latter claim.

Lamont (1985) has shown that the critical Reynolds number defining the boundary between laminar and transitional flow is approximately $2 \bullet 10^5$, and varies little with change in the angle of attack. However, the critical Reynolds number boundary between transitional and fully turbulent separation of the boundary layers is a strong function of the angle of attack. It is expected that the results would vary slightly with a change in forebody fineness ratio, but that the trends would remain the same.

Keener (1986), in his extensive, seminal work on visualization of forebody separation, qualitatively corroborated these findings by analyzing the separation geometry as a function of Re_D. In addition, Keener was able to show that boundary layer separation of all three types could occur simultaneously on the forebody: Laminar separation near the nose, transitional in the mid-section and turbulent for the remainder.

Lamont discovered that the results in the laminar and turbulent ranges were repeatable for the same Re, α, and ϕ, while the results with transitional separation were not repeatable. Lamont's pressure distributions showed that laminar and turbulent boundary separation produced nonzero yaw forces through asymmetry of the flow ahead and behind the separation lines. This behavior suggests that the

asymmetric wake is dominating the separation of the boundary layers, in a manner qualitatively similar to the impulsively started cylinder in crossflow. In contrast, the yaw forces produced by transitional separation were due only to flow asymmetry ahead of the separation lines, as the pressure distributions showed symmetric flow after separation. Interestingly, Lamont determined that transitional separation can produce yaw forces that are practically zero (indicating symmetric vortex formation) or yaw forces of similar magnitude to those produced through turbulent or laminar separation.

It is important to note that for most testing where the yaw force is of interest, the Re_D should be at least 2-4 million in order to ensure fully turbulent, full-scale Reynolds numbers for all relevant angles of attack. Assuming a base diameter of 15 cm (about 6"), and a standard atmosphere, the freestream velocity would need to be approximately 380 m/s (above Mach = 1, unless the tunnel could be pressurized) to achieve the required Reynolds number. Obviously, needing to work at these velocities can be prohibitive, and therefore it is difficult to perform tests at full-scale Reynolds numbers, where the results would be of the most use. Fortunately, Hall (1987) have investigated the possibility of using artificial roughness elements to achieve turbulent boundary layers, and have shown that it is possible to have fully turbulent separation at Reynolds numbers as low as $2 \bullet 10^5$.

1.2.15 Tip Reynolds Number (Re_t)

Bridges and Hornung (1992) have suggested that because of the inherent dominance of the tip geometry that the characteristic length for determining the Reynolds numbers should be the nose tip radius, resulting in a tip Reynolds number (Re_t). Although the laminar/transitional and transitional/turbulent boundaries were determined as a function of Re_t, the results were not strong enough to coerce investigators to stop characterizing flows using Re_D. For bodies with sharp tips (no tip radius), it was suggested that the local radius or diameter be used as the characteristic length. The Reynolds number in this case would be a varying quantity, being zero at the nose tip and increasing to Re_D at the end of the forebody. This suggestion is not without merit, for Lamont (1985) showed that using the local sectional diameter produces a good collapse of the boundaries between laminar/transitional separation and transitional turbulent separation.

1.2.16 Effect of Re_D on the Asymmetry Onset Angle (α_A)

Stahl and Ashgar (1996) showed that the angle of attack at which the asymmetry is first observed is a weak function of the Reynolds number, so that for tests performed at low Reynolds numbers, the conical forebody tended to first exhibit asymmetric flow at $\alpha_A > 2\delta$. As the Reynolds number is increased, it was seen that the values for α_A coalesced with the previously known angle of onset, $\alpha_A = 2\delta$. The fact that the asymmetry the onset is a function of the Reynolds number was foreshadowed in tests performed by Zilliac (1989). Stahl and Ashgar surmised that the onset of asymmetry may be characterized by the ratio of vortex strength to separation distance, but more information is necessary to confirm this theory.

1.2.17 Compressibility Effects: The Slender Forebody Flow as a Function of Mach Number

Because of the geometric similarities, the generic slender forebody at incidence is more closely related to missiles than to aircraft. Since missiles are unmanned, they are able to perform drastic maneuvers at high speeds. This is in contrast to aircraft, where maneuvers are many times limited by the physical capabilities of the pilot, and thus are performed at Mach numbers well below the transonic range. Therefore, it is not surprising that the topic of a large number of investigations (Bannik and Nebbeling 1978, Graham and Hankey 1982, Keener 1986, Pagan and Molton 1991, Thomson and Morrison 1991, Wardlaw 1974, Schiff et al. 1991 Vanden and Belk 1993) is the flow over slender axisymmetric at high Mach numbers, since it is this regime where the missiles operate.

Many investigators have shown that the yaw force on slender bodies decreases as the Mach number increases (Keener and Chapman 1977). In fact, as M_∞ approaches the sonic level, the yaw forces consistently drop to near zero. This result parallels that of a 2D cylinder in crossflow, where the time-dependent side force nears zero in the transonic range. In the 2D case, the vortex shedding location moves from the cylinder to the wake neck at high Mach numbers, thereby reducing the flow transience in the vicinity of the cylinder. Note that the flow asymmetry still exists, but its effect on the body is limited by the shock pattern. One exception to the rule appears to be a slender body of elliptic cross-section with the major axis parallel to the angle of attack plane. Keener et al. (1977) discovered that for this body, the yaw forces remain large up to M = 0.70.

1.2.18 Natural Flow Unsteadiness

There have been relatively few investigations into the natural unsteadiness of the flow over slender forebody/afterbody combinations. In fact, several investigators performing tests on isolated forebodies in low-turbulence airstreams reported that the wake flow was without noticeable natural unsteadiness, except perhaps near angles of attack near the occurrence of maximum overall yaw force.(Keener 1986, Zilliac 1989) However, Wardlaw & Yanta (1984) determined that the fluctuations in surface pressures were lowest when the sectional side force at that location was highest. The lack of natural unsteadiness has been observed in computational efforts as well (Graham/Hankey, 1982)

Thomson & Morrison measured the frequencies in the wakes of several slender bodies and compared the results to those predicted with the IFA. They concluded that the flow may be qualitatively modeled by the IFA, but the relation was far from exact. In particular, the Strouhal numbers predicted by the IFA were equivalent to those seen behind a 2D cylinder.

Peake, Owen and Higuchi conducted an investigation into the nature of the boundary layer and free shear flow over a cone for $M > 0.6$, and it was noted that for $\alpha/\delta > 2.5$, the vortical flow unsteadiness increases. The surface pressure fluctuations were found to be minimum at the primary separation lines and maximum at the primary reattachment point. The authors noted that the behavior of the pressure fluctuation extrema was directly opposite to that observe during investigations of 2D boundary layers

In an investigation of a blunt forebody, Hoang & Telionis (1991) determined the dominant frequencies of vortical heaving in the wake of a hemisphere cylinder and the change of the frequencies with angle of attack. Lowson & Ponton investigated symmetry breaking of conical flows, and they described a possible mechanism for vortex interaction (see section on wake vortex flow above).

The most detailed investigation into natural unsteadiness was performed by Degani & Zilliac (1990), who found three types of fluctuation in the wake of a tangent-ogive cylinder/afterbody. Low-frequency fluctuations corresponded to vortex shedding in the manner of the von Karman street, while high-frequency fluctuations were most likely caused by shear-layer instabilities. In addition, moderate frequencies were discovered, and it was thought that they were caused by vortex interaction, but further investigation was required to be certain. It should be noted that there is a distinct possibility that for given freestream conditions and model orientation there is a unique type of unsteadiness produced by

each of the three axial regimes visualized by Ramberg (1983) and described by Tobak, Degani and Zilliac (1990).

At very high angles of attack, the flow is nearly bistable. The fact that intermediate states do exist was observed by Degani & Tobak (1991) (see Convective and Global Hydrodynamic Instabilities above). A theoretical discussion concluded that the presence of natural unsteadiness enables the intermediate near-zero states. That is, the flow asymmetry switches sides with frequencies large enough so that the time-averaged yaw force is near zero.

Lamont & Hunt (1976) and Hunt & Dexter (1978) stressed the importance of testing slender forebodies in low turbulence environments with rigid model mounts. Freestream turbulence increases the amount of natural unsteadiness inherent in the problem, which can result in meaningless time-averaged data due to severe fluctuations in the measured quantities. Lamont & Hunt also determined that the level of unsteadiness varied with the roll angle (ϕ).

1.2.19 Effects of the Presence of an Afterbody

Keener, Chapman and Kruse (1976) determined that the addition of an afterbody had no substantial effect upon the forebody flow. However, the addition of an afterbody can affect α_S and the magnitude of the yaw force that exists for the combination of bodies.

Addition of an afterbody may potentially decrease α_S, especially if the afterbody fineness ratio is large. Far from the nose region, the instability that governs the flow is a global type (see Convective and Global Hydrodynamic Instabilities), being basically the same instability that leads to alternate shedding of vortices in the case of the 2D cylinder in crossflow. The onset angle of this asymmetry may be lower than that or the onset of the convective instability that occurs on the forebody. Thus, the flow over the afterbody may become asymmetric while the flow over the forebody is still in a symmetric state.

The presence of an afterbody may drastically affect the nature of the measured yaw force, due to the nature of the yaw-force distribution with axial distance. The yaw-force distribution, whatever it may be for a particular body geometry, orientation and freestream conditions, is allowed to extend to the afterbody. One example is that when dealing with a forebody alone, blunting the tip almost always reduces the yaw force from the unblunted state. However, because the first half-cycle of the yaw-force

distribution is now allowed to extend (even though its amplitude is decreased) to an afterbody, the overall yaw force may be increased.

1.2.20 Comments on Experimental Investigations

Because of the limitations of theoretical and (until recently) computational approaches, the slender forebody problem has been attacked mainly through experimental techniques. Normally, investigations over a particular geometry are carried out so that certain parameters are isolated. Most researchers concerned with aircraft and missile forebodies would like to have variations of the yaw and normal forces with angle of attack for various Reynolds and Mach numbers. Ideally, as in the case of geometries that have little separated flow or constrain separation to occur at sharp edges, the force variations should be universally valid for the given test conditions. However, in the case of the slender forebody, the model roll angle, flow unsteadiness and nominally small changes in model geometry (especially near the forebody tip) contribute to nonrepeatability and inconsistency of investigations. Also, there has been some past difficulty (partially remedied) in determining the effect of the Reynolds number.

1.2.21 Comments on Computational Investigations

Except for the lowest angle-of-attack regime, where $\alpha < 5°$, it is almost impossible to determine the flowfield and pressure distribution in a theoretical fashion for angles of attack where separation occurs. For this reason, experimental investigations have made up the bulk of the research on this subject, especially before the late 1980's, at which time the available computing power had become sufficient to enable meaningful computational investigations to be undertaken with viscous codes.

Computational efforts involving inviscid codes can be classified as either two-dimensional or three-dimensional. Because of the lack of computing power, early computational investigations attempted to use crossflow analogies and relations to determine the nonlinear aerodynamic coefficients. That is, the flow about the circular cross-section of the forebody (the y-z plane in Figure 4) at a particular axial location was treated as completely separate from axial component of the flow (the x-direction in Figure 4), resulting in what was essentially a two-dimensional problem. It was soon established that two-dimensional analyses of forebody flows were very restricted in their accuracy because of the need to fit the underlying assumptions and because the actual flow is strongly three-dimensional in nature, profoundly affecting the development of the boundary layer.

Initial investigations with three-dimensional inviscid codes used traditional panel-type codes normally used with lifting surface configurations. The major drawback in the use of these codes was that the wake structures need to be known or determined a priori. The accuracy of these linear methods was compromised, even at low angles of attack, because of the strong nonlinearities present due to the interaction between the vortices themselves and between the vortices and the body.

As three-dimensional vortex-lattice codes showed usefulness in accurately predicting the flowfield and lifting forces on many configurations, they were employed in the slender forebody problem. These codes were able to determine the position of the wake vortices and the corresponding pressure distributions on the forebody simultaneously, so that the nonlinear effects could be modeled. Investigations using the vortex-lattice codes were able to predict the aerodynamic coefficients within the spread of experimental data. The one major drawback in their use is the need for separation criteria, because bluff-body separation is not well defined. Using minimum pressure coefficient criteria in a crossflow plane has not proven to be as reliable as using experimental data as a basis for the separation line locations. Unfortunately, this enslaves the computational work to experiment, which is a handicap because of the density of experimental data needed to define the separation lines, and because the experimental work itself is subject to several difficulties as outlined above.

It can be stated that, in general, the only computational investigations that can reasonably predict the nature of the flow over a slender forebody above $\alpha = 5°$ are nonlinear vortex-lattice codes and viscous codes. These succeed because they correctly model the three-dimensional nature of the flow and for the nonlinear interaction of the wake vortices and the body.

The advent of time-dependent Navier-Stokes computations enabled investigators to calculate surface and flowfield quantities at a large number of points. Appropriate turbulence modeling was introduced by Degani and Schiff (1991) Zilliac (1986, 1991). Hartwich & Hall (1990) computed flows where laminar separation followed by transition, reattachment and subsequent turbulent separation was modeled.

Because the viscous codes were complex and computationally intensive, and because the nature of the problem disallowed the use assuming symmetric flowfields at high α, these codes were very expensive and time-consuming to execute. However, they provided much-needed insight into the nature of the three-dimensional flow, providing information on vortex trajectories, streamlines, velocity fields,

surface skin-friction lines, helicity, surface pressures and forces that generally compared well with experimental data. The only real drawback is that data exists only for selected angles of attack, roll angle and body geometry, due to the extraordinary computing expense.

Perhaps the greatest contribution that has been made by the Navier-Stokes codes has been in the area of assessing the nature of the instability that governs the flow. In computational investigations, it has been possible to compute perfectly symmetric flows at angles of attack where such flows cannot exist experimentally (Degani & Schiff 1991). Given such a flow, its reaction to disturbances can then be determined.

1.3 Slender Forebody Vortex Control

1.3.1 Introduction

Even before the flow over slender forebodies was well understood, many researchers attempted to alleviate the problem, and return the flow to a symmetric state. Control mechanisms have evolved to be more complex and effective, due mostly to a better grasp of the underlying fluid mechanics around the forebodies at high incidence. The past decade has seen a large number of investigations devoted to the subject of forebody vortex control. Methods used for the control of forebody flow falls into two broad categories: Passive and active.

One reason why forebody vortex control has excellent potential is that it can provide large yaw moments at $\alpha > 35°$ where the rudder starts to degrade and to higher angles of incidence where the rudder eventually becomes ineffective. On the other hand, forebody vortex control cannot provide a substantial moment for $\alpha < 35°$, because the flow instability that is leveraged does not lead to a sufficiently strong flow asymmetry. It is obvious that conventional and forebody vortex control methods complement each other throughout a large range of incidence angles. By applying a control method that uses both conventional and forebody vortex control techniques, substantial control can be applied to angles of attack of 65° or more.

It is important to remember that in order for a control method to be truly effective, it must be able to be installed inside or on the forebody of an actual production flight vehicle. For this reason, it is important that the control system be lightweight, low in volume, and not require a large amount of the

energy resources of the aircraft, missile or spacecraft. These are typical concerns when considering an active control system.

Testing of Complete Configurations

Many investigators have found that a control technique that is effective for forebody-alone testing is rendered ineffective because the forebody vortices interact with other vortical structures. In general, it appears that vortices generated by upstream structures or disturbances can be dominated by strong vortices (usually generated by sharp-edged separation) that originate downstream. For example, nose-boom strakes are rendered ineffective by forebody strakes, which are in turn dominated by chine vortices, which are dominated by the LEX vortices. Because the vortex interactions are difficult to model can induce forces and moments that cannot be easily predicted, it is imperative that complete configuration testing take place before a particular control method can be qualified as applicable.

1.3.2 Passive Control Methods

The goal of passive control is to force the flow over the forebody to be symmetric over the wide range of flow conditions experienced during application. Common passive control techniques include blunting the forebody, modifying the forebody cross-sectional geometry, adding strakes, chines or nose booms, employing grit strips or rings to affect the nature of separation, and using a porous forebody. The disadvantage of passive control is that it can univocally defeat (at all angles of attack) the tendency for the flow to become asymmetric, so that a possible source of yaw control is neglected.

Geometric Modifications

The extent to which forebody tip geometry dominates the flow has been demonstrated beyond any doubt. Therefore, any alteration of the forebody geometry could be construed as an attempt to control the flow. Blunting the forebody is a proven method for reducing the amount of natural asymmetry generated by the forebody (Roos and Magness 1993), as is changing the circular cross-section to a more elliptic shape with the major axis perpendicular to the crossflow (Smith 1994). Moskovitz et al. (1991) designed a forebody tip with cross-sections that were an elliptic-to-circular blend. This tip succeeded in producing a near-sinusoidal, regular, repeatable and predictable yaw force distribution with roll angle.

Forebody Strakes

Strakes attached near the tip of the forebody can be very effective flow control devices if properly sized, shaped and located (both circumferentially and axially). Strakes may be added to a forebody that has static yaw instability in order to produce an aircraft with more desirable stability characteristics (Cornelius and Lucius 1995). Large symmetric strakes can dominate the forebody flow, all but eliminating the asymmetric flow at high angles of attack (Modi et al. 1992, Fu and Lan 1992,). However, if small strakes are wisely placed, they can be just as effective, because they can impact the flow in a location that provides more leverage (Malcolm and Ng 1990).

Because the location of the strakes can greatly affect the flow (Ng and Malcolm 1991), and because small strakes can be effective, it appears likely that the strakes act as large geometric perturbations, impacting the vortical flow through displacement effects rather than by injecting additional vorticity or momentum. Strakes are generally ineffective at low to moderate angles of attack ($\alpha < 30°$), and generate the largest changes in the flow for $\alpha = 45° - 60°$. This range depends on configuration to a great extent (Malcolm and Ng 1990, Modi and Stewart 1992),. This result could be expected if strakes are acting as geometrical disturbances, because the angle of attack needs to be sufficiently high so that they can perturb the inviscid flow. Given that the circumferential location for a disturbance to have maximum impact on the flow was found to be near $\theta = \pm 135°$ from the windward ray, it is not surprising that strakes were found to have considerable control power when placed between $\theta = 105° - 120°$, generating yaw moments of nearly the same magnitude as those generated by the rudder at lower angles of attack (Rao et al. 1986, Malcolm and Ng, 1990).

Although disturbances located windward seem to reap the most benefits in terms of available control power, that location may not be the best choice, depending on the results one wishes to achieve. For example, Rao et al. (1986) showed that two strakes located at $\theta = \pm 120°$ and deployed symmetrically did not necessarily produce symmetric flow, although a single strake was able to cause considerable yaw moments. In contrast, Rao & Sharma (1994) examined deployable strakes on the windward side of a forebody of diamond-shaped cross-section and found that symmetric deployment resulted in zero yaw force in the mean, to $\alpha = 70°$. They also discovered that the strake deployment increases suction on the windward side of the body, and decreases the leeward suction, so that up to a 30% reduction in C_N can be achieved at high angles of attack.

Chined Forebodies

The chined forebody has become popular for three reasons: (1) Its radar profile is much less than the standard unchined forebody; (2) Like strakes, chines give better yaw directional stability characteristics to the forebody; (3) Because separation is now restricted to the sharp edge of the chine, a chined forebody produces strong, symmetric vortices at all angles of attack. Having already shown that chined forebodies at incidence were free of vortex asymmetries for $\beta = 0°$, Roos & Magness (1993) examined the yaw directional stability for a chined 3.5 caliber tangent-ogive forebody for $0° < \alpha < 60°$ and $-15° < \beta < 0°$. For $\alpha < 15°$, the flow over the forebody is attached, and the chined forebody is directionally unstable ($dC_n/d\beta > 0$) due to crossflow drag. For $15° < \alpha < 45°$, the chined forebody is directionally stable ($dC_n/d\beta < 0$) due to the existence of a vortex-induced restoring force caused by increased suction from the upwind vortex and decreased suction from the downstream vortex. However, for $\alpha > 45°$, the upwind vortex is strengthened to the point that premature vortex breakdown occurs, the restoring force is lost, and the forebody becomes directionally unstable. The stability results for $20° < \alpha < 40°$ were confirmed computationally by Ravi & Mason (1994) for flow over several chined tangent-ogive cylinders. In addition, they determined that the largest contribution to directional stability comes from the aft part of the forebody, where the chine sweep angle is almost 90°. Smith (1994) showed that the addition of chines to F-16 forebody produced more acceptable yaw stability characteristics, and that the chine vortices were immune to any influence from forebody strakes. Mendenhall & Lesieutre (1992) performed a computational potential flow investigation of the vortical flow over a chined ogive-type fighter forebody for angles of attack up to 30°. For up to 20°, the predicted leeside surface pressures are very close to those measured experimentally.

Addition of Nose Booms

Malcolm and Ng (1991) investigated the effect of adding a nose boom to the forebodies of fighter configurations, and discovered that the nose-boom wake tends to dominate the other sources of forebody asymmetry for moderate to high α. Modi & Stewart (1992) found that nose booms could reduce the yaw force on a conic forebody by 50%, but that in order to do so, the boom must be aligned precisely with the cone.

Porous Forebodies

One of the most ingenious passive control methods, initially developed by R.M. Wood and Bauer, is the porous forebody. By enabling instantaneous communication of pressures across the forebody, the asymmetries in the flow and yaw forces are alleviated. Modi & Stewart (1992) tested a forebody that was porous for the first 20% of its length, and found that the yaw force could be reduced up to 50% from the baseline case. A subsequent investigation by Modi et al (1992) showed that 86% of the yaw force could be removed through the use of porosity. It was suggested that microscopic porosity might be better suited for this type of application. Bauer & Hemsch (1994) confirmed the potential of this concept by showing that the yaw forces and flow asymmetry over a porous forebody could practically be eliminated. By comparison of normal force characteristics, they concluded that the porous forebody generates turbulent separation. Pressure sensors inside the forebody revealed that the pressure was constant and the velocity very low.

Other Passive Control Methods

Several other control methods have been applied, with varying results. Grit collars and strips have been shown to be lass than satisfactory. However, a specially designed vortex-generator collar proved very effective, reducing C_n by a factor of 2 from the baseline case. Degani (1991) showed that a splitter plate, installed along the leeward ray for the entire length of the forebody/afterbody combination, suppresses the formation of asymmetric vortices. It was noted that although the splitter plate was successful at removing the low-frequency instabilities associated with vortex shedding, the high-frequency fluctuations associated with shear-layer instabilities were still present.

1.3.3 Active Control Methods

Active control attempts to achieve full control over the magnitude and sign of the yaw force so that the flow may be forced to be symmetric, but the tendency for the flow to be asymmetric may be utilized for maneuvering when required. This type of control can be achieved using deployable surfaces that alter the geometry of the forebody, employing suction or blowing near the nose tip or by rotating the forebody at variable rates. Because the tip of the forebody plays a dominant role in the development of the asymmetric flow, employing air jets near the tip of the nose has proven to be an inviting and feasible method for vortex control. The disadvantage of the active control methods are that by their very nature they are much more complicated to apply, most likely requiring actuators of some sort and (at some point)

a feedback control loop. However, these obstacles can be overcome with some effort and the resulting expansion of control and flight envelope is definitely worth the expense.

Mass-Flow Injection

Injecting mass flow (or applying suction) from ports, slots or nozzles is an efficient and effective forebody control technique. Many different configurations have been tested, but most can be separated into three main categories: (1) Nozzle or jet blowing, (2) mass flow from tangential slots and (3) microblowing. Nozzle and jet blowing involves the injection of mass at high speed into the forebody vortices, directly affecting the vortex strength. Tangential slot blowing is the ejection of high-speed mass from slots into the boundary layer on the forebody. The slots are configured so that the slot flow exits tangent to the body. Microblowing, a forebody-vortex control technique developed by Roos (1994, 1996), involves the ejection of mass from forward-pointing nozzles very near the forebody tip.

In all three of the control techniques involving mass flow, the location of the mass-flow injection (or suction) port is very important. In general, higher control power is realized the closer the blowing/suction ports are to the forebody tip (Malcolm and Ng, 1990, LeMay et al. 1992). In the cases of nozzle and tangential slot blowing, the nozzle outlet configuration is an important parameter. For nozzle blowing, the orientation of the nozzle has a large bearing on its effectiveness. Perhaps the most important result is that all of the mass-flow injection techniques can achieve proportional control of the flow for at least some part of the range of mass flow. It appears that in order to exploit this trait, mass-flow controllers capable of extremely fine adjustments will be required, especially if control is desired at very high angles of attack.

Nozzle Blowing

Nozzle blowing is probably the most popular forebody vortex control technique involving mass flow. The In general, there are three types of nozzle blowing: Forward blowing, in which the nozzles protrude from the surface and face upstream; aft blowing, in which the nozzles protrude from the surface and face downstream face downstream; normal blowing, in which the nozzles are generally flush with the forebody surface and the mass flow is directed perpendicular to the forebody surface.

In all types of nozzle blowing, the ports are most effective when located on the leeward side of the model. Circumferential nozzle locations in the range from $120° < \theta < 135°$ have been shown to be

optimal. Nozzle mass-flow methods have been shown to alter the forebody flow by directly affecting the vorticity and velocity fields (Peake et al. 1980). Peake, Owen & Johnson (1980) suggested that leeward blowing techniques may have potential because the leeward enclosing saddle point is the location where disturbance amplification by the hydrodynamic instability first occurs. They also postulate that the shedding of vortices may be attributed to amplification of disturbances at secondary (interior) saddle points. Suction or blowing from the leeward surface has the potential to create disturbances in the vicinity of these saddle points, therefore it has the potential to affect the global flow.

Normal Nozzle Blowing

Normal suction or blowing is the easiest mass-flow control method to apply, because the angular orientation of the nozzle is not a parameter. Investigations by Guyton and Maerki (1992) on reduced scale fighter configurations with normal blowing ports located on the forebody at $\theta = \pm 135°$ showed that blowing induced a yaw force opposite to the blowing side. Wake flow visualization revealed that blowing displaced the vortex above the blowing port, which allowed the vortex on the opposite side to move closer to the body, increasing the suction on that side. Experiments performed by Bernhardt & Williams (1997) revealed that suction from normal ports can be more effective than blowing. The input-to-output power gain was about 108 at $Re_D = 3.0 \cdot 10^4$. In addition, they discovered that suction produces a side force towards the suction side, the reverse of the blowing effect. Based on flow visualization results (Guyton and Maerki (1992)), it appears likely that mass flow directed normal to the forebody surface acts as a displacement mechanism, rather than as a mechanism to inject energy or momentum into the vortical flow. However, an alternative explanation in which suction and blowing can alter the flux of surface vorticity delivered to the vortices has been suggested (Bernhardt and Williams 1995).

Aft Nozzle Blowing

Aft nozzle blowing can be an effective method of forebody vortex control for $\alpha > 30° - 40°$ (Lanser and Meyn 1994, Guyton and Maerki, 1992, Gittner and Chokani 1994, Malcolm 1991). For aft nozzle blowing, the ejected mass flow strengthens and adds momentum to the vortex on the blowing side and brings it closer to the forebody surface, while the vortex on the non-blowing side is weakened and displaced from the surface (Gittner and Chokani 1994). The net effect of the vortex manipulation is to produce more suction of the blowing side, thus producing a yaw force in that direction. The displacement of the non-blowing side vortex most likely occurs as an indirect result of the strengthening of the blown vortex. Further proof that aft nozzle blowing techniques operate by injecting momentum into the flow

comes from the fact that a blowing coefficient based on nozzle momentum (C_μ) scales the blowing effects across large ranges of M and Re_D (Mosbarger 1994).

Aft nozzle blowing has been shown to be more effective than both normal blowing and forward nozzle blowing (Malcolm and Ng 1990). The effectiveness of aft blowing can be greatly increased by canting the nozzles inward (Smith and Nunn 1976, Guyton and Maerki 1992), and altering the exit geometry. In fact, nozzles canted inboard at approximately 60° have been shown to give optimal flow control effectiveness for the F-16 (Mosbarger 1994) fighter configuration. It appears that this optimal angle is not a function of freestream conditions or model orientation.

Exit geometry has a strong effect on flow control effectiveness of the nozzle. Several investigators have shown that slotted nozzles provide greater control power. Gittner and Chokani (1994) determined that the most effective nozzles were those that had broad exits with area centers close to the surface rather than thin exits with higher area centers.

Tangential Slot Blowing

Tangential slot blowing has been shown to be a viable method of forebody vortex control at moderate to high angles of attack. Its main disadvantage is that it generally requires more mass flow than other methods to achieve similar results (Smith and Nunn 1976). Tangential blowing operates by energizing the boundary layer with a Coanda-type jet. This delays separation on the blowing side and results in a strengthened vortex with increased suction. The result is a yaw force to the blowing side. Control reversal has been documented however, especially in cases where the forebody is tested as a part of a complete aircraft configuration (Crowther and Wood 1993, Gee et al. 1994). The control reversal occurs because the strengthened vortex is susceptible to premature (with respect to the no-blowing case) vortex breakdown in the LEX or wing region, and may be due in part to interaction with LEX vortices. Careful placement and sizing of the slots can minimize this effect. Like aft nozzle blowing, tangential slot blowing effects scale well with the momentum coefficient C_μ, and less well with the mass flow coefficient $C_{\dot{m}}$ (Crowther and Wood, 1993).

One advantage of tangential slot blowing over nozzle blowing is its ability to remove an aircraft from “deep stall”. This condition occurs at high angles of attack when all available control mechanisms cannot produce a sufficient pitch-down moment to remove the aircraft from its stalled state. It has been

determined that symmetric tangential slot blowing at small rates can produce large pitch-down moments (LeMay et al. 1992, Guyton and Maerki 1992).

Crowther and Wood (1993) showed that vortex control could be exercised to $\alpha = 90°$, although slots along the entire length of the forebody and large quantities of mass flow are required. They also determined that moving the slot location windward increased the control power until "slot stall" occurred at a critical angle. Slot stall is characterized by a loss of yaw control moment and hysteresis in the C_n-α curve. Gee et al. (1994) found that slot blowing could alter the dominant frequency of flow fluctuations in the wake, showing that this type of control could be used to reduce buffeting of control surfaces.

Microblowing

Microblowing uses configurations that look similar to those employed in forward nozzle blowing. However, there is one important difference. The mechanism by which microblowing affects the forebody flow is a displacement effect rather than a momentum effect. In this way, it is more similar to normal nozzle blowing. Forward blowing from the leeward side at $\theta = \pm 135°$ near the forebody tip displaces the blowing side vortex in much the same way that a geometric disturbance would affect the flow. The displaced vortex weakens, the opposing vortex moves closer to the body and strengthens, with a resulting yaw force away from the blowing side. Roos (1994, 1996) has shown that microblowing effects scale with $C_{\dot{m}}$ rather than with C_μ, giving further credence to the claim that microblowing affects the flow through vortex displacement. The microblowing technique relies on affecting the flow very near the tip of the forebody, so that the disturbance has more control leverage.

Microblowing may be used with blunted forebodies so that the baseline flow is nearly symmetric. In these cases it was found that the amount of available control power that could be generated by microblowing decreased as bluntness increased (Roos 1996). The potential of microblowing may be seen in Roos' investigation of microblowing applied to a hemisphere cylinder, in which proportional flowfield control was achieved over a configuration which has naturally occurring symmetric flow at all angles of attack. It is interesting to note that for the hemisphere cylinder, microblowing produces a yaw force to the blowing side, opposite to that seen in the case of slender bodies.

Microblowing is effective for $\alpha > 35°$, but is most effective for $\alpha > 50°$, where it can produce yawing moment levels similar to other proven nozzle blowing configurations, but with 1% of the mass

flow rate (Roos 1996). Pulsed microblowing does not have a substantial benefit over steady microblowing (Roos and Manor 1997).

Rotatable Strakes

Ng & Malcolm (1991) investigated the effect of using circumferentially rotatable strakes. They were found to be an efficient method of vortex manipulation for $45° < \alpha < 65°$, but the control power was found to depend strongly on strake position and planform area. Dual strakes, in contrast to a single strake, allowed a continuous and relatively smooth variation of C_n with strake rotation. The strakes were also effective for $-20° < \beta < 20°$. It was thought that the ability to vary the angle between the strakes (it was fixed in these experiments) would provide added flexibility, which is the key to the application of many vortex control techniques.

Strake-blowing combinations have been found to be very effective. The strakes can be sized and located to provide symmetric flow and yaw stability at all angles of attack, and then mass-flow techniques can be applied in order to maneuver. Sizing of the strakes is very important, because large strakes large can interfere with the ability of the mass-flow control method to generate sufficient yaw power to maneuver.

Rotating Forebodies

Rotating all or part of the forebody about its axis of symmetry can produce symmetric or asymmetric flows. Levin & Degani examined the flow over a forebody with a rotating tip at spin rates up to 3.5x104 RPM, and observed that at high α and low spin rates, the flow was symmetric in the mean because the vortices were switching rapidly between opposed asymmetric states. As the spin rate increased, an asymmetric, steady vortical pattern presided. Modi and Stewart (1992) investigate spin rates up to 2000 RPM and found that for spin rates near 200 RPM, the yaw force could be reduced by up to 75% from the baseline case. Clark et al. (1973) performed cursory tests on a rotating forebody to determine the magnitude of the Magnus effects, which were determined to be small or nonexistent. Although these investigations were only preliminary, it is obvious that this method has potential for control of the forebody vortices through adjustment of the spin rate. However, there is some doubt as to the viability of this method during a maneuver, where the spin direction may have to be switched rapidly in order to maintain control. The feasibility of application of this method is questionable.

1.4 Three-Dimensional Separation over Slender Bodies: Natural and Forced Flow Unsteadiness

Closer to the problems discussed in this dissertation are problems involving unsteady motions, natural or externally driven. The author of this dissertation and his collaborators reviewed the literature in this area and published this material in the open literature (Zeiger et al. 2004). In this paper we reviewed the work on unsteady flows over slender bodies at incidence, but kept our attention on the basic character of unsteady three-dimensional separation and separated flow. In this sense, our understanding extends to other types of three-dimensional flows like flows over planar bodies and in particular swept wings. The separated region has a strong upstream influence and therefore controls its own origin, namely separation. The separated region is made up of rolled vortices that interact with each other. This interaction can take different forms which depend on the three-dimensional character of the vorticity content of the vortices and the direction of the outer flow. The term "outer" is used here as an extension of the term used in boundary-layer theory. In this theory we define as outer flow the flow outside the boundary layer. This is inviscid flow. In the case of separated flow, we could define as outer flow essentially the flow which was "outer" with respect to the boundary layer. This does not provide a distinction between the oncoming stream and the wake because the vortical structures entrain outer flow.

If vorticity at separation is normal or nearly normal to the oncoming free stream, then vorticity rolls into large structures which engage in a periodic-in-time, alternate shedding from the body. But the space in the wake is filled with "dead air". In fact, with vortices forming further away from the body, the wake region closest to the body is essentially filled with very slow moving fluid, and therefore the pressure there is essentially constant.

By introducing larger vorticity components normal to the separation line and larger outer-flow components parallel to the separation line, we essentially stretch the vortex sheets along their axes and convect the dead air downstream. Caution is necessary here, because gradually increasing the velocity component along the axis of the body is like starting from a 90° incidence and gradually decreasing it. Now more energetic vortices can be sustained next to the body. Eventually these vortices cease to shed and stay attached to the body. This does not mean that vorticity released at separation does not leave the vicinity of the body, it just convects along the vortex sheets that telescope away from the body.

The interaction of the vortices could lead to three distinct phenomena. The first is the common vortex shedding. This is the periodic-in-time shedding of vortices. The second is the development of steady but asymmetrically arranged in space vortices. In the first case, the patterns are periodic in time. In the second they are steady, but in a cross-flow plane, they are periodic in space. All vortices consist of vortex sheets which are fed with vorticity from the line of separation. These vortex sheets in both cases eventually are cut off from their feeding source. In the case of vortex shedding, they are released in the flow and drift downstream creating a von Karman vortex street. In the second case they eventually peel off the body. We call this "vortex separation". The term should not be confused with the term "flow separation". Vortices that separate from the body turn and realign themselves with the outer flow. The first process populates the far wake with vortices that contain vorticity nearly normal to the outer flow. These vortices are commonly known as rollers. The second process fills the wake space with vorticity parallel to the outer flow. This is essentially a swirling motion. These vortices are the streamers.

A third and less known and less understood process of vortex interaction is between vortices aligned with the flow. Streamers were thought of as being steady, but convincing, albeit limited evidence indicates that streamers undulate in time. We call this the "dancing" of vortices. Some researchers chose the term "vortex interaction" for this phenomenon of three-dimensional separated flow. We too are using this term but we believe that this choice is not appropriate, because all three of the processes discussed are due to vortex interaction.

In most of the work reviewed in Zeiger et al. (2004) these processes are discussed but so far we understand very little about how they interact and interfere with each other. One of the reasons is the fact that so far, both our experimental and computational tools were very limited. Now we should be able to map out the instantaneous velocity field in three dimensions and along many planes or other measuring or computational domains in space. Another area we need to extend our efforts is flows over larger Reynolds numbers. We do not expect that in this domain any new significant patterns or phenomena will be identified. Larger Reynolds numbers will induce turbulent flow sooner and therefore lead to turbulent separation. Such flows in a way may be more consistent and easier to reproduce. We believe that the effect on the wake shapes and modes of vortex interaction will again be significant for large-Reynolds number flows. The material presented in this dissertation may shed some light on such problems.

1.5 Overview of the Current Investigations

After a careful review of the literature, it can be concluded that the steady mean flow over a slender forebody/afterbody combination at incidence is relatively well understood. However, an extensive investigation of the instantaneous velocity and vorticity fields existing in the wake of a slender body have not been undertaken with the accurate time-resolved measurement techniques that presently exist. It also seems that there are some discrepancies concerning the natural unsteadiness inherent in the flow. Specifically, the unsteadiness as a function of axial distance and angle of attack has not been well documented on any slender body. Understanding the role of the natural unsteadiness is important in gaining a better knowledge of the slender forebody problem.

Given the great interest in aircraft and missile maneuverability, it is worth noting that very little is known about the fluid mechanics of maneuvering slender bodies. A great amount of literature documents the steady problem. However, the amount dedicated to the maneuvering problem (which by its very nature will probably be more difficult to understand) is very small in comparison. Much information is needed concerning the forces, moments, surface pressures, velocity and vorticity fields of slender bodies performing basic maneuvers such as pitching and coning (velocity-vector roll at incidence). Although the aircraft and missile design communities have been able to overcome the basic lack of understanding of the fluid mechanics to this point, it is obvious that with some understanding of the flow physics, future products could be much more efficient, reliable and effective.

Great strides have been taken in the last fifteen years in the field of forebody vortex control. However, with few exceptions, the control techniques have not been tested in a maneuvering environment, where the flow development is vastly different than in the steady case. Questions abound: Is the optimum controller placement the same for unsteady conditions as for steady? Is the same amount of deflection of/mass flow from the controller needed for effective operation in unsteady flow? The control mechanism can maintain steady symmetric flow, but can it return an unsteady asymmetric flow to a symmetric state? Perhaps most importantly, what delays can be expected between the application of the control mechanism and the response of the flow? The answers to these questions may be found by studying the effectiveness of proven steady flow-control techniques in the case of a maneuvering body.

In light of the literature review, the current investigation focuses on the unsteady flow over a 3.5 caliber tangent-ogive forebody with cylindrical afterbody (a typical combination). Below is a short summary of the remainder of the document:

Experimental Setup (Chapter 2):

In this section, the experimental setup and data acquisition process is documented for the facilities (ESM Water Tunnel, ESM Wind Tunnel and the VPI & SU Stability Tunnel) and types of data acquisition (surface pressure data, LDV, PIV). An error analysis is made for relevant quantities.

Natural Unsteadiness over a Stationary Slender Forebody (Chapter 3):

The natural unsteadiness that exists in the vortical flow as a function of the angle of attack: We hope to document the dominant frequencies and the corresponding mechanisms for the three regimes of vortex shedding described by Degani and Zilliac.

Unsteady Flow over a Forebody Undergoing Coning Maneuvers (Chapter 4):

Surface Pressures and Sectional Yaw Force Coefficients during Coning Maneuvers:

In Chapter 4, the fluid mechanics during coning motions (velocity vector roll) are documented. Specifically, time-dependent surface pressures are acquired at several axial locations on the tangent-ogive during coning motions of varying reduced frequencies and directions, and for several incidence angles of the model. By analyzing the pressures, and the sectional yaw-force coefficients resulting from the integration of the pressures, the response of the flow to the maneuvers is determined.

Moving Wall Effect:

The moving wall effect, developed and extended to the case of maneuvering slender bodies by Ericsson (1980, 1981) is an attempt to explain the effect of body motion on the development of the boundary layer and corresponding free shear layers. In the simplest terms, the moving wall effect states that body motion in the flow direction will delay separation, while body motion opposite to the flow direction will promote separation. This effect is very similar to that observed in the case of the two-dimensional rotating cylinder where Magnus lift is generated. Ericsson postulated that the moving wall effect is large for slender bodies in coning motions. The pressure signatures on the model are used as a

basis for a discussion of whether the moving wall effect properly explains the effect of the motion on the flow for the Reynolds numbers and reduced frequencies seen in these investigations.

Effectiveness and Applicability of a Vortex Control Technique:

The micro-blowing vortex control technique (proven for non-maneuvering conditions) pioneered by Fred Roos (1994, 1996) is applied to the maneuvering tangent-ogive cylinder. Data are acquired with and without the application of the control, and the results are compared in order to determine the effectiveness and control authority of the technique.

Unsteady Flow over a Forebody Undergoing Pitching Maneuvers (Chapter 5):

Laser-Doppler velocimetry (LDV) is employed to map out several planes of the velocity field over the tangent-ogive cylinder undergoing a pitching maneuver for different pitch axis locations. The data are analyzed to determine the nature of the flowfield delay. The ensemble-averaged velocity data are used to calculate the corresponding vorticity and turbulent kinetic energy fields. Symmetry and steady-state variables are defined and used to analyze the development of the flow. The flow topography is discussed.

Conclusions (Chapter 6):

The conclusions are summarized in Chapter 6. Recommendations for additional investigations and techniques are discussed.

Chapter 2 - Experimental Method: Facilities, Instrumentation, Data Acquisition and Reduction

"In our numerical work, if the data looks right, it probably is right." – Dr. Dean Mook, during a lecture in an advanced inviscid flow class focusing on panel and vortex-lattice methods.

"Matt, in experimental work, if the data looks right it's probably wrong!" – Dr. Ngoc Hoang (colleague of the author and former student of Dr. Telionis), immediately after hearing the quote above, as he pored over electronics and manuals in the hope of solving the latest in a long line of DyPPiR problems.

2.1 The Engineering Science and Mechanics Wind Tunnel

The Engineering Science and Mechanics (ESM) Wind Tunnel, constructed in 1983, is an open-circuit low-speed wind tunnel. The tunnel convergence has a contraction ratio of 5.2 to 1. The test section dimensions are 51 cm x 51 cm x 125 cm. Four nylon screens and one set of honeycombs placed near the entrance of the tunnel reduce the turbulence level. Adjusting the relative diameters of the drive pulleys sets the speed of the tunnel. At the time of testing, the tunnel was powered by a 5-hp motor, and could achieve free-stream velocities from 4 m/s to 13.7 m/s. The tunnel was fitted with a new fan and 15-hp motor in 2000, which allows operation at speeds in excess of 20 m/s. The turbulence level does not

exceed 0.51% at a free-stream velocity of 8.23 m/s, except for regions very near the tunnel walls, where the maximum turbulent intensity was measured to be 1.25% (Seider, 1983). The flow across the test section has a velocity variation of less than 2.5%. More information about the design, construction and calibration of the ESM Wind Tunnel may be found in Seider [1983]. A schematic of the ESM Wind Tunnel is shown in figure 2.1 (Klute [1999])

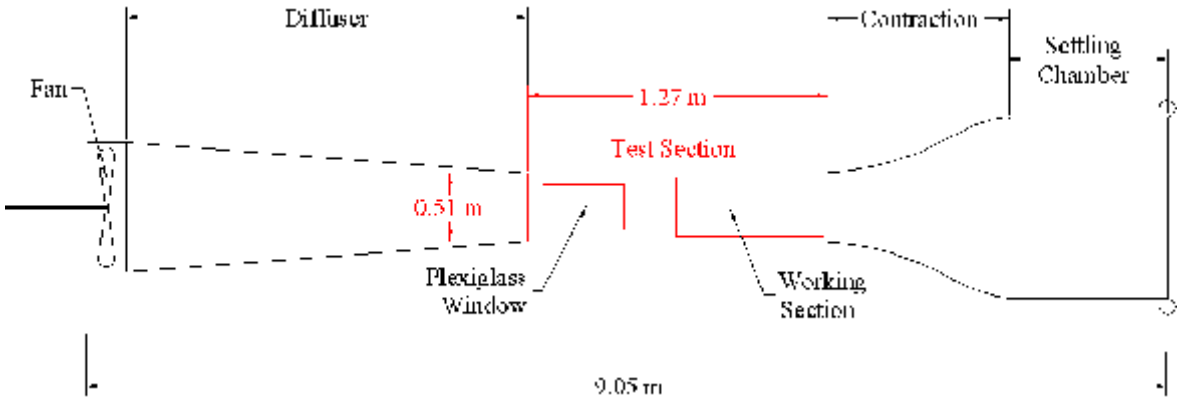

Figure 2.1 The ESM Wind Tunnel.

2.1.1 Coning Model Mount in the ESM Wind Tunnel

Coning motions in the ESM wind tunnel are performed using the mechanism depicted in Fig. 2.2. A 3/4 hp DC motor drives the input shaft of a 16:1 worm gear reducer. The output shaft of the gear reducer is coupled by a miter gear pair to a shaft mounted along the centerline of the tunnel and aligned with the freestream velocity vector. The model is mounted to the horizontal shaft such that its angle of attack is held fixed as the shaft rotates. The angle of attack of the model can be adjusted in 10° increments between 35° and 65°.

An IBM PS/2 Model 60 computer dedicated to controlling the motor contains a Data Translation DT 2905 data acquisition board with 12-bit digital-to-analog (D/A) converter. This board is capable of sending a 0-5 V signal to an optically-isolated amplifier. The amplified control signal may range from 0 to 20 V and is sent to a regenerative drive motor controller, which in turn sends a corresponding voltage to the DC motor. The motor controller is configured so that it can drive the motor in either direction, depending on the input signal from the computer. A signal of approximately 10 V from the computer stops the motor. The entire motor-control system is calibrated by sending known control voltages from the computer and recording the output voltage from the optically-isolated amplifier and the motor voltage.

In this way, a preprogrammed array of voltage values may be loaded into the computer memory. During data acquisition, the motor-control computer receives an external trigger. On this command, the computer sends the pre-programmed array of voltages to the motor controller at a specified frequency.

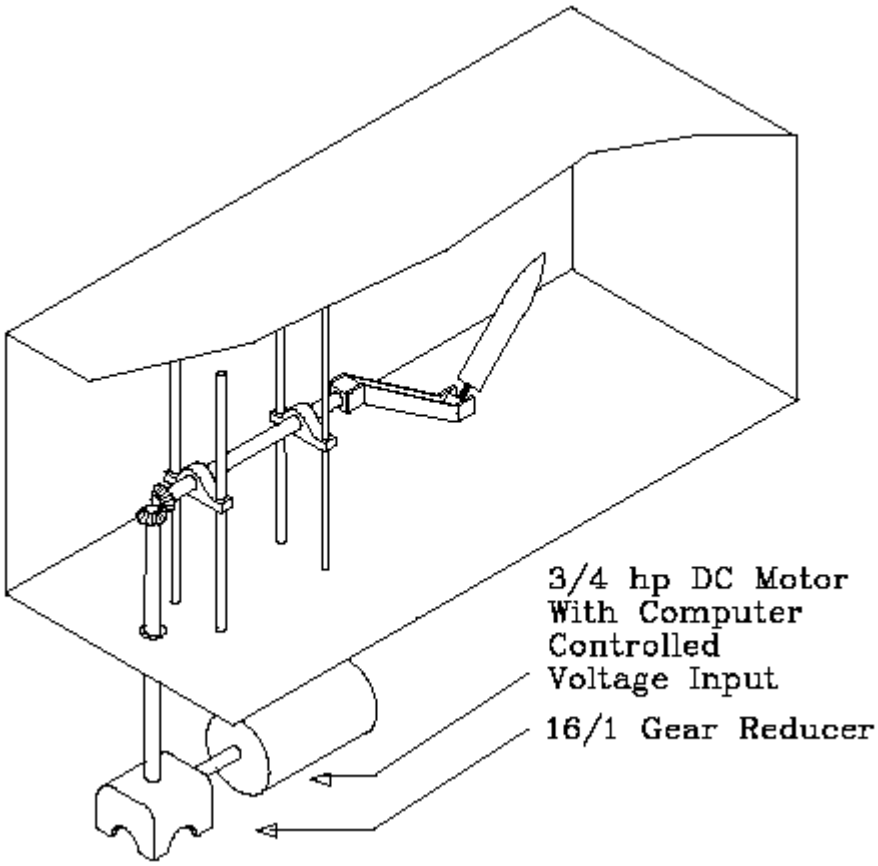

Figure 2.2 Test-Section Setup to Acquire Data Over a Coning Tangent-Ogive Cylinder in the ESM Wind Tunnel.

2.1.2 Digital Encoder and Electronic Circuit for Position Feedback

To ensure accurate positioning of the model, feedback is provided by a Hewlett-Packard digital rotational encoder with supporting electronics. The encoder shaft is connected by gearing to the horizontal shaft that supports the model. The encoder is not shown in figure 2.2, but its location is between the two sets of vertical supports on which the bearings are mounted. In order to improve accuracy, the encoder is geared up at a 48:15 ratio so that its rotational rate is higher than that of the

model. The output of the encoder is a dual square wave, with the pulses 180º out of phase. There are 256 output pulses per full rotation of the encoder shaft. Because of the gearing, there are 820 pulses per rotation of the model, or 2.28 pulses/deg. This results in an encoder resolution of 0.439 degrees/pulse.

The supporting electronics convert the dual square-wave pulses of the encoder to a corresponding voltage in the following manner. The square-wave pulses are routed to two different receivers. The first is an SN54LS74 Bistable Latch (flip-flop), which determines which pulse is leading the other. The output of the latch is a stable binary one in one of the directions of rotation. When the direction of motion changes, the output is a stable binary zero. This direction signal is passed to the base unit of a three-unit set of 4-bit up-down counters (MC14516). This set of counters is capable of counting up to 4095, which corresponds to 5 rotations of the model shaft, far greater than the requirement for the coning motions performed. The direction signal specifies the direction in which the counters are to count. In addition, the up-down counters are the second receivers of the rotational encoder pulse-train. As each low-to-high pulse is received, the counters increment or decrement one count depending on the sign of the direction pulse. The 12 bits of counter output are sent directly to a 12-bit D/A converter (Analog Devices AD7541), which operates in four-quadrant multiplication mode with dual 711KN operational amplifiers to provide a ±10 V output. This voltage output is then acquired simultaneously with the pressure data.

Tests of the encoder accuracy were performed in which the encoder was turned forward and backward through several full rotations and the output voltage measured. Repeatability error of the encoder was determined to be ±2.4 mV in two rotations. Since the circuit calibration results in a calibration constant of 0.01688 Volts/degree, ±2.4 mV corresponds to ±0.14°. Bit error from the data acquisition board is 1 bit out of 4096 for a range of ±10 V, which corresponds to ±4.8 mV. Again using the circuit calibration, ±4.8 mV means that the angular uncertainty due to bit error of the board is ±0.289°. Adding these two errors in quadrature results in an overall angular error of ±0.321°.

It might be asked why the digital output of the counters is not acquired directly by the data acquisition system, rather than converting it to a voltage only to reconvert to digital on acquisition. The answer lies in ease of use and availability of digital input. For the manner in which the encoder signal was acquired, only one physical data line was required, versus twelve for required pure digital acquisition. At the time the encoder circuit was designed, twelve digital inputs could not be sampled by the data acquisition system available.

2.2 The Engineering Science and Mechanics Water Tunnel

The ESM Water Tunnel was manufactured by Engineering Laboratory Design (ELD). It can operate as a free surface tunnel, but for all data presented in this work the tunnel is filled completely and covered. The tunnel operates in a closed loop in the vertical plane with up to 2,500 gallons of water. The settling chamber leads to the 24" x 24" x 72" Plexiglas test section via a three-way convergence. A 4500-gpm pump is driven by a 20-hp motor provides flow which can attain a maximum speed of 1 m/s, corresponding to a maximum Reynolds number per unit length of 9900/cm. The freestream turbulence level in the test section is less than 2%. A schematic of the ESM Water Tunnel is shown in figure 2.3

The ESM Water Tunnel is the facility used for LDV and PIV investigations of the flow around the tangent-ogive cylinder. Optical access to the test section is generally available from the sides and bottom of the test section, as free surface considerations or presence of the cover usually prohibits data acquisition through the top. In addition, there is optical access from directly downstream of the test section through a smaller (30.5 cm x 61 cm) window. This downstream window is typically used as a viewport for the high-speed digital camera during PIV acquisition, to perform flow visualization and acquire data illuminated by a vertical laser sheet.

2.3 The VPI & SU Stability Wind Tunnel

The Virginia Tech Stability wind tunnel is a continuous, closed-loop subsonic wind tunnel. The maximum achievable flow speed is 275 ft/s in a 6-foot by 6-foot by 25-foot test section. This facility was constructed in 1940 at the present site of the NASA Langley Research Center by NASA's forerunner, NACA. Use of the tunnel at Langley in the determination of aerodynamic stability derivatives lead to its present name. In 1959, the wind tunnel was moved to Virginia Tech, where it has since been located outside of Randolph Hall. A picture of the outside of the Stability Wind Tunnel is shown in figure 2.4.

The settling chamber has a contraction ratio of 9 to 1, and is equipped with seven anti-turbulence screens. This combination provides an extremely smooth flow in the test section. The turbulence levels vary from 0.018% to 0.045% depending on the freestream velocity. The average velocity fluctuation across the test section is about 0.5%, and flow angularities are limited to 2° maximum. The settling chamber is 3 m long and the diffuser has an angle of 3°. The ambient temperature and pressure in the test

section is nearly equal to the ambient outdoor conditions due to the presence of an air exchanger. During testing, the control room is maintained at the same static pressure as the test section.

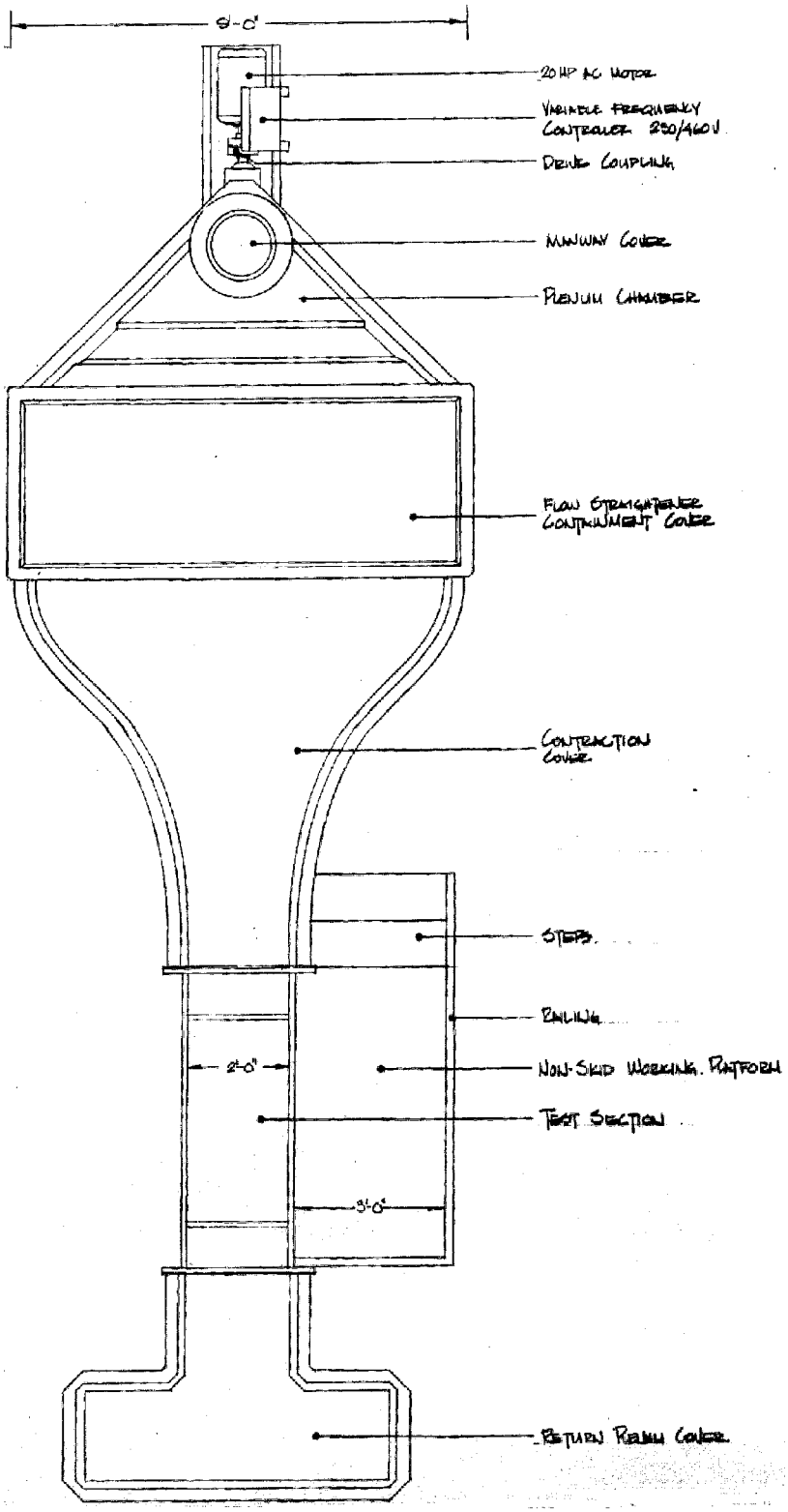

Figure 2.3 Top View of the ESM Water Tunnel

Figure 2.4 The Virginia Tech Stability Wind Tunnel. The Air Exchange Tower is Clearly Visible. The Tunnel Fan and Motor Assembly is Located Inside the Tunnel to the Left of the Air Exchanger. (Photo by Aerospace and Ocean Engineering Department, VPI & SU – Used under fair use, 2013).

The tunnel fan has a diameter of 14 feet and is driven by a 600-hp motor. Between 1994 and 1996, the tunnel fan and driving motor were completely reconditioned, restoring them to near-original states. The present research was conducted around and after this restoration. The Virginia Tech Stability Wind Tunnel is shown schematically in figure 2.5.

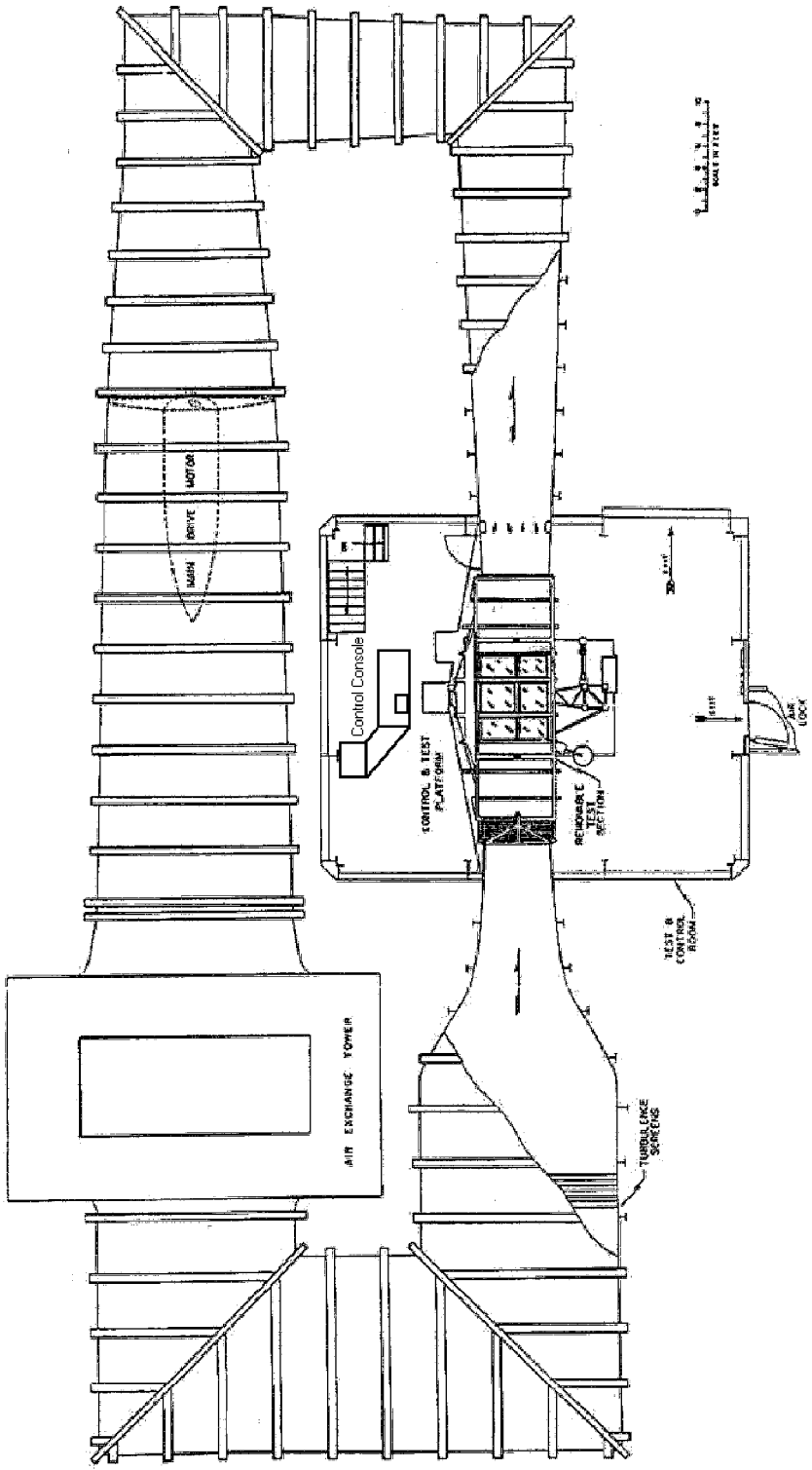

Figure 2.5 Top View of Virginia Tech Stability Wind Tunnel (Diagram from Aerospace & Ocean Engineering Department, VPI & SU. Used under fair use, 2013).

2.3.1 The Dynamic Plunge, Pitch and Roll (DyPPiR) Model Mount

While in the Virginia Tech Stability Wind Tunnel, the models were mounted on the Dynamic Plunge-Pitch-Roll (DyPPiR) model mount system, which was designed and developed specifically for use in the Stability Tunnel. The DyPPiR is capable of maneuvering a model simultaneously in plunge, pitch and roll at frequencies up to 10 Hz, depending on the amplitude of the motion and model inertia. The DyPPiR is computer-controlled, and therefore is capable of performing arbitrary, preprogrammed motions. The motions of the DyPPiR components are controlled through the use of ASCII motion files, which are used as the signal commands for the DyPPiR. High-pressure (3000 psi) hydraulic actuators with electronic feedback-control loops are employed for accurate and repeatable three-degrees-of-freedom maneuvering of up to a 150-lb sting-mounted model plus 550 lbs of DyPPiR hardware. The DyPPiR system allows truly unsteady maneuvers to be performed in Reynolds numbers approaching $4 \cdot 10^6$/m. Many different maneuvers are possible, within the capabilities of the system and the bounds of the tunnel. The maximum capabilities of the DyPPiR are a 1.5-m range and 9.1 m/s rate in plunge, ±45° range and 8 rad/s (458 deg/s) rate in pitch, and a ±140° range and 6 rad/s (344 deg/s) rate in roll. The uncertainty in the plunge, pitch and roll positions are 0.0584 cm, 0.053° and 0.164°, respectively (Hoang, et. al. [1994]), which shows the accuracy and repeatability of the DyPPiR. A schematic of the DyPPiR with the ESM tangent-ogive model mounted is shown in figure 2.6.

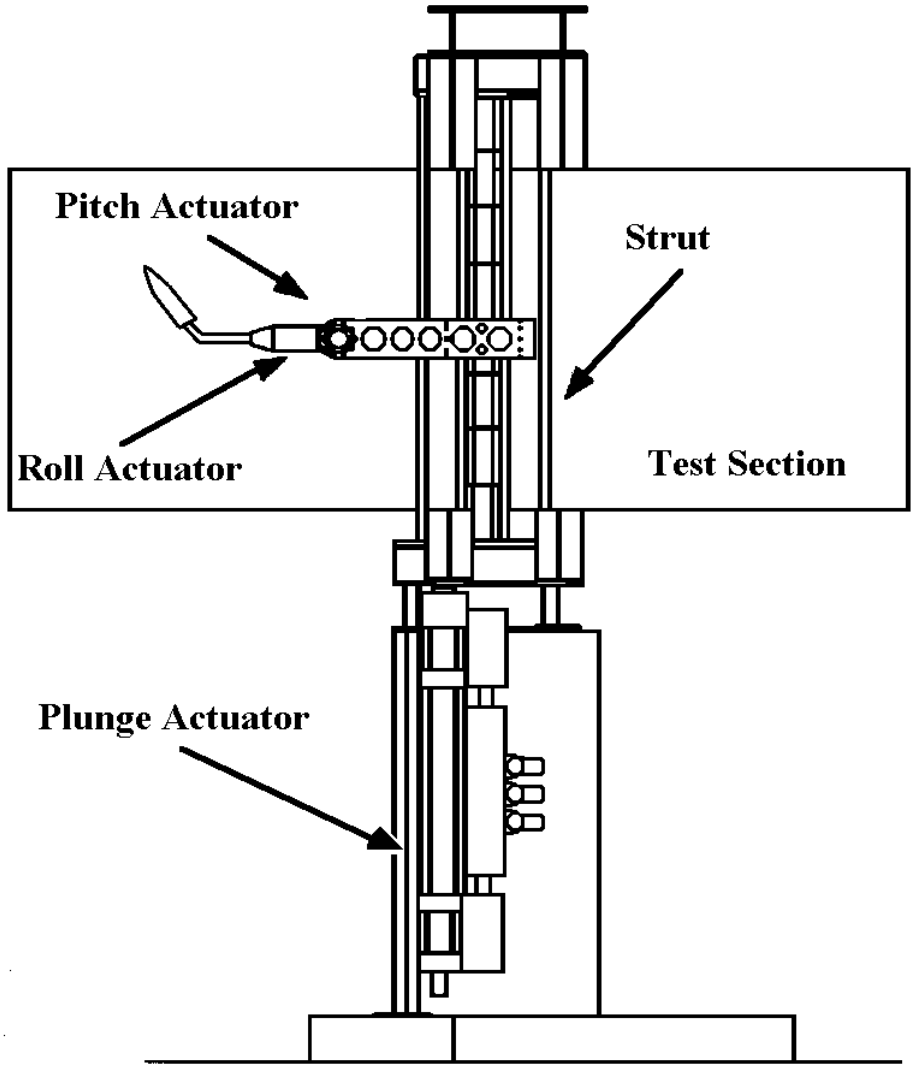

Figure 2.6 The Dynamic Plunge, Pitch and Roll Dynamic Model Mount (DyPPiR), Installed in the Virginia Tech Stability Wind Tunnel. The Ogive Models are Mounted with a 50°-Offset Block.

The DyPPiR foundation consists of two concrete pylons directly beneath the aft part of the test section. The plunge actuator is located between the pylons, and the piston of the actuator extends vertically into the test section and connects to the underside of the DyPPiR carriage. The DyPPiR carriage runs on two sets of vertical rails that are mounted within a streamlined strut. The pitch actuator is situated on the upstream side of the carriage, and the roll actuator is mounted on the pitch actuator. The tangent-ogive cylinder models are mounted on the DyPPiR with a 50°-offset block, so that when the axis of the roll actuator is aligned with the free stream, the model is positioned at an angle of attack of 50°,

allowing the model to perform coning motions. A picture of the DyPPiR with the tangent-ogive stability tunnel model installed is shown in figure 2.7.

Specific information about the DyPPiR design is given in Ahn [1992]. The DyPPiR has been tested and subsequently validated through its use in several experiments (Hoang, et. al. [1994], Wetzel, et. al. [1998], and Schaeffler [1998]). The reader is referred to the above references for more information concerning the programming of the DyPPiR, DyPPiR motion files, and DyPPiR instrumentation.

Figure 2.7 The DyPPiR Strut, Carriage, Pitch Actuator and Roll Actuator in the VPI & SU Stability Wind Tunnel with the D = 12.7 cm Stability Tunnel Model Installed. Note that Due to the Presence of the Pitch-Offset Block, the Model is at = 50° with the Pitch Actuator Level, Allowing the Coning Motions to be Performed. Author Included for Scale.

2.3.2 Implications of the Use of Slats in the Stability Tunnel Test-Section

In an effort to decrease blockage effects, slats have been designed for use in the test section of the Virginia Tech Stability Wind Tunnel. Although the blockage created by the Stability Tunnel model and the DyPPiR strut were not excessive, any blockage reduction would be beneficial because, as Whitfield [1999] observed, blockage corrections for unsteady testing are unknown. The open sections of the walls

allow streamlines to displace outside of the test section, increasing the effective area allowed to the flow in the region of the model and the DyPPiR. Willet performed tests on the blockage-reducing effect of slat installation for several models. It was found that the slats allowed the correct prediction of drag force even for blockage ratios up to 25%.

The slats are constructed from ¾" plywood, and are installed on all four surfaces of the test section for the entire length of the test section. The ratio of the open area allowed by the slats to the total wetted surface area of the test section is known as the open-air ratio. For tests with the Stability Tunnel model, the open-air ratio was 37.4% (Whitfield[1999]).

Because the test section and control room are maintained at the same pressure during testing, there should be no induced flow from outside the test section. While the time-averaged induced flow may be zero, there is a flow oscillation caused by interaction between the relatively stagnant air of the control room and the moving air in the test section, as occurs frequently in cavity-type flows. As the speed of the flow is increased, the frequency of flow vibration also increases. The vibration and extra drag due to the slats limits the top speed of the facility with slats installed to about 145 ft/s.

The flow vibration can actually be physically felt in the control room, which means that the vibration is of relatively low frequency. This is in fact the case, as it was discovered that the dynamic pressure from the Pitot-static tube registered a frequency near 10 Hz at a freestream speed of 36.5 m/s. In addition, it appears that the presence of the slats may induce a nonzero pressure or flow gradient in a transverse direction. This will be seen in the discussion of the data resulting from these tests, which exhibit changes in the mean sectional yaw force as the model is moved from side to side in the test section.

2.4 The TSI Laser-Doppler Velocimetry (LDV) System

The TSI laser-Doppler velocimetry system used to acquire velocity fields in the ESM Water Tunnel is a two-component system that uses a 35-Watt Helium-Neon (He-Ne) laser as its source. This system is shown in figure 2.8. The system operates in direct backscatter mode. Included in the optics train are a beam collimator, two beam splitters, two polarization axis rotators, two beamsplitting modules,

40-MHz and 60-Mz Bragg cells with associated beam-steering modules, a single photomultiplier, a 2.27:1 beam expander and a transmitting lens. The beam expansion is executed on the final optics, after passing through the photomultiplier, so that the effective collection aperture in backscatter mode is increased. This in turn increases the signal-to-noise ratio (SNR) 11.7 times from the original SNR without beam expansion. In addition, the beam expander decreases the measurement volume diameter 2.27 times, and increases the measurement volume length by 5.15 times. Two different transmitting lenses are employed, depending on whether the system is aligned from the bottom or side of the test section. These lenses have focal lengths of 250 mm and 350 mm, and are used when the system is aligned from the bottom and side of the ESM Water Tunnel, respectively. Pertinent statistics for the laser beams and measurement volume are given in table 2.1 for both lenses.

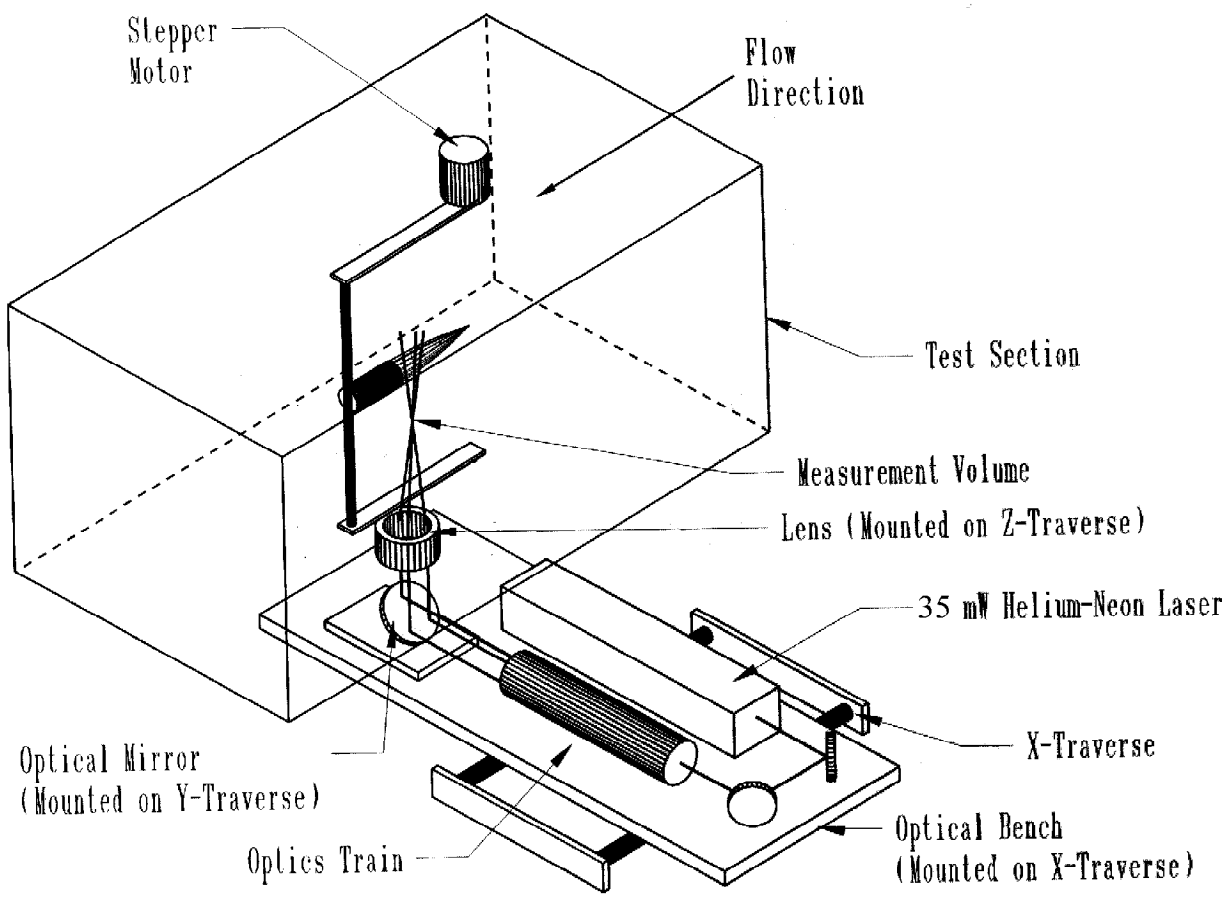

Figure 2.8 The TSI LDV System as Used in the ESM Water Tunnel for Acquisition of Velocity Fields around a Pitching Tangent-Ogive Cylinder. As Shown, the Beams Enter the Test Section from the Bottom, Allowing the Determination of Two Velocity Components. The System is then Realigned from the Side of the Tunnel (Not Shown) to Acquire the Third Component. The Model Pitches in the Horizontal Plane.

By passing the original beam through the beam splitters, three beams of approximately equal strength result. One of these beams is passed through the 40-MHz Bragg cell, one through the 60-MHz Bragg cell, and one is left unshifted. The three beams are focussed at one point, and are paired so that one component of velocity is measured from the signal between the 40-MHz and 60-MHz shifted beams, and one component of velocity is measured from the signal between the 40-Mhz shifted and unshifted beams. The frequency shifting of the beams makes it possible to use a single photomultiplier to acquire both signals by downmixing the resulting photomultiplier signal by 20 MHz (for the first set of beams mentioned above), and by 40 MHz (for the second set of beams). Thus, the original signal results in two signals, each containing the information for one of the velocity components. In addition to the frequency shifting mentioned above, further shifting of the original signal is performed at about twice the Doppler frequency. This frequency is not downmixed from the signals, so that a particle with zero velocity will result in a positive frequency (the shift frequency), making measurement of reversed flow possible. A picture of the tangent-ogive cylinder model used for LDV experiments is shown mounted in the ESM Water Tunnel in figure 2.9. This picture also shows the laser beams focussed from the side of the tunnel, with the measurement volume clearly visible.

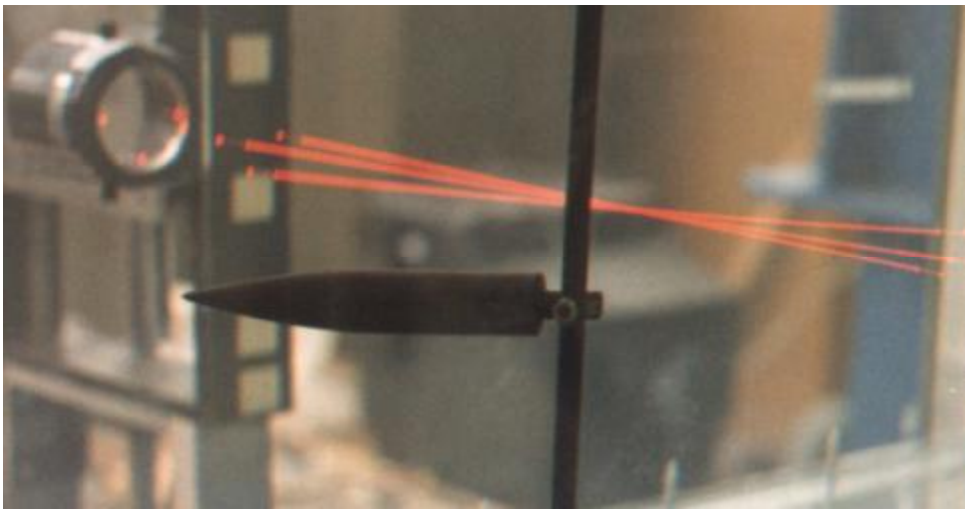

Figure 2.9 The LDV Water Tunnel Model Mounted in the ESM Water Tunnel. The LDV System is Aligned from the Side of the Tunnel, with the Measurement Volume Clearly Visible to the Right of the Vertical Shaft.

Both downmixed signals resulting from the original photomultiplier signal are sent to two TSI counters, Models 1980 and 1990. Signal processing by the counters was performed in non-coincidence 8-cycle mode. This mode required that a particle traverse at least eight fringes of the measurement volume (of the 16 possible) to be validated. The counters have a voltage output, which is proportional to the

measured frequency. The constant of proportionality is a function of the panel settings on the counters. The output voltages from both counters are connected to the PC-based data acquisition system.

Typically, LDV seeding must be added to the flow in order to achieve appropriate data rates. For the present research, silicon carbide seeding was used. Silicon carbide has a density of 3.2 g/cm^3, a refractive index of 2.65 and a mean diameter of 1.5 μm. Some settling of the seeding occurred, so reseeding of the water tunnel was carried out about every twelve hours, or when the data rate decreased to a point such that reseeding was necessary. Since each set of data took approximately twenty-four hours to acquire, at least one reseeding took place during acquisition of each dataset. The seeding was performed at a location downstream of the model as the model was resetting to the initial position, thus minimizing the effect on the experiment.

Table 2.1 Laser Beam and Measurement Volume Specifications for the TSI LDV System Employed in the ESM Water Tunnel

Effective Beam Diameter – $D_{e^{-2}}$ Exiting Laser: 1.25 ± 0.1 mm After Beam Expander: 2.838 mm	Lens 1: 250 mm Focal Length, Used from Bottom of Tunnel	Lens 2: 350 mm Focal Length, Used from Side of Tunnel
Convergence Half-Angle, κ	**4.05°**	**2.89°**
Fringe Spacing, $d_f = \frac{\lambda}{2 \cdot \sin\kappa}$	**4.45 μm**	**6.273 μm**
$d_{e^{-2}} = \frac{4\lambda f}{\pi D_{e^{-2}}}$ (f = lens focal length)	**71.0 μm**	**99.4 μm**
Measurement Volume Diameter, $d_m = \frac{d_{e^{-2}}}{\cos\kappa}$	**71.2 μm**	**99.5 μm**
Measurement Volume Length, $l_m = \frac{d_{e^{-2}}}{\sin\kappa}$	**1.006 mm**	**1.970 mm**
Number of Fringes	**16**	**16**

The laser and optics train are mounted on an optical bench, which is in turn mounted on a large traversing mechanism (the x-traverse in fig. 2.8, allowing motion parallel to the axis of the test section. On the optical bench are mounted mirrors and the focussing lens needed to direct the beams emanating from the beam expander into the test section. One mirror is mounted on another traverse which allows for horizontal motion perpendicular to the axis of the test section (the y-traverse in fig. 2.8). A third traverse (the z-traverse in fig. 2.8) rides on the y-traverse, and carries the focussing lens (plus an additional mirror

if the alignment of the system is from the side of the test section). This latter traverse allows vertical motion perpendicular to the test section axis. All of these traverses are driven by stepping motors. Position feedback from each traverse is provided by a Linear Variable Differential Transducer (LVDT). The accuracy of the LVDT's and the resolution of the stepping motor/lead screw combinations result in the location of the measurement volume being known accurately to 0.06 mm (60 μm), much less than the length of the measurement volume.

2.4.1 Uncertainty Analysis for the Velocity Measured with the LDV System

The velocity that corresponds to the frequency output from the LDV data acquisition system may be found from

$$V = f\frac{\lambda}{2\cdot\sin\kappa} \tag{2.1}$$

where f is the measured Doppler frequency, λ is the wavelength of the laser light and κ is the half-angle of the two incident beams that generate the measurement volume. For a He-Ne laser, the wavelength of the coherent light is 632.8 nm. Kline & McKlintock [1953] presented a method for error propagation in calculated quantities. This method is now generally accepted by scientists and engineers as the most appropriate way to propagate error through calculated quantities. If there are n measured quantities x_1, x_2…, x_n with errors δx_1, δx_2…, δx_n then the error associated with a function of these quantities, $y(x_1, x_2,\ldots, x_n)$ is given by

$$\delta y = \left\{\left[\left(\frac{\partial y}{\partial x_1}\right)\delta x_1\right]^2 + \left[\left(\frac{\partial y}{\partial x_{21}}\right)\delta x_2\right]^2 + \ldots + \left[\left(\frac{\partial y}{\partial x_n}\right)\delta x_n\right]^2\right\}^{\frac{1}{2}} \tag{2.2}$$

Applying this method to equation 2.1, and assuming that the error in the known wavelength is negligible, we find that

$$\delta V = \left\{\left[\left(\frac{\lambda}{2\cdot\sin\kappa}\right)\delta f\right]^2 + \left[\left(-\frac{f\lambda\cos\kappa}{2\cdot\sin^2\kappa}\right)\delta\kappa\right]^2\right\}^{\frac{1}{2}} = \left\{\left[\frac{V}{f}\delta f\right]^2 + \left[\frac{V}{\tan\kappa}\delta\kappa\right]^2\right\}^{\frac{1}{2}} \tag{2.3}$$

The uncertainty in the frequency measurement is due to the combination of errors arising from the TSI counters and the data acquisition system. Wilder [1992] determined that the worst-case uncertainty in the frequency measurement due to this system is $\delta_f = 0.01f$. The velocity is calculated based on the focal length of the lens and the beam spacing. The alignment mask used with the TSI system allows the beams to be located accurately within one-half beam diameter (1.42 mm) of the correct location. This difference, when considered in combination with the focal length of the lenses, results in an error of $\delta\kappa = 0.229° = 0.057\kappa$ for the 250 mm focal-length lens, and $\delta\kappa = 0.164° = 0.057\kappa$ for the 350 mm focal-length lens. Substituting the values for $\delta\kappa$ and δf into equation 2.3, it is found that the uncertainty in the measured velocity for both the 250 mm focal-length and the 350 mm focal-length lenses are essentially equal at $\delta V = 0.058V$.

2.5 The Edwards Barocel Precision Pressure Transducer

The Edwards Barocel model 590D precision pressure transducer was used as a pressure standard for all investigations involving pressure acquisition. The calibration of the ESP pressure scanner discussed in the following section is performed by applying generated pressures to the ESP and at the same time reading them with the Barocel. The Barocel has a range of 0 – 100 torr and an accuracy of 0.05% of the pressure reading plus 0.001% of the full scale of the unit. The Barocel is used together with a Datametrics model 1450 Electronic Manometer, which provided LED readout of the sensed pressure as well as support functions for the Barocel.

2.6 The Pressure Systems Inc. ESP Pressure Scanner

Pressure acquisition for all investigations was accomplished through the use of several Pressure Systems Inc. (PSI) ESP pressure scanners. These scanners are small, high-density packages containing multiple differential sensors. ESP packages contain 8, 16, 32 or 64 channels. Each pressure sensor is a miniature piezoresistive pressure transducer, and all of the pressure transducers in a module share a common silicon substrate. The output of each transducer is internally amplified to ±5 V full-scale, and

these analog outputs are multiplexed within the scanner. The settling time inherent in the multiplexer corresponds to a maximum sampling rate of 20 kHz. This allows near-simultaneous sampling of the ESP. For instance, thirty-two ports can be sampled in 1.6 ms. However, the pressure port geometry limits the frequency response of the ESP to 50 Hz at the pressure inputs. Since the transducers are differential, a reference pressure must be chosen. In all cases in the present work, the reference pressure was the tunnel freestream static pressure. The static accuracy of the ESP's, including nonlinearity, hysteresis and non-repeatability effects, is 0.10% of the full scale at constant temperature after a full calibration.

The electrical connection to the ESP is generic, so that pressure scanners of various styles, ranges or number of ports may be interchanged without having to change the PC-ESP interface or data acquisition software. The connection is made through a fifteen-pin connector. Six-bit digital addressing allows the selection of one of up to sixty-four individual ports. The analog output of the selected port then exists on the output pin of the electrical connector. Other electrical lines carry a precision five-volt reference source, power and ground.

The ESP's employed in the present research were 32-channel units, the sizes of which were 25.4 cm x 30.5 cm x 63.5 cm (HD style) and 25.4 cm x 45.7cm x 63.5 cm (RL Style). The small size of the ESP's allowed them to be installed very close to the model in the ESM Wind Tunnel, or actually inside the model in Stability Tunnel model. This in turn allowed the flexible tubing runs connecting the ESP to the pressure ports to be minimized, keeping the pressure attenuation and phase-lag small and maximizing the frequency response of the system.

Without the use of the ESP's, surface pressure acquisition on a maneuvering vehicle could not have been carried out without employing surface-mount pressure sensors such as those available from Kulite or Entran. While these units have far greater frequency response, they have three drawbacks: Inadequate pressure resolution for the relatively low freestream velocities at which most tests were carried out, increased data acquisition complexity for equivalent number of pressure ports and increased cost. The lowest pressure range available or the surface-mount units is ±2 psi (±55.2" H_2O). For a 12-bit data acquisition board, the bit error is 5.5 times as large as for the ±10" H_2O ESP. If the surface-mount units were used, the bit error would be the largest contributor to the error in the pressure coefficients (c.f. section 2.9.2), even larger than the static error of the ESP. In addition, if for example twenty-four surface pressures are to be acquired near-simultaneously, then twenty-four surface-mount units would need to be employed, meaning that twenty-four data acquisition channels would need to be available. This would require the use of several data acquisition boards or two extra multiplexers external to the data acquisition

computer. Finally, the cost of each surface-mount transducer is approximately $1100, which means that twenty-four would total over $26,000. The advantage of the surface-mount transducers would be their high frequency response. However, the cost advantage of the ESP's is obvious, since the cost of a 32-channel ESP is about $6000. In their capacity to measure multiple unsteady pressures in low-speed flows with dominant frequencies less than 50 Hz while installed within the test facility or model, the ESP's are unequalled in their performance and ease of use.

2.6.1 Calibration of the ESP Pressure Scanners

The ESP pressure scanners were calibrated using the method recommended by the manufacturer, Pressure Systems, Inc (PSI). This method involves a second-order polynomial to relate the sensed pressure P to the resultant voltage V:

$$P = C_0 + C_1V + C_2V^2 \tag{2.4}$$

where C_0, C_1 and C_2 are referred to as the calibration coefficients. There will be one set of these coefficients for each ESP channel.

In addition to the input pressure ports resident on the unit, each ESP has five additional pressure input ports that are used during the calibration of the ESP. These ports are labeled on the ESP as C1, C2, CAL, CAL-REF and RUN-REF. For older ESP's, a single reference port is used, essentially merging the functions of the CAL-REF and RUN-REF ports into one port labeled REF. The ESP is designed with an internal piston through which all of the input channels run. By applying 100 psi of dry air to C1, the piston is shifted, and the ESP is put into calibration mode. Shifting the piston opens all of the input channels to the CAL port on the positive side and CAL-REF port on the negative side. The pressure inputs that are meant to be acquired during data acquisition are sealed from the transducers by O-ring interfaces along the piston. In this way, a known differential pressure may be applied between CAL and CAL-REF. Typically, the calibration pressures are referenced to atmospheric pressure. This pressure, applied to all of the transducers simultaneously, results in a voltage which may be acquired by the data acquisition computer. By generating three different known pressures and reading the resulting voltages, the constants in equation 2.4 (three for each ESP channel) may be determined by Gauss-Jordan elimination. The ESP may be returned to run mode by applying 100 psi of dry air to the C2 port. The transducers will now respond to the difference between the individual channel input pressures and the RUN-REF pressure.

In order to generate the calibration pressures, a water tower is used. This is constructed by attaching an open-ended chamber to a threaded rod. The chamber is inverted in a cylinder filled with water. By rotating the threaded rod, which is fixed to the outside cylinder, it is possible to change the depth H to which the chamber is submerged. This effectively changes the pressure of the trapped air as well. This pressure is channeled by flexible tubing and sent to the ESP as a calibration pressure. At the same time, this pressure is read by the Barocel precision pressure standard that is discussed in section 2.5. A schematic of the water tower is shown in figure 2.10 (Schaeffler [1998])[§]. Typical calibrations involve the application of the calibration pressure P to CAL, then to REF, each referenced to atmospheric pressure. This results in two calibration points, P and –P. The third calibration point is usually taken with equal pressures applied to CAL and REF, resulting in zero pressure differential.

The ESP is also subjected to zero-offset calibrations before each data acquisition period. For these calibrations, the ESP is put into calibration mode and subjected to zero differential pressure between the CAL and REF ports. Then, the C_0 coefficient is recalculated using equation 2.2, obtained from equation 2.1 with P = 0:

$$C_0 = -C_1V - C_2V^2 \tag{2.5}$$

Zero-offset calibrations take less time to perform than full calibrations, and are helpful in maintaining the calibration and accuracy of the ESP. A zero-offset calibration should never be used in place of a full calibration, especially if the ambient temperature is quite different than the temperature at which the C_1 and C_2 constants were calculated. However, if a full calibration has recently been performed, a zero-offset calibration before each run preserves the static accuracy of the ESP. For the investigations resulting in the pressure data presented herein, a full calibration was performed every hour or less, and zero-offset calibrations (where only C_0 was changed) were performed before every set of ensembles.

Because the ESP units are sensitive to temperature changes, with the thermal zero shift and thermal span shift being 0.014% full-scale/°C and 0.005%/°C, respectively. Because of this sensitivity, the ESP's need to be calibrated often, especially if the temperature is not constant with time. The most

[§] The water tower arrangement was known affectionately by all present and recently graduated students of the ESM Fluid Mechanics Laboratory as the "Tower of Power." Although it was an essential part of all pressure data acquisition events, it was not a complicated piece of equipment. In fact, it was just a plastic cup inverted in a piece of PVC pipe, put together in one day by Erik Panzer in 1993. It survived remarkably well in its original design for more than a decade , a testament to Mr. Panzer's ingenuity and the age-old motto: "If it works, don't fix it."

common cause of abrupt temperature changes occurs when the ESP is placed inside a wind tunnel. It is imperative that the ESP's be allowed to arrive at a steady-state temperature before calibration.

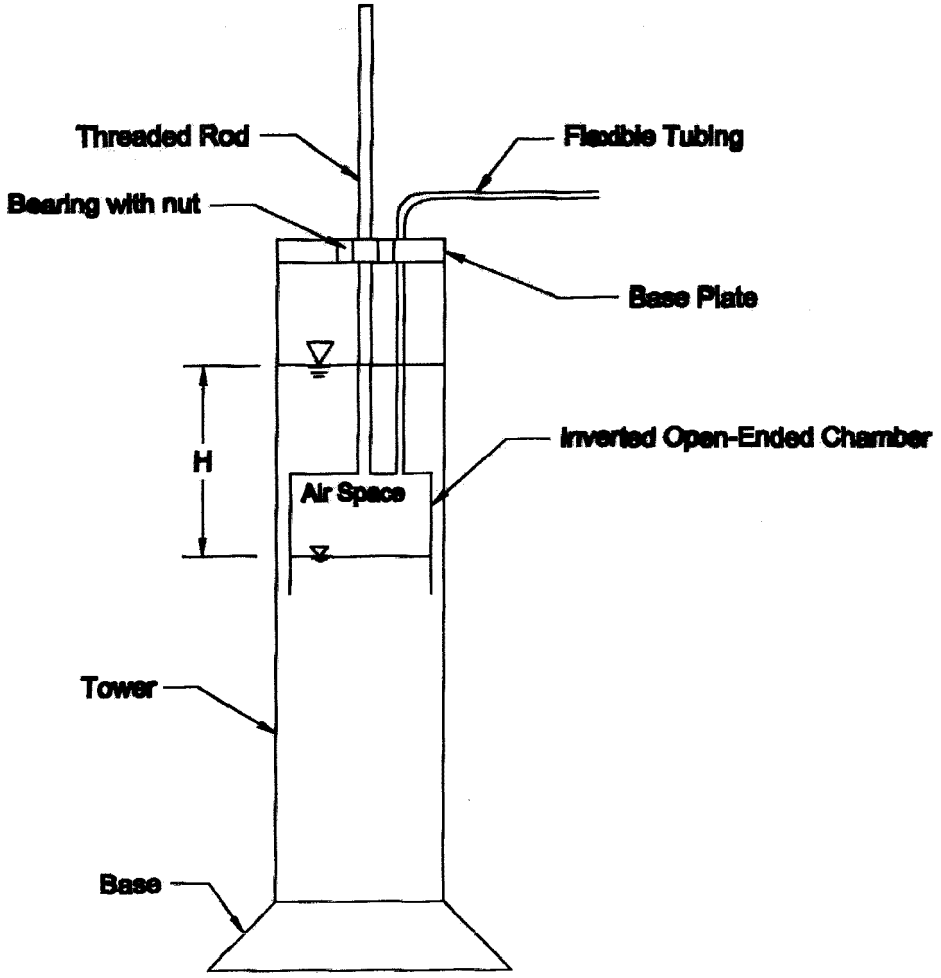

Figure 2.10 The Calibration Pressure Generator (Cross-Section). The Air Trapped in the Inverted Chamber Increases Pressure as H Increases. (Schaeffler [1998]. Used under fair use, 2013)

2.6.2 Uncertainty Analysis for the Measured Pressure Coefficients

The differential pressures applied at the pressure ports on the tangent-ogive body are measured by the ESP's and subsequently converted into dimensionless pressure coefficients. The pressure coefficient is defined as

$$C_p = \frac{P - P_\infty}{\frac{1}{2}\rho U_\infty^2} = \frac{\Delta P}{q} \tag{2.63}$$

where P_∞ is the freestream static pressure, the reference pressure for all ESP measurements considered here, ΔP is the differential port pressure measured by the ESP, and q is the dynamic pressure (= $P_o - P_\infty$ assuming incompressible flow). The dynamic pressure is measured by employing a Pitot-static tube and measuring the differential pressure between the total and static ports. In this section, the error in the pressure coefficients is determined. The ESP is used to measure both the numerator and denominator of equation 2.3, and thus both ΔP and q are subject to the measurement errors of the ESP.

Kline & McKlintock [1954] presented a method for error propagation. This method is now generally accepted by scientists and engineers as the most appropriate way to propagate error through calculated quantities. If there are n measured quantities x_1, x_2…, x_n with errors δx_1, δx_2…, δx_n then the error associated with $y(x_1, x_2, \ldots, x_n)$ is given by

$$\delta y = \left\{ \left[\left(\frac{\partial y}{\partial x_1} \right) \delta x_1 \right]^2 + \left[\left(\frac{\partial y}{\partial x_2} \right) \delta x_2 \right]^2 + \ldots + \left[\left(\frac{\partial y}{\partial x_n} \right) \delta x_n \right]^2 \right\}^{\frac{1}{2}} \tag{2.74}$$

Applying the method of equation 2.74 to the definition of the pressure coefficient in equation 2.3, we find

$$\delta C_P = \left\{ \left[\left(\frac{\partial C_P}{\partial (\Delta P)} \right) \delta (\Delta P) \right]^2 + \left[\left(\frac{\partial C_P}{\partial q} \right) \delta q \right]^2 \right\}^{\frac{1}{2}} = \left\{ \left[\frac{\delta (\Delta P)}{q} \right]^2 + \left[-\frac{\delta q \cdot \Delta P}{q^2} \right]^2 \right\}^{\frac{1}{2}} \tag{2.85}$$

But since the measurement of q and P are made by the same instrument and in the same manner, they are subject to the same uncertainties, so $\delta q = \delta(\Delta P) = \delta P$. Substituting for the error quantities, expanding and rearranging equation 2.85 results in

$$\delta C_P = \left\{ \frac{([\delta P]^2 [q^2 + (\Delta P)^2]}{q^4} \right\}^{\frac{1}{2}} \tag{2.96}$$

We observe that the largest value of δC_P for a given q would result when ΔP is a maximum. The relation of q and ΔP is such that for the tangent-ogive cylinder, $(\Delta P)_{Max}$ is no greater than -2q (i.e. the highest observed pressure coefficient is not greater than 2 in magnitude). Using ΔP = -2q as a worst-case scenario, equation 2.96 becomes

$$\delta C_P = \left\{ \frac{([\delta P]^2 \cdot 5q^2}{q^4} \right\}^{\frac{1}{2}} = \left\{ \frac{(5[\delta P]^2}{q^2} \right\}^{\frac{1}{2}} = \frac{\sqrt{5} \cdot \delta P}{q} \qquad (2.10)$$

which gives the uncertainty in the measured pressure coeffcient as a function of the uncertainty in the measured pressures and the dynamic pressure of the test.

There are three distinct ESP uncertainty cases to be treated: a ±10" H_2O ESP operating in the ESM Wind Tunnel, a ±10" H_2O ESP operating in the Virginia Tech Stability Tunnel, and a ±20" H_2O ESP operating in the Virginia Tech Stability Tunnel. There are four contributions to the uncertainty in the pressure measurement: (1) The static uncertainty of the ESP: δP_1 (2) The pressure uncertainty due to accelration of the ESP: δP_2 (3) The bit error associated with the analog-to-digital conversion of the presure by the data acquisition board has an associated pressure uncertainty: δP_3 (4) The uncertainty in the measurement of the calibration pressures by the Barocel pressure transducer: δP_4.

The static error associated with the ESP units is ±0.1% of the full scale, which corresponds to δP_1 =± 0.01" H_2O for the ±10" H_2O ESP, and δP_1 = ±0.02" H2O for the ±20" H_2O ESP. These were the static uncertainties regardless of the facility in which the units were used.

The maximum acceleration of the ESP for all of the dynamic tests performed occurred during ramp coning motions executed by the DyPPiR. The average coning rate during these tests was $\dot{\gamma}$ = 5.62 rad/s (322°/s). The acceleration to this speed took place in 0.49 s, resulting in an average angular acceleration of $\ddot{\gamma}$ = 114.7 rad/s^2. The ESP units were mounted approximately 32 cm from the coning axis during the motion, resulting in a perpendicular acceleration of $\ddot{y}$ = 30.1 m/s^2 (3.06·g). Since the pressure uncertainty due to perpendicular acceleration is ±0.008%/g, an acceleration of 3.06·g results in worst-case pressure errors of δP_2 = ±0.00243" H_2O for the ±10" H_2O ESP, and δP_2 = ±0.00486" H_2O for the ±20" H_2O ESP.

The data acquisition boards used to acquire the pressure data were manufactured by Computer Boards, Inc. In general, the error in the A/D conversion for these boards is 1 bit out of 4096 during a 12-bit conversion. For data acquisition in the ESM tunnel, the board employed was set to a range of ±5 V, which corresponds to 2.44 mV/bit. During the entry to the Virginia Tech Stability Tunnel, a board with programmable gains was used. This board was set to a range of ±2.5 V, which corresponds to 1.22 mV/bit.

In order to convert the bit-voltage errors to pressure errors, typical calibration coefficients need to be assumed. Since we are dealing with a change in voltage the constant term in equation 2.1 will not play a role. The last term in equation 2.2 involves the square of the voltage, which can be neglected relative to the linear term for small voltage variations. Therefore, the pressure error for a small change in voltage will be dominated by the term involving the calibration coefficient C_1. An average C_1 is 3.42" H_2O /V for the ±10" H_2O ESP, and 4.48" H_2O for the ±20" H_2O ESP. For the ±10" H_2O ESP, this results in δP_3 = ±0.00834" H_2O in the ESM Wind Tunnel and δP_3 = ±0.00417" H_2O in the Virginia Tech Stability Wind Tunnel. For the ±20" H_2O ESP, this results in δP_3 = ±0.00547" H_2O in the Virginia Tech Stability Wind Tunnel, the only location in which it was used.

The Barocel precision pressure transducer that served as a pressure standard for all pressure data acquisition has an accuracy of ±0.05% of the reading plus ±0.001% of the full scale of the unit. Since the Barocel in employed here is 100 torr full scale, and typical calibration pressures were on the order of 6 torr, the error associated with calibration by the Barocel is 0.004 torr, or $\delta P_4 = \pm 2.135 \cdot 10^{-3}$ " H_2O.

Adding all of the pressure errors in quadrature so that $\delta P = [(\delta P_1)^2 + (\delta P_2)^2 + (\delta P_3)^2 + (\delta P_4)^2]^{1/2}$, we determine that for the ±10" H_2O ESP, δP = ±0.0134" H_2O in the ESM Wind Tunnel and δP = ±0.0113" H_2O in the Virginia Tech Stability Wind Tunnel. For the ±20" H_2O ESP the error in pressure δP = ±0.0214" H_2O. Using typical dynamic pressure values for q in equation 2.7 (0.30" for the ESM Wind Tunnel and 3.042" for the Virginia Tech Stability Wind Tunnel) results in pressure coefficient errors of δC_P = ±0.0999, ±0.00831, respectively for the ±10" H_2O ESP used in the ESM and Stability Tunnels. For the ±20" H_2O ESP the error in pressure results in δC_P = ±0.0157.

2.6.3 Effect of Flexible Tubing on the Accuracy of the Pressure Measurements

The ESP's are connected to the pressure ports by lengths of flexible tubing. For all investigations performed, the tubing used was Tygon R-3603 Laboratory tubing with an inside diameter of 0.794 mm (1/32") and an outside diameter of 2.38 mm (3/32"). In all cases, the length of the tubing connections never exceeded 38 cm (15"). It has been shown that for this type and length of tubing, the pressure attenuation and phase difference at the transducers are very small for input frequencies up to 25 Hz (Rediniotis [1992]). For the flow dynamics considered in investigations involving pressure acquisition, the frequencies of concern will be on the order of the maneuver frequency, which is an order of magnitude lower than 25 Hz. For tubing lengths of 30.5 cm (12"), the amplitude response and the phase lag at 25 Hz was found to be 1.018 and –6.34°, respectively.

Chapin [1983] conducted similar experiments with ESP's and tubing characteristically attached to the ESP units, and found that for tubing lengths of 34 cm and a frequency of 30 Hz, the amplitude response was 1.03 and the phase lag was about 7°. Testing was performed with longer lengths of tubing, and it was discovered that tubing lengths of up to 76 cm (30") still performed well for frequencies of up to 30 Hz, but performed poorly at higher frequencies. If tubing lengths are restricted to 34 cm, then the full 50 Hz frequency response of the ESP units can be realized with an amplitude response of 1.1 and a phase lag of about 10°.

2.7 The Oxford Laser Particle-Image Velocimetry (PIV) System

The source of the PIV laser sheet was a 45-Watt copper-vapor pulsing laser, delivering approximately 5.5mJ/pulse at its optimum operation. Using a set of optics in a telescopic arrangement, a laser sheet was delivered into the test section. The PIV setup is shown in figure 2.11. The laser was synchronized with a high-speed CCD camera (EG&G MD4256) using a timer board (Real Time Devices, model TC524). The acquisition image rate was 256 images/sec with a resolution of 256x256 pixels. Digital images were automatically stored in the image buffer of an SB4001 Adaptive Optics frame grabber. Hollow silver-coated glass particles from Potters Industries with 10-30 microns average diameter were used as flow tracers. The data acquisition process is digital, eliminating the tedious and time-consuming tasks of film digitization and allowing the real-time observation of the flow field.

The high sampling rate of the data acquisition process introduced significant problems in the adequate illumination of the flow field. In order to compensate for the energy losses and deliver sufficient illumination in the area under investigation, a set of optics specially coated for the exact wavelength of the laser was employed. This resulted into decreasing the losses through the optics from approximately 40% to less than 10%. In addition, the camera was fitted with an 80-300 mm Nikon lens with f-stop of 2.8 to allow more light on the sensor during the limited exposure time of 3.9 milliseconds. These improvements allow data acquisition rates of up to 1000 frames/sec, which otherwise would not have been possible. A one-dimensional fiber-optic LDV system was used to take a fixed-point velocity measurement of the free stream. In order to avoid background noise in the PIV images no LDV particles were added to the flow.

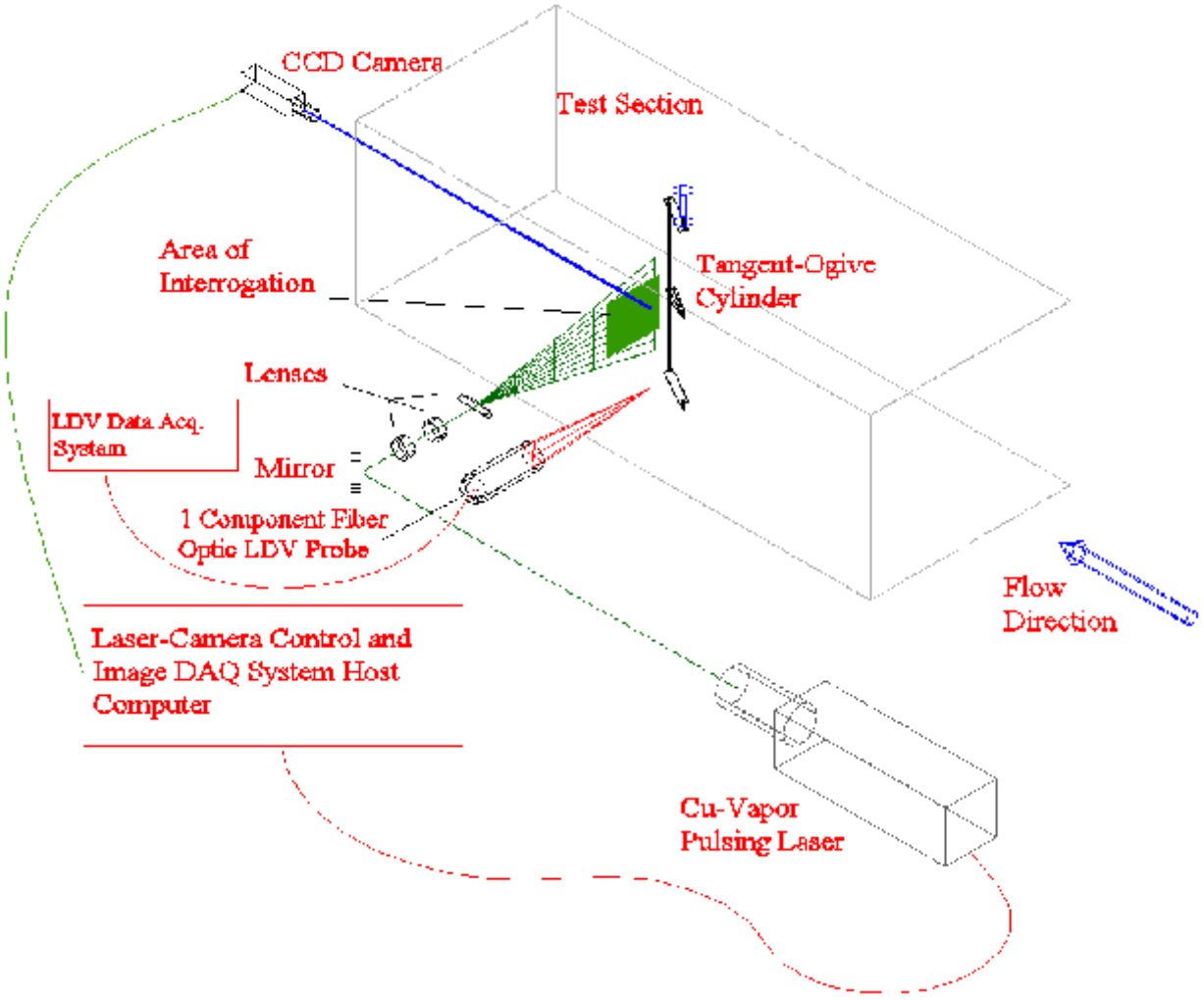

Figure 2.11 PIV Setup in the ESM Water Tunnel.

2.7.2 Uncertainty Analysis for Velocities Measured with PIV[§]

The present DPIV system implementation is limited to the investigation of low-speed liquid flows. This drawback results from two hardware limitations. The minimum possible time interval between two consecutive frames is 1 ms while the moderate pixel resolution of the digital camera limits the maximum field of view. Because of the desired number of independent velocity vectors per frame (32 in each direction), the maximum in-plane displacement between two consecutive frames is constrained to 8 pixels or less. The uncertainty of the velocity estimation can be quantified as:

$$\left(\frac{\sigma_u}{u^2}\right)^2 = \left(\frac{\sigma_{\Delta X}}{\Delta X^2}\right)^2 + \left(\frac{\sigma_{dt}}{dt^2}\right)^2 \qquad (2.11)$$

Where σ denotes the uncertainty of the subscripted quantity. For such low velocities and by using a digital interrogation procedure the uncertainty σ_{dt} is negligible. Thus the only error source will be introduced by the displacement estimation. Assuming a typical particle image diameter of 2 pixels in order to optimize the correlation peak detection algorithm, the uncertainty of the velocity estimation is on the order of 1% of the maximum resolvable velocity.

The uncertainty in the average fluctuations in the velocity components can be determined by using the fact that the statistical uncertainty of the estimation of a fluctuating quantity is inversely proportional to the square root of the number of samples used. Therefore, for a typical experiment with 2000 time records, the uncertainty of the estimation of U_{rms} or V_{rms} is on the order of 2% of the mean value. However, in the case of the in plane turbulent kinetic energy one has to consider the fact that there is no contribution to the estimation of the third velocity component.

2.8 Models

All four models used in the present research are 3.5-caliber tangent-ogive forebodies with cylindrical afterbodies. Therefore, all are geometrically similar, except for their overall fineness ratios, which are due to the difference in afterbody length. All of the models were designed by the author, using the geometric ratios for the tangent-ogive, as discussed in Appendix D. The models will be called by the

[§] Uncertainty analysis for the PIV system is based on results from Vlachos [2000], modified to apply to the investigations performed for this work.

following names: the LDV model, the PIV model, the ESM Wind Tunnel model and the Stability Tunnel model.

2.8.1 ESM Water Tunnel Models

LDV Model:

The model employed in the LDV experiments is a 3.5 caliber tangent-ogive cylinder of base diameter D = 28.575 mm and overall length L = 171.4 mm, resulting in a fineness ratio of 6.0. The model is made of stainless steel, machined by a computerized milling machine to a precise geometry. The tip is rounded with a diameter of d_t = D/50 (2% blunted). Because laser-Doppler velocimetry is used to acquire the velocity fields around the model, it is painted with black paint used in marine applications, reducing the amount of reflected light entering the measurement volume.

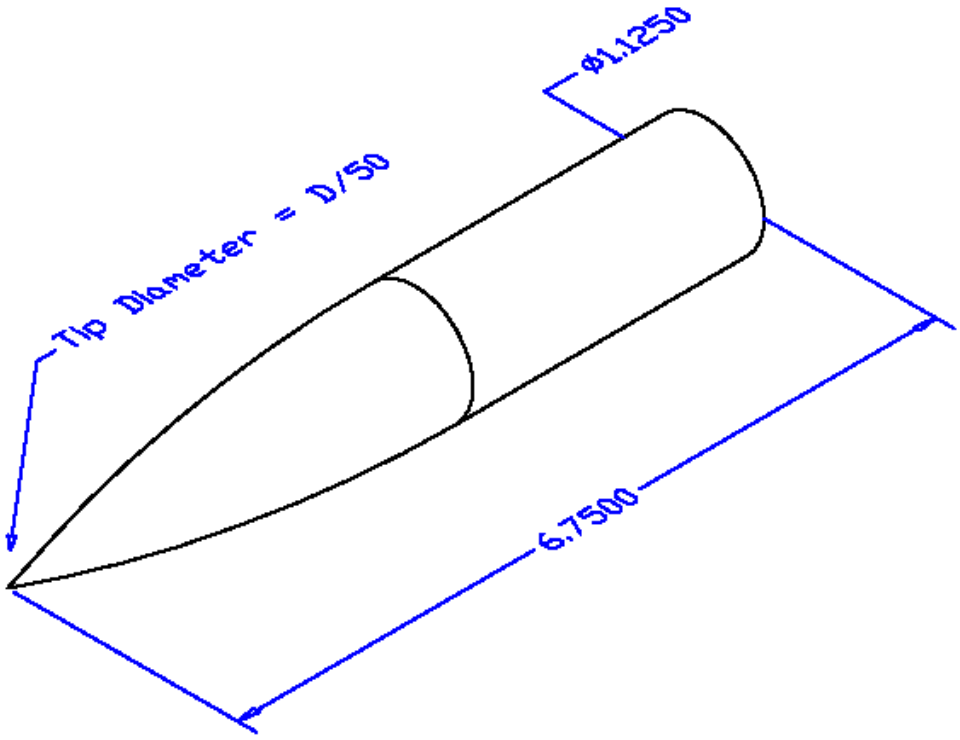

Figure 2.12 The LDV Model, Employed in the ESM Water Tunnel. Material is Stainless Steel. All Dimensions in Inches.

This paint has proven to be very resistant to peeling, cracking and chipping even when constantly exposed to water for up to two weeks. This ensures that the nose geometry remains consistent from the beginning to the end of the experiment. In order to induce a constant flow asymmetry, it is necessary to

affix a small bump made of hard epoxy/resin to the nose tip region. The bump extends 1/2 mm from the surface. It is affixed at approximately $\phi = 90°$ from the windward ray and 1 mm from the forebody tip. This assures that the asymmetry is equally biased for the duration of acquisition. The LDV model is shown in figure 2.12.

PIV Model:

The model used in the experiment was a 3.5 caliber tangent-ogive cylinder of fineness ratio 16. The base diameter of the model was 0.25" (12.7 mm). The model was machined without blunting the tip. The model was constructed from a transparent acrylic rod to pass as much of the incident laser light as possible, which reduced glare. The model was designed to be fitted to the same model mount as the LDV model. The PIV model dimensions are shown in Figure 2.13.

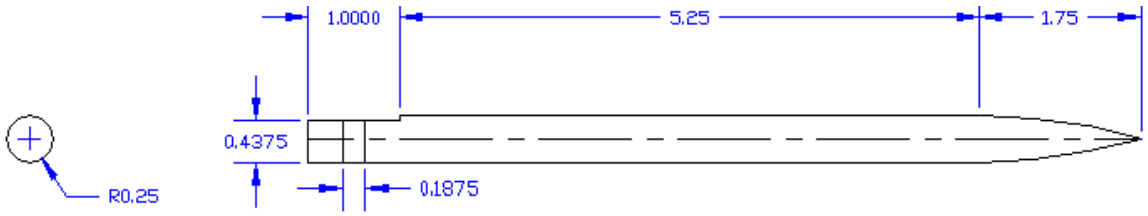

Figure 2.13: ESM Water Tunnel Model Used in PIV Investigations. The Model Is a 3.5 Caliber Tangent-Ogive Cylinder. Material is Transparent Acrylic. Dimensions in Inches

2.8.2 ESM Wind Tunnel Model

The model employed in the ESM wind tunnel tests is a 3.5 caliber tangent-ogive forebody with a cylindrical afterbody. The base diameter is D = 5.08 cm and the overall length of the model is 38.1 cm, resulting in a fineness ratio of 7.50. The model was machined out of aluminum using a computerized milling machine in order to decrease the number of surface imperfections. The tip of the model is rounded with a diameter of $d_t = D/50$. The model is instrumented with four sets of 24 evenly spaced pressure taps. These are aligned circumferentially and located at x/D = 1.81, 2.81, 3.75 and 5.25. The model is equipped with a small port near the tip of the nose to enable flow control by blowing. The port is 1 mm in diameter and is located at x/D = .41 from the tip. The blowing port faces predominantly forward, making an angle of approximately 20° with the axis of the model. During testing, the blowing port is located at $\theta = -135°$, which is on the starboard side of the model. The model is schematically shown in figure 2.14.

2.8.3 Stability Tunnel Model

The 3.5-caliber tangent-ogive cylinder employed in the Virginia Tech Stability Tunnel has a base diameter of 5" and an overall length of 27.5", corresponding to an overall fineness ratio of 5.50. The tip diameter of the model is d_t = D/20 (5% blunted). Five sets of circumferential pressure ports are installed at x/D = 1.25, 2.00, 2.75, 3.75 and 4.75. Each set of ports has 20 pressure ports spaced at 9° intervals over the pressure side of the model and 24 ports spaced at 7.5° intervals, for 44 pressure ports overall. Microblowing ports used to effect forebody vortex control are installed in the style used by Roos et. al. (1996). The diameter of the blowing ports is 0.216 cm (0.085") or 0.017·D. and they are located at x/D = 0.20. The model is designed to allow the placement of two ESP pressure scanner units inside the model,

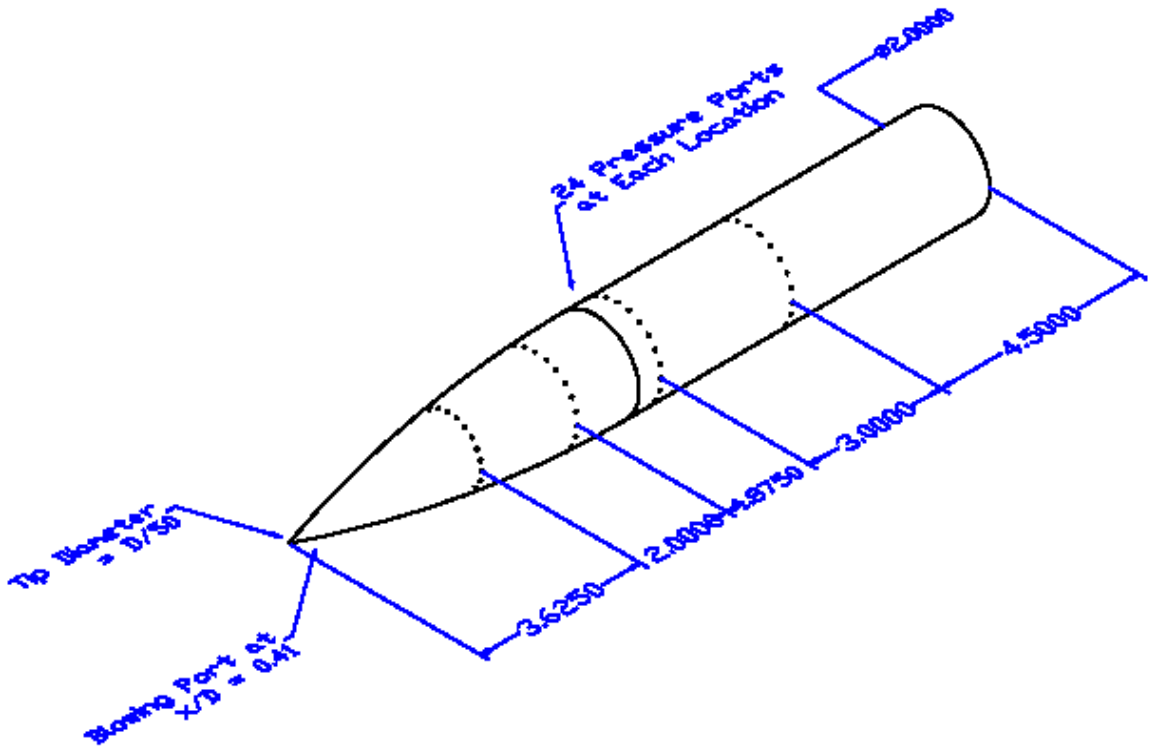

Figure 2.14 3.5 Caliber Tangent-Ogive Cylinder, the ESM Wind Tunnel Model. Base Diameter is 2 Inches (5.08 cm). Pressure Port Locations at x/D = 1.81, 2.81, 3.75 and 5.25. Blowing Port Located at x/D = 0.41. Material is Aluminum. All Dimensions in Inches.

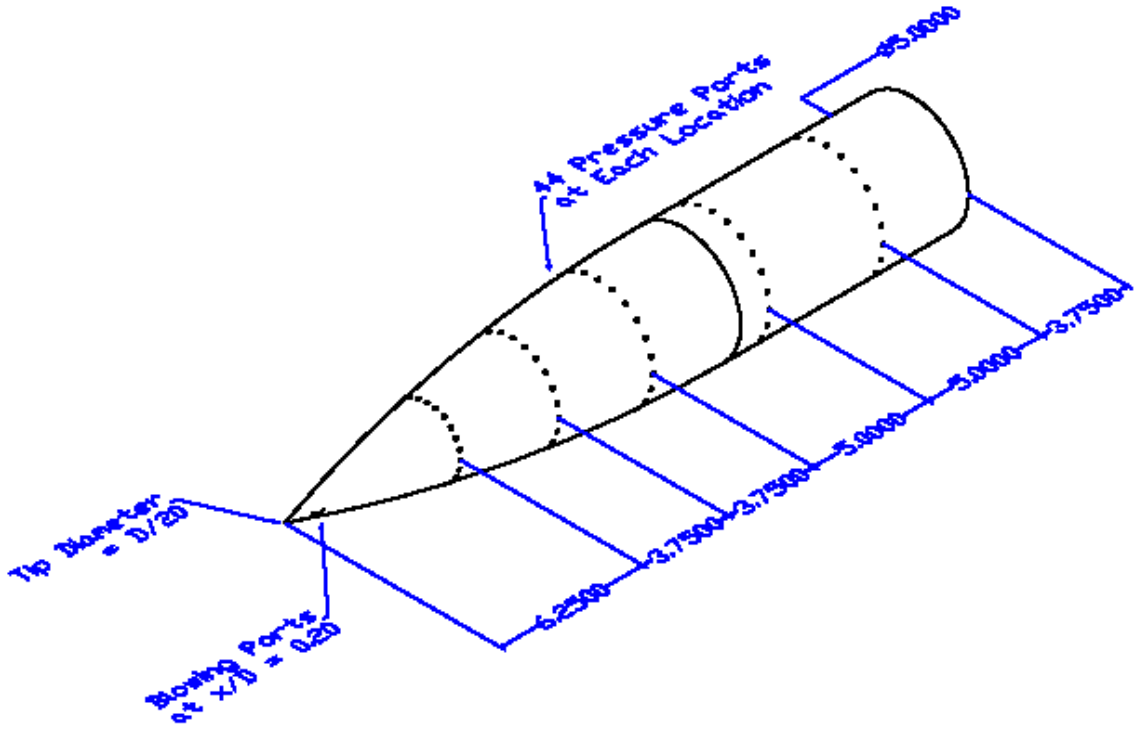

Figure 2.15 The Stability Tunnel Model. Base Diameter D = 5 Inches (12.7 cm). Pressure Port Locations at x/D = 1.25, 2.00, 2.75, 3.75 and 4.75. Blowing Ports at x/D = 0.20. Material is Aluminum. All Dimensions in Inches.

so the model bulkheads have passages for the required electronic and pneumatic support for these units. The entire model is built around a stainless steel mounting rod. The rest of the model is constructed from aircraft aluminum to minimize weight, and the assembled model with instrumentation weighs about 15 lbs. The Stability Tunnel Model is shown in figure 2.15.

2.9 Mass Flow Injection System Used for Flow Control

Similar mass-flow injection systems for the implementation of forebody blowing are used in the ESM Wind Tunnel and the Virginia Tech Stability Wind Tunnel. In each facility, compressed air at 80-100 psi is used as the flow source, but is regulated to less than 15 psi before entering the rest of the system. After exiting the regulator, the air is routed to a solenoid valve. This valve is used to turn the blowing on and off. The solenoid valve is actuated electrically by a relay that is a part of a circuit designed to delay the blowing by a specified amount of time. The valve is normally open, so that if power to the control circuit is completely removed, steady-state blowing will result.

Different delay circuits were used depending on the facility, but are essentially equivalent in operation. The circuit used in the ESM Wind Tunnel is a capacitor-resistor circuit that delays the same digital trigger as sent to the motor controller. The trigger is delayed based on a pre-programmed digital value and passed to the relay controlling the solenoid valve. The delay circuit used in the Stability Tunnel is integral with the Computer Boards, Inc. DAS08 data acquisition board. This board contains three 16-bit counters, one of which is loaded with a predetermined count and is clocked by the computer's bus clock, which is determined by a software routine. This trigger is also used as a gate to the counter or delay circuit, which then begins to count down. When the count reaches zero, a low-to-high transition occurs at the counter output. The output of the counter is connected to the relay controlling the solenoid valve, thereby activating the blowing.

When using either circuit, frequency of counting is known, so the delay time can be accurately controlled by varying the loaded count. The external trigger to commence data acquisition is sent by the data acquisition computer in the ESM Wind Tunnel tests, and by the DyPPiR computer in the Stability Tunnel tests, in each case on execution of the maneuver.

In both facilities, the solenoid valve that allows the blowing to occur is connected to the blowing port by a length of flexible tubing. The length of the tubing is 9.1 m (30 ft), and the inside diameter of the tubing is 0.3175 cm (0.125"). Because of the length of tubing involved, there is a time delay between the switching of the solenoid valve and steady-state blowing from the ports on the model. In order to investigate feedback control, it would be desirable to have a plenum and associated solenoid valve inside the model. However, the amount of space available was limited by the size of the models and by the volume of tubing needed to carry the surface pressures. Since blowing delays could not be brought to a minimal level, investigation of blowing control was limited mainly to the application of constant blowing rates.

In order to determine the delay inherent in the 9.1-m tubing length, a test involving a Hewlett Packard frequency analyzer and an Endevco, Inc. pressure transducer was designed. Both the analyzer and the pressure transducer are capable of responding to frequencies in excess of 2kHz. The pressure transducers were mounted so as to be able to sense the dynamic pressure at the blowing port outlet. The HP analyzer measured the voltage difference between the power control to the solenoid valve and the output of the pressure transducer. By observing the time record of this signal while blowing is triggered, it was possible to determine the time at which the solenoid valve opened, when mass flow began at the blowing-port outlet and when the mass flow reached the steady state. . The delay of blowing onset due to

the 9.1-m tubing length was found to be 0.0444 s. The delay from blowing onset to steady-state blowing was found to be 0.333 s. When the mass flow meter was employed (in the Stability Tunnel), its signal was used to determine the delay from blowing onset to steady-state blowing. These pneumatic delays were found to independent of the driving pressure for the range of driving pressures used in these investigations.

2.9.1 The Hastings Mass Flow Meter

For data in the Stability Tunnel for which forebody blowing was employed, the mass flow ejected from the blowing ports was measured by an HFM-200 mass flow meter manufactured by Hastings Instruments, Inc. This mass flow meter is a fast-response model capable of measuring up to 20 standard liters per minute (SLPM, 1 SLPM = $2.155 \cdot 10^{-5}$ kg/s) of an inert gas at up to 500 psig. The output of the meter is a 0-5 V signal that is inherently linear. Errors in accuracy, linearity and repeatability are 1.02% of the full scale of the meter. The unit is insensitive to changes in temperature with the voltage output varying at <0.1% of the full scale. The meter is equipped with a manual zeroing mechanism so that the voltage output can be set to zero volts with no flow. This task was performed before each use of the mass flow meter.

2.9.2 Uncertainty Analysis for the Mass Flow Coefficient

The measured mass flows are converted into dimensionless mass flow coefficients. In order to compare with previous results, the mass flow coefficient is defined in the same manner as Roos [1996]:

$$C_{\dot{m}} = \frac{\rho A V}{\rho_\infty S U_\infty} = \frac{\dot{m} U_\infty}{2qS} \tag{2.12}$$

where S is the planform area of the tangent-ogive forebody, and ρ, A and V are the exit density, area and velocity, respectively for the control flow. Using the method of Kline & McKlintock [1953] as shown in equation 2.7, and assuming that the error in the calculation of the planform area is negligible (due to precise knowledge of the body geometry), the uncertainty in the mass flow coefficient can be expressed as

$$\delta C_{\dot{m}} = \left\{ \left[\left(\frac{\partial C_{\dot{m}}}{\partial \dot{m}} \right) \delta \dot{m} \right]^2 + \left[\left(\frac{\partial C_{\dot{m}}}{\partial q} \right) \delta q \right]^2 + \left[\left(\frac{\partial C_{\dot{m}}}{\partial U_\infty} \right) \delta U_\infty \right]^2 \right\}^{\frac{1}{2}}$$

$$= \left\{ \left[\frac{U_\infty}{2qS} \delta \dot{m} \right]^2 + \left[-\frac{\dot{m} U_\infty}{2q^2 S} \delta q \right]^2 + \left[\frac{\dot{m}}{2qS} \delta U_\infty \right]^2 \right\}^{\frac{1}{2}} \tag{2.13}$$

$$= C_{\dot{m}} \left\{ \left[\frac{\delta \dot{m}}{\dot{m}} \right]^2 + \left[\frac{\delta q}{q} \right]^2 + \left[\frac{\delta U_\infty}{U_\infty} \right]^2 \right\}^{\frac{1}{2}}$$

Uncertainty for the Stability Wind Tunnel Setup

Typical data for a set of ensembles in the Virginia Tech Stability Wind Tunnel in which forebody blowing was employed has average values and uncertainties of freestream variables as listed in Table 2.2. The uncertainties listed are those in the mean values as determined by averaging the data over 20 ensembles while employing Chauvenet's criterion. More information concerning the ensemble averaging of results, determination of uncertainties and application of Chauvenet's criterion may be found in section 2.10.

Table 2.2 Typical Average Values and Uncertainties of Freestream Variables for Data Acquired During Stability Tunnel Testing in which Forebody Blowing was Employed.

Variable	Average Value	Uncertainty
Temperature, T_∞	302.5 K	0.00435 K
Static Pressure, P_∞	95, 100 Pa	1.06 Pa
Dynamic Pressure, q	772.2 Pa	0.0404 Pa
Density, ρ	1.095 kg/m^3	$2.0 \cdot 10^{-5}$ kg/m^3
Freestream Velocity, U_∞	37.6 m/s	0.00104 m/s

The planform area (S) of a 3.5 caliber tangent-ogive forebody can be determined from the ogive geometry (see Appendix D) to be $2.343 \cdot D^2$, which in the case of the D = 5" Stability Tunnel model is 0.4067 ft^2 (0.0378 m^2). Examining the factory calibration data for the mass flow meter, it can be observed that $\frac{\delta \dot{m}}{\dot{m}}$ never exceeds 0.04, or 4%. Substituting into equation 2.12 we find that

$$\delta C_{\dot{m}} = C_{\dot{m}} \left\{ [0.04]^2 + \left[5.23 \cdot 10^{-5}\right]^2 + \left[2.77 \cdot 10^{-5}\right]^2 \right\}^{\frac{1}{2}} = 0.04 \cdot C_{\dot{m}} \tag{2.14}$$

or the uncertainty in the mass flow coefficient is 4% of the calculated value. Note that the errors in the last two terms under the radical in equation 2.14 contribute an insignificant amount of uncertainty compared with the first term.

2.10 Acquisition and Reduction of Wind-Tunnel Data

2.10.1 Data Acquisition

The method of pressure data acquisition varied little between the two wind-tunnel facilities. Pressure data were acquired by employing the ESP modules, which were mounted inside the test sections and allowed to ride along with the model during the motions. The ESP's were actually placed inside of the Stability Tunnel Model. The ESP's were connected to dedicated support boards to allow digital addressing and voltage regulation for the units. Since the ESP's have a maximum frequency response of 50 Hz, they were sampled at anywhere from 100 Hz (Nyquist frequency for 50 Hz maximum frequency in signal) to 250 Hz (to be able to correctly resolve the signal amplitude at 50 Hz). Sampling time and sampling frequency were also dictated somewhat by the amount of space available for data and the fact that increased amounts of data increased data reduction time. Sampling was done by a CIO-DAS08 12-bit A/D data acquisition board in the ESM Wind Tunnel and by a programmable-gain CIO-DAS08-AO 12-bit A/D data acquisition board in the Stability Wind Tunnel. Both of these boards are manufactured by Computer Boards, Inc. and are essentially interchangeable as far as hardware connections are concerned.

In both facilities, one extra channel of data needed to be acquired. In the Stability Wind Tunnel it was the voltage from the mass flow meter, and in the ESM Wind Tunnel it was the voltage from the rotational encoder. Since both of these voltages had ranges that were different from that of the ESP, it was necessary to employ an additional 12-bit A/D data acquisition board with a different voltage range setting.

The method of averaging multiple ensembles was used in all experiments presented in this work that involve model motion. In order to employ this method, the unsteady motion is executed multiple times, with data acquisition triggered at the same time relative to the motion. The resulting data are averaged over the number of ensembles, or times the motion was executed. The result is a time-series of data, with each data point representing the average result over the number of ensembles.

Data Acquisition in ESM Wind Tunnel:

Pressure data during coning motions are acquired at $\alpha = 45°$ and 55°, for $k_c = \pm 0.016$ and ± 0.041 and for constant and delayed blowing with several different rates. The coning axis is located at $x_c/D = 3.23$ for $\alpha = 45°$ and at $x_c/D = 3.82$ for $\alpha = 55°$. The velocity is maintained at approximately 10.4 m/s for all data sets, meaning that the Reynolds number is $Re_D = 29.4 \cdot 10^4$. Corresponding steady data are also acquired. Each motion is performed 40 times and the results are ensemble averaged. There are four sets of circumferential pressure ports at x/D = 1.81, 2.81, 3.75 and 5.25, with each set containing twenty-four ports. Because only the ±10" H_2O 32-channel ESP could be employed because of the pressure resolution required in this low-speed facility, only one set of ports could be connected to the ESP. This meant that all four sets of pressures were acquired at different times. During the switching of the ports, the afterbody of the model was never removed from the coning mount, and was therefore replaced in almost exactly the same position in the test-section. The nose of the model was threaded onto the afterbody, so there was only one possible alignment between the two. This insured that the nose always had the same orientation during testing.

Since the drive train for the coning motion and also the encoder involve gears, accurate maneuvers and position feedback required that play in the gears be minimized. Therefore, each motion of the model is started by moving past the start location in the direction opposite to the desired motion. Then the motion direction is reversed and the model brought to the start location. In this way, the miter gears and the encoder gears are meshed. This practice greatly reduced the spread of position data. The flow around the model is allowed to reach the steady state before the motion is triggered.

Once the model reached the start position, the main computer responsible for pressure and position data acquisition sent a trigger. This trigger is passed to the delay circuit that controls the solenoid valve used for mass flow injection, to the motor-control computer and to the additional board to acquire the angular position. The motion is delayed by 0.1 s once pressure acquisition commences. The pre-programmed motion is then executed, and the model is returned to the start location as outlined

above. The data from the current ensemble are taken from memory and saved to disk, and a new motion is ready to begin.

Data Acquisition in Stability Wind Tunnel:

Circumferential surface-pressure data are acquired during pitching motions from $\alpha = 10°$ to 55° for $k_p = 0.00296$ and 0.00592 and $x_p/D = 0.0$. Pressure data are also acquired during coning motions for $k_c = 0.0057$, 0.0114, 0.170 and 0.196. The coning axis is located at $x_c/D = 6.23$ for all motions. The Reynolds number is maintained very close to $2.75 \cdot 10^5$ for all tests, with an average freestream velocity of approximately 37 m/s. For each type of motion, pressures are acquired with and without forebody blowing. All pressure data are acquired at a rate of 250 Hz for a duration of 3 seconds. Each motion is executed twenty times and the results are ensemble averaged. Corresponding steady data are also acquired.

Although the Stability Tunnel model has 5 sets of circumferential pressure ports with 44 ports in each set, only data for the first three sets of ports at x/D = 1.25, 2.00 and 2.75 were acquired. Both the ±10" H_2O ESP and the ±20" H_2O ESP were employed due to the number of pressures to be acquired. When switching the pressure ports, the afterbody of the model was not removed from the 50° offset block. The forebody and afterbody were constrained to fit together in only one way with very tight tolerances. While this caused the author much consternation and to use unbecoming language while getting the model ready for data acquisition, it also ensured that the model could always be placed at the same location and orientation during testing.

Boundary-layer trip strips made from duct tape were attached to the model during testing. These trips were placed at $\theta = \pm 55°$ from the windward stagnation point and had sawtooth edges to promote flow transition. The trip strips were not extended to the forebody tip, but were stopped at x/D = 0.5. The trips were also briefly interrupted when crossing the lines of circumferential pressure ports. According to Lamont [1982], the flow over the 3.5 caliber tangent-ogive forebody should start to exhibit transitional separation characteristics for $Re_D > .5 \cdot 10^5$. By installing the trip strips, it was hoped that turbulent separation might be achieved. While this was not the case, the surface pressures reveal that the flow experienced transitional separation for $Re_D = 2.75 \cdot 10^5$. Without the trip strips, the separation was laminar for the same Reynolds number. Thus, the trip strips did succeed in changing the boundary-layer state at separation. This enabled surface pressures on a maneuvering model in the transitional Reynolds number regime to be acquired for the first time in a wind-tunnel experiment. The trip strips can be easily seen in figure 2.16

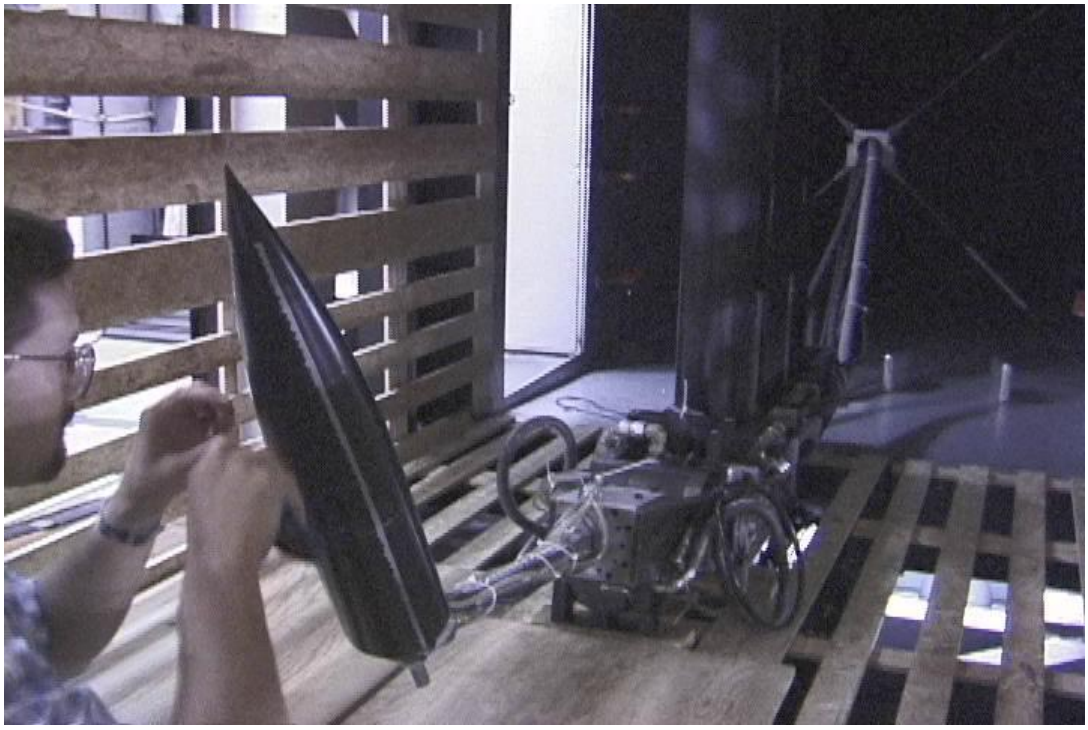

Figure 2.16 Stability Tunnel Model Installed on the DyPPiR Model Mount. Sawtooth Boundary-Layer Trip Strips Located on the Model at $\theta = \pm 55°$ Can Be Easily Seen.

In the Stability Tunnel, the DyPPiR is responsible for triggering the data acquisition at the same instant the motion commences. The model is set to the start position for the desired motion, and then the trigger is sent. The trigger is passed to the pressure data acquisition computer and to the delay circuit controlling the solenoid valve used for mass flow injection. The motion is delayed for 0.5 s the trigger is sent. During the motion, the DyPPiR computer acquires command and error signals for all three degrees of freedom of the DyPPiR and all pertinent test-section thermodynamic data. This data acquisition is performed at 250 Hz by a 12-bit A/D data acquisition board manufactured by Metrabyte. When data acquisition ends, the model is reset to the initial position and the flow is allowed to achieve a steady state before the next motion is performed.

2.10.2 Data Reduction

All wind-tunnel data is reduced by one program, which performs several operations on the original pressure data, calculates several variables derived from the pressure data, incorporates the motion and thermodynamic data, then writes all data to disk in a format suitable for graphing. The operations on the original data include ensemble averaging using Chauvenet's criterion, rectifying all pressure data to precise times and using wavelet techniques to remove pressure fluctuations caused by the presence of the test-section slats mentioned in section 2.3.2. The variables calculated from the pressure data include the

uncertainty in the ensemble-averaged pressure coefficients (δC_p), the sectional yaw force coefficient (C_y), the sectional normal force coefficient (C_n), the uncertainties in these quantities (δC_y, δC_n), and the difference between the instantaneous and steady-state C_y (ΔC_y).

Ensemble Averaging the Pressure Data Using Chauvenet's Criterion

Ensemble averaging is useful in resolving the mean effect of the maneuvers. Typically, multiple maneuvers are performed without changing any other flow or model parameters. If N motions are executed, then there will be N time records of data. In order for the ensemble-averaged data to be meaningful, it is essential that the motion of the model occur at the same interval of time for each record and that the motion is executed repeatably. If this is the case, then the ensemble-averaged pressure coefficient can be calculated from

$$\overline{C_p} = \frac{1}{N}\sum_{n=1}^{N} C_{p,n} \tag{2.15}$$

Equation 2.15 is be used to determine $\overline{C_p}$ for each sample in the time records. The result of this process is a single time record with ensemble-average pressure coefficients, reflecting the mean effect of the motions. From this point forward we will take C_p to denote the ensemble-averaged pressure coefficient.

Chauvenet's criterion states that given a set of N values x_i with a mean $\bar{x}$ and a standard deviation σ, then if any of the x_i have a value such that based on σ less than half of a sample would be expected to exhibit that value, then that sample should be discarded and the usable number of samples reduced to N – 1. The application of Chauvenet's criterion during ensemble averaging of the pressure coefficients is in the manner set forth by Taylor [1982]. The mean and standard deviation for the set of pressure coefficients are calculated. Employing the error function with the calculated standard deviation, the value of each sample is used to determine how many samples would be expected to lie at that value. If the answer is less than 0.5, then the sample is discarded. Chauvenet's criterion is not reapplied after the removal of samples. Using Chauvenet's criterion causes no more than one of twenty samples to be removed from the data acquired in the Stability Wind Tunnel, and no more than three in forty samples for data acquired in the ESM Wind Tunnel.

Rectifying Pressure Data to Precise Times

During pressure data acquisition, the ESP's are addressed and allowed to settle for at least 50 μs. Then the voltage corresponding to the address is sampled, and the address is incremented. This process continues until all of the pressure ports have been sampled. There are two frequencies associated with the acquisition process. One is the frequency at which the ESP is sampled from port to port, called the burst rate. Since the ESP's must be allowed the 50 μs settling time, the maximum burst rate is usually 20 kHz, although this rate can be increased when sampling multiple ESP's with certain sampling algorithms. Typical burst rates ranged from 15 kHz to 18 kHz. The second frequency is the frequency at which sampling of the entire set of pressures commences. This is the stated sampling rate of data acquisition. When sampling large numbers of ports, the time required for port sampling (i.e. the number of ports divided by the burst rate) cannot be greater than the inverse of the sampling frequency. If this occurs, correct time-stamping of the data will not be possible.

Since all pressure data are not acquired at the same instant, there is always a problem with the time that should be associated with calculated quantities that require integration of all of the pressures, such as C_y and C_n. This problem becomes more severe when large numbers of ports are sampled. For instance, if the sampling rate of 32 ports are sampled at 250 Hz with a burst rate of 15 kHz, then the total sampling time is 0.00213 s, which is more than half of the 0.004 s dictated by the sampling rate. For this reason, linear interpolation between consecutive port samples is used to rectify all pressures to the time associated with the first sampled port. If this is not done, then the integration of the pressure coefficients into sectional forces results in quantities that cannot be placed accurately in time because of the large spread in the times associated with the individual pressures.

Employing a Wavelet-Based Technique for Smoothing of Pressure Data

The presence of the slats in the Stability Wind Tunnel (section 2.3.2) causes flow and pressure oscillations in the test section. Typical time records of dynamic pressure and surface pressure data are shown in figure 2.17a. The dynamic pressure is taken from the Pitot-static tube. Although it may appear that the dynamic pressure is nearly constant, its FFT shown in figure 2.17b reveals a very strong peak between 10 and 11 Hz. An FFT of surface pressure data at $\theta = 90°$ (figure 2.17c) shows that the same frequency is responsible for the very large pressure fluctuations seen in the corresponding time record of figure 2.18a. The fact that the frequencies are nearly equal to each other gives strong evidence for the amplification of the freestream oscillation as the flow develops over the body. An algorithm to reduce the pressure fluctuations before ensemble averaging was sought, but unfortunately none was robust enough to

remove the 10-11 Hz fluctuations without affecting the pressure variances due to the motion. Fourier methods cannot be used because they assume periodic boundary conditions, which are invalidated by the ramp motions.

Like the Fourier transform, the discrete wavelet transform (DWT) is a fast, linear operator on a dataset containing a number of data points that is an integer power of two. Unlike the Fourier transform, the DWT is highly localized in space and in time, so there is no assumption of periodic boundary conditions. The DWT employed here is that described in Press et. al. [1997]. This DWT uses a set of orthogonal wavelet filter coefficients to convert the time record into multiple hierarchies, each containing more samples than the last by a power of two. Thus, if the dataset contained 128 samples, then the largest hierarchy would have 64 wavelet coefficients, the next largest 32, and so on. The larger hierarchies are able to describe very transient pieces of the data, while the smallest hierarchies are responsible for the slowly varying "smooth" part of the data. Once the time records are converted into wavelet space, different data smoothing techniques can be tried. Essentially, the wavelet coefficient series is truncated, then an inverse DWT is applied to convert the data back to real time. An example of this process is shown in figure 2.18, where a sample noisy square-wave signal in figure 2.18a is operated on by the DWT of high order, producing the corresponding wavelet coefficients. The frequency associated with the wavelet coefficients increases with wavelet number in figure 2.18b. Truncation based on wavelet coefficient values can succeed in nearly recovering the original square wave, as shown in figure 2.18c. Wavelet techniques operating on the pressure coefficients before ensemble averaging were tried and were somewhat successful. However, there was difficulty identifying the wavelet coefficients in each hierarchy that were responsible for the 10-11 Hz pressure fluctuations.

More success was achieved by ensemble averaging the pressure coefficients first. Since the pressure fluctuations were independent of the data acquisition procedure, they can be considered a random process. Assuming that enough ensembles of data were acquired, the remnants of the pressure fluctuations that remain after ensemble averaging could be considered to be noise. Therefore, a noise removal procedure in wavelet space, based on the characteristics of random noise (from Mallat [1998]), is used to remove almost all of the remainder of evidence of pressure fluctuations. A set of twelve Daubechies wavelet filter coefficients are used in the wavelet transform. In order to make the number of samples an integer power of 2, the original 751 samples are augmented with zero padding on each end of the signal, resulting in 1024 samples. After the smoothing process is complete, the zero padding is removed to recover the smoothed signal. An example of the effectiveness of the DWT is shown in figure 2.19. In figure 2.19a, the pressure data are not smoothed, while the data in figure 2.19b are smoothed

with the noise-removal process discussed above. Unfortunately, since this procedure cannot remove the fluctuations before the data are averaged, the uncertainties associated with the ensemble-averaged pressure coefficients remain rather high.

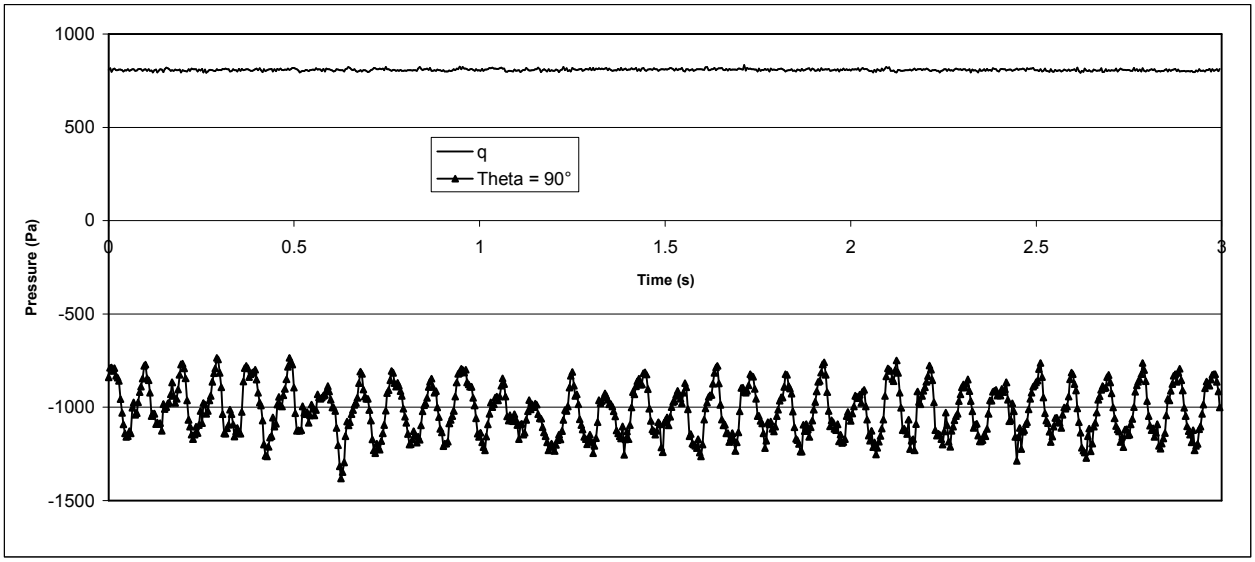

Figure 2.17(a) Time Records of Dynamic Pressure (from a Pitot-Static Tube) and a Surface Pressure Port Located 90° from the Windward Stagnation Point. Both Series Are Acquired Simultaneously. The Pressure Fluctuations are Much More Pronounced at the Location on the Model.

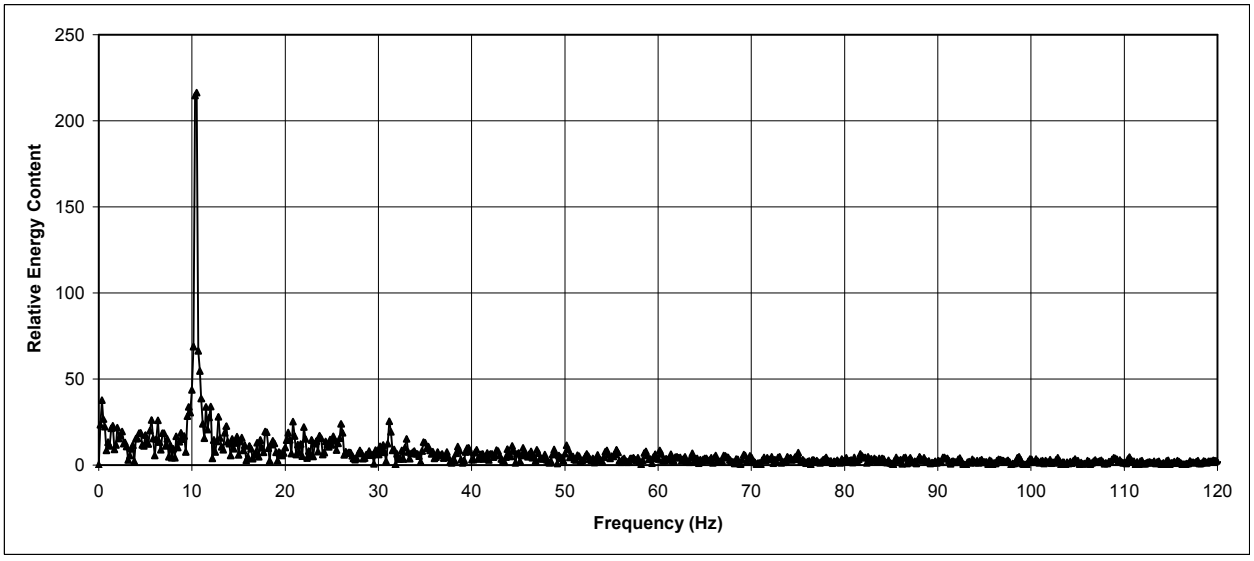

Figure 2.17(b) FFT of the Dynamic Pressure Data Shown in (a). A Dominant Peak is Evident Between 10 and 11 Hz.

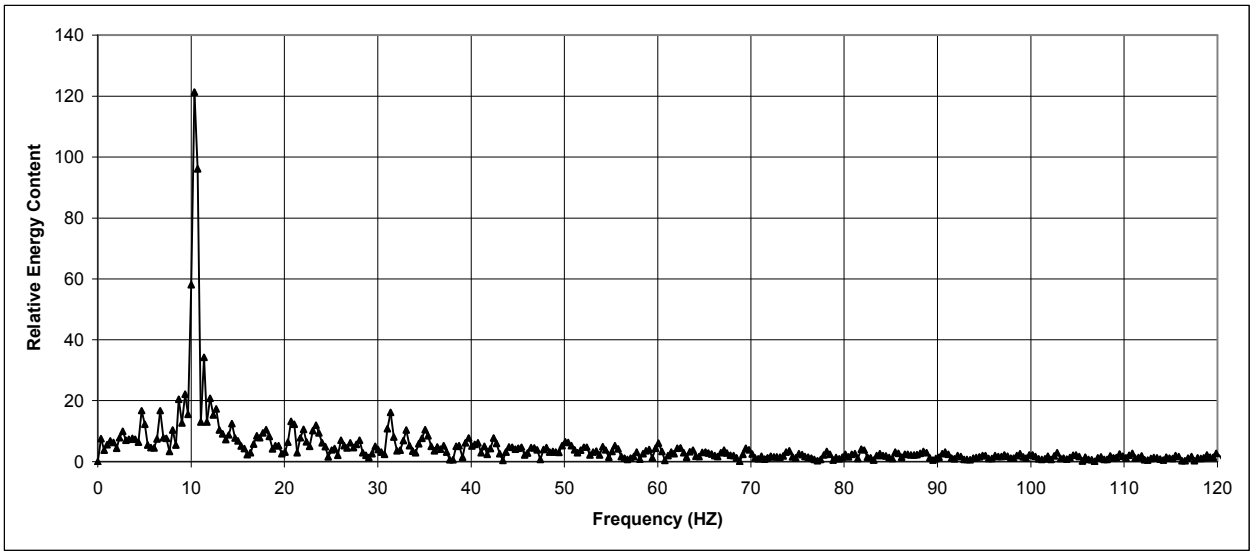

Figure 2.17(c) FFT of the Surface Pressure Data Shown in (a). As in (b), a Dominant Peak is Evident Between 10 and 11 Hz. This Signifies that the Large Fluctuations Seen in the Surface Pressure Data are an Amplification of the Fluctuation in the Dynamic Pressure.

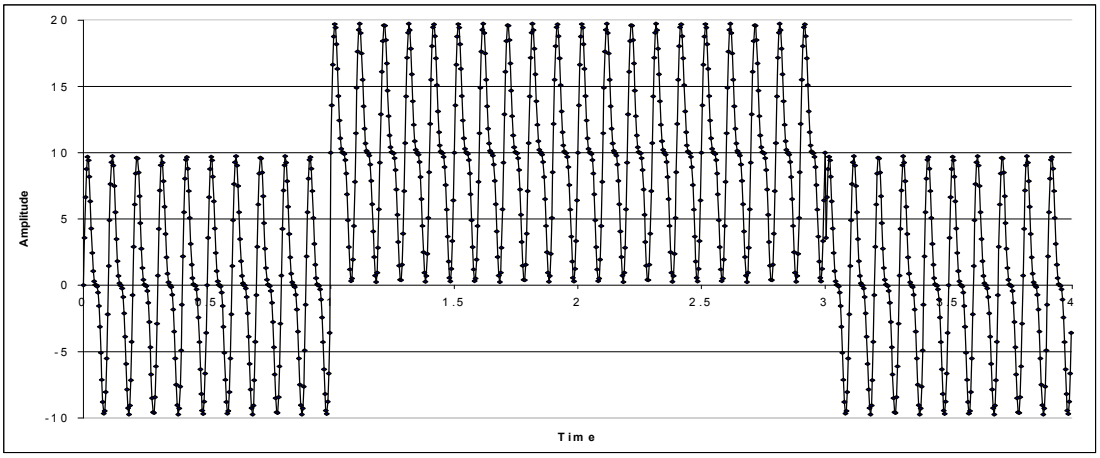

Figure 2.18 (a)

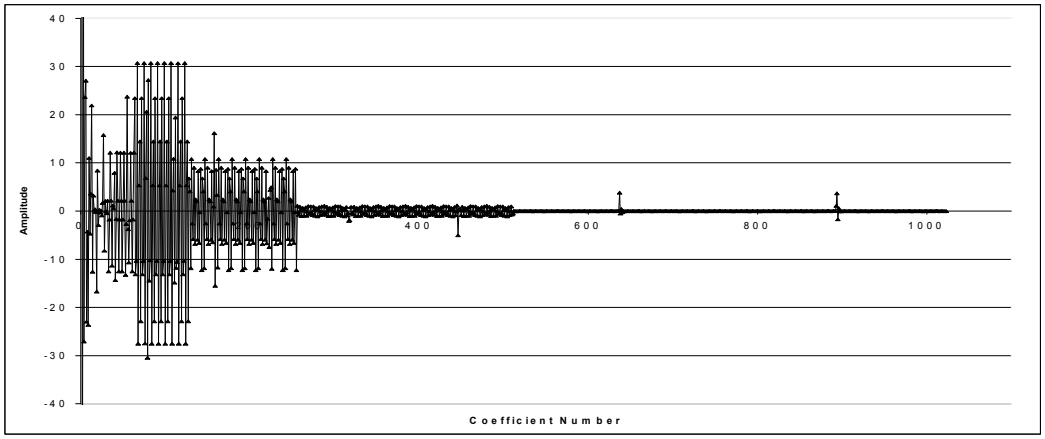

Figure 2.18 (b)

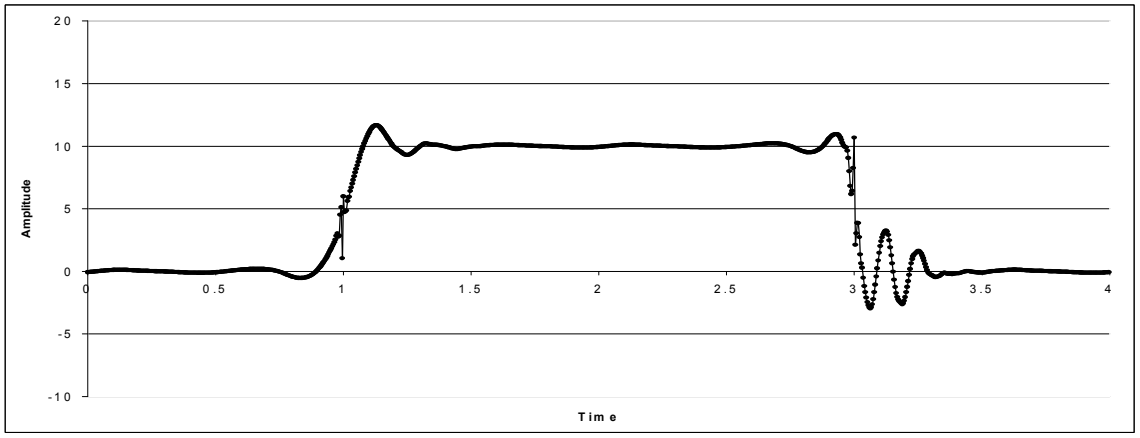

Figure 2.18 (c)

Figure 2.18 An Example of the Wavelet Smoothing Process. A 1024-Sample Square-Wave Signal with Noise (a) is Transformed into Wavelet Space with a High-Order DWT, Resulting in the 1024 Wavelet Coefficients Displayed in (b). Most of the Wavelet Hierarchies are Discernable in (b), with the "Smooth" Wavelet Coefficients on the Left and Those Corresponding to High-Frequency Changes on the Right. Selective Truncation of Wavelet Coefficients, Followed by an Inverse DWT, Results in the New Signal in (c), Where Much of the Noise Has Been Suppressed, while the Form of the Signal is Maintained.

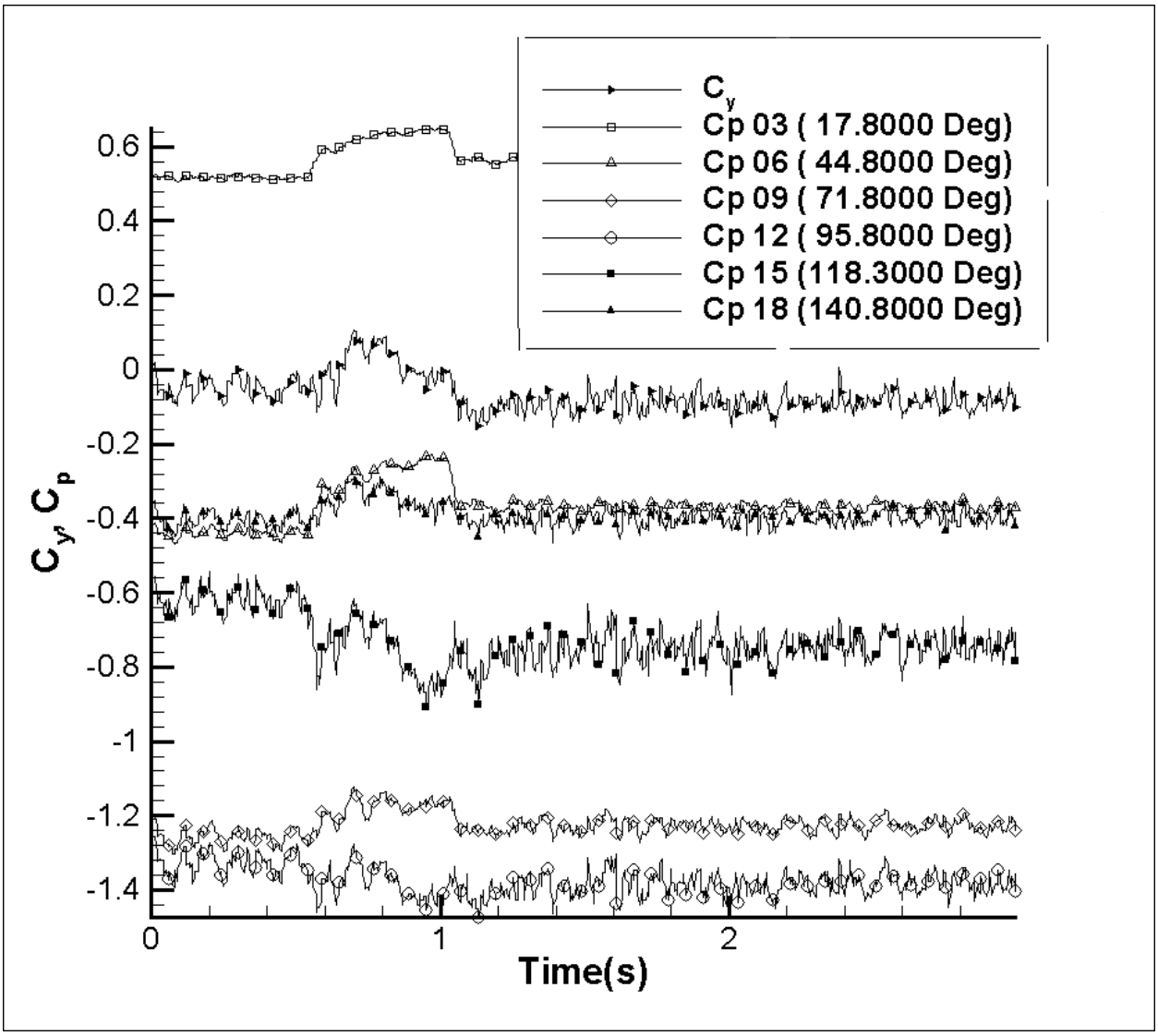
C_y
Cp 03 (17.8000 Deg)
Cp 06 (44.8000 Deg)
Cp 09 (71.8000 Deg)
Cp 12 (95.8000 Deg)
Cp 15 (118.3000 Deg)
Cp 18 (140.8000 Deg)
0.6
0.4
0.2
0
-0.2
-0.4
-0.6
-0.8
-1
-1.2
-1.4
C_y, C_p
0
1
2
Time(s)

(a)

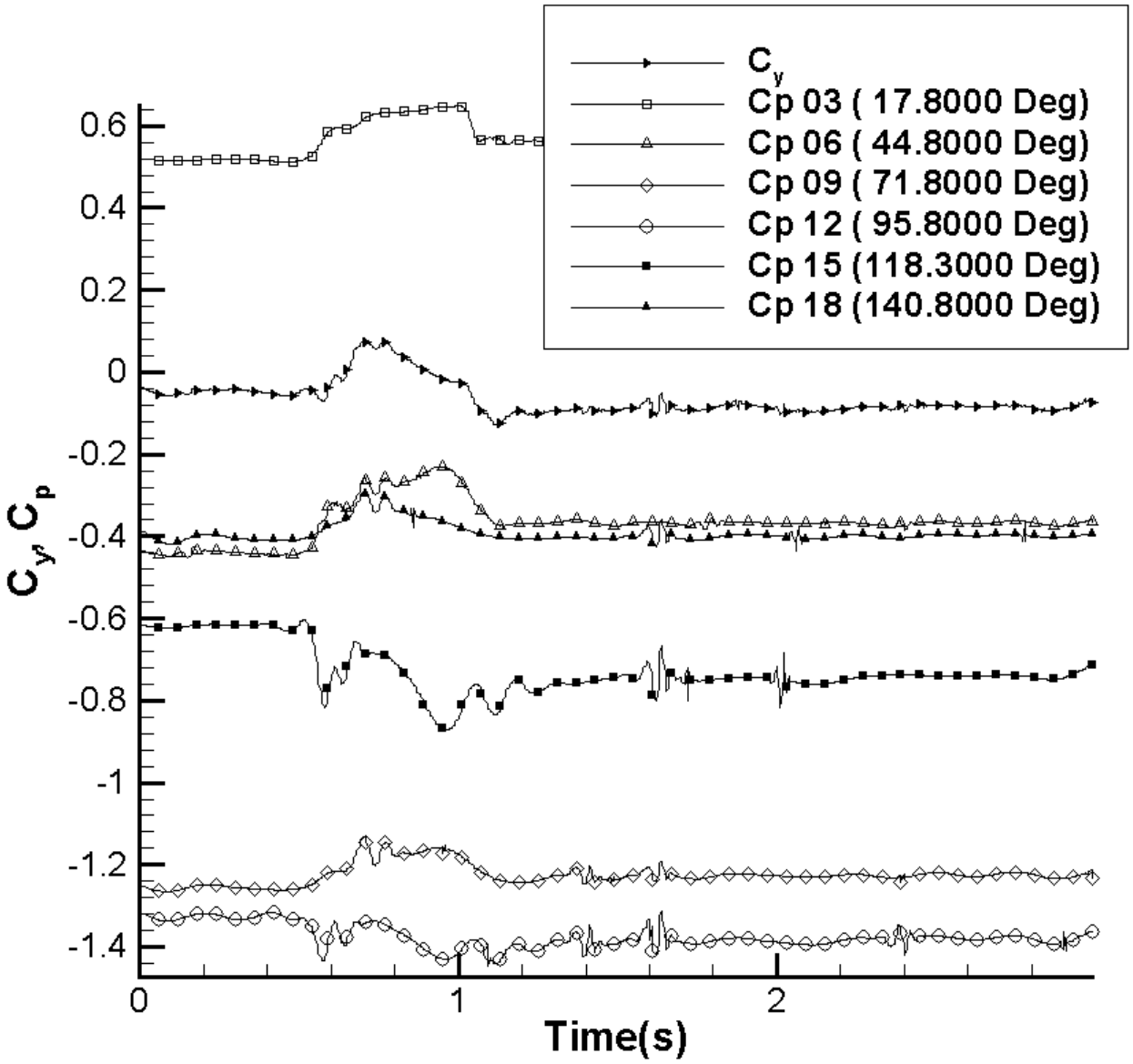

(b)

Figure 2.19 Application of the Wavelet Smoothing Process to Pressure Coefficient Data Acquired in the Stability Tunnel: (a) No Smoothing of Data, Only Ensemble Averaging; (b) Ensemble-Averaged Data is has Subsequent Noise Removed through Use of DWT.

Calculation of Secondary Values from the Pressure Data

Once all of the modifications to the original pressure coefficients are finished, other pertinent quantities may be calculated. The dimensionless sectional yaw and normal forces are calculated from

$$C_y = \frac{d}{2 \cdot D} \oint_{\theta} C_p \sin\theta \cdot d\theta \tag{2.16}$$

and

$$C_n = \frac{d}{2 \cdot D} \oint_{\theta} C_p \cos\theta \cdot d\theta \tag{2.17}$$

respectively. D is the base diameter of the tangent-ogive forebody (the characteristic length) and d is the (local) diameter where the set of pressure ports is located. Since the pressure coefficients are known only at discrete points, the integrals are calculated by using the trapezoidal rule. For N discrete circumferential pressure ports, this results in the following equations for the sectional yaw and normal force, respectively:

$$C_y = \frac{d}{4 \cdot D} \sum_{i=1}^{N} \left[(C_{p,i} + C_{p,i+1}) \cdot \sin\left(\frac{\theta_i + \theta_{i+1}}{2} \right) \cdot \Delta\theta_i \right] \tag{2.18}$$

$$C_n = \frac{d}{4 \cdot D} \sum_{i=1}^{N} \left[(C_{p,i} + C_{p,i+1}) \cdot \cos\left(\frac{\theta_i + \theta_{i+1}}{2} \right) \cdot \Delta\theta_i \right] \tag{2.19}$$

where θ_i and $C_{p,i}$ are the angular position and ensemble-averaged pressure coefficient of the i^{th} port, respectively. The angular difference $\Delta\theta_i = \theta_{i+1} - \theta_i$, where $\theta_{N+1} = \theta_{i=0}$ due to the circular nature of the integration. Because of the way that θ is defined, positive sectional yaw force is toward the starboard side, while positive sectional normal force is toward the lee side.

The uncertainty in C_y and C_n may be determined by the application of the method of Kline and McKlintock [1953] (equation 2.2) to equations 2.18 and 2.19. Assuming that the uncertainty in d, D and are negligible (all being due to machining accuracy), and realizing that the uncertainty in angular position $\delta\theta$ will be the same for all ports, the uncertainty in the sectional yaw force may be expressed as

$$\delta Cy = \left\{ \left[\left(\frac{\partial C_y}{\partial C_{p,i}} \right) \cdot \delta C_{p,i} \right]^2 + \left[\left(\frac{\partial C_y}{\partial C_{p,i+1}} \right) \cdot \delta C_{p,i+1} \right]^2 + \left[\left(\frac{\partial C_y}{\partial \theta_i} \right) \cdot \delta\theta_i \right]^2 + \left[\left(\frac{\partial C_y}{\partial \theta_{i+1}} \right) \cdot \delta\theta_{i+1} \right]^2 \right\}^{\frac{1}{2}}$$

$$= \frac{d}{4 \cdot D} \left\{ \left[\sum_{i=1}^{N} \sin\left(\frac{\theta_i + \theta_{i+1}}{2} \right) \cdot \Delta\theta_i \, \delta C_{p,i} \right]^2 + \left[\sum_{i=1}^{N} \sin\left(\frac{\theta_i + \theta_{i+1}}{2} \right) \cdot \Delta\theta_i \, \delta C_{p,i+1} \right]^2 + \left[\sum_{i=1}^{N} \left(C_{p,i} + C_{p,i+1} \right) \cdot \cos\left(\frac{\theta_i + \theta_{i+1}}{2} \right) \cdot \Delta\theta_i \, \delta\theta_i \right]^2 \right\}^{\frac{1}{2}} \tag{2.20}$$

The calculation for the uncertainty in the sectional normal force coefficient is similar:

$$\delta C_n = \frac{d}{4 \cdot D}\left\{\left[\sum_{i=1}^{N}\cos\left(\frac{\theta_i + \theta_{i+1}}{2}\right)\cdot\Delta\theta_i\,\delta C_{p,i}\right]^2 + \left[\sum_{i=1}^{N}\cos\left(\frac{\theta_i + \theta_{i+1}}{2}\right)\cdot\Delta\theta_i\,\delta C_{p,i+1}\right]^2 + \left[\sum_{i=1}^{N}\left(C_{p,i} + C_{p,i+1}\right)\sin\left(\frac{\theta_i + \theta_{i+1}}{2}\right)\cdot\Delta\theta_i\,\delta\theta_i\right]^2\right\}^{\frac{1}{2}} \tag{2.21}$$

For actual calculations, all of the geometric data are known a priori, $\delta\theta_i$ is estimated at 0.75° worst-case based on the accuracy with which the models can be placed in the facilities, and $\delta C_{p,i}$ is determined during ensemble averaging. If the standard deviation associated with the ensemble-averaged $C_{p,i}$ is σ, then $\delta C_{p,i} = \frac{\sigma}{\sqrt{N}}$, where N is the number of usable ensembles after application of Chauvenet's criterion.

In order to better ascertain the deviation of the sectional forces from the steady state, the variable ΔC_y is defined as the difference between C_y and the average C_y before the model motion. ΔC_n is defined in the same manner for the sectional normal force.

2.11 LDV Data Acquisition and Reduction

The TSI laser-Doppler velocimetry system as described in section 2.4 is installed adjacent to the ESM Water Tunnel. This section describes the data acquisition process for the data discussed and presented in Chapter 5.

2.11.1 LDV Data Acquisition

The LDV data acquisition process begins with the alignment of the LDV system discussed in section 2.5. Next, the LVDT's that provide position feedback for the three traverse axes are calibrated. The model is installed and pitched to the position of α = 36.74°. In order to place the measurement volume into the correct plane, the latter is first placed on the trailing edge of the model at θ = -90°. This location is always used as the starting point, so that the location of each data plane is determined in the same manner. From the location on the trailing edge, the relative location of the data plane can be found through application of simple geometry. Note that when the model is placed at α = 36.74°, these planes are perpendicular to the model axis. The beams are then moved to the start location within the data plane, the model is placed at the initial angle of incidence and data acquisition commences.

The data acquisition computer, an IBM PS/2 Model 55, acquires data with an installed Data Translation DT2905 12-bit A/D data acquisition card. This card also has D/A capability with dedicated memory, so that a preprogrammed pulse train can be sent to the pitching motor without help from the CPU, which must be dedicated to data acquisition. A software trigger starts the data acquisition and the motion at the same instant. Two thousand time records are acquired at 500 Hz or 550 Hz, depending on the experiment. Data are acquired for eight data planes and for two motions, one from $\alpha = -2.86°$ to $\alpha = 54.74°$ and one from $\alpha = 18.74°$ to $\alpha = 54.74°$. Both motions had a reduced frequency of $k_p = 0.096$. The freestream velocities varied but are always close to 25 cm/s, corresponding to Re_D near $7.0 \cdot 10^3$. The motion is repeated ten times at each measurement location, and the time records are ensemble averaged. One hundred evenly-spaced time records are written to disk. The measurement volume is moved to the next location with feedback from the LVDT's, and the process is repeated. Then entire process is automated, so that all that needs to be done is to ensure that the tunnel is adequately seeded. Each plane of data required approximately 24 hours to complete.

There is no feedback associated with the stepping motor, but the model motion was tested extensively for repeatability, and there is no reason to believe that the motion is compromised in any way. Any deviation from the scheduled motion would have resulted in the model returning to the wrong start location, which would have been immediately noticed. Since the pitching maneuver is executed ten times at each measurement point, and there are about 600 points per plane and eight total planes (each requiring acquisition from two sides of the test section), the model maneuver was executed on the order of 100,000 times to acquire the data presented here.

2.11.2 LDV Data Reduction

Application of a Local-Least Squares Interpolation/Smoothing Algorithm

During the acquisition of LDV data in the ESM Water Tunnel, there were several issues that involved the validity of data due to the model passing through the laser beams, or due to the model being positioned very close to the measurement volume. Since the model pitched through the laser beams, it disturbed the measurement volume and invalidated the data collecting during the time the beams were blocked by the model. After the model cleared the measurement volume, the effects of it having passed through the beams was still evident, as there was a finite lag in the LDV response from the time the beams were cleared to the time the data was again reliable. If the model was positioned very close to the measurement volume, laser light was reflected by the model back into the measurement volume. The

model was painted black, but this served only to minimize the effects of the reflected light, and did not completely eliminate the effects.

First-order local least-squares interpolation/smoothing routines were employed in an attempt to predict and/or smooth the velocity fields. In all cases, this process proceeded in three steps: (1) Identification of the points which were blocked or affected by the proximity of the model; (2) Removal and re-prediction of the removed points; (3) Smoothing of the entire plane, including the newly re-predicted points.

In the first step, the locations of points where the beams were blocked at a particular time were calculated through knowledge of the location of the model. This information can be directly calculated from the model location as a function of time. A direct comparison of the model location with the location of the measurement volume gives the blockage status.

In the second step, the removed data is re-predicted. The re-prediction uses flow symmetry considerations for points on the windward side of the model. A second-order local-least squares technique is used to calculate the data. With this method, data from the closest 8 points (on a spatial basis) are employed, and a second-order surface is fitted to the pertinent variable (say u, v or w).

In the third step, the entire plane is smoothed by using as input the data from the closest 8 points to the point being smoothed. Figure 2.20 shows the results of this interpolation/smoothing process. Note that the points located underneath the model at t = 0.480 s in figure 2.20a are blocked and were re-predicted as shown in figure 2.20b. Also, the interpolation method minimizes the area affected by the model glare (the blue contours above the model). However, the method has only a slight effect on planes where there are no points are blocked from LDV beam access (figure 2.20c and 2.20d), as would be expected for a well-designed process.

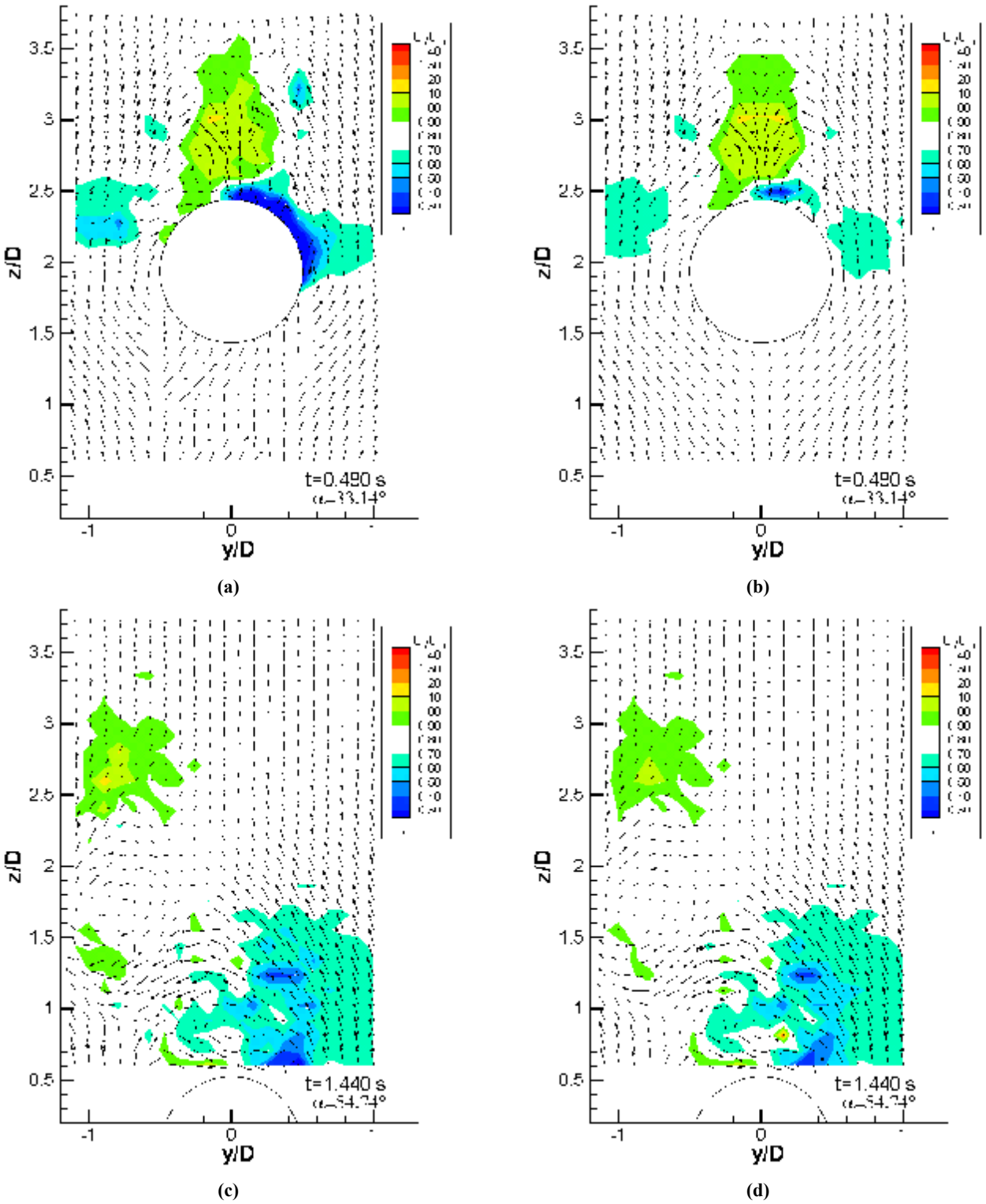

Figure 2.20 Application of Local-Least Squares Interpolation/Smoothing Algorithm to LDV Data at x/D = 5: (a) Original Velocity Field at t = 0.480 with Blocked Beams and Noise from Reflected Light; (b) Smoothed and Interpolated Velocity Field Corresponding to (a); (c) Original Velocity Field at t = 1.440; (d) Smoothed Velocity Field Corresponding to (c).

Calculation of Additional Variables from the Velocity Data

Two additional flow variables are calculated from the LDV velocity data and presented in Chapter 5: Axial vorticity, ω_x (the x-component of vorticity) and the turbulent kinetic energy (TKE). The calculation of the TKE from the calculated mean standard deviation of the ensemble-averaged mean flow is straightforward. The calculation of the vorticity depends on the method used to calculate the spatial derivatives. For interior points of a plane of data, a fourth-order central differencing scheme is employed. For the boundary points of the plane, a second-order forward or backward differencing is used, as appropriate.

2.12 PIV Data Acquisition and Reduction

The Oxford Laser PIV system is set up adjacent to the ESM Water Tunnel in order to acquire velocity fields around a stationary 3.5 caliber tangent-ogive cylinder (the PIV model). This section describes the details of the setup and data reduction.

2.12.1 Model Setup and Data Acquisition

PIV data were acquired at two angles of attack: $\alpha = 40°$ and $\alpha = 55°$. The model is positioned and held stationary with a stepper motor. The model mount is the same as that used in LDV data acquisition, as shown in figure 2.8 At each angle of attack, data are acquired with the camera in two locations. First, the camera is positioned downstream of the model and the optics are adjusted so that laser sheets normal to the freestream velocity are projected into the test section. Figure 2.21 shows the model, coordinates and positions of the planes of acquired data with the model at $\alpha = 55°$. The setup is similar for $\alpha = 40°$. The viewing area is adjusted to 4.25-cm square. The optics are mounted on a traversing table, with the position monitored by an LVDT, allowing accurate positioning to 0.06 mm. With this setup, fourteen planes were acquired with the model at $\alpha = 55°$, and nine planes at $\alpha = 40°$.

After acquiring data with the camera positioned downstream, the camera is realigned so that its view is parallel to the y-axis of the model, and the optics are adjusted so that horizontal laser sheets were parallel with the freestream. With this particular setup, seven more planes of data parallel to the freestream velocity are acquired for each angle of attack. For each PIV data plane, 2048 frames are acquired at 256 frames per second, for a total of 8.0 s of data acquisition. In addition, flow visualization of each plane is recorded at 30 frames per second.

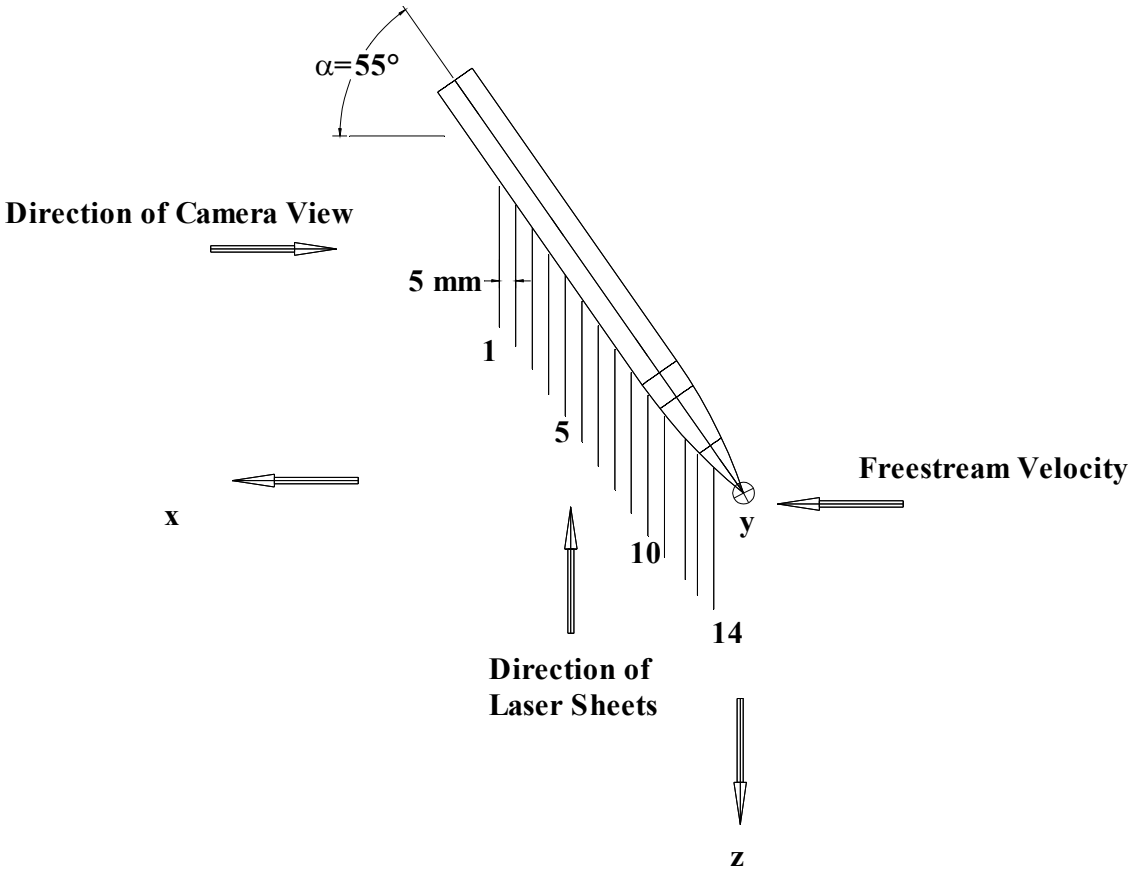

Figure 2.21: Model Setup at α = 55° in the ESM Water Tunnel with Coordinate System and Position of Planes of PIV Data Acquisition. This Setup Allows Acquisition of Planes Normal to the Freestream.

2.12.2 Digital PIV Software and Data Analysis[§]

In order to minimize the effect of light reflected from the model, the digital images are preprocessed. For each pixel location, all 2000 frames are analyzed to determine the minimum pixel value. This minimum value is subsequently subtracted from each frame at the pixel location in question. This process allows the PIV reduction software to determine the velocity more accurately in areas of high glare. However, particles that did not reflect sufficient light to increase the baseline pixel values are lost through this procedure. Figure 2.22 shows the effect of this glare-reduction process on a typical image. The processing of the images results in more accurate velocities in regions where glare has previously been evident.

[§] Parts on the removal of glare from the images is solely the author's discussion. Discussion of the PIV image-processing, calculation of the secondary variables from the velocity fields and resolvable scales is based on results from Vlachos [2000] and Zeiger, et. al. [2001].

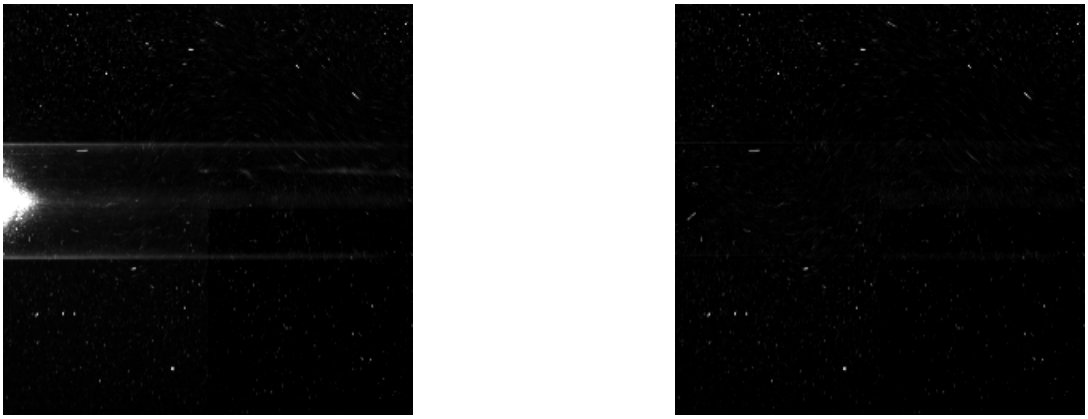

(a) **(b)**

Figure 2.22: Removal of Reflected Light from DPIV Image (a) Original Frame (b) Processed Frame

The processing task for the PIV images was carried out with Visiflow, a software package developed by AEA, on a Pentium II 450 based PC. Each frame took approximately four seconds to process. The image dynamic range was 8-bit resulting in 256 shades of gray. Standard dual-frame single-exposure cross-correlation was used to extract the velocities resulting in 61x61 vectors placed in a uniform grid. Based on the dimensions of the field of view the distance between adjacent vectors is four pixels, which is 5% of the cylinder base diameter. Since the CCD camera outputs directly in a digital format, any error resulting from the digitization is considered negligible. The use of 10-micron neutrally buoyant particles as flow tracers eliminates any errors due to the seeding. A three-point Gaussian peak estimator for the correlation peak in used, achieving sub-pixel accuracy of 0.1 pixel for the peak detection process. The vector validation process employed criteria about the velocity magnitude and the continuity of the calculated vectors, and a quality factor of the estimated cross-correlation peak point considering the existence of multiple peaks in the interrogation window. Interpolation was carried out using a local weighted-average approach. Finally, the data were smoothed using a 5 x 5 Gaussian filter. Any other sources of error resulting from the digitization of the images or from the seeding particles are not considered. The digitization error is eliminated by the use of the digital camera, while the use of particles that are small in diameter and neutrally buoyant practically eliminates them as a source of error.

Once the velocity vectors are evaluated, we obtain the spatial velocity distribution for a sequence of about 2000 instants of the flow. From this point, data analysis tools are employed in order to extract information about the physical phenomena involved. Various flow properties are calculated namely: in-plane vorticity, U_{rms}, V_{rms}, and the in-plane turbulent kinetic energy resulting from the two measured velocity components, and the in-plane Reynolds stresses.

Vorticity fields calculated from the PIV data were determined by applying fourth-order compact schemes to reduce the contribution of the truncation error to the overall error of the calculation. In most cases, vorticity is calculated from experimental results using explicit, second-order schemes, or is calculated from the circulation. Comparisons with artificial data were carried out and it was shown that the compact implicit schemes are more accurate, but are slightly slower computationally.

By performing extensive overlapping to increase the spatial resolution of the flow field a typical number of 61x61 vectors with a step size of four pixels can be achieved. In order to meet the Nyquist criterion, the maximum characteristic length scale L for the flow cannot exceed one half of the field of view. In order for this to occur, the grid step size should be at least 3% L. Comparing this spatial resolution with the Kolmogorov microscale for a typical step size on the order of 1 mm we realize that we can resolve scales that are approximately one order of magnitude larger than the finest turbulent scales.

In addition, the cross-correlation procedure allows us to resolve only linear displacements of a certain pattern of particles. Thus it is immediately understood that any fluctuations within the interrogation window cannot be resolved. The latter combined with the fact that because of the overlapping process same particle images correlate with each other results to a bias and over-smoothing of the velocity estimation. This problem is more severe in cases where high velocity gradients are present in the flow.

Chapter 3 - The Dynamic Character of the Vortical Flow over a Stationary Slender Axisymmetric Body

3.1 Introduction

The flow over slender forebodies has been the subject of intense research for almost four decades. Several authors review the substantial amount of literature written on the subject of flow over slender forebodies at incidence (Hunt 1992, Ericcson and Reding 1981). Most of the research performed has been aimed at determining the nature of the asymmetric mean flow and control of that asymmetry.

In contrast to this concentration on the mean flow, there have been only a handful of investigations discussing the natural unsteadiness over axisymmetric bodies. Hunt and Dexter (1979) found that freestream unsteadiness and model vibration could drastically affect experimental measurements. They also observed situations where the vortex asymmetry switched from one side to the other, with both states being relatively stable configurations. Wardlaw and Yanta (1982) simultaneously measured surface pressures and wake velocity fields over a slender forebody. They showed that varying levels of sectional yaw force are coupled with changes in the mean vortex pattern, with the highest yaw forces accompanying the most asymmetric vortex patterns. Surface pressure fluctuations were found to be lowest when the sectional yaw force was highest. Hoang and Telionis (1991) determined the frequencies of vortex heaving in the wake of a hemisphere cylinder. Calarese (1982) used hot-wire probes to investigate the flowfield fluctuations over a tangent-ogive cylinder. Degani and Zilliac (1990) measured circumferential surface pressures and found that the flowfield over the tangent-ogive cylinder for $\alpha > 30°$ is naturally unsteady to a high degree. Low-frequency von Karman shedding and high frequency shear-layer fluctuations were documented. Moderate frequencies between those mentioned above lead the investigators to surmise that some other type of vortex interaction was present, but the physical process associated with this new interaction was has yet to be identified. Further review of the natural unsteadiness over axisymmetric bodies may be found in Zeiger, et al. (2004).

The aim in this Chapter is to document the natural unsteadiness of the flowfield over a tangent-ogive cylinder, a typical slender forebody/afterbody combination. While the mean flowfield over this

body has been documented with data along planes obtained with LDV (Wardlaw and Yanta 1982), with multi-hole probes (Thomson and Morrison 1971) and computationally (Degani 1991, Degani and Schiff 1991), never has the mean flow been investigated in a three-dimensional sense while including the unsteady aspects. We will analyze multiple planes of unsteady data and the corresponding time-averaged quantities to better understand the nature of the unsteadiness. In-plane streamlines, vorticity, turbulent kinetic energy (TKE) and the standard deviations of the velocity components will be presented.

3.2 Experimental Setup and Procedure

3.2.1 Facilities and the Model

The model used in the experiment was a 3.5 caliber tangent-ogive cylinder of fineness ratio 16. The base diameter of the model was 12.7 mm (1/2"). The model was constructed from a transparent acrylic rod to pass as much of the incident laser light as possible, which reduced glare. Model dimensions are shown in Figure 3.1.

The experiment was carried out in the ESM Water Tunnel, as described in Chapter 1. The tunnel operates in a closed loop in the vertical plane with up to 2,500 gallons of water. The settling chamber leads to the 24" x 24" x 72" Plexiglas test section via a three-way convergence. A 4500-gpm pump driven by a 20-hp motor provides flow which can attain a maximum speed of 1 m/s, corresponding to a maximum Reynolds number per unit length of 9900/cm. The freestream turbulence level in the test section is less than 2%.

For the PIV laser sheet, the light source was a 45-Watt Copper vapor pulsing laser, delivering approximately 5.5mJ/pulse at its optimum operation. Using a set of optics in a telescopic arrangement, a laser sheet was delivered into the test section. The laser was synchronized with a high-speed CCD camera (EG&G MD4256) using a timer board (Real Time Devices, TC524). The number of images acquired was 256 images/sec with a resolution of 256x256 pixels. Digital images were automatically stored in the image buffer of an SB4001 Adaptive Optics frame grabber. Hollow silver-coated glass particles from Potters Industries with 10-30 microns average diameter were used as flow tracers. The data acquisition process is digital, eliminating the tedious and time-consuming tasks of film digitization and allowing the real time observation of the flow field.

The high sampling rate of the data acquisition process introduced significant problems in the adequate illumination of the flow field. In order to compensate for the energy losses and deliver

sufficient illumination in the area under investigation, a set of optics specially coated for the exact wavelength of the laser was employed. This resulted into decreasing the losses through the optics from approximately 40% to less than 10%. In addition, the camera was fitted with an 80-300mm Nikon lens with *f*-stop of 2.8 to allow more light on the sensor during the limited exposure time of 1/256 seconds. These improvements allowed data acquisition rates of up to 1000 frames/sec, which otherwise would not have been possible. A one-dimensional fiber optic LDV system was used to take a fixed-point velocity measurement of the free stream. In order to avoid background noise in the PIV images no LDV particles were added to the flow. Figure 3.2 shows the experimental setup in the ESM Water Tunnel. This Figure is repeated here for completeness.

Data were acquired at an angle of attack of 56°. The model was positioned and held with a stepping motor. The tunnel speed was adjusted to 0.28 m/s, corresponding to a Reynolds number of about 3500. At each angle of attack, data were acquired with the camera in two locations. First, the camera was positioned downstream of the model and the optics adjusted so that laser sheets normal to the freestream velocity were projected into the test section. Figure 3.3 shows the model, coordinates and positions of the planes of acquired data with the model at $\alpha = 56°$. The viewing area was adjusted based on the observed flow in the measurement plane, but was normally about 1.5 x 1.5 inches. The optics are mounted on a traversing table, with the position monitored by an LVDT, allowing accurate positioning to 0.05 mm. With this setup, fourteen planes were acquired with the model at $\alpha = 56°$.

3.2.2 PIV Software and Data Analysis

In order to minimize the effect of light reflected from the model, the digital images were preprocessed. For each pixel location, all frames were analyzed to determine the minimum pixel value. This minimum value was subsequently subtracted from each frame at the pixel location in question. This process allowed the PIV processor to determine the velocity more accurately in areas of high glare. However, particles that did not reflect sufficient light to increase the baseline pixel values were lost through this procedure. Figure 3.4 shows the effect of this glare-reduction process on a typical PIV frame.

The image-processing task for the PIV images was carried out with Visiflow, software developed by AEA, on a Pentium II 450 based PC, processing one frame every 4 seconds. For each plane of interrogation, 2000 frames were acquired with a sampling frequency of 256 frames per second. The

image dynamic range was 8-bit resulting in 256 shades of gray. Standard dual-frame single-exposure cross-correlation was used to extract the velocities resulting in 61x61 vectors placed in a uniform grid. Based on the dimensions of the field of view the distance between adjacent vectors is four pixels, which is 5% of the cylinder base diameter. Since the CCD camera outputs directly in a digital format, any error resulting from the digitization is considered negligible. The use of 10-micron, neutrally-buoyant particles as flow tracers eliminates any errors due to the seeding. A three-point Gaussian peak estimator for the correlation peak is used, achieving sub-pixel accuracy of 0.1 pixel for the peak detection process. Considering the error from the vector validation and interpolation process, the overall uncertainty of the velocity is estimated to less than 1% full scale with respect to the free stream velocity. The vector validation process employed criteria about the velocity magnitude and the continuity of the calculated vectors, and a quality factor of the estimated cross-correlation peak point considering the existence of multiple peaks in the interrogation window. Interpolation was carried out using a local weighted-average approach. Finally, the data were smoothed using a 5x5 Gaussian filter.

Any other sources of error resulting from the digitization of the images or from the seeding particles[12] are not considered. The digitization error is eliminated by the use of the digital camera, while the use of particles that are small in diameter and neutrally buoyant practically eliminates them as a source of error. The errors from the interpolation and the filtering procedure are embedded in the overall error evaluation and there is no need to treat them independently.

In most cases, vorticity is calculated from experimental results using explicit second order schemes or is calculated from the circulation. The vorticity calculation was performed by applying fourth-order compact schemes[13] to reduce the contribution of the truncation error to the overall error of the calculation. Comparisons with artificial data were carried out and it was shown that the compact implicit schemes are more accurate, but are slightly slower computationally.

3.3 Results and Discussion

3.3.1 Flow Regimes and Instabilities

The flow regimes and instabilities present in the flow over a slender axisymmetric body are relatively well known, but they are worth a short revisit. The three existent regimes of the flow are shown in Figure 3.5 (Tobak et al., 1990). These regimes are modeled after the flow visualization done by Ramberg (1983). In the first regime, far from the influence of the forebody, the flow behaves much as

that over an infinite cylinder in yaw. The vortical structures shed from the body propagate nearly parallel to the body axis, and the shedding frequency can be shown to correspond to that associated with von Karman vortex shedding (i.e. $St_{VK} = 0.21 \cdot \sin\alpha$) (Degani and Zilliac, 1990). The flow in this regime is unsteady, but nearly symmetric in the mean. In the third regime, asymmetric vortices (with a corresponding nonzero mean yaw force) dominate the flow. While the forebody vortices may be subject to some unsteadiness, which has been shown to depend on the mean-flow turbulence levels, these vortices do not exhibit the periodic unsteadiness associated with regime three. Consequently, the flow in the forebody region may be thought of as generally steady, but asymmetric in the mean. In the second regime, oblique vortex shedding occurs as the shedding that would normally propagate parallel to the body axis is influenced by the forebody vortices. The asymmetric flow in the third regime is caused by disturbing a convectively unstable flow near the forebody tip, while the asymmetry and unsteadiness in the first regime are caused by a global instability in the wake of the body (Degani, 1991, Degani and Tobak, 1991). The influence of both instabilities is present in regime two. Presentation and analysis of the PIV data will focus on this regime.

An analysis of existing data on the natural unsteadiness over slender forebodies (Telionis et al., 1991 with data from Degani and Zilliac, 1990) revealed that coherent shedding frequencies corresponding to alternate shedding are not observed in surface pressure data until there are four vortical structures present at an axial location. In other words, two vortices have been shed and are not garnering vorticity directly from the body at the axial station in question, but only from upstream. The ability to capture the entire wake is limited in this investigation by the capabilities of the digital camera. It was not possible to capture more than two or three vortices in the measurement plane. Since the unsteadiness near the surface of the body is a prime cause of surface pressure fluctuations, we chose to concentrate on the vortical structures close to the model. For this reason, vortices further from the body (the forebody vortices convected downstream) were not observed, although unsteadiness associated with these vortices would be more important when considering downstream effects such as tail buffeting. In order to determine how many vortices are present in a given plane of measurement, the analysis of Telionis et al., 1991 (which was based on theory provided by Hall, 1987), is applied to determine vortex separation locations. These locations are listed in Table 3.1. Based on these results, the number of vortical structures in each plane are calculated and displayed in Table 3.2, where the $x'/D = x/(D \cdot \cos\alpha)$ location is where the measurement plane crosses the body axis.

Table 3.1 Mean Flow Vortex Separation Locations

	Vortex Separation Location, x'/D
1st Vortex Separation	2.6
2nd Vortex Separation	4.5
3rd Vortex Separation	7.8

Table 3.2 Vortical Structures in Plane of Measurement for Mean Flow

Measurement Plane Location, x/D	Measurement Plane Root Location, x/(Dcosα)	Number of Vortices in Measurement Plane
3.46	6.16	4
4.25	7.56	4
4.65	8.27	5
5.43	9.66	5
5.83	10.37	5

3.3.2 Velocity and Vorticity Fields

Data presented here represent results from five of the fourteen planes of PIV data acquired at $\alpha = 56°$. The velocity fields are used to calculate the vorticity. All of these quantities are then averaged over 2048 frames to determine the mean fields. The mean velocity field is then used in the calculation of the standard deviations of the two velocity components. In addition, streamlines of the velocity field are calculated. The streamlines may then be superimposed on contour plots of the other functions. All velocities are nondimensionalized by U_∞, and all lengths are nondimensionalized by the cylinder base diameter D. The origin for the z-coordinate for each plane of measurement is located at the surface of the model on the leeward meridian.

Time-averaged contours of vorticity along with corresponding streamlines are shown in Figure 3.6. At all locations presented here, the forebody vortices have been shed, so that the flow may be said to be in the second regime, where oblique shedding is occurring and the flow is influenced by both the convective and absolute instabilities. The initial frame at x/D = 3.46 is acquired at a location where four vortices are present. Two of these are shown in the frame. A saddle evident in the upper left-hand corner of the frame signifies the presence of another negative-vorticity vortex existing just off the frame to the left. The fourth structure is a forebody vortex that must exist to the right of the measurement plane. At this location just downstream of the forebody-afterbody junction, the vortical pattern is highly asymmetric. As the x/D coordinate is increased to 4.25 (Fig. 6b), the vortex originally hidden to the left of the frame appears, moving with it the saddle point, which becomes apparent in the upper right-hand corner of the frame. This saddle is observed to be a major feature of the flow, because its position dictates the positions of the vortices emanating from the upper side of the body. Figure 3.6c reveals that the vortex in the upper left-hand corner of the frame is found to have an unstable focus (in the mean). In addition, this figure shows that the large lobe of vorticity from the lower vortex is "pinched off" from the remainder of the vortex, leaving a more symmetric vortex formation near the body (Figure 3.6d). Referring to Table 3.2, we see that at x/D = 4.65, an additional vortex is to appear, which would correspond with the shedding of the positive-vorticity structure. This shed structure disappears from the field of view by x/D = 5.83, leaving just two vortices and the saddle point visible. Note that the distance between the upper vortex and saddle point increases during the sequence Fig. 6a-f, allowing the vortical region to grow.

According to previous results (Wardlaw and Yanta, 1982), the flow observed here should have increased unsteadiness when it is symmetric, and decreased unsteadiness when highly asymmetric. This is observed to be true when examining Fig. 7, which shows contours of σ_v superimposed on mean streamlines for the same set of planes as in Fig. 6. The regions exhibiting large σ_v can be thought of as having oscillations parallel to the y-axis. In Fig. 6a, where the flow is asymmetric, σ_v is seen to have smaller regions of high value when compared to Fig. 7d, where the mean flow is nearly symmetric. The value of σ_v may be as large as 21% of the freestream velocity. The unstable focus and the saddle do not have much associated unsteadiness in the y-direction, while the region immediately to the right of the saddle appears to be the site of increased activity between the vortical structures. As the vortex on the lower side of the body is shed (Figs. 6c and 7c), the region of high σ_v is enlarged, and remains this way in Fig. 7d. However, there is a sharp decrease in the unsteadiness between Figs. 7d and 7e, even though the mean-flow streamlines are similar. The region of increased σ_v on the lower border of the frames in Fig. 7

is associated with the interaction of the outer flow with the cylinder wake, and it is observed from the streamline pattern that there are no time-averaged vortical structures in this region.

In direct contrast to σ_v, Fig. 8 shows that the unstable focus and the saddle lie in regions of increased σ_w, denoting increased unsteadiness and oscillation parallel to the z-axis. It appears that large values of σ_w are mainly associated with the saddle, which lies in or very near the region of highest for all frames in Fig. 8. On the other hand, the lower vortex has smaller associated σ_w. It is observed that σ_w can be up to 16% of the freestream velocity. This is especially true in Figs. 8a and 8e, whereas Figs. 8b-d show that the releasing of the lobe of the lower vortex results in an increased σ_w. In general, Figs. 7 and 8 reveal that the unsteadiness associated with vortical structures near the body is relatively small, but increases in regions occupied by shed vortical structures.

A time series of the vortical flow at x/D = 4.65 is shown in Figure 3.9. Like the mean flow (Fig. 6c), this time series shows that the lower vortex generally occupies a large region of space near the body, and the upper vortex is confined to a smaller region in the upper left-hand corner of the frame (Fig. 9a). As the upper vortex expands, vorticity from lower vortex is gradually released to the right. In Fig. 9e, the upper vortex manages to occupy much of the region near the body, but this is short-lived as it is quickly shed, allowing the lower vortex to again occupy its favored position (Fig. 9f).

Once released, the free vortex on the lower side is represented by a stable focus (Figs. 9b, 9d and 9e), an unstable focus (Fig. 9c) and a limit cycle (Fig. 9f). The singularities associated with the regions of negative vorticity tend to be unstable foci or limit cycles. The released upper vortex is represented in Fig. 9f as a stable limit cycle, and the previously shed vortex appearing in Figs. 9a-b is represented by an unstable focus. The concept of the limit cycle in the flow topology over a delta wing, and the association of the limit cycle with the vortex breakdown phenomena is presented by Visbal (no year listed). The physical process associated with the presence of limit cycles for this flow is not clear at the present time.

A similar time series is shown in Figure 3.10 for the flow at x/D = 5.43. At this location, the mean flow has a more symmetrical vorticity distribution (Fig. 6d). However, examination of Figure 3.10 indicates that this symmetry is not due to a pair of standing symmetrical vortices, but rather to the fact that the two vortices are involved in alternating asymmetric patterns of approximately equal lengths of time. This is in contrast to the flow seen at x/D = 4.65, where the mean flow is much more asymmetric, and the vortex pattern favors one side for a longer period of time.

It may also be observed that the vorticity moves away from the body in this plane is different for the upper and lower vortices. The time series shows that the upper vortex expands to the right, eventually pinching off the lobe of the lower vortex (Fig. 10b-e). Then, a large negative-vorticity region is released en masse (Fig. 10f), allowing the lower vortex to dominate most of the region closest to the body once again.

The lower vortex nearest the body at x/D = 5.43 does not develop a focus, mimicking the mean flow (Fig. 6d). A focus associated with positive vorticity does appear (with a corresponding saddle, a necessity) as part of the lower vortex is released to the right. This focus is initially a stable node (Fig. 10a), but quickly becomes an unstable limit cycle (Fig. 10b-e). The upper vortex, which appears as an unstable focus in the mean streamline pattern, appears as an unstable focus in Figures 3.10b and 3.10e, otherwise as a stable focus. Of course, this time series does not represent the entire set of data from which the mean streamlines were derived. This example shows that one must be careful when using the mean flow topology to analyze an inherently unsteady flow, because the instantaneous topology may be vastly different.

3.4 Conclusions

The natural unsteadiness in the flow over a 3.5 caliber tangent-ogive cylinder at incidence is investigated experimentally at a Reynolds number of 3500. The analysis of the data concentrates on the flow aft of the forebody where oblique shedding occurs and where the flow is roughly equally influenced by the convective and absolute instabilities present in the flow. This results in an unsteady flow that is asymmetric in the mean.

Flow nearer the forebody is observed to be highly asymmetric, but this asymmetry decreases with downstream location. The asymmetry in this region is not found to be caused by a stationary asymmetric vortex structure as exists over the forebody, but rather by an unsteady set of vortical structures with an asymmetric mean position. In addition, the asymmetry is associated with slightly different vorticity-shedding modes, depending on which sign of vorticity is released.

The degree of flow unsteadiness, as shown through the examination of the standard deviation of the mean velocity components is dependent on the mean flow asymmetry. This agrees with previous results from analysis of surface pressure and flowfield data (Wardlaw and Yanta, 1982). The standard deviations in the v- and w-components of the velocity are found to reach levels in excess of $0.21U_\infty$ and

$0.16U_\infty$, respectively. Regions of high σ_v are found to occur in the regions between vortical structures of opposite sign after they have been shed, leading to the conclusion that the releasing of the structures allows the interaction. Regions of large are observed near the saddle point associated with the upper vortex, showing that the movement of the vortical structures towards and away from the body occurs in this region.

Analysis of the singularities occurring in the streamline patterns corresponding to the mean flow shows that the vortex associated with more unsteadiness in the z-direction is represented by an unstable focus. However, this topology is seen to vary widely when analyzing the instantaneous topology. Limit cycles are seen in the unsteady topology. Although their presence is not linked to any physical process at this time, it is unlikely that they are associated with vortex breakdown, as in the case of flow over delta wings.

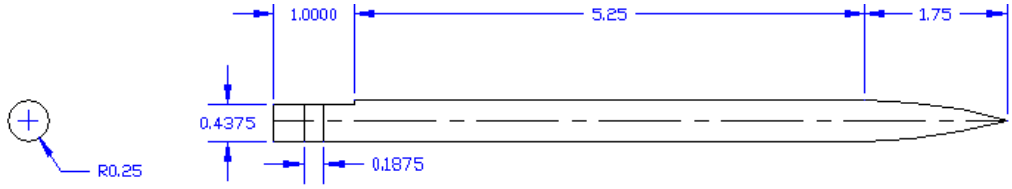

Figure 3.1: 3.5 Caliber Tangent-Ogive Cylinder Model. Material is Transparent Acrylic. All Dimensions in Inches

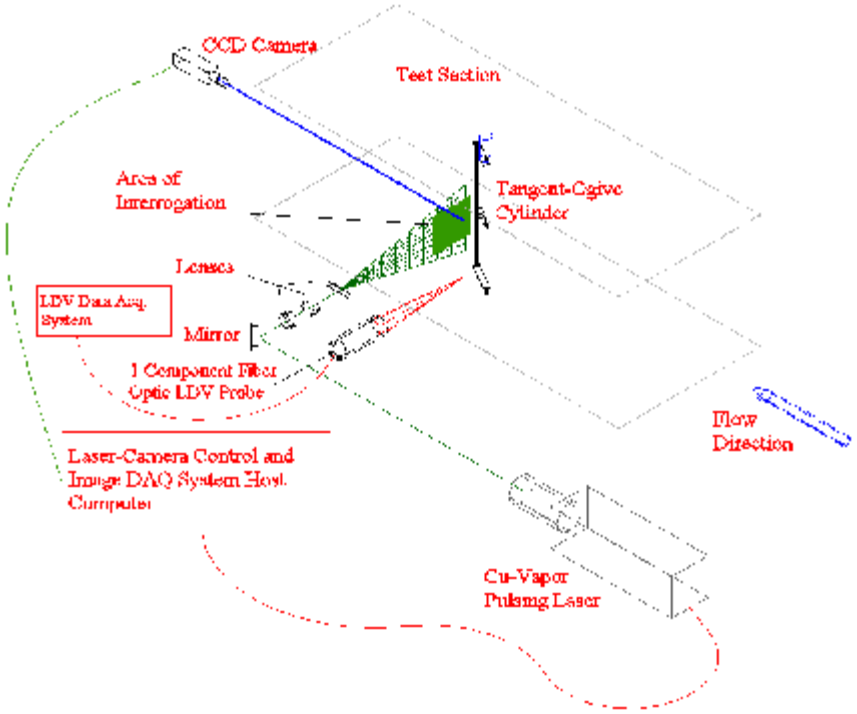

Figure 3.2: PIV Experimental Setup in the ESM Water Tunnel for Acquiring Planes of Data Normal to the Freestream Velocity

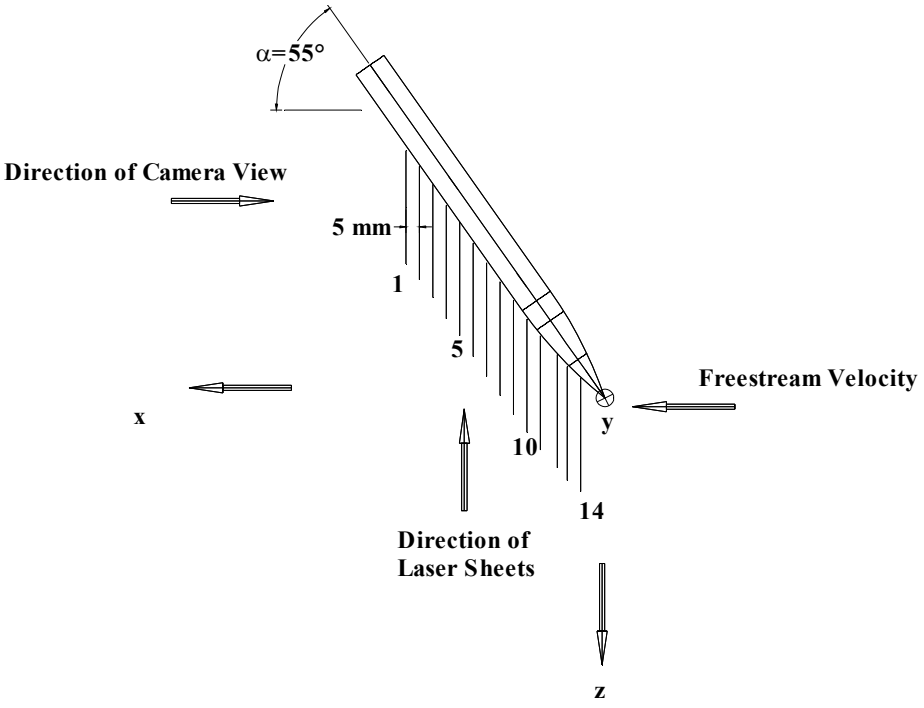

Figure 3.3: Model Setup in the ESM Water Tunnel at α = 56° with Coordinate System and Position of Planes of PIV Data.

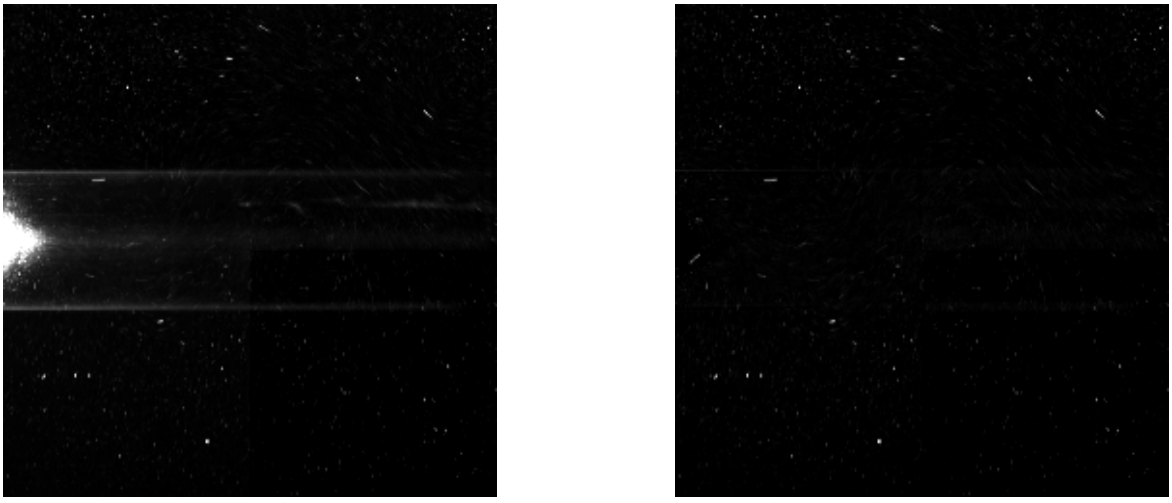

(a) **(b)**

Figure 3.4: Reduction of Reflected Light from Model (a) Original Frame (b) Processed Frame

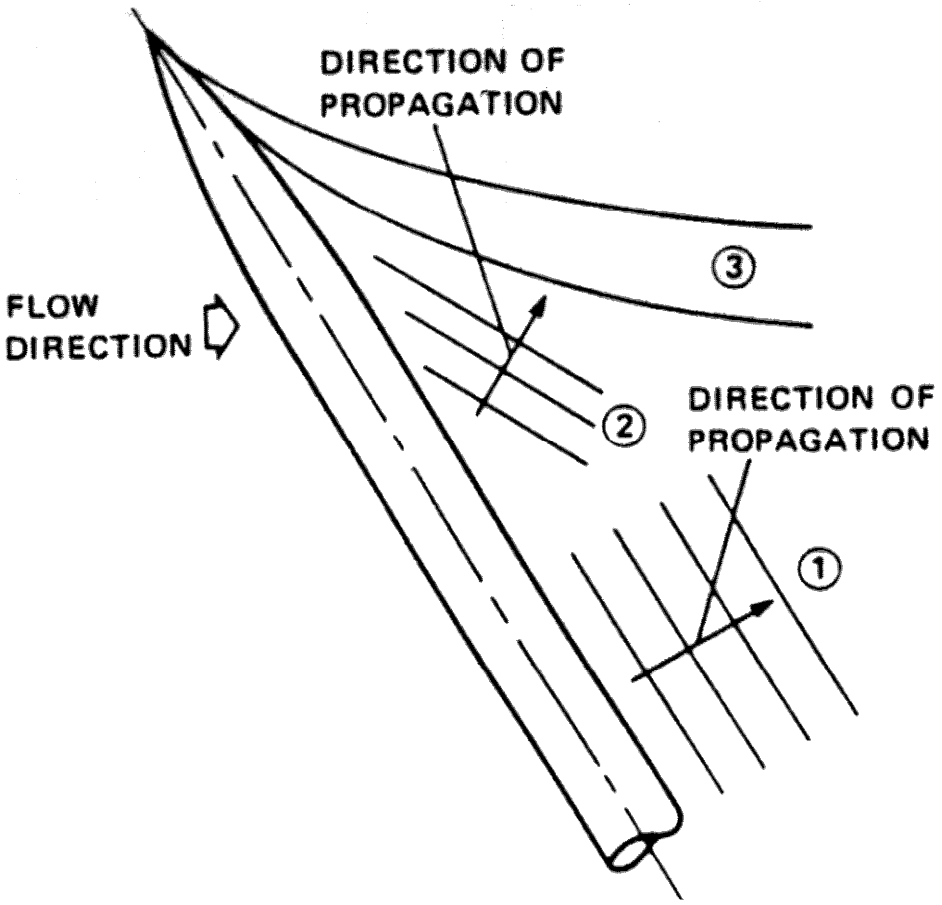

Figure 3.5: Flow Regimes over a Semi-Infinite Slender Axisymmetric Body (Repeated from Chapter 1). Parallel Shedding, Flow Governed by Absolute Instability. 2) Oblique Shedding, Convective and Absolute Instabilities Influence Flow, 3)Asymmetric Forebody Vortices, Flow Governed by Convective Instability

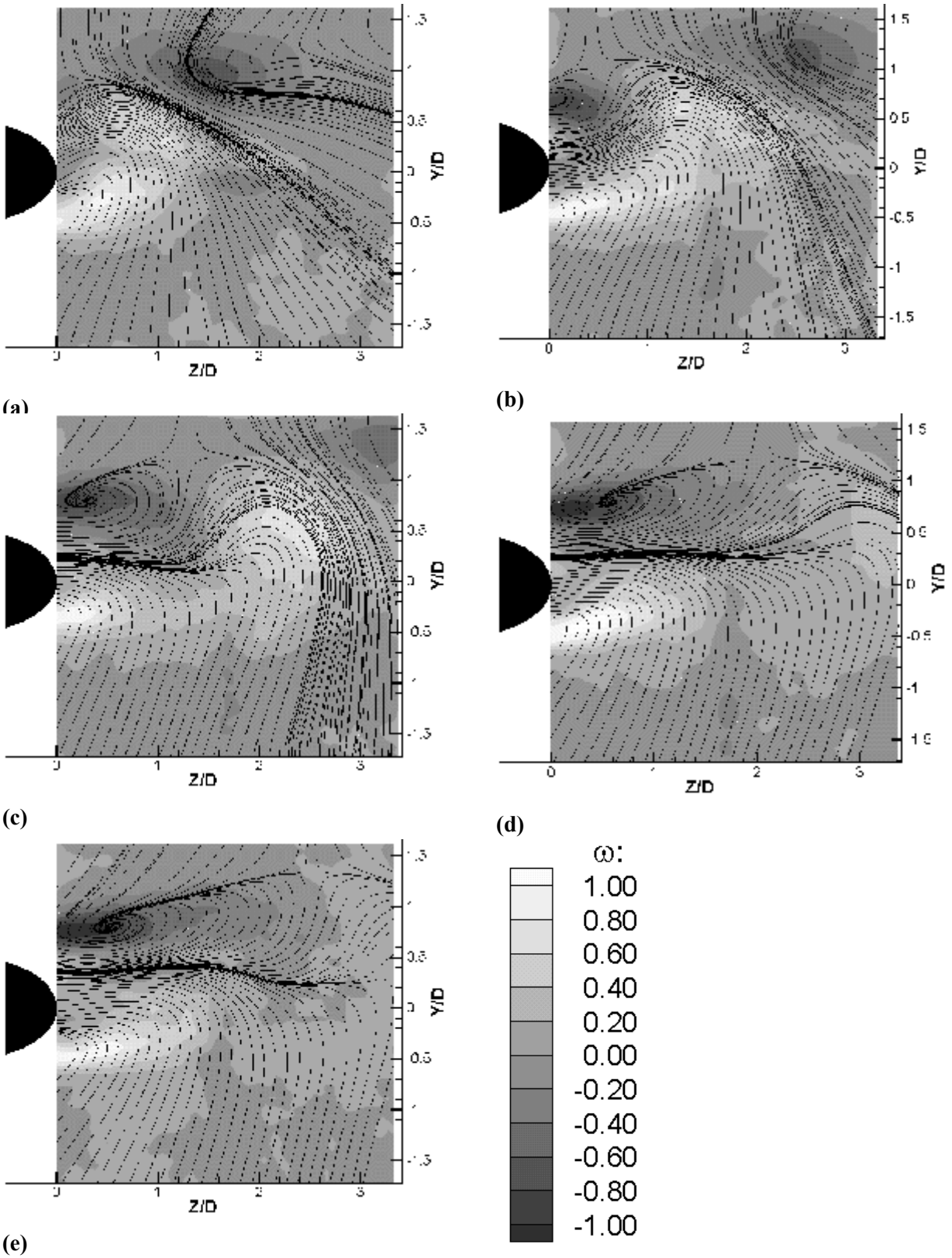

Figure 3.6: Mean-Flow Streamlines and Contours of In-Plane Vorticity at $\alpha = 56°$: x/D = 3.46, (b) x/D = 4.25, (c) x/D = 4.65, (d) x/D = 5.43, (e) x/D = 5.83.

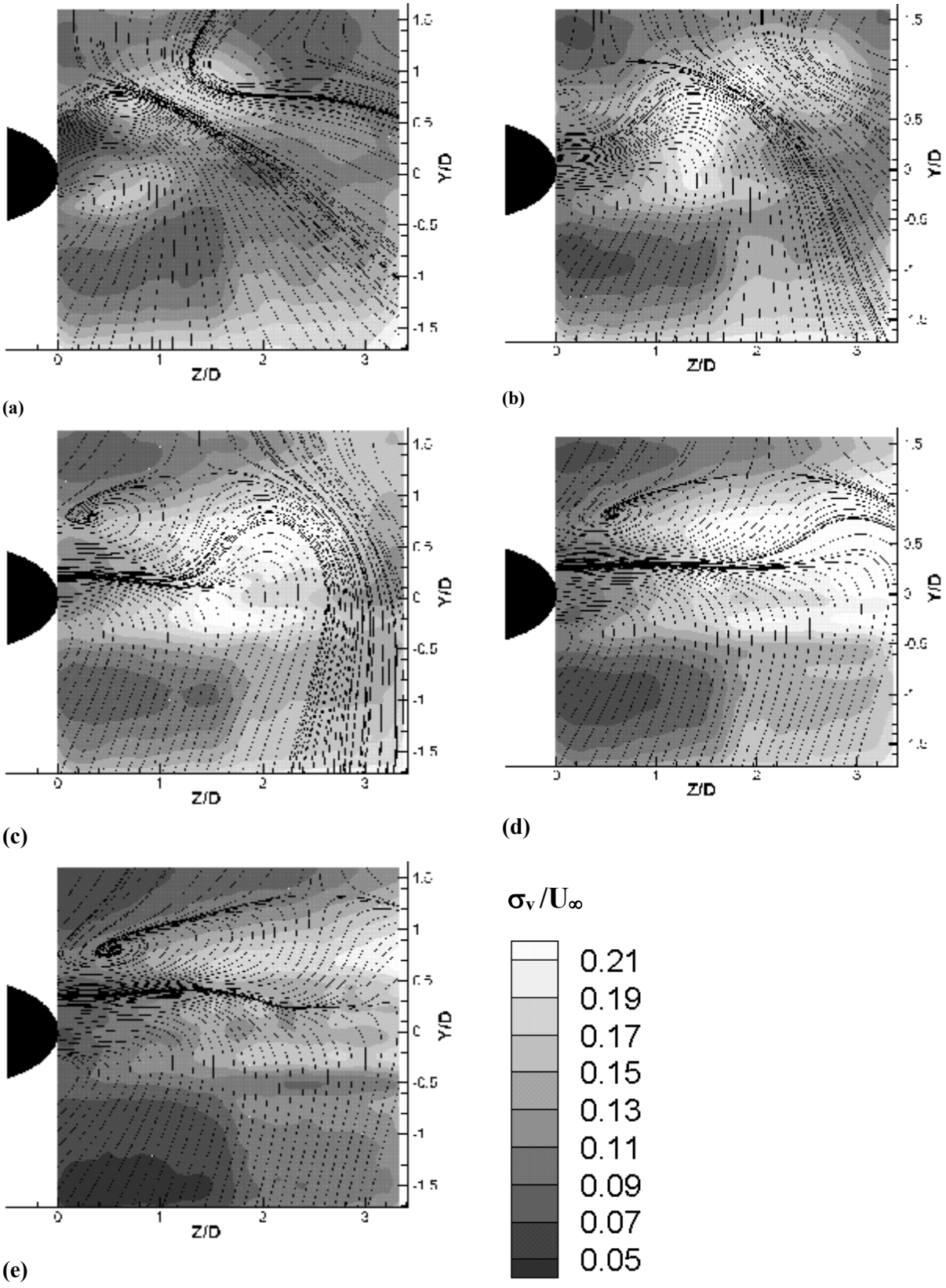

Figure 3.7: Mean-Flow Streamlines and Contours of σ_v/U_∞ at $\alpha = 56°$: x/D = 3.46, (b) x/D = 4.25, (c) x/D = 4.65, (d) x/D = 5.43, (e) x/D = 5.83.

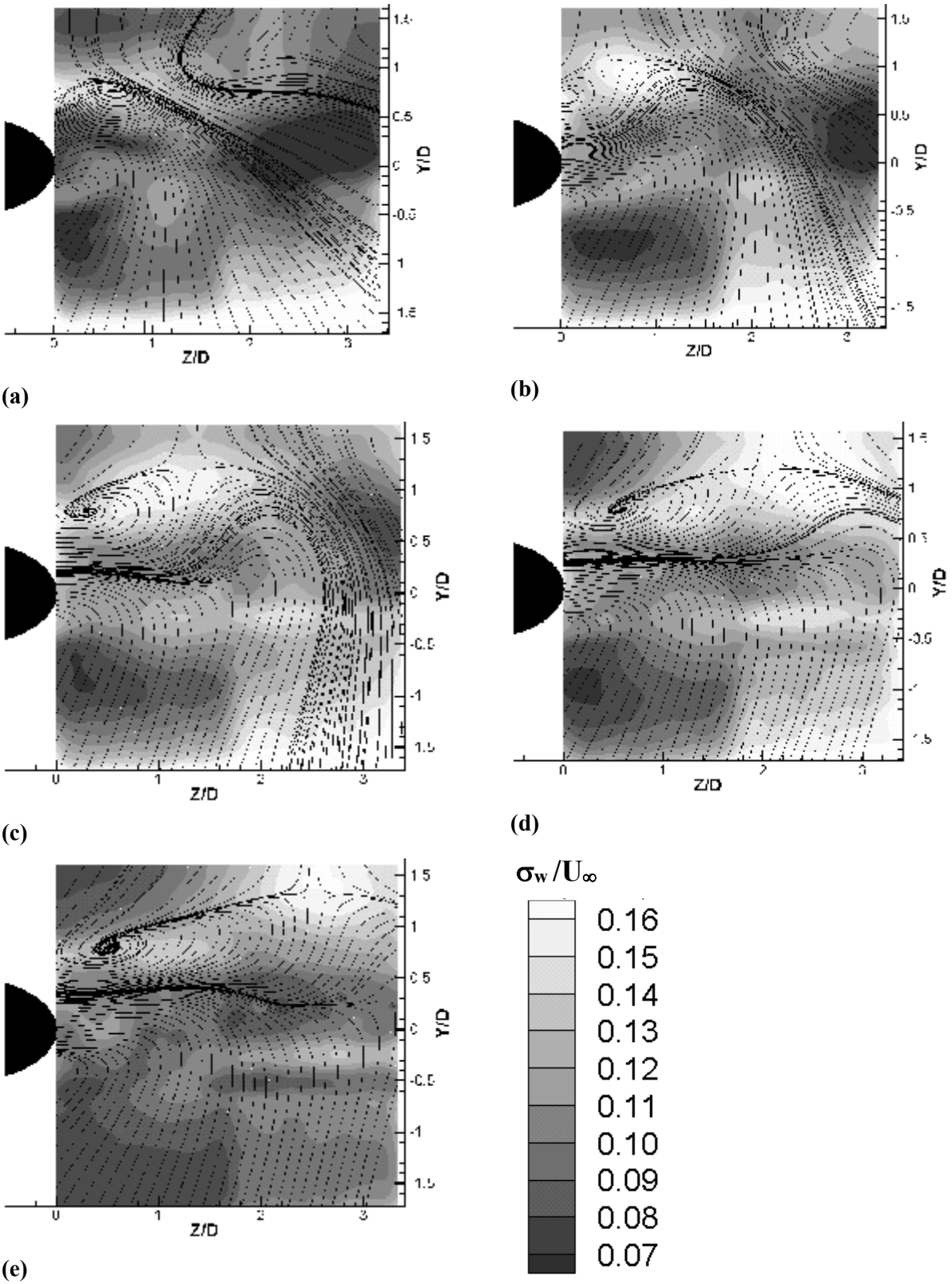

Figure 3.8: Mean-Flow Streamlines and Contours of σ_w/U_∞ at $\alpha = 56°$: x/D = 3.46, (b) x/D = 4.25, (c) x/D = 4.65, (d) x/D = 5.43, (e) x/D = 5.83.

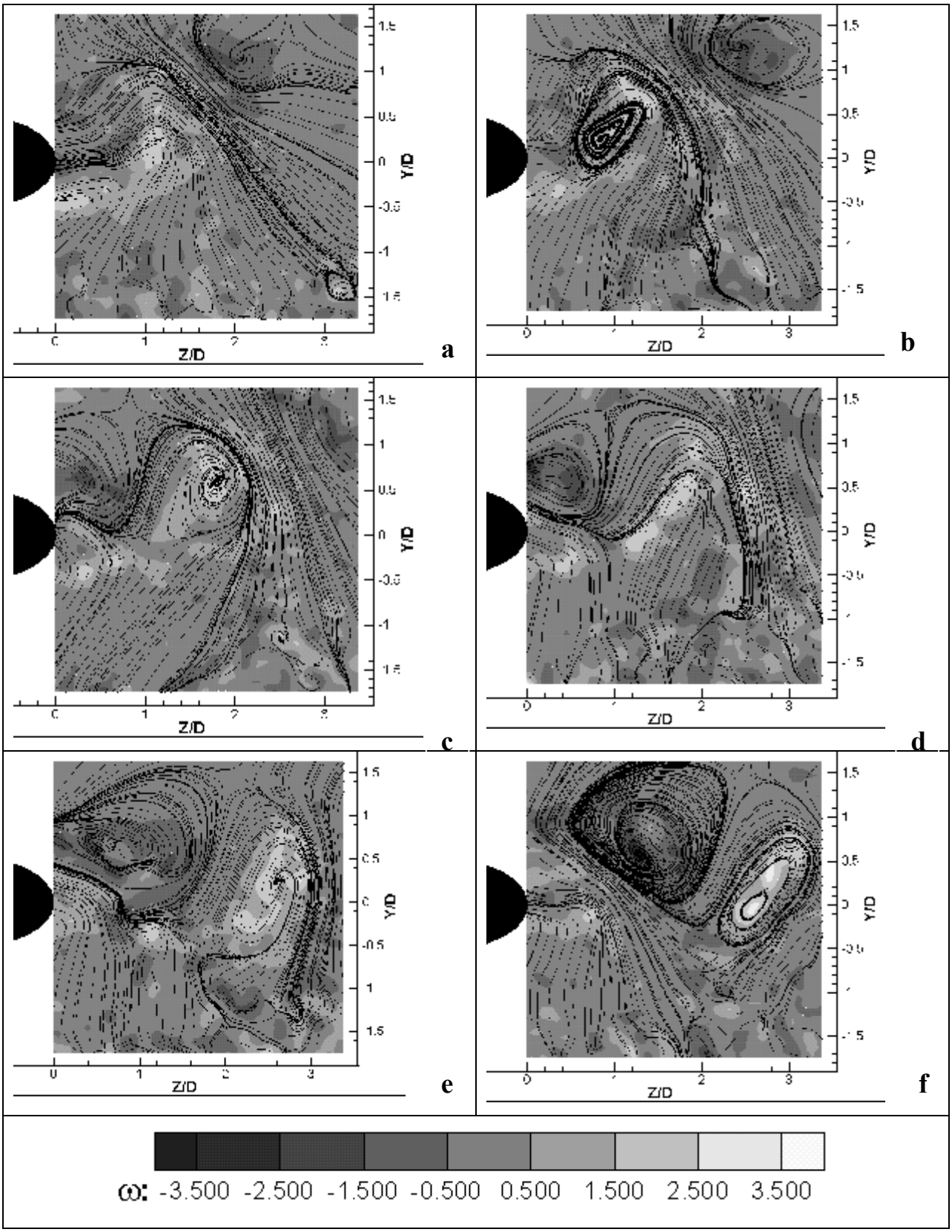

Figure 3.9: Temporal Development of the Flow at x/D = 4.65: t = 0.00 s (b) t = 0.320 s (c) t = 0.398 s (d) t = 0.477 s (e) t = 0.789 s (f) t = 0.867 s

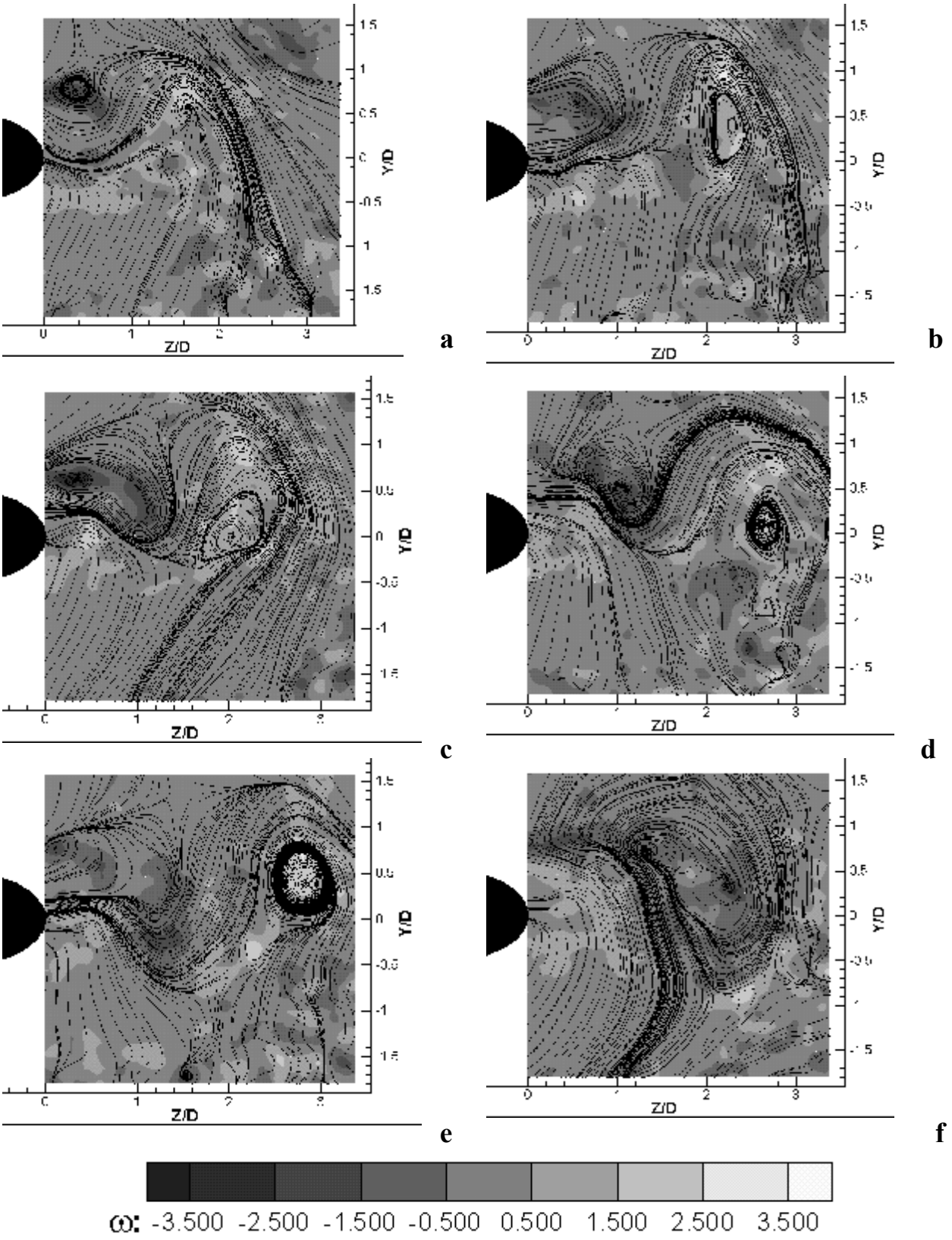

Figure 3.10: Temporal Development of the Flow at x/D = 5.43: t = 0.242 s (b) t = 0.484 s (c) t = 0.711 s (d) t = 0.867 s (e) t = 1.101 s (f) t = 1.258 s

Chapter 4 - Effect of Coning Motion and Blowing on the Asymmetric Side Forces on a Slender Forebody

4.1 Introduction

Many modern fighter aircraft configurations have been fitted with axisymmetric, slender forebodies that produce an asymmetric vortex pattern when placed at high angles of attack. Most missiles are also subjected to this asymmetry. The side forces produced by this asymmetry may be greater than the normal force on the forebody, and the yaw moment produced can dominate the moment available from conventional control surfaces buried in the wake of the aircraft. Uncontrolled, the forebody flow pattern can be a great detriment to stability at high angles of attack. However, if these forces and moments could be controlled and utilized, they could not only provide safety from departure and spin, but also augment the maneuverability of the aircraft.

Because of the rewards involved, there has been a high degree of interest in the subject of forebody vortex control (Skow and Erickson [1982], Malcolm [1993], Bernhardt and Williams [1993], Celik and Roberts [1992], Roos and Magness [1993], Crowther and Wood [1993], Malcolm and Ng [1990], Alexan et al. [1994]). Many different methods of control have been used, but some of the most effective and versatile are those that involve suction or blowing from slots or ports very near the tip of the forebody. It has been shown that the mass flow rates needed to manipulate the flow are manageable (Roos [1996]). In fact, proportional control has been achieved for a stationary model (Williams and Bernhardt [1990]).

In order to ascertain if the effectiveness of these control methods extends to the unsteady regime, this paper presents results for models undergoing coning maneuvers. The main thrust of the investigation is to determine if the asymmetry created through the use of forebody control is maintained throughout the motion as well as to examine the effect of delaying the blowing onset until after the start of the motion.

4.2 Coning Maneuvers with Laminar Separation

4.2.1 Experimental Setup, Data Acquisition and Processing

The model used in this investigation was a 3.5 caliber tangent-ogive cylinder of fineness ratio 16. The testing took place in the ESM Wind Tunnel, and surface pressure data were acquired with ESP pressure scanners. The model, tunnel and the pressure scanner data acquisition system are described in more detail in Chapter 2.

Surface pressures are acquired over the model as it performs four coning motions of varying reduced frequency. In addition, constant and delayed blowing modes are used in conjunction with several different values of C_m to determine how combined model motion and blowing affect the flow over the forebody.

The freestream velocity is always maintained at U_∞= 10.4 m/s, corresponding to $Re_D = 3.50 \bullet 10^4$ and thus ensuring that laminar separation is realized in all cases. When $\alpha = 45°$, the coning axis intersects the model axis at $x_c/D = 3.23$, and when $\alpha = 55°$, at $x_c/D = 3.82$. The blowing port is always positioned at $\theta = -135°$, on the starboard side of the model.

The reduced frequencies of the coning motions are $k_c = \pm 0.058$ and $k_c \pm 0.023$, with positive motions resulting in the nose moving to starboard. The motions are shown in figure 4.2.1, and the reduced frequencies are calculated from the maximum slope of the ramp part of each motion. The motions do not commence until approximately t* = 25 after data acquisition begins, so that the steady-state pressure distributions are recorded at the beginning of the sequence of data frames.

The C_m used in the investigation varied from $1.38 \bullet 10^{-3}$ to $2.72 \bullet 10^{-3}$. These were sufficient to manipulate the leeward vortices to the extent that a reversal or near-reversal of the overall side force is realized. One important difference between the present case and those of Malcolm and Ng [1990] is that approximately ten times the mass flow rates are used here. In all likelihood, the reason greater mass flow is required is that the blowing port for the present case is further from the ogive tip, reducing its effectiveness.

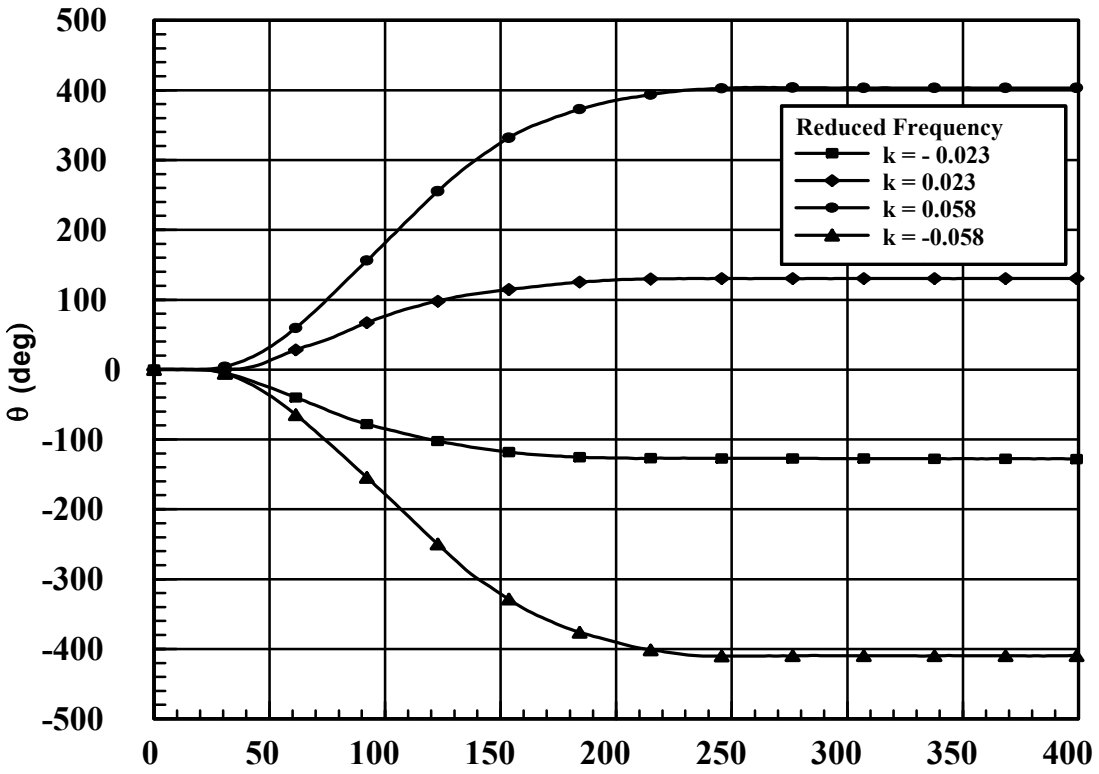

Figure 4.2.1: Ramp Coning Motions in ESM Wind Tunnel.

When delayed blowing is employed, the delays used are t* = 97.2 (t = 0.475 s) and t* = 79.0 (t = 0.386 s). These delays are from the start of data acquisition to the onset of blowing. An additional time of t* = 68.2 (t = 0.333 s) is required for the blowing to achieve the steady state. The delays are independent of the driving pressure used to produce a particular blowing rate.

For a given axial location, blowing mode, C_m and k_c, the motion is performed 40 times and the results are ensemble averaged, employing Chauvenet's criterion. The surface pressures are integrated around the circumference of the model in order to calculate the sectional side force coefficient, C_y:

$$C_y = \frac{d}{2 \cdot D} \oint_{\theta} C_p \sin\theta \cdot d\theta \qquad [4.1]$$

Positive side force is to starboard, negative to port. The side force results from the flow asymmetries shown schematically in figure 4.2.2, where the vortex arrangement is exaggerated. An imbalance of pressure exists due to asymmetric separation with respect to the angle of attack plane, resulting in a side force towards the region of suction.

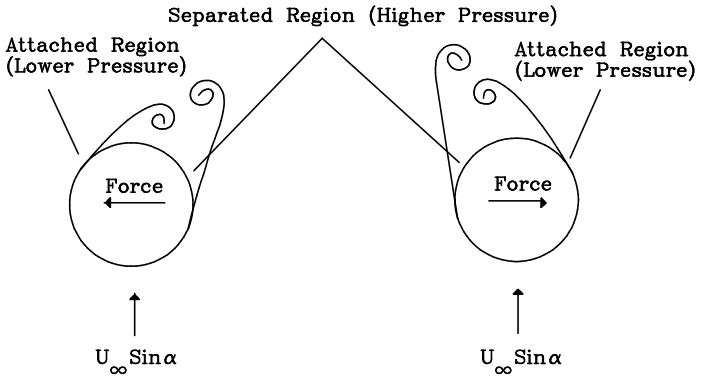

Figure 4.2.2: Asymmetric Vortex Arrangement and Creation of Side Force (Vortex Arrangement Exaggerated).

4.2.2 Results and Discussion

Variation of the steady (no motion) side forces with axial distance for various blowing rates are shown in figure 4.2.3. For $\alpha = 45°$ (figure 4.2.3a), a negative sectional side force exists at every axial location, implying that an overall negative side force is present, at least for that portion of the model over which measurements were obtained. Note that the relative magnitude of the overall side force may be discerned approximately by looking at the area under the sectional curve. A small amount of blowing produces a further decrease (more negative) in the overall side force, in agreement with the effects seen by Roos [1996]. With increased blowing ($C_m = 2.16 \bullet 10^{-3}$), the overall side force increases, with a dramatic reversal of the sectional side force at x/D = 3.75. The flow physics causing this effect are not well understood, but additional testing may reveal them. It is probable that the location of the blowing port and the magnitude of C_m are involved, in addition to the natural instability.

When α is increased to 55° (figure 4.2.3b), low blowing rates tend to slightly decrease the magnitude of the sectional side forces. However, higher C_m causes the side force to "flip" as evidenced at x/D = 1.8125 and 2.8125 (data were not acquired for $C_m = 2.72 \bullet 10^{-3}$ at the aft ports).

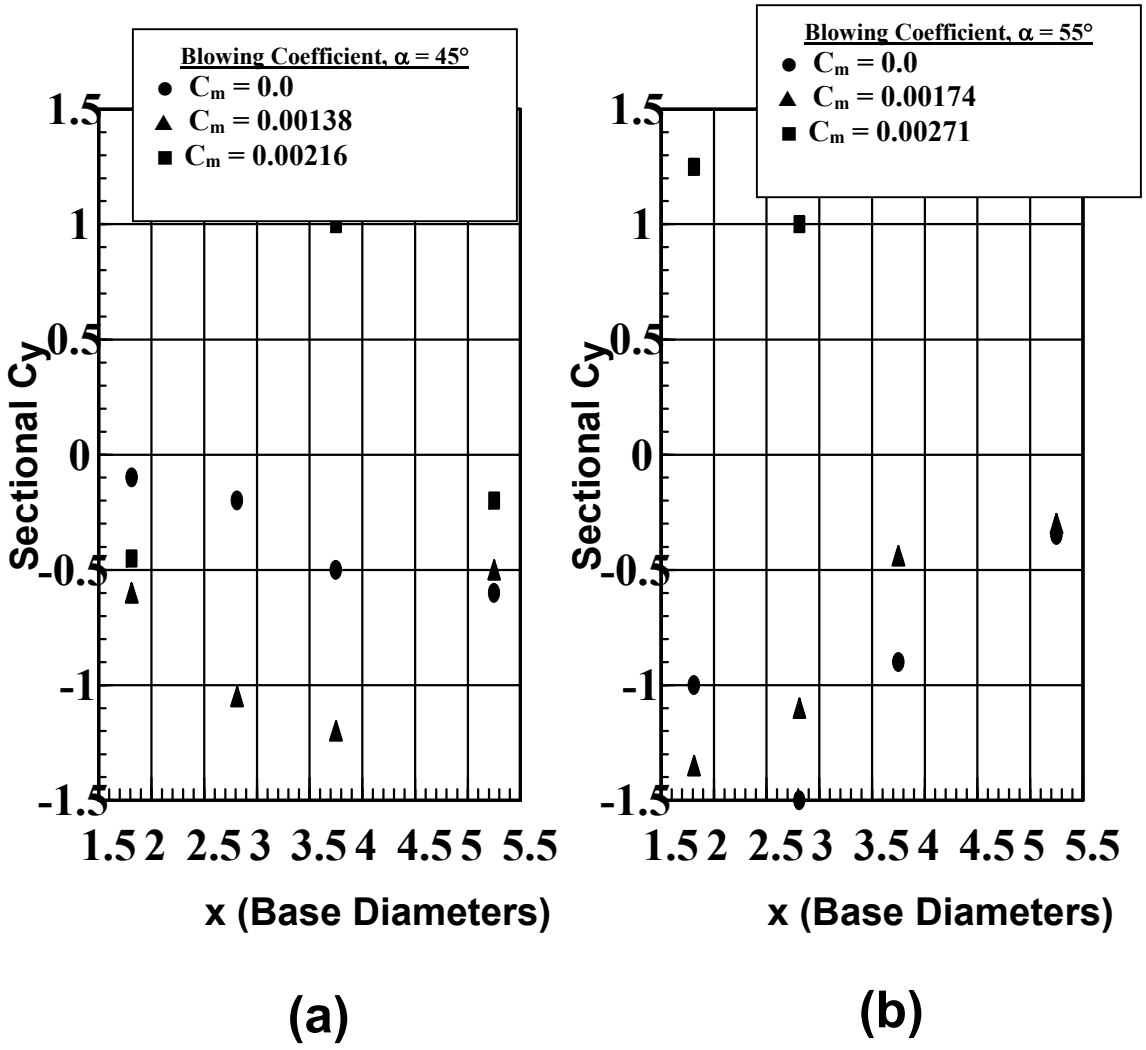

Figure 4.2.3: Steady (no motion) Variation of Sectional Yaw Force with Axial Location (a) α = 45°, (b) α = 55°.

Coning and Blowing at α=45°

Dynamic plots of sectional C_y at x/D = 1.8125 are shown in figure 4.2.4. For cases with no blowing, motions with $k_c > 0$ induce a negative side force, $\Delta C_y < 0$, and $k_c < 0$ cause $\Delta C_y > 0$. That is, the vortex configuration tends to realign itself such that the sectional side force opposes the motion. This effect corroborates the results given in Schiff and Tobak [1970] and Yoshinaga et al. [1981]. For $C_m = 0$, equal magnitude and opposite direction motions produce equal magnitude ΔC_y, but in opposite directions. At this axial station, constant blowing seems to be effective, because there is little change to the side force when the blowing is established. One exception is the case for $k_c = -0.058$, where there is an appreciable ΔC_y for $C_m = 1.38 \cdot 10^{-3}$. Analysis of other axial stations will show if the blowing is effective for the entire length of the model.

Delayed blowing results in immediate departure of C_y from the $C_m = 0$ case to the corresponding constant blowing curve. However, the flow seems to respond more slowly during $k_c = \pm 0.058$ motions than for $k_c = \pm 0.023$ motions, perhaps giving a hint that the flow may be governed by more than one time scale, or it could mean that local effects compete with the convective effect from the nose to slow the transition.

Figure 4.2.5 depicts the sectional force, C_y vs. time for x/D = 2.8125. For $C_m = 0$, we see that the trend seen at x/D = 1.8125 is repeated, with the sectional side force opposing the motion of the nose. The effects of the motion at this location are increased, when compared to cases where x/D = 1.8125. As a general rule, it seems that as distance from the nose increases, motion effects also increase. For $C_m = 1.38 \cdot 10^{-3}$ and $k_c = -0.058$ (figure 4.2.5c), the constant blowing is ineffective and the sectional side force undergoes a dramatic rise. This shows that there exists a situation in which the blowing does not succeed in maintaining the side force initially applied. However, the same value of C_m provides adequate sustenance of C_y during the other three motions. The delayed blowing case for $k_c = 0.058$ again shows a slow transition to the constant blowing line, when compared with the "snap" reactions to blowing initiation for the other three motions.

The transient sectional side force plots for x/D = 3.75 are shown in figure 4.2.6. We have already seen that the steady sectional C_y switches from negative to positive when C_m is increased from $1.38 \cdot 10^{-3}$ to $2.16 \cdot 10^{-3}$. For $k_c = 0$ and delayed blowing (figure 4.2.6a), a strange phenomenon occurs. When the blowing is delayed, the side force reacts first to the negative side. As C_m increases toward its steady value of $2.16 \cdot 10^{-3}$, C_y again transitions quickly to the corresponding positive value. Similar effects are seen during maneuvering of the model. Since this type of transition is definitely unwanted, we would like to avoid this situation by limiting our blowing coefficients. By utilizing pneumatic control from both sides of the nose, two-way manipulation of the vortex structure could be achieved without resorting to high blowing rates, which would give rise to the situation seen here. This method has already been used with success in steady testing (Roos and Magness [1993], and Roos [1996]).

Figure 4.2.6 also shows that the effect of the motion observed at previous axial locations is repeated here. In fact, if we compare figure 4.2.7, which contains the corresponding plots for x/D = 5.25, we see that for $\alpha = 45°$, the sectional C_y opposes the motion of the nose. In other words, the flow over the entire model is canted to one side, ignorant of the local effects which change as the axial stations pass the coning axis. In addition the effects due to model motion become more pronounced the further the

measurement station is from the nose, not the coning axis, as evidenced by comparing data for x/D = 3.75 to that of x/D = 1.8125. These effects make a strong case for the argument that the convective asymmetry emanating from the nose tip dominates the local effects during coning motion of the model.

Figure 4.2.6c (k_c = -0.058) again shows the failure of $C_m = 1.38 \cdot 10^{-3}$ to maintain the steady value of C_y while the motion is executed. $C_m = 2.16 \cdot 10^{-3}$ appears to be equivalent to or better than the lower blowing coefficient for all motions. Regardless of its success in sustaining C_y during the motion, any blowing suffices to shorten the time over which the motion affects the side force.

At x/D = 5.25, as shown in figure 4.2.7, there is increased unsteadiness as the axial location is increased. In addition, we see no-blowing cases in which C_y is delayed drastically in reaching the steady state, or does not reach the steady state at all ($C_m = 0$ for $k_c = \pm 0.058$).

Finally, we observe in figures 4.2.6 and 4.2.7 that motions of equal reduced frequency but opposite sign do not produce ΔC_y of similar magnitude. It appears that at these aft axial positions, the flow resists displacement toward the negative side. This effect is very noticeable in figure 4.2.7 where for k_c = -0.058, ΔC_y = 1.8 whereas ΔC_y = -0.5 for k_c = 0.058. However, the two motions in question do produce similar values of sectional C_y (around ±1) at maximum displacement.

To better understand the flow physics, we refer to figure 4.2.8, displaying polar plots of $-C_p$ vs. the azimuthal angle θ for $\alpha = 45°$ are shown. Curves are shown for blowing with fixed model, i.e. $k_c = 0$, and for a moving model with zero blowing, i.e. $C_m = 0$. In this way, we can look at the separate effects of motion and blowing. The view of these plots is looking upstream from the pilot's position. The pressure distributions for motion cases are taken when the sectional C_y is at maximum displacement from the steady case. The sectional C_y acts toward the vertical half-plane which contains more area inside the curve. To create sectional C_y to starboard, the right vortex stays attached and creates a large area of suction on the right side of the model. In contrast, the left vortex detaches and the separated flow beneath this vortex results in high pressure on the left side of the model. For sectional C_y to port, the opposite is true. We also see that blowing and motion appear to use the same physical process to create asymmetric C_y, as demonstrated by comparable pressure shifts from the steady case.

Coning and Blowing at α=55°

The transient development of the sectional side force for various axial locations at $\alpha = 55°$ are given in figures 4.2.9 to 4.2.12. At this angle of attack, the vortices assume the (pseudo) bi-stable state.

That is, they become very hard to displace from their natural asymmetric position. When they are displaced by blowing or motion, they tend to proceed directly to a position diametrically opposed to the original position, creating a C_y of equal magnitude but opposite sign. Symmetric or near-symmetric vortical arrangement cannot be achieved naturally.

When the model is set in motion with no blowing at $\alpha = 55°$, the same trend observed at $\alpha = 55°$ is repeated for the foremost three measurement positions, with ΔC_y opposite to the motion of the nose. However, for x/D = 5.25 (figure 4.2.12), the ΔC_y is in the same direction as the motion. The cause of this phenomenon is still not known. It has been argued that the convective instability has dominated the local effects. If this is still the case, then the only plausible explanation is that separation effects enable the convective asymmetry to reverse the side force. This is possible, because x/D = 5.25 is very near the axial location where the steady sectional C_y switches signs (see figure 4.2.3).

When blowing is introduced at $\alpha = 55°$, we see from figure 4.2.3b that $C_m = 1.74 \bullet 10^{-3}$ and $C_m = 2.72 \bullet 10^{-3}$ produce opposite overall C_y. For the two foremost ports where both of these blowing rates were used, it is shown that when the motion and the blowing produce opposite effects separately, the blowing is ineffective at maintaining C_y during the motion. This can be seen in figure 4.2.10b with $C_m = 2.72 \bullet 10^{-3}$, where the motion would normally decrease C_y and the blowing has produced a positive C_y. When they are combined, the blowing fails to maintain positive C_y. By contrast, when blowing and motion produce equivalent ΔC_y, there is very little change in the sectional C_y during the motion, as shown in figure 4.2.10b with $C_m = 1.74 \bullet 10^{-3}$.

In order to get a better idea why these phenomena occur, we refer to figure 4.2.13, which shows polar plots of $-C_p$ vs. θ for $\alpha = 55°$. These plots are presented in the same manner as those of figure 4.2.8. For x/D = 1.8125 and x/D = 2.8125, these plots show that $k_c = 0.058$ and $C_m = 1.74 \bullet 10^{-3}$ produce equivalent pressure distributions, as do $k_c = -0.058$ and $2.72 \bullet 10^{-3}$. To be effective during coning motions at this angle of attack, the pneumatic control employed in these experiments must produce a sectional side force that acts opposite to the motion of the nose. This means that this type of blowing appears to be effective if we want to stop motion of the nose, but not to augment or drive motion of the nose for a sustained period of time.

Two other interesting features are shown in figure 4.2.13. First, motion does not appear to affect the pressure distribution significantly at x/D = 3.75, and blowing affects the pressures very little. The cause for the severe drop in pressure at $\theta = 90°$ is not known. Until further results back up this effect, it is

assumed that there was a malfunction in the data acquisition system at this location (pinched hose, etc.). The second interesting effect is the trend reversal with motion of ΔC_y, observed at x/D = 5.25. At no other axial measurement station does constant blowing at $C_m = 1.74 \bullet 10^{-3}$ and positive motion produce similar pressure distributions. We can therefore conclude, knowing that the blowing with $k_c = 0$ causes pressure distributions to change due to an entirely convective phenomena, that the motion effects are also due to the same convection, and are not caused locally.

Finally, when considering delayed blowing at $\alpha = 55°$, there are many instances where the flow can take several hundred time units to proceed to a sectional C_y near the corresponding constant blowing case. Compare this to approximately 20-50 time units for many of the delayed blowing cases seen at $\alpha = 45°$.

For all cases where $k_c = 0$ and delayed blowing is employed, it is possible to determine when the sectional C_y curves begin to deviate from the curves where $C_m = 0$. If this time is determined for all axial stations, the velocity of propagation of the disturbance can be calculated. It was determined that for $\alpha = 45°$ and $\alpha = 55°$, this velocity is approximately equal to $0.8 \bullet U_\infty$and changes very little with the angle of attack, at least in the range tested. According to the impulsive flow analogy (IFA) discussed in Chapter 1, this propagation velocity should be close in value to the component of U_∞ along the axis of the model, $U_\infty \bullet \cos\alpha$. For $\alpha = 45°$, this component is equal to $0.71 \bullet U_\infty$ and is equal to $0.57 \bullet U_\infty$ for $\alpha = 55°$. Therefore, there must be an additional axial velocity induced by the vortical flow, especially at $\alpha = 55°$, in order to account for the difference between the measured disturbance propagation and the axial convection velocity theorized in the IFA. In Chapter 5, the vortical flow over a tangent-ogive cylinder is investigated, and in some cases, the axial velocity in the cores of the leeside vortices is higher than the free stream velocity. This increased velocity in the vortex cores could account for the increased propagation velocity at $\alpha = 45°$ (from $0.71 \bullet U_\infty$, theoretical to $0.80 \bullet U_\infty$, measured). However, the extent of the increased core velocities is not enough to account for the increased propagation velocity at $\alpha = 55°$ (from $0.57 \bullet U_\infty$, theoretical to $0.80 \bullet U_\infty$, measured).

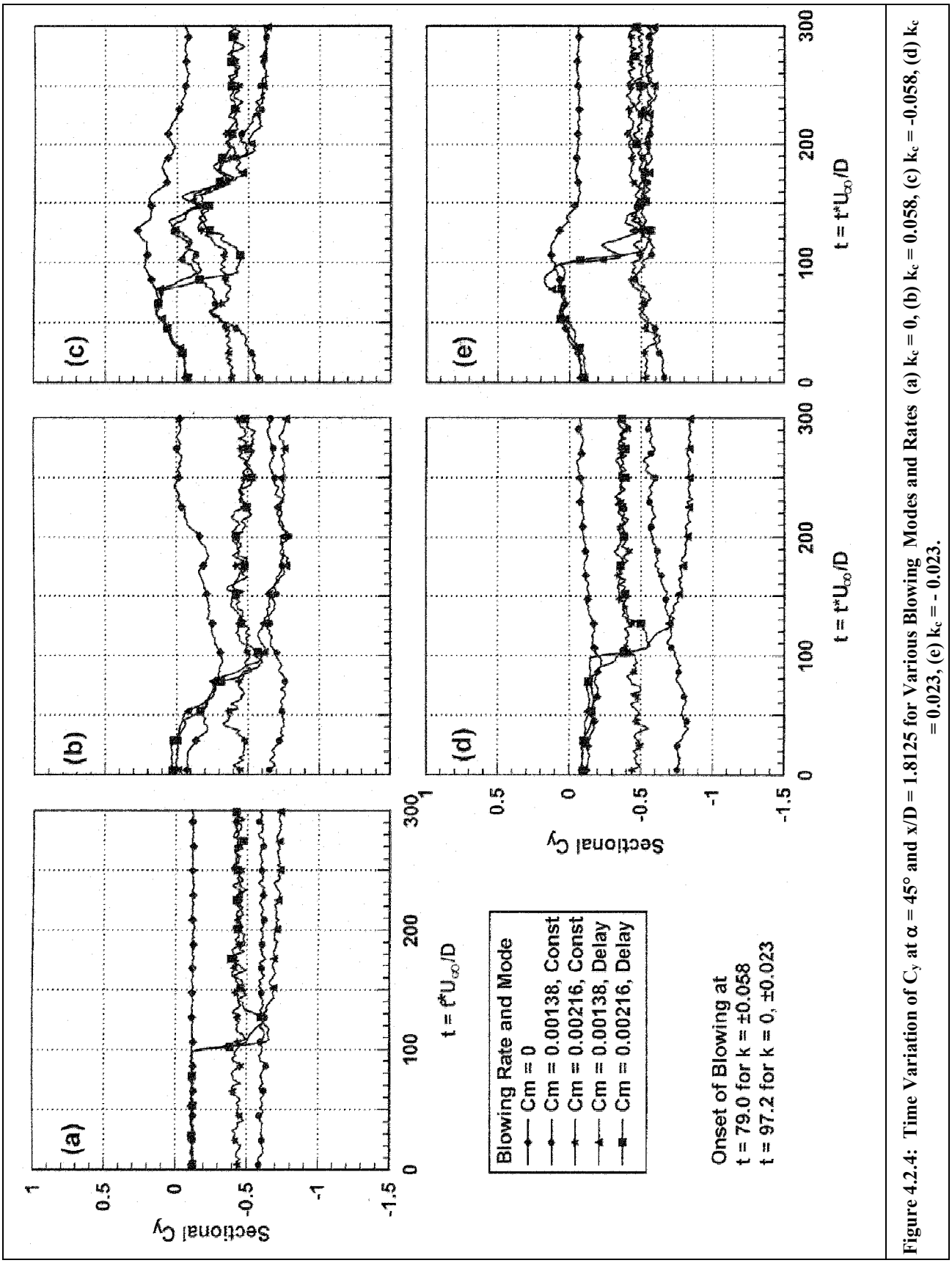

Figure 4.2.4: Time Variation of C_y at $\alpha = 45°$ and x/D = 1.8125 for Various Blowing Modes and Rates (a) $k_c = 0$, (b) $k_c = 0.058$, (c) $k_c = -0.058$, (d) $k_c = 0.023$, (e) $k_c = -0.023$.

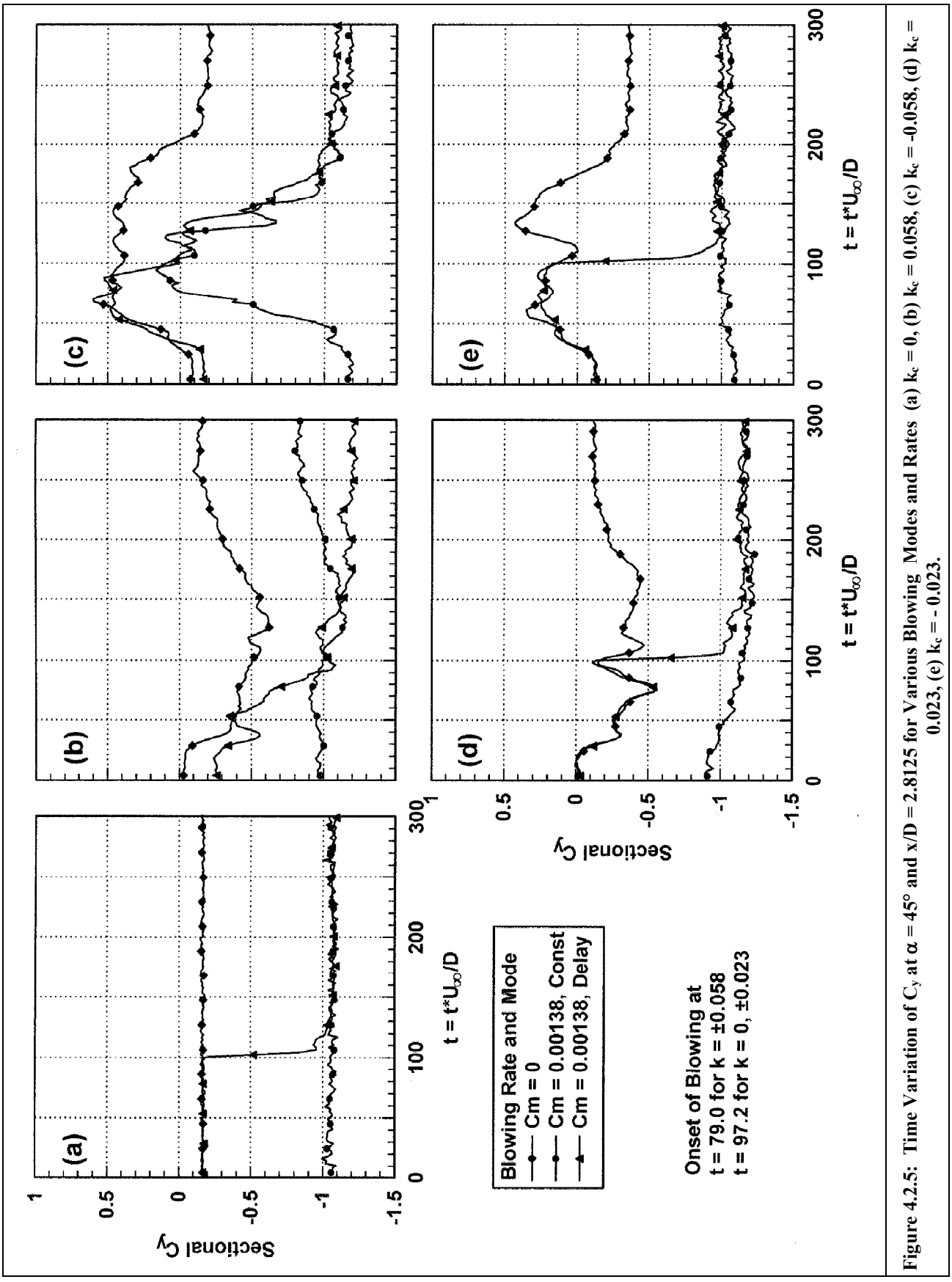

Figure 4.2.5: Time Variation of C_y at $\alpha = 45°$ and x/D = 2.8125 for Various Blowing Modes and Rates (a) $k_c = 0$, (b) $k_c = 0.058$, (c) $k_c = -0.058$, (d) $k_c = 0.023$, (e) $k_c = -0.023$.

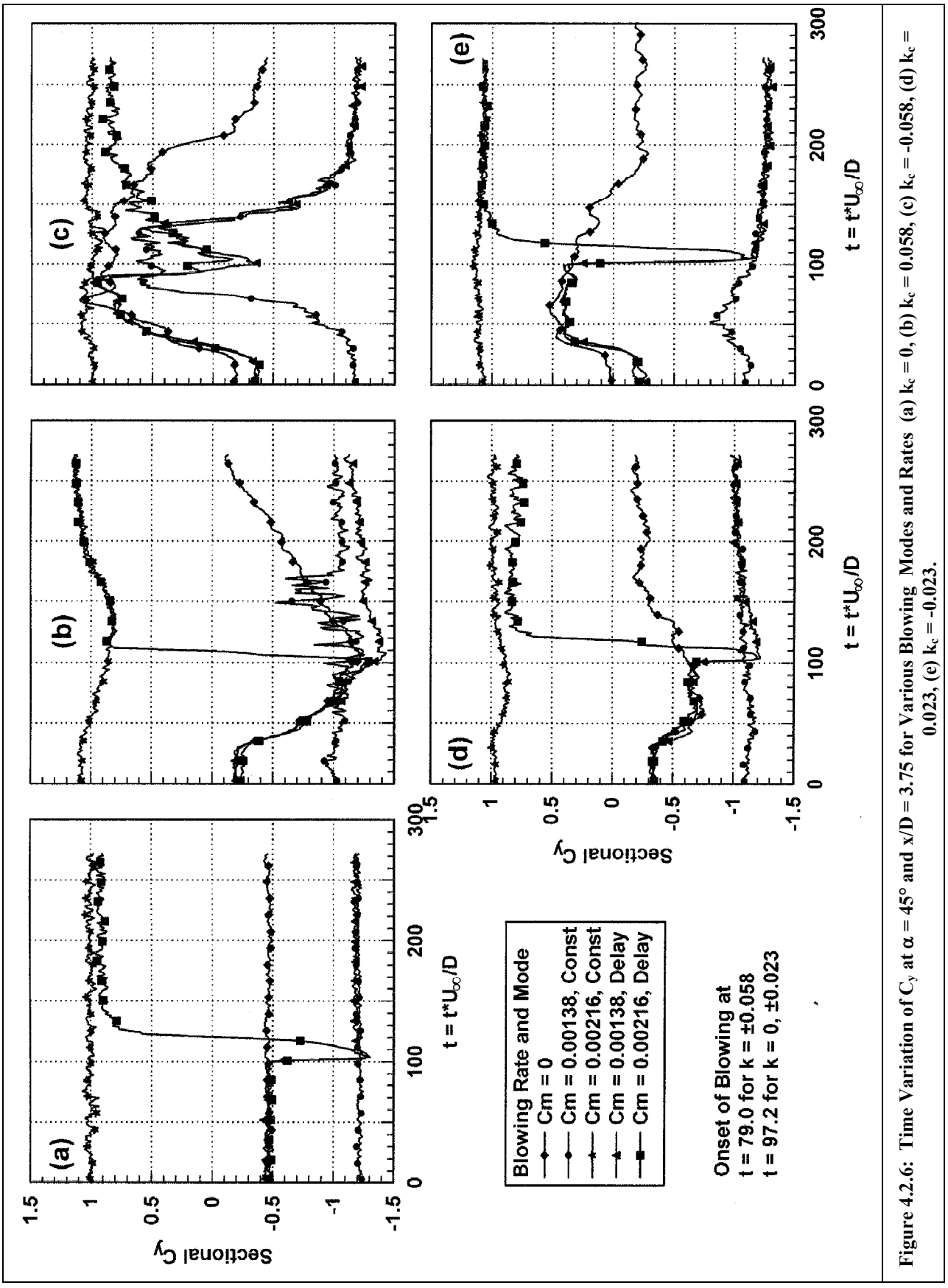

Figure 4.2.6: Time Variation of C_y at $\alpha = 45°$ and x/D = 3.75 for Various Blowing Modes and Rates (a) $k_c = 0$, (b) $k_c = 0.058$, (c) $k_c = -0.058$, (d) $k_c = 0.023$, (e) $k_c = -0.023$.

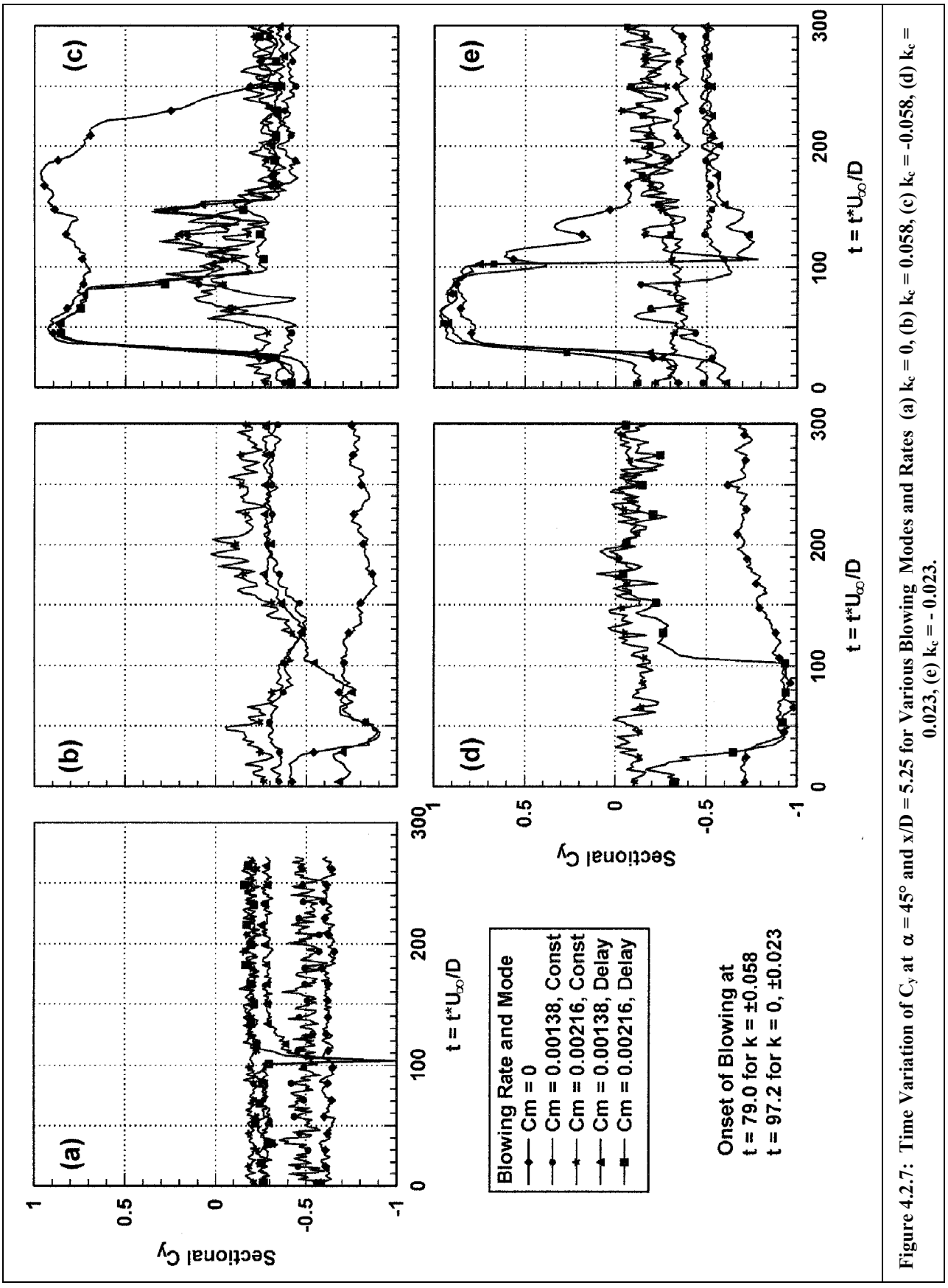

Figure 4.2.7: Time Variation of C_y at $\alpha = 45°$ and x/D = 5.25 for Various Blowing Modes and Rates (a) $k_c = 0$, (b) $k_c = 0.058$, (c) $k_c = -0.058$, (d) $k_c = 0.023$, (e) $k_c = -0.023$.

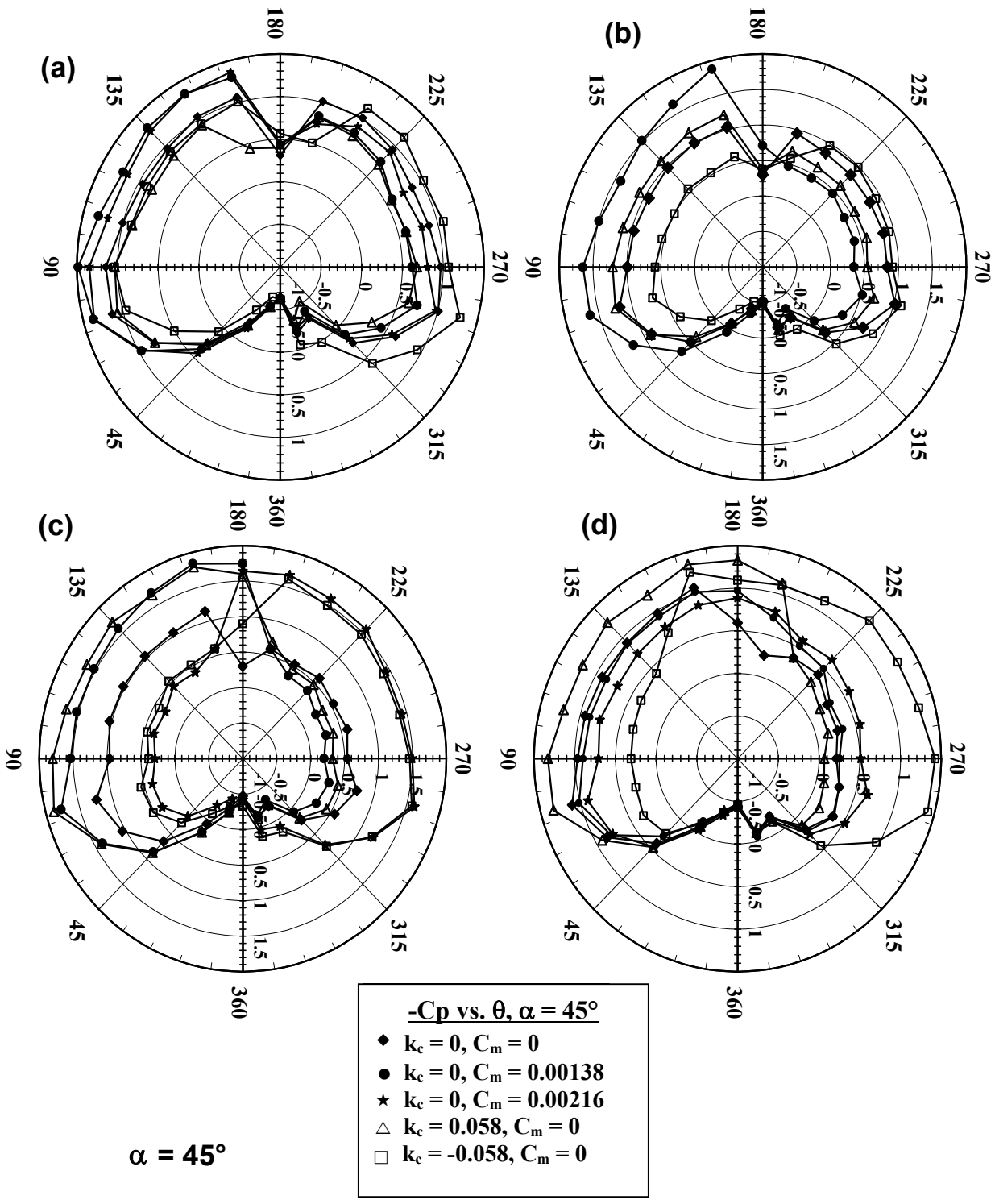

Figure 4.2.8: Pressure Distributions vs. θ (Pilot's View) for α = 45° to Analyze Separately the Effects of Motion and Blowing (a) x/D = 1.8125 (b) x/D = 2.8125 (c) x/D = 3.75 (d) x/D = 5.25. Note that Pressure Coefficients have Reversed Sign, so that $C_p > 0$ Indicates Suction.

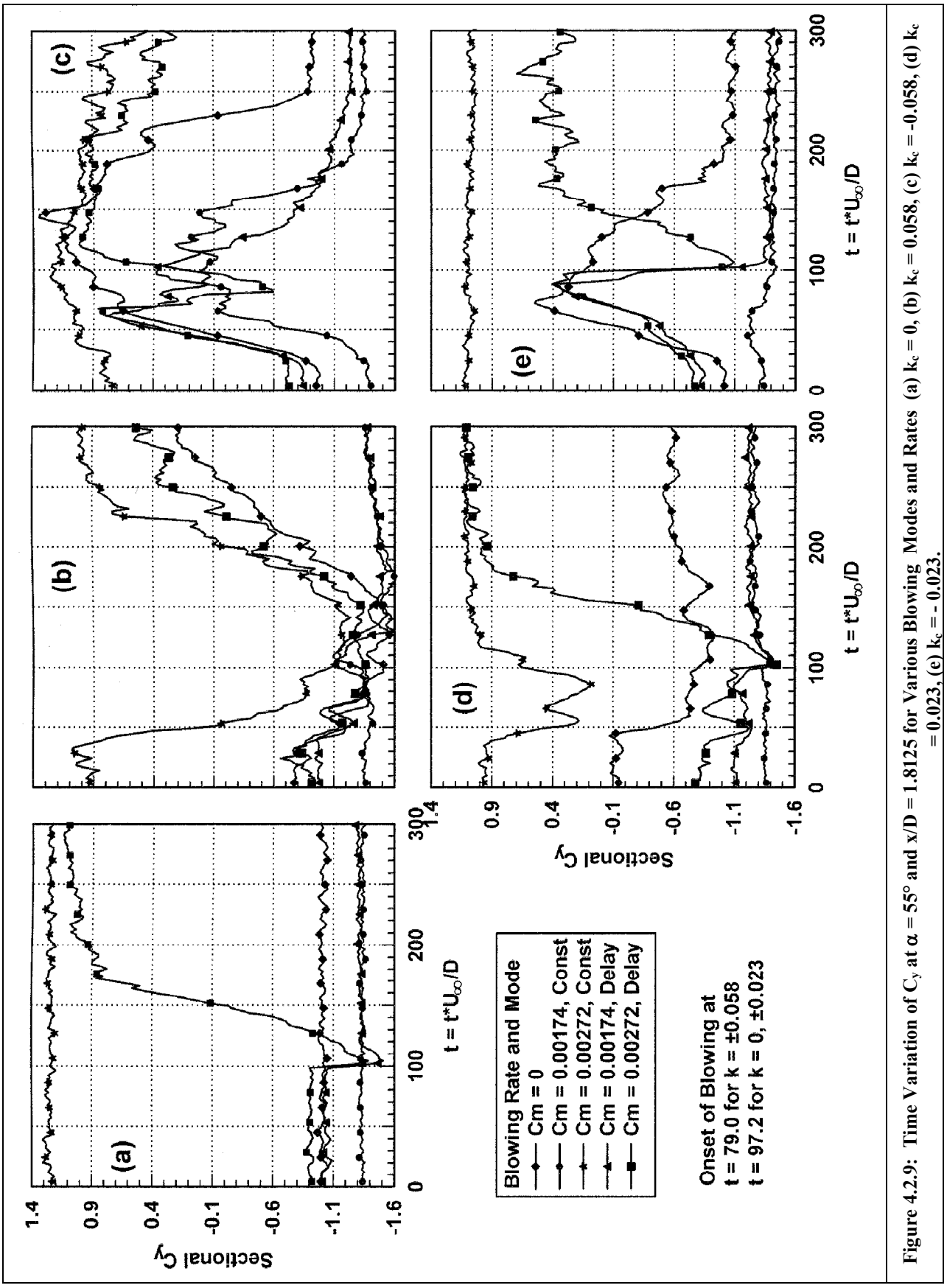

Figure 4.2.9: Time Variation of C_y at $\alpha = 55°$ and x/D = 1.8125 for Various Blowing Modes and Rates (a) $k_c = 0$, (b) $k_c = 0.058$, (c) $k_c = -0.058$, (d) $k_c = 0.023$, (e) $k_c = -0.023$.

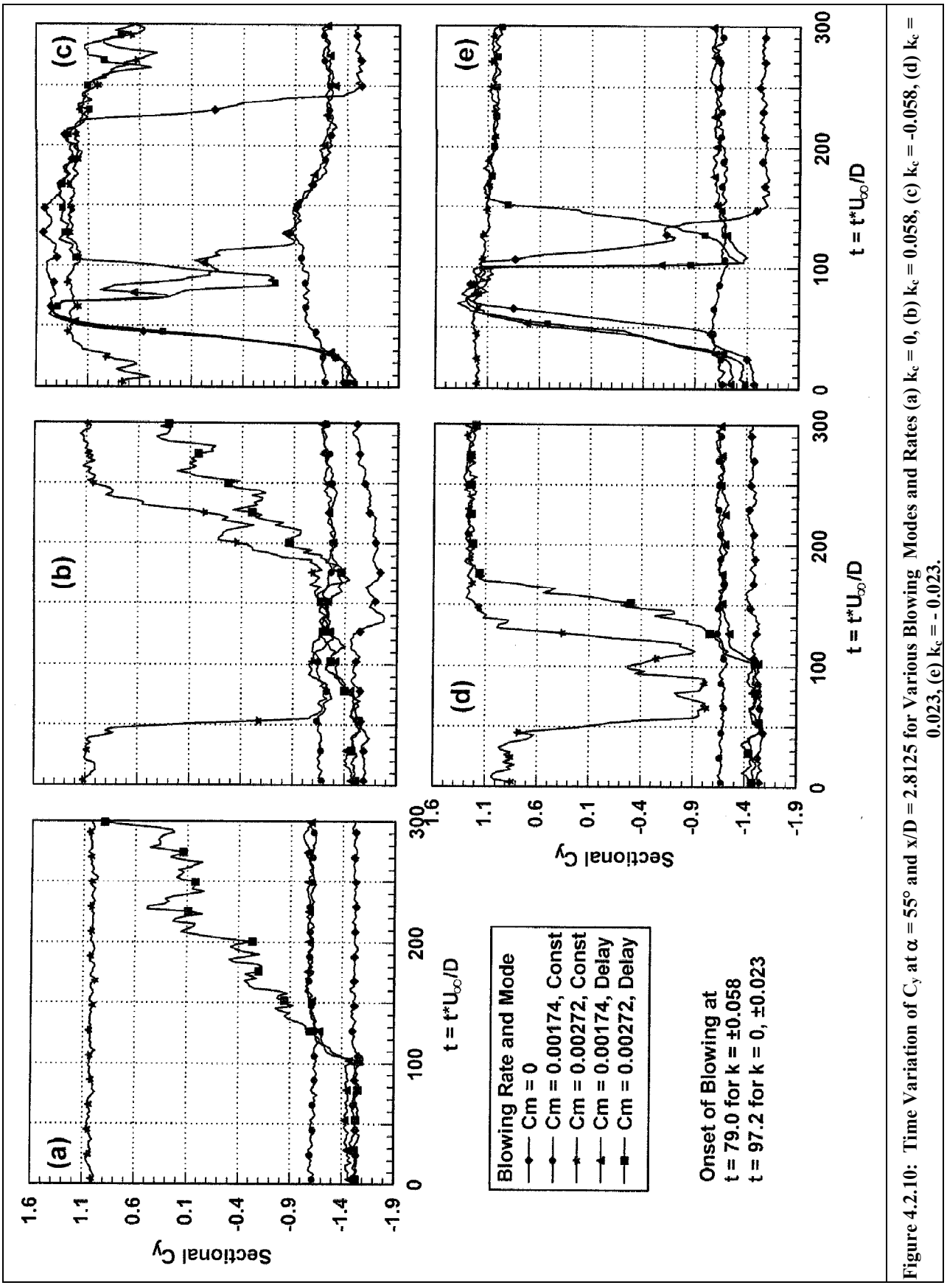

Figure 4.2.10: Time Variation of C_y at $\alpha = 55°$ and x/D = 2.8125 for Various Blowing Modes and Rates (a) $k_c = 0$, (b) $k_c = 0.058$, (c) $k_c = -0.058$, (d) $k_c = 0.023$, (e) $k_c = -0.023$.

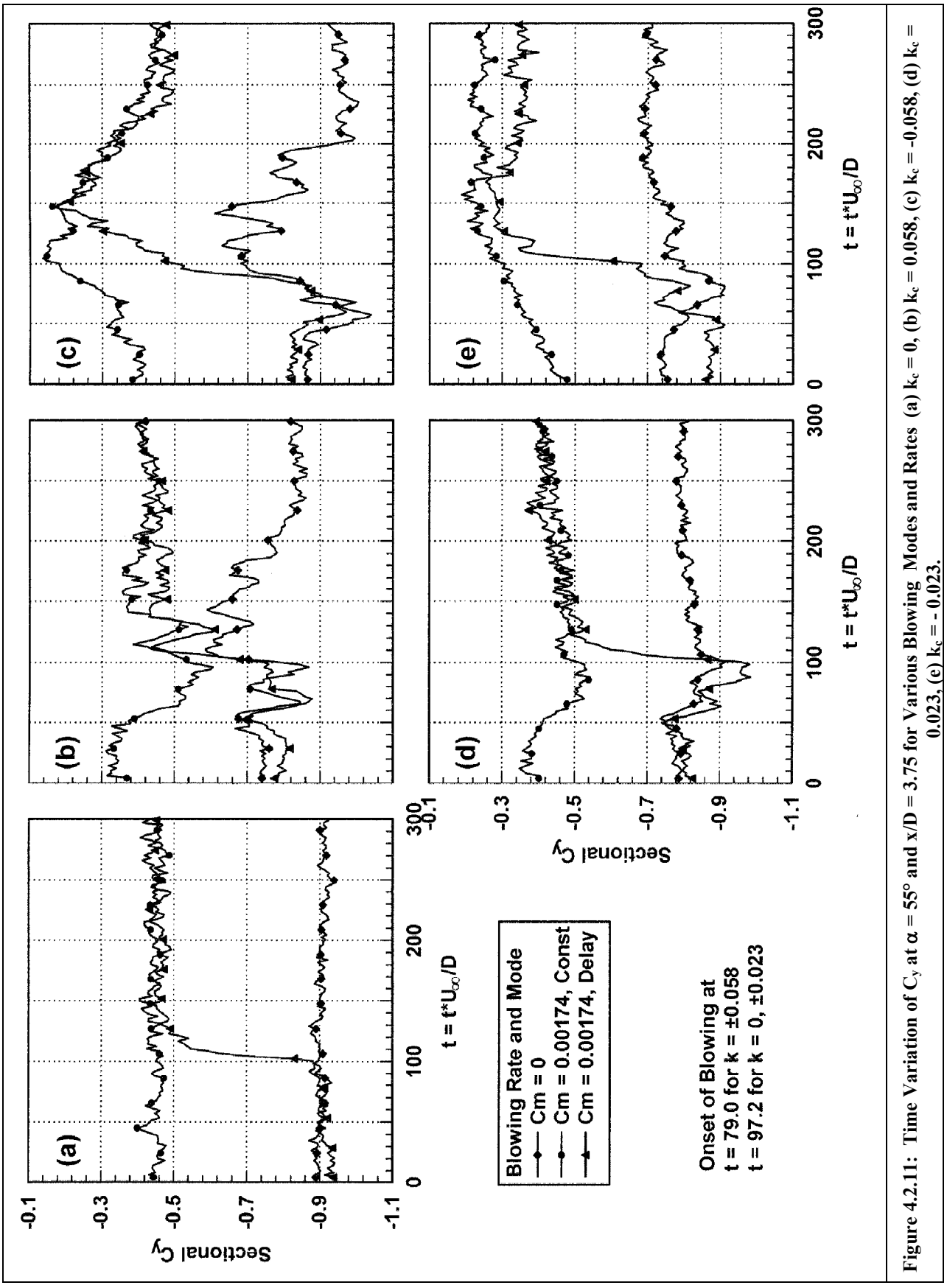

Figure 4.2.11: Time Variation of C_y at $\alpha = 55°$ and x/D = 3.75 for Various Blowing Modes and Rates (a) $k_c = 0$, (b) $k_c = 0.058$, (c) $k_c = -0.058$, (d) $k_c = 0.023$, (e) $k_c = -0.023$.

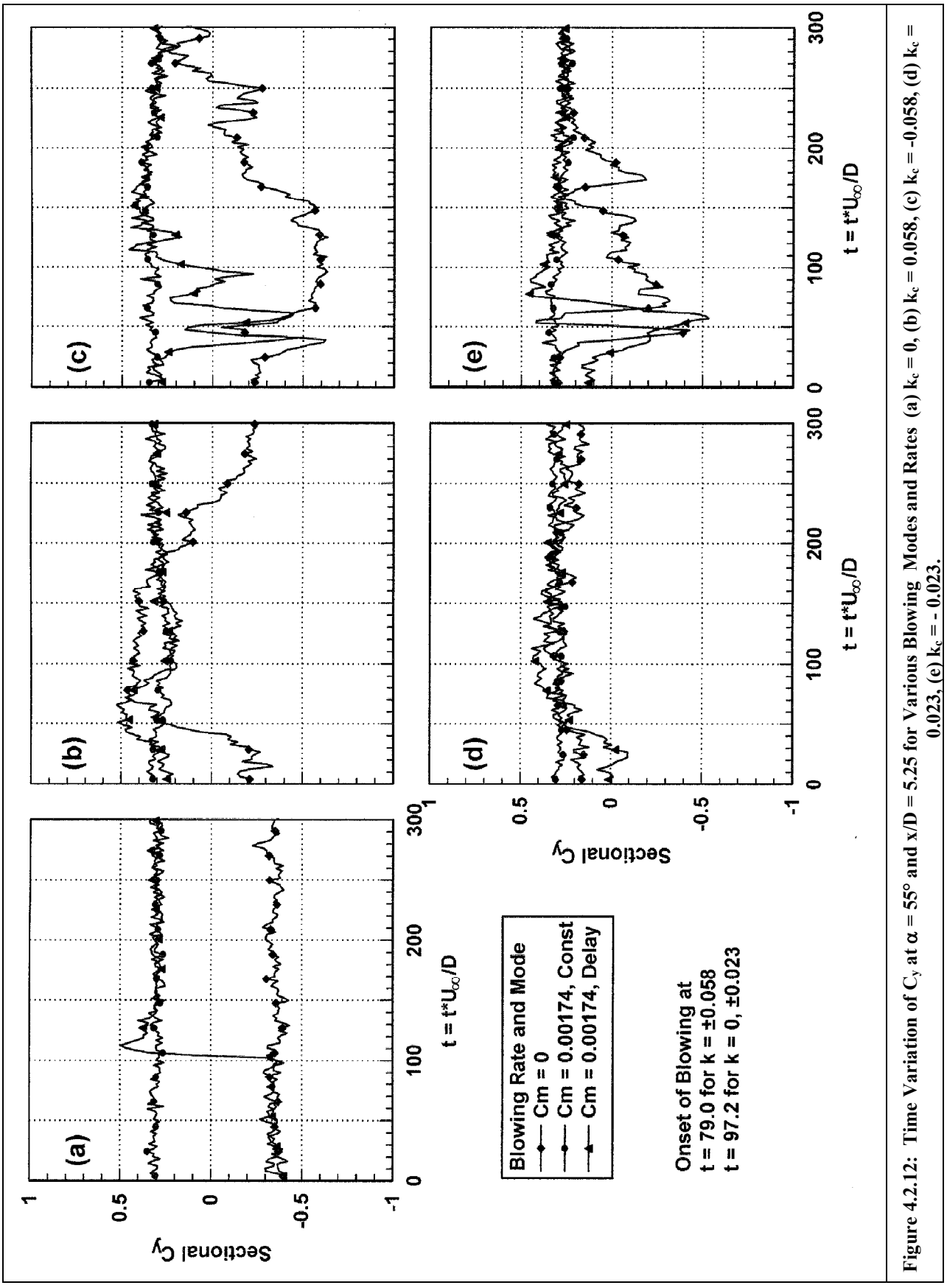

Figure 4.2.12: Time Variation of C_y at $\alpha = 55°$ and x/D = 5.25 for Various Blowing Modes and Rates (a) $k_c = 0$, (b) $k_c = 0.058$, (c) $k_c = -0.058$, (d) $k_c = 0.023$, (e) $k_c = -0.023$.

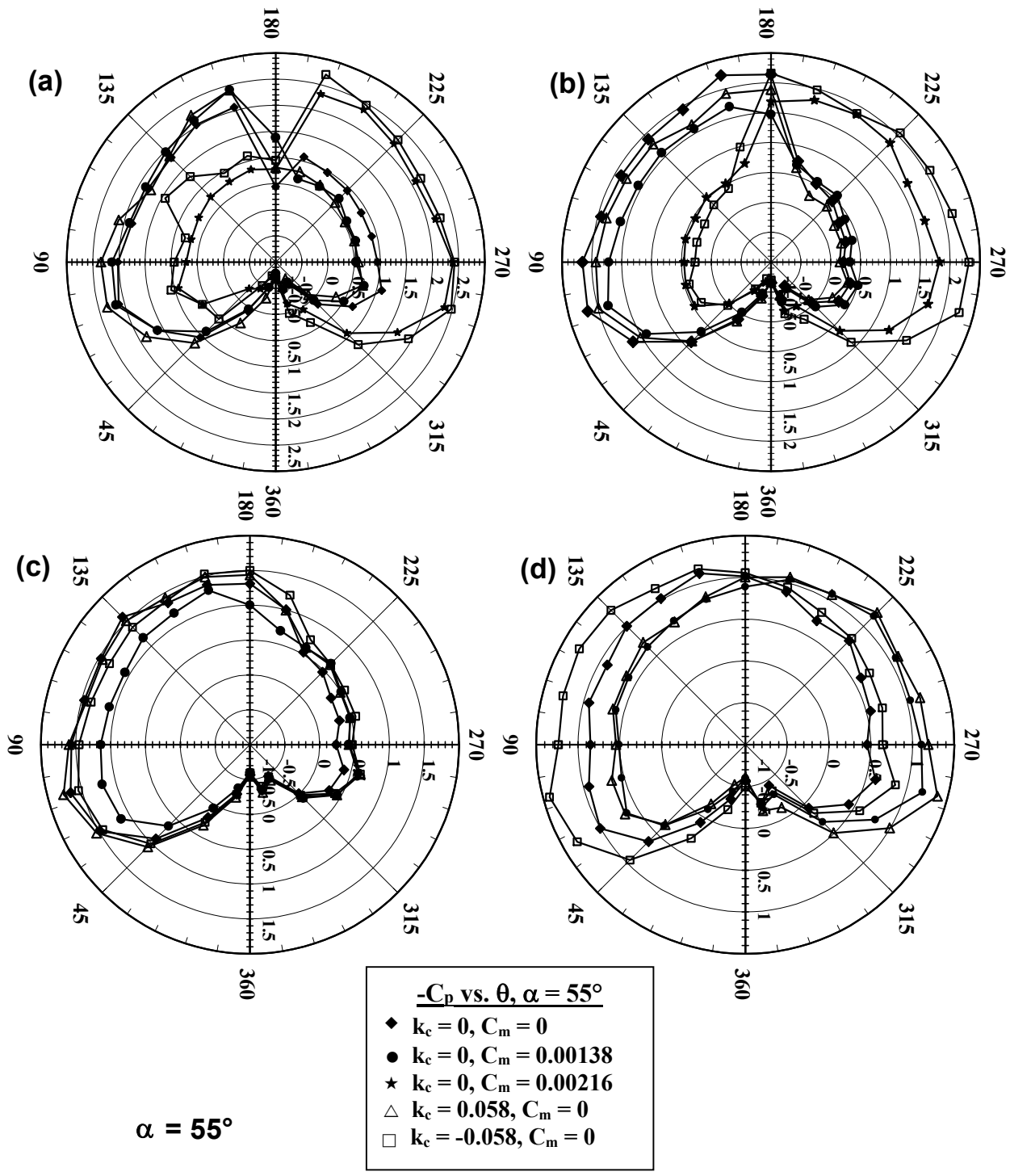

Figure 4.2.13: Pressure Distributions vs. θ (Pilot's View) for α = 55° to Analyze Separately the Effects of Motion and Blowing (a) x/D = 1.8125 (b) x/D = 2.8125 (c) x/D = 3.75 (d) x/D = 5.25. Note that Pressure Coefficients have Reversed Sign, so that $C_p > 0$ Indicates Suction.

4.3 Coning Maneuvers with Transitional Separation

The asymmetric flow over slender forebodies at high angles of attack has been well investigated over the past twenty-five years. The steady problem, in which the body remains stationary, represents the major part of the body of literature, and discussion of the major findings for stationary models can be found in Section 1.2. More recently, attention has been turned to control methods (see Section 1.3) and maneuvering slender forebodies (see Section 1.4). One of the major concerns that have arisen concerning these lines of investigation is whether general trends observed at lower Reynolds numbers will also hold during maneuvers conducted at higher Reynolds numbers, in the transitional or turbulent flow separation regimes.

The vortex asymmetry that dominates the flow over slender forebodies has been shown to be a fickle element, subject to change with small variations in model geometry and freestream character. The effect of Reynolds number can be quite drastic, due to uneven transitioning of the boundary layer. The critical Reynolds number is approximately 2.5×10^5, with fully turbulent separation occurring for $Re_D > 1.5 \times 10^6$ for $\alpha = 55°$.

When the model is set in motion, the flow becomes even more complex, due to the effect of the moving model on the boundary layer separation. However, the need to understand these unsteady flow phenomena is imperative in order to progress to control of the flow during maneuvers. Tests at high Reynolds number and in unsteady flow conditions are necessary to confirm and justify the accuracy of the data resulting from investigations conducted at lower Reynolds numbers, and also the usefulness of control methods employed at lower Reynolds numbers.

4.3.1 Experimental Setup, Data Acquisition and Processing

Tests are conducted in the 6' x 6' VPI & SU Stability Tunnel, using the DyPPiR model mount to perform the coning maneuvers. The Stability Tunnel and DyPPiR are described in more detail in section 2.3.

The 3.5-caliber tangent-ogive cylinder, as described previously in section 2.8.3, has a base diameter of 5" and an overall length of 27.5". The tip diameter of the model is d_t = D/20 (5% blunted). Five sets of circumferential pressure ports are installed at x/D = 1.25, 2.00, 2.75, 3.75 and 4.75. Each set of ports has 20 pressure ports spaced at 9° intervals over the pressure side of the model and 24 ports spaced at 7.5° intervals, for 44 pressure ports overall. Microblowing ports used to effect forebody vortex control are installed in the style used by Roos [1994,1996]. The diameter of the blowing ports is 0.216 cm (0.085") or 0.017•D. and they are located at x/D = 0.20.

Coordinates and variables associated with this problem are shown in figure 1.3 (see Chapter 1). The coning rate is defined as $\dot{\gamma}$, and the coning rotation is around the velocity vector, regardless of the incidence angle.

Pressure acquisition for all investigations was accomplished through the use of several Pressure Systems Inc. (PSI) ESP pressure scanners, as described in section 2.6. Since the transducers are differential, a reference pressure must be chosen. In all cases in the present work, the reference pressure was the tunnel freestream static pressure.

The ESP's employed in the present research were 32-channel units. The small size of the ESP's allowed them to be installed inside the model in Stability Tunnel model. This in turn allowed the flexible tubing runs connecting the ESP to the pressure ports to be minimized, keeping the pressure attenuation and phase-lag small and maximizing the frequency response of the system. For similar experimental setups involving the ESP, tests performed indicated that for frequencies of 100 Hz or less, the delay in the response of the transducers leads to an uncertainty less than 2% of the actual value (Rediniotis, [1992]).

A mass-flow injection systems for the implementation of forebody blowing was used to send air through the blowing ports of the tangent-ogive cylinder model. Compressed air at 80-100 psi is used as the flow source, but is regulated to less than 15 psi before entering the rest of the system. After exiting the regulator, the air is routed to a solenoid valve. This valve is used to turn the blowing on and off. The solenoid valve is actuated electrically by a relay that is a part of a circuit designed to delay the blowing by a specified amount of time. The valve is normally open, so that if power to the control circuit is completely removed, constant steady-state blowing will result. For the testing documented in this section, constant blowing (no delay) was used.

For data in the Stability Tunnel for which forebody blowing was employed, the mass flow ejected from the blowing ports was measured by an HFM-200 mass flow meter manufactured by Hastings Instruments, Inc, as described in section 2.9.1. The measured mass flows are converted into dimensionless mass flow coefficients. In order to compare with previous results, the mass flow coefficient is defined in the same manner as Roos [1996]:

$$C_{\dot{m}} = \frac{\rho A V}{\rho_\infty S U_\infty} \qquad [4.2]$$

where S is the planform area of the tangent-ogive forebody, and ρ, A and V are the exit density, area and velocity, respectively for the control flow. The planform area (S) of a 3.5 caliber tangent-ogive forebody can be determined from the ogive geometry (see Appendix D) to be $2.343 \cdot D^2$, which in the case of the D = 5" Stability Tunnel model is 0.4067 ft^2 (0.0378 m^2). For all tests documented in this section, the mass flow coefficient was maintained at $C_{\dot{m}} = 1.35 \times 10^{-4}$.

4.3.2 Data Acquisition

Pressure data were acquired by employing the ESP modules, which were mounted inside the test sections and allowed to ride along with the model during the motions. The ESP's were actually placed inside of the Stability Tunnel Model. The ESP's were connected to dedicated support boards to allow digital addressing and voltage regulation for the units. Sampling was performed by a programmable-gain 12-bit A/D data acquisition board. One extra channel of voltage data were acquired, corresponding to the mass flow rate.

The method of ensemble-averaging multiple executions of the same maneuver was used. In order to employ this method, the unsteady motion is executed multiple times, with data acquisition triggered at the same time relative to the motion. The resulting data are averaged over the number of ensembles the motion was executed using Chauvenet's criterion (see section 2.10.2). The result is a time-series of data, with each data point representing the average result for the number of ensembles.

Pressure data were acquired during coning motions for k_c = 0.0057, 0.0114, 0.170 and 0.196. The model is mounted such that its axis of symmetry is always at α = 50°. The coning axis (held horizontal at 11" below the tunnel centerline for all coning maneuvers) is located at $x_c/D = 6.23$ for all motions. The Reynolds number is maintained very close to $2.75 \cdot 10^5$ for all tests, with an average

freestream velocity of approximately 37 m/s. For each type of motion, pressures are acquired with and without forebody blowing. All pressure data are acquired at a rate of 250 Hz for a duration of 3 seconds. Each motion is executed twenty times and the results are ensemble averaged.

Although the Stability Tunnel model has 5 sets of circumferential pressure ports with 44 ports in each set, only data for the first three sets of ports at x/D = 1.25, 2.00 and 2.75 were acquired. Both the ±10" H2O ESP and the ±20" H2O ESP were employed due to the number of pressures to be acquired. When switching the pressure ports, the afterbody of the model was not removed from the 50° offset block. The forebody and afterbody were constrained to fit together in only one way with very tight tolerances, ensuring that the model could always be placed at the same location and orientation during testing.

Boundary-layer trip strips made from duct tape were attached to the model during testing. These trips were placed at $\theta = \pm 55°$ from the windward stagnation point and had sawtooth edges to promote flow transition (see figure 2.16). The trip strips were not extended to the forebody tip, but were stopped at x/D = 0.5. The trips were also briefly interrupted when crossing the lines of circumferential pressure ports. According to Lamont [1982], the flow over the 3.5 caliber tangent-ogive forebody should start to exhibit transitional separation characteristics for $Re_D > 2.5 \bullet 10^5$. The surface pressures reveal that the flow experienced transitional separation for $Re_D = 2.75 \bullet 10^5$. Without the trip strips, the separation was very similar to the laminar separation patterns seen at lower Reynolds number. Thus, the trip strips did succeed in changing the boundary-layer state at separation.

In the Stability Tunnel, the DyPPiR is responsible for triggering the data acquisition at the same instant the motion commences. The model is set to the start position for the desired motion, and then the trigger is sent. The trigger is passed to the pressure data acquisition computer and to the delay circuit controlling the solenoid valve used for mass flow injection. The motion is delayed for 0.5 s the trigger is sent. During the motion, the DyPPiR computer acquires command and error signals for all three degrees of freedom of the DyPPiR and all pertinent test-section thermodynamic data. This DyPPiR data acquisition is performed at 250 Hz by a 12-bit A/D data acquisition board manufactured by Metrabyte. When data acquisition ends, the model is reset to the initial position and the flow is allowed to achieve a steady state before the next motion is performed.

4.3.3 Data Reduction

Having acquired the port pressures on the tangent-ogive model and the freestream total and static pressures (from the tunnel Pitot-static tube), the pressure coefficient for each pressure port is calculated according to:

$$C_p = \frac{P - P_\infty}{\frac{1}{2}\rho U_\infty^2} = \frac{\Delta P}{q} \qquad [4.3]$$

Then the ensemble-averaged pressure coefficient can be calculated from

$$\overline{C_p} = \frac{1}{N}\sum_{n=1}^{N} C_{p,n} \qquad [4.4]$$

Equation 4.4 would be used to determine the average C_p for each sample in the time records. The result of this process is a single time record with ensemble-average pressure coefficients, reflecting the mean effect of the motions. From this point forward we will take C_p to denote the ensemble-averaged pressure coefficient.

Once the pressure coefficients are ensemble averaged, the dimensionless sectional yaw forces are calculated from

$$C_y = \frac{d}{2 \cdot D}\oint_\theta C_p \sin\theta \cdot d\theta \qquad [4.5]$$

The time is also converted to a dimensionless time t* by using U and the characteristic length $D\cos\alpha$, so that the time is non-dimensionalized by the time required for the freestream flow to convect one base diameter axially over the model.

4.3.4 Results and Discussion

Sectional yaw coefficients as a function of t* are shown in figure 4.1, for four different reduced frequencies at x/D = 1.25. Note that all of the motions are in the negative direction (nose to port), and that the motions are plotted in red against the right-hand axis. As in all cases presented here, the sectional yaw force and the motion directions coincide, so that a positive C_y would be directed in the direction of positive coning motion. In every case in figure 4.1, the flow reacts quickly to both the beginning and end of the coning motion. We see that for low reduced frequencies, such as k_c = -0.0057, the existing sectional side force is reinforced, so that the coning motion in the negative direction would continue. This is similar to that effect seen by Yoshinaga, et al [1991]. Similar to previous results seen in previous data from the authors, higher reduced frequencies produce a "drag" effect, so that C_y reacts to oppose the motion (see k_c = -0.0170 and -0.0196).

Finally, we see that for faster motions at higher reduced frequencies, the C_y does not return to its previous steady state once the motion stops. This is most certainly a tunnel effect, and a result of the tip of the model approaching the tunnel walls and the flow about the ogive tip being affected. At lower reduced frequencies, the model could be maintained near the center of the tunnel, because there was no need for large angular motions as there would be at the higher reduced frequencies of motion. This effect is apparent in the "crossover" in steady-state values between the positive and negative motions in figure 4.2.

In figure 4.2, it may be seen that the reaction of the sectional yaw force is analogous for positive and negative motions. However, the magnitude of the reaction is not always the same. For instance, at k_c = ±0.0196, we see nearly equal displacements from the steady state for both positive and negative motions, but this is not the case for k_c = ±0.0170.

Figure 4.3 shows the C_p distribution for the case of k_c = -0.0057 shown in figure 4.1. Figure 4.4 shows the C_p distribution for k_c = -0.0196 in figure 4.1. The idea here is to compare how the pressure distribution (and thus the sectional yaw force reacts). For figures 4.3-4, we have chosen a steady, pre-motion pressure distribution, and also a distribution which represents the largest deviation from the pre-motion state. The non-dimensional times for these distributions are given in figures 4.3-4, so that they can be easily correlated with Figure 4.1.

It has been argued that the asymmetry itself, or changes in the asymmetry with motion are due to non-symmetrical separation conditions on either side of the axisymmetric body. While it is inherently hard to get a very accurate determination on the separation locations from the pressure distributions, we can see that the flow on both sides is not separated until at least 110° from the stagnation point. In addition, the general shape of the pressure signatures of the two vortices are similar. In figure 4.3, which represents a case where the negative yaw force is reinforced. We see the greatest difference in the curves to be near and leeside of the suction peaks. This represents a situation where the strength of the vortices is changed, but the there is little displacement of the vortices themselves relative to the model. By contrast, in figure 4.4 we see that there is a general change in the strength and position of the vortices, as the pressure signature has shifted horizontally as the vortices realign themselves behind the rapidly shifting model.

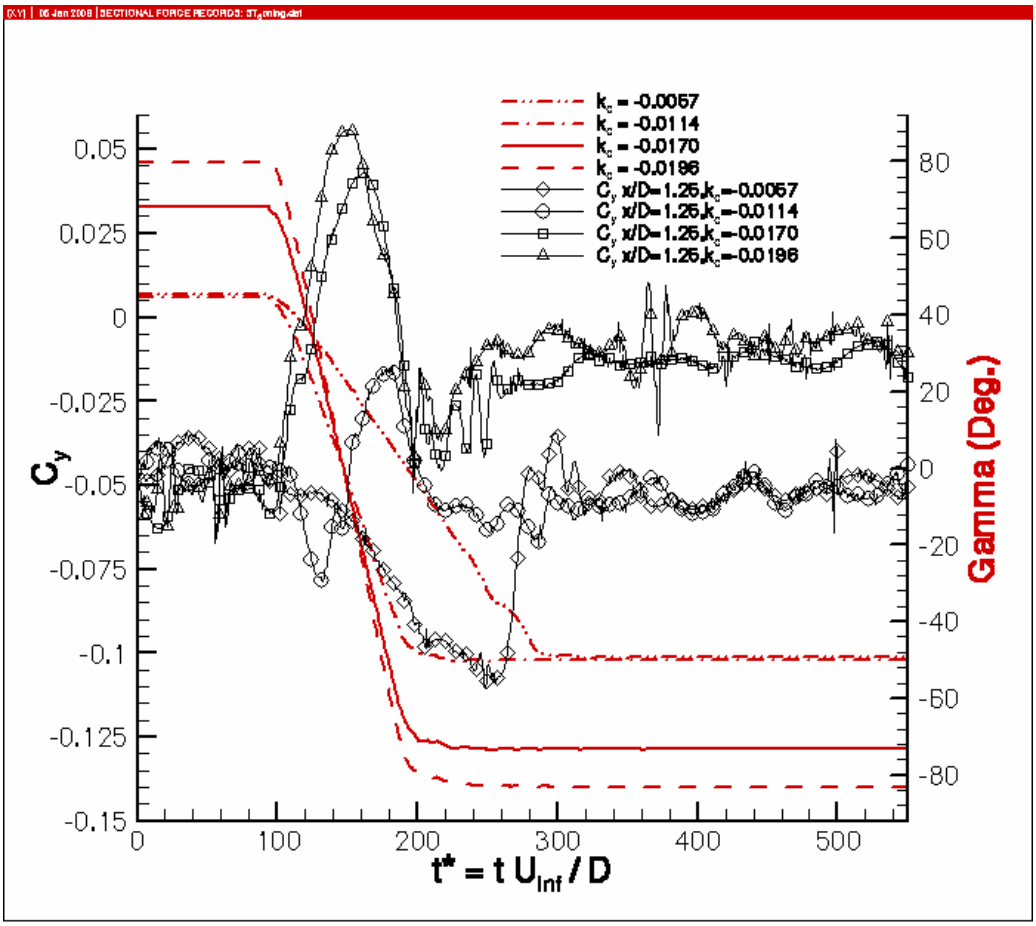

Figure 4.1: Sectional Yaw Force Time Series for Four Different Coning Rates (All Negative) at x/D = 1.25.

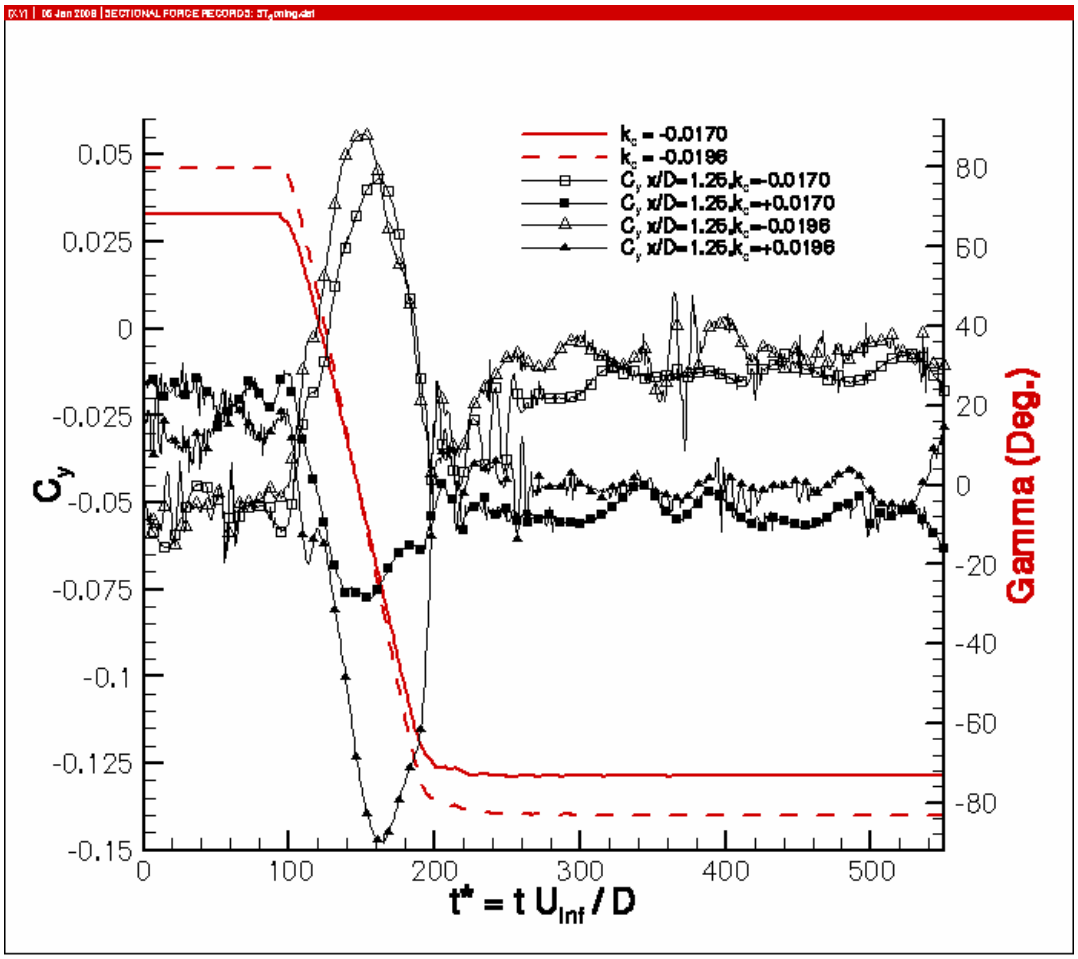

Figure 4.2: Sectional Yaw Force Time Series for Two Different Coning Rates (Both Directions) at x/D = 1.25. Note Crossover of Start/End Values.

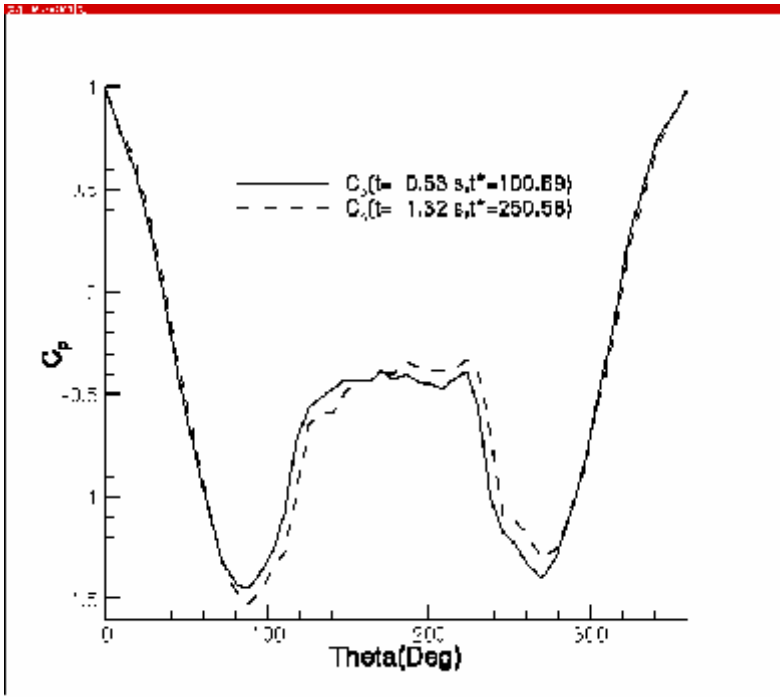

Figure 4.3: Pressure Distribution for k_c = -0.0057, x/D = 0.125 (as shown in Figure 4). Shown Are the Two Pressure Distributions Corresponding to the Pre-Motion State (Solid Line) and the Largest Deviation of C_y from the Pre-Motion State (Dashed Line).

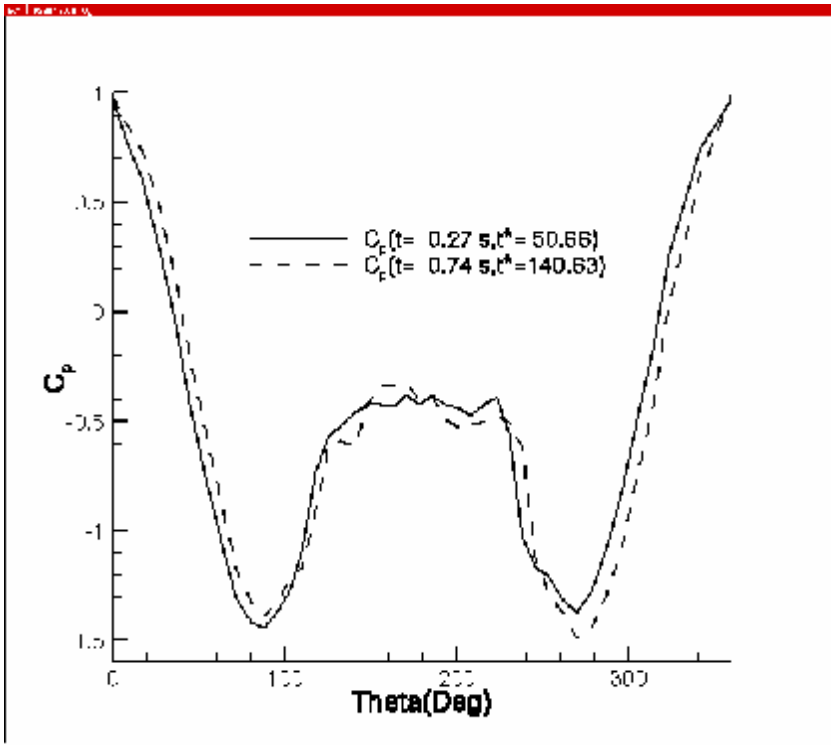

Figure 4.4: Pressure Distribution for k_c = -0.0196, x/D = 0.125 (as shown in Figure 4). Shown Are the Two Pressure Distributions Corresponding to the Pre-Motion State (Solid Line) and the Largest Deviation of C_y from the Pre-Motion State (Dashed Line).

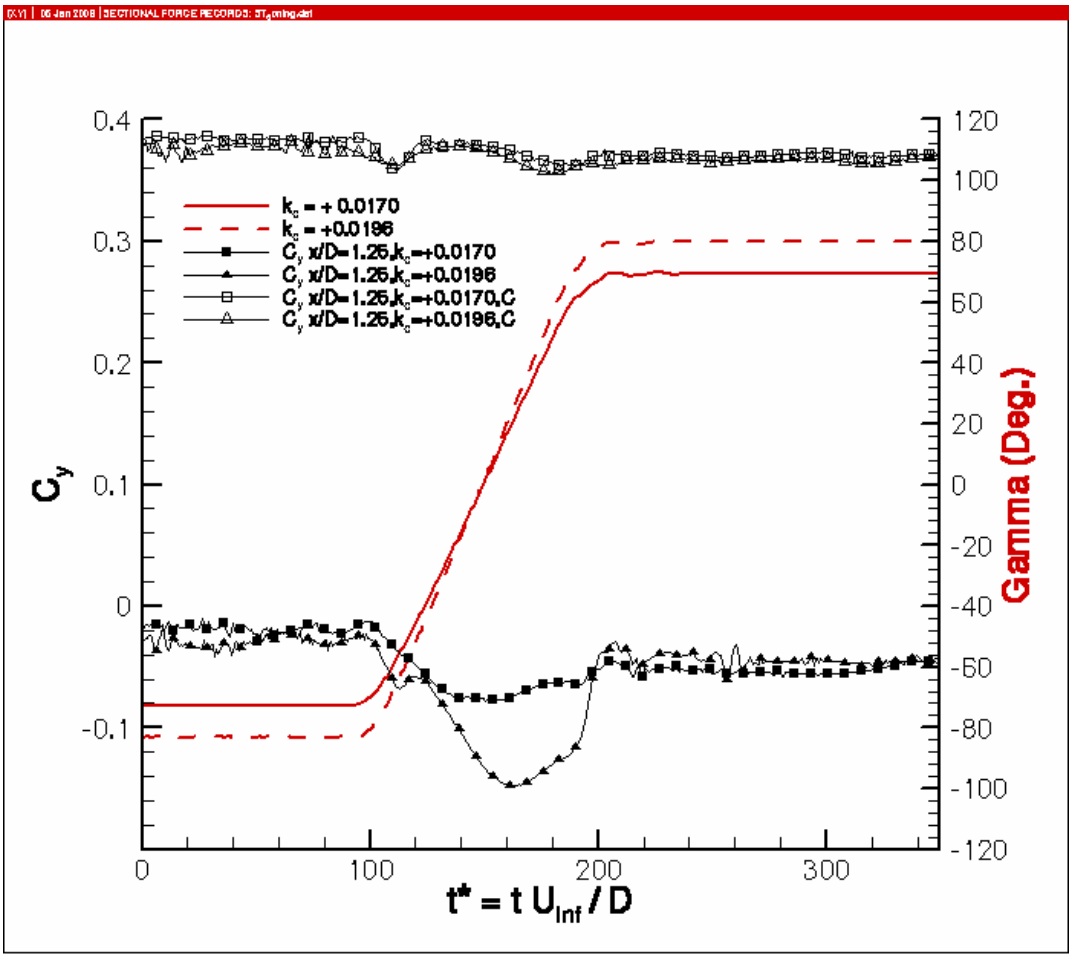

Figure 4.5: Sectional Yaw Force Time Series for Two Different PositiveConing Rates at x/D = 1.25. Note that "C" Represents Cases with Microblowing Control, which is Seen to be Effective at Maintaining the Pre-Motion C_y, Compared to the No-Blowing Case.

In figure 4.5, we see a comparison of the effects of microblowing and the no-blowing case for x/D = 1.25. Microblowing acts very near ogive tip, the point where the vortex asymmetry is generated. By injecting a small amount of mass flow towards the tip, microblowing succeeds in leveraging the convective instability that causes the vortex asymmetry. Here the blowing is from the port side of the tip, which results (as expected) in a yaw force in the positive direction.

Note that the microblowing maintains the pre-motion yaw force better than with no blowing. In fact, the effect of the motion on the C_y is minimal. Thus, we see that microblowing (which has been shown to cause linear response in the yaw force, Roos [1996]) also has the control authority to maintain the commanded yaw force during maneuvering. In figure 4.6, we see a similar effect of microblowing on axial stations at x/D = 2.00 and 2.75. Note that the motion of the body causes greater displacement of the

C_y from the pre-motion state. This was seen previously by the authors in lower-speed coning-maneuver tests in a separate facility. The sectional side force reacts proportionally with respect to distance from the ogive tip. This is expected when considering the fact that the asymmetry results from a convective asymmetry at the ogive tip.

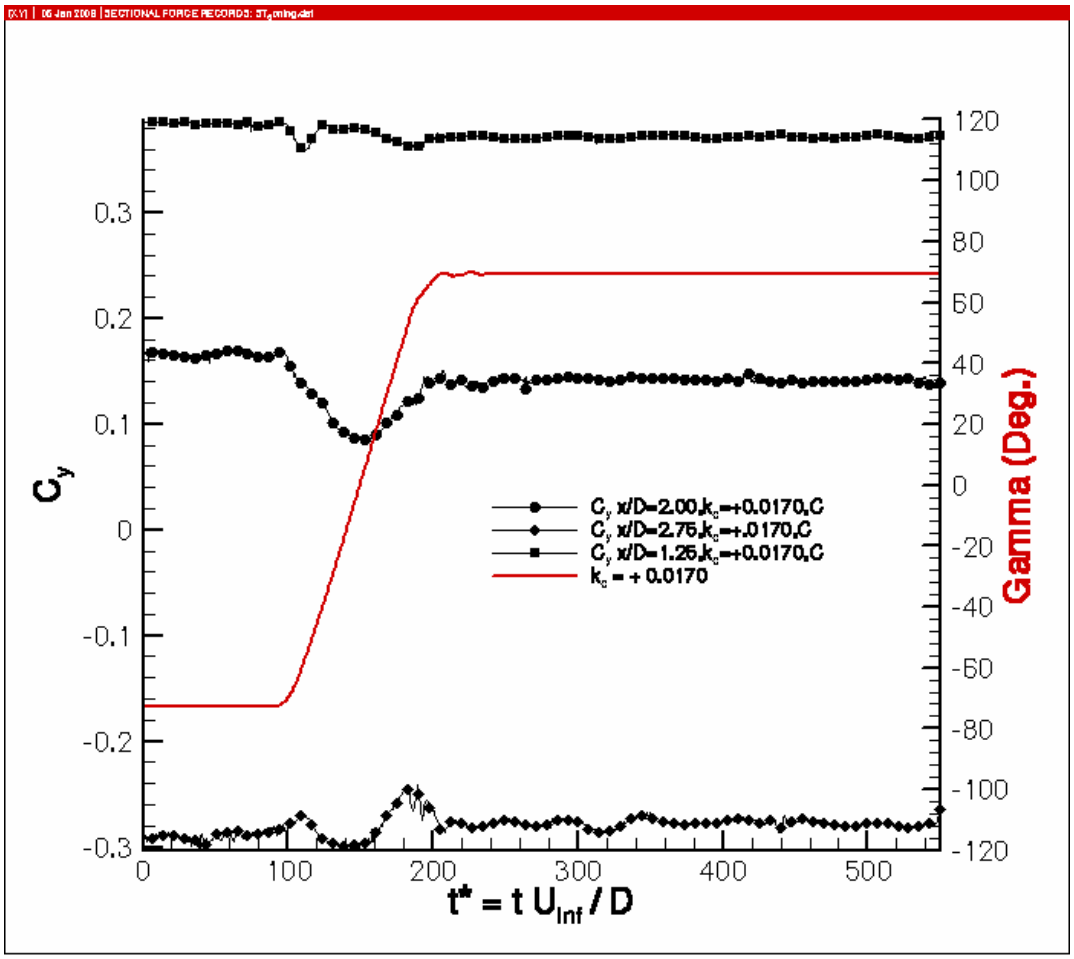

Figure 4.6: Sectional Yaw Force Time Series for k_c = 0.0170 at x/D = 1.25, 2.00 and 2.75. Note that "C" Represents Cases with Microblowing Control, which is Seen to be Effective at Maintaining the Pre-Motion C_y Down the Entire Nose of the Model

Chapter 5 - Flow Characteristics During Pitching Maneuvers

5.1 Introduction

Due to the need to understand and control the flow over missiles and aircraft during high-angle-of-attack maneuvers, where conventional control methods do not suffice, it is important to investigate the flow characteristics exhibited by axisymmetric bodies during dynamic motion. It is worth noting that only a handful of investigations provide data for a maneuvering axisymmetric body. To our knowledge, there are no velocity data for asymmetric flow over a slender forebody in a dynamic state. Experimentally-obtained unsteady pressure and velocity data are critical to understanding the fluid dynamics of the unsteady motion, which in turn is practically necessary in order to properly design controllers to utilize the asymmetry to advantage or to destroy the asymmetry, returning the flow to a symmetric state. Many of the vortex control methods that to this point have been successful with a stationary model could be improved with knowledge of the developing flow structures associated with a maneuvering forebody.

One specific interest is the delay in the return of the vortex-dominated flow to an equilibrium state following the maneuver, and the dependence of this delay on different parameters such as pitch-axis location and reduced frequency of the maneuver. Montividas, et al.[1989] used flow visualization to determine the effects of Reynolds number, pitch-axis location and pitch rates on the flowfield over a pitching cone-cylinder. Various regimes of flow were mapped, and characteristics of the regimes were discussed, qualifying the transience of the flowfield as a function of pitch axis location. In addition, a non-dimensional pitch-rate parameter $k_p = \dot{\alpha}\, L / U_\infty$ was defined, where $\dot{\alpha}$ is the angular rate, L is the distance from the pitch axis to the tip of the forebody, and U_∞ is the freestream velocity. Although this parameter collapsed the various regime maps at different Reynolds numbers, it has a shortcoming in that its value is zero when the pitch axis is at the nose ($x_p = 0$), regardless of the actual dimensional pitch rate.

This chapter presents the results of an investigation seeking to quantify pressures and velocities about a 3.5-caliber tangent-ogive cylinder performing ramp pitching motions. This experimental water-tunnel investigation utilizing LDV techniques yields three-dimensional velocity and vorticity fields over

the pitching body with laminar separation. The unsteady data are obtained at three axial stations for two different pitch-axis locations, giving a better indication of the pitch-axis effects on the development of the flowfield. The unsteady data are analyzed to determine the inherent delays in the arrival of the convective asymmetry and in the progression to the steady state. The topology of the unsteady flow is presented and analyzed. It is determined that the velocity, vorticity and topology all contain important qualitative and quantitative information that can be used to characterize the pitching slender forebody.

5.2 Forebody Pitching Maneuvers with Laminar Separation

Lamont [1982] showed that crossflow over a 3.5-caliber tangent-ogive body begins transitional separation for Re_D between $2.0 \cdot 10^5$ and $3.0 \cdot 10^5$, depending on the angle of attack and axial station. For the data presented in this section, the Reynolds numbers are low enough (Re_D near $7 \cdot 10^3$) so that even with added crossflow velocity due to the pitching motion, the boundary layer is in a laminar state at separation. There is no direct evidence of this claim for the water-tunnel investigations. However, the pressure distributions from tests in the ESM Wind Tunnel (Re_D near $3.5 \cdot 10^4$), bear out this fact. Figure 5.2.1(a) shows the pressure distribution from tests in the ESM Wind Tunnel at x/D = 2.8125 at $\alpha = 55°$. The separation pattern shows good comparison with the laminar separation patterns presented by Lamont [1980] (with independent boundary-layer state verification by Poll [1982]), shown here as figure 5.2.1(b). Note that separation occurs at or before $\theta = 90°$ and the asymmetric pressure levels on the leeside of the body after flow separation. The low-speed water-tunnel tests discussed in this chapter would show the same separation characteristics as those in the wind tunnel, given the lower test Reynolds numbers. The model, instrumentation and experimental setups for this investigation are discussed in Chapter 2.

5.2.1 Unsteady Effects During Model Motion

The evolution of the flow over a slender forebody pitching from low to high angles of attack can be divided into two time domains. Here, we assume that the initial angle of attack is such that no asymmetric vortex exists, and that the model undergoes a forced ramp pitching motion, which is the case for all pitching investigations performed in this work. During the early stages of flow development at low angles of attack, the vortices will develop symmetrically. Because the convective asymmetry emanating from the forebody tip must have time to develop and convect downstream over the body, local effects will determine the nature of the flow. Therefore, vortex size and strength will be largely due to the increased crossflow velocity (or decreased crossflow velocity, for axial stations ahead of the pitch axis) caused by

the pitch-up motion. Keeping in mind that, for the model fineness ratio and nose bluntness used in these investigations, the steady flow does not show asymmetric vortex patterns until the angle of attack is at least 34°, we wish to see how long this first domain can persist to high angles of attack, especially for points far from the forebody tip. Since the flow development has yet to be exposed to the overriding influence of the convective instability, it could be likened to the development over an infinite inclined cylinder with changing incidence. Any flow asymmetry present in this time domain must be connected

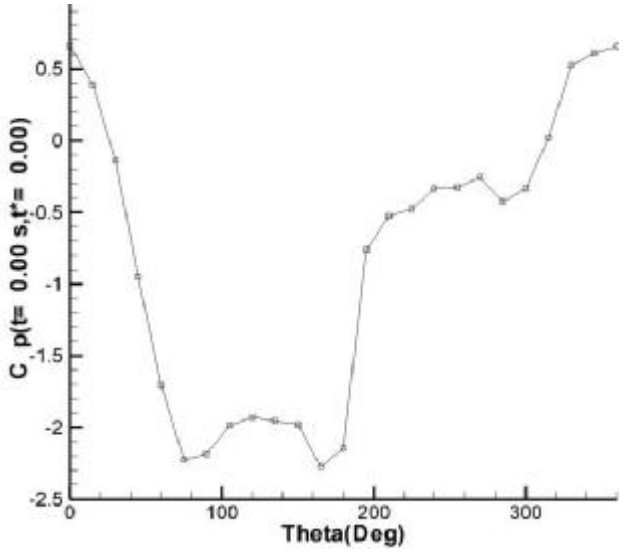

Figure 5.2.1(a): Circumferential Pressure Data to Ascertain Boundary Layer State at Separation: Pressure Data Acquired at x/D = 2.813, α = 55°, L_N/D = 3.5 in the ESM Wind Tunnel, Re = 3.5•10^4.

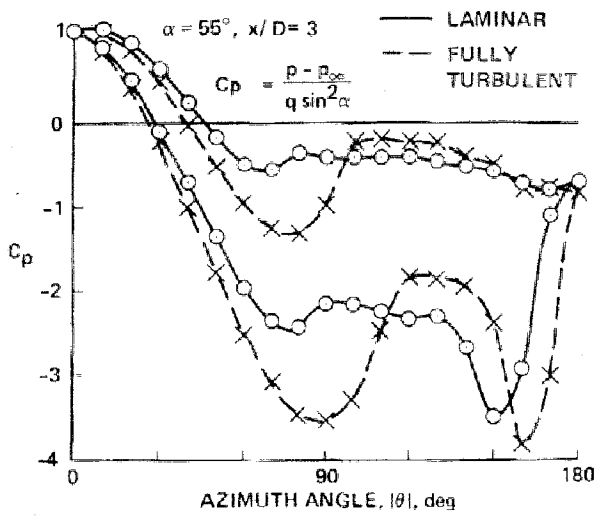

Figure 5.2.1(b): Circumferential Pressure Data Acquired at x/D = 3.0, α = 55°, L_N/D = 2.0 in the NASA Ames 12-ft Pressure Tunnel.

with the global (temporal) asymmetry that causes asymmetric vortex shedding for two-dimensional cylinders in crossflow.

The second time domain exists after the convective asymmetry reaches the axial location of interest. At this time, the flow is quickly moved toward an asymmetric flow pattern, with subsequent flow development to the steady state. During this period, it is possible, especially at axial locations sufficiently far from the forebody tip, to observe flow asymmetries in both directions (i.e. the asymmetry is first disposed to one side, and then reverses to the other). This can be explained as follows: When the body has reached a sufficiently large angle of attack to induce asymmetric flow at the tip, the asymmetry begins to convect down the body. However, the angle of attack may still be increasing (or decreasing, in the case of a pitch-down motion). The extent of the first half-cycle of the sinusoidal-type sectional yaw force (the sign of which directly corresponds to vortex asymmetry, as shown by Wardlaw & Yanta [1984]) is dependent on incidence angle. If the angle of attack is changing, and the direction of vortex asymmetry at a particular axial location can vary with angle of attack, so we see that it is possible for the crossflow to switch signs as it passes through one asymmetric flow state on the way to a different (steady-state) asymmetric flow state. So, while the model is maneuvering, the flow at any axial location may be affected by the combination of the convective asymmetry and the model motion.

5.2.2 Unsteady Three-Dimensional Velocity Fields

In the ESM water tunnel, a 3.5 caliber tangent-ogive cylinder is pitched to a high angle of attack for two different pitch axes, one at $x_p/D = 0$ (at the forebody tip) and another at $x_p/D = 4$. The reduced frequency of the maneuver is $k_p = 0.096$, and the Reynolds number is $Re_D = 7.144 \cdot 10^3$. Three planes of three-dimensional velocity data are acquired for each pitch axis, at x/D = 3, 4, and 5. The details of data acquisition and reduction are discussed in Chapter 2. All velocities have been nondimensionalized by U_∞ and all distances by D. The components of velocity have been aligned to the plane of measurement, so that u is perpendicular to the measurement plane and v and w are in the measurement plane. The locations of the measurement planes and pitch axes, coordinate frames and extent of model motion are shown in figure 5.2.2. The model is held stationary at $\alpha = 18.74°$ for 0.08 s, and then the model is pitched to 54.74°, as shown in figure 5.2.3. The model is held at the final angle until data acquisition is finished, then it is returned to the starting location. In order to make the discussion of the flowfields easier, it was decided to assign an order to the vortical structures that appear in the measurement plane. This designation is shown in figure 5.2.4, where a symmetric and asymmetric vortex pattern are shown for clarity.

The unsteady nature of this problem makes it a bit more difficult to nondimensionalize time. Typically, time is nondimensionalized by a combination of the characteristic length and velocity. However, using $t^* = t \cdot U_\infty / D$ would be equivalent to placing the body in crossflow (i.e. $\alpha = 90°$). Instead, we decided to define the dimensionless time in terms of an averaging integral:

$$t^* = \int \frac{U_\infty}{D}(\cos\alpha)dt \tag{5.1}$$

Since U_∞ and D are constant over time, they can be taken outside the integral. The nondimensional time for the motion used here is shown as a function of time in figure 5.2.5.

The velocity field for $x_p = 0$ is shown in figures 5.2.6 – 5.2.22. The axial velocity field is depicted using color contours, while the in-plane components are combined into a vector field that is overlaid on the axial field. Since the freestream makes an angle of 36.74° with the measurement plane, the value of u far from the body is $U_\infty \cos(36.74°) = 0.801$. Values of u between 0.70 and 0.90 are graphed in white, showing areas where the u value does not differ much from its value when no model is present. All velocity values within the cylinder are set to zero. Measurements for all three measurement locations are presented together to allow easy comparison and analysis of axial flow development.

The flowfield at x/D = 3 and $x_p/D = 0$ gives evidence of unsteady flow development around an impulsively-started body, as discussed in Telionis [1970]. As the model begins to move, the flow is potential, and vortex development is minimal. As expected, vortex development is most apparent at x/D = 5, as may be seen in figures 5.2.7 – 5.2.12. During this sequence, the vortices are observed to be symmetric. Each axial station exhibits a growing vertical region of flow directly behind the cylinder which is characterized by a high u-component (up to $1.2 \cdot U_\infty$ in figure 5.2.9), as the flow attempts to follow the body in its motion. However, by t = 0.680 s, the symmetric vortices in all three planes are located directly above the model as depicted in figure 5.2.11, where regions of very high axial velocity may now be found to coincide with the vortex cores. These vortices are strong, well-defined structures that are similar to those occurring over delta wings, except that the axial velocity is not as high. As the model decelerates slightly at then end of its motion, the mutual interaction of the vortices brings them down into close contact with the body. As the flow progresses to the point where the motion stops (figure 5.2.13), we observe that the vortices at x/D = 3 and x/D = 4 retain the high core velocity. However, this in not the case with the vortices at x/D = 5, which actually exist near regions of velocity deficit ($u < 0.7$).

Figure 5.2.14 shows the beginning of the dramatic shift to asymmetric flow. Both the in-plane and axial velocities are seen to be asymmetric at x/D = 3. It may be difficult to notice the in-plane asymmetry, but this is easier to discern if one looks at the vertical cant of the vectors in the lowest row of measurement. The vortices at x/D = 4 appear to be maintaining their in-plane symmetry, but the symmetry in the axial component has been broken, with the first vortex now showing higher u in its core than the second. The asymmetry in the axial component of velocity also occurs at x/D = 5, and there is also asymmetry near the primary saddle point. The in-plane asymmetry at x/D = 5 is in the same direction as that occurring at x/D = 3 at the same instant, but this asymmetry is not apparent at x/D = 4. Figure 5.2.14 also shows that large regions of axial velocity deficit have infiltrated the region directly over the body, separating the two vortices. This could be construed to be similar to the chordwise velocity deficit that appears over airfoils after undergoing a pitch-up motion.

The convective asymmetry has arrived at x/D = 4 by t = 1.00 s, as shown in figure 5.2.15. There are three items of great interest at this time: First, it is apparent that nearer the forebody tip, at x/D = 3 and x/D = 4, the second vortex is moving to a position almost directly over the body. As it does so, it retains the high axial velocity near the geometric center of the vortex as defined by the in-plane components. In contrast, the axial velocity associated with the first vortex moves to the outside part of the in-plane vortex. At x/D = 3, this will remain the case, even in the steady state.

Second, the axial velocity is definitely asymmetric for x/D = 5, although the in-plane components are symmetric. However, the size of the symmetric vortices relative to that of the body cross-section makes it easy to see why the flow cannot remain stable in this arrangement. The second vortex has lost completely its higher core velocity and is beginning to show signs of breaking down, much like delta-wing vortices at high incidence. An explanation for the axial asymmetry leading the in-plane asymmetry could be that since the asymmetry is convective, moving with the local velocity, it would seem likely that the core of the vortex, with its high local velocity, would first experience asymmetry.

Third, Wardlaw & Yanta [1982] noted that as the angle of attack is increased through α_A, the asymmetry would make itself apparent first at the primary leeward saddle. Figure 5.2.15 shows that his may not occur when the increase in incidence angle is done in an unsteady manner. By comparing to figure 5.2.14 for x/D = 4, it is obvious that the first movement of the vortex pair is to the left, not upwards, allowing the position and geometry of the primary saddle to remain largely unchanged. It may be that in this case the first asymmetry may be seen in the asymmetric locations of the foci representing

the formerly symmetric vortices. This will be seen more clearly in section 5.2.4, where flow topology is discussed.

Figures 5.2.16 – 5.2.19 show the progression of the three planes towards the steady state. At x/D = 4 and x/D = 5, the second vortex continues to break down and exhibits an extremely large region of axial velocity deficit by t = 1.760 (figure 5.2.20). By this time, the third vortex has formed, moving in underneath the broken-down second vortex. The third vortex has a high core velocity, up to $1.3 \cdot U_\infty$. Keep in mind that the flow patterns in these planes represent a standing mean asymmetric pattern, quite unlike the well-known von Karman vortex street. Figure 5.2.21 depicts the steady-state flowfield for $x_p/D = 0$.

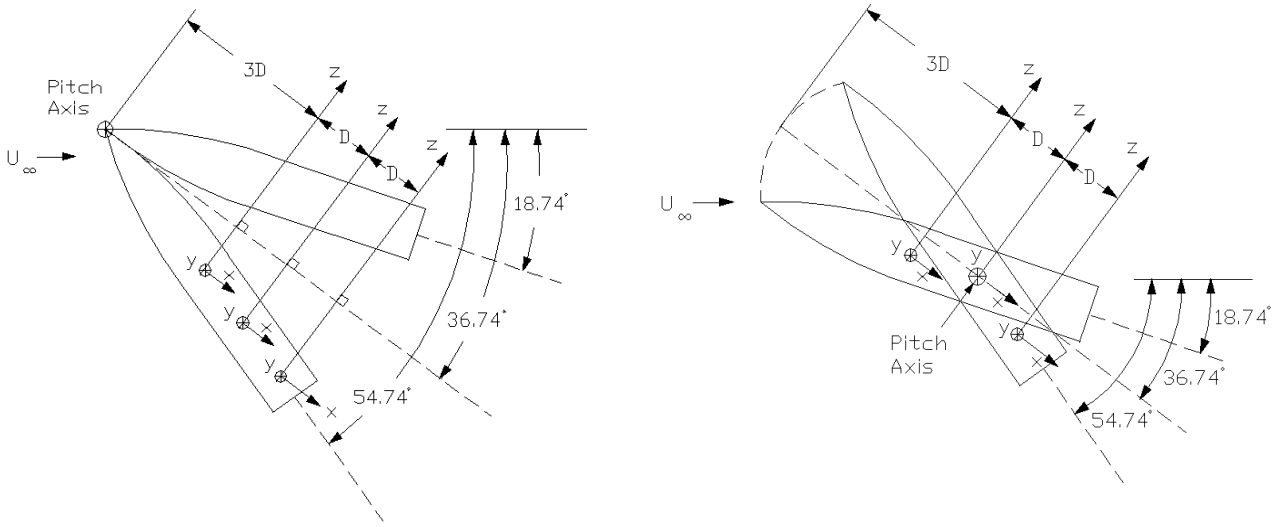

Figure 5.2.2 Coordinate Systems and LDV Measurement Plane Orientations for ESM Water Tunnel Tests: (a) $x_p/D = 0$; (b) $x_p/D = 4$.

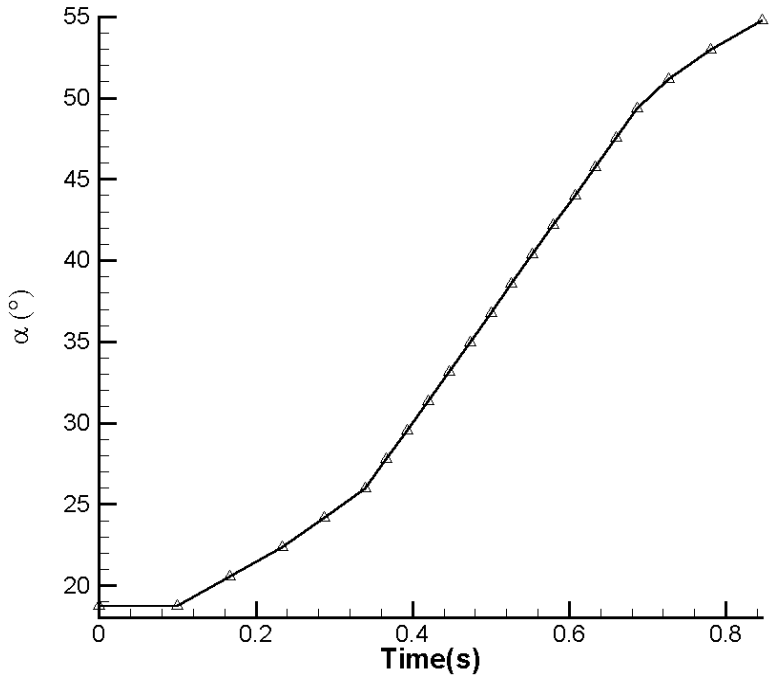

Figure 5.2.3 Ramp Pitching Motion Executed During LDV Data Acquisition. The Model is Held at 54.74° Until the End of Data Acquisition, then Returned to 18.74°, the Starting Angle of Attack.

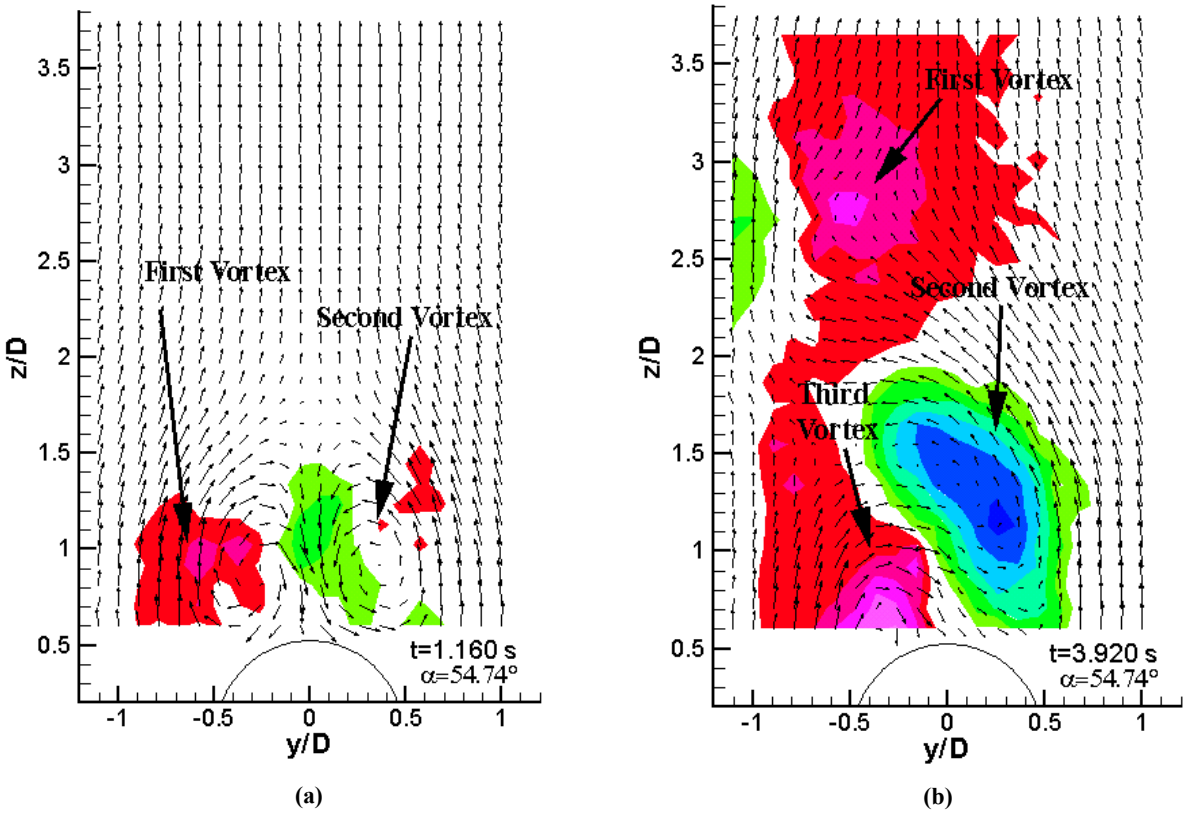

(a) **(b)**

Figure 5.2.4 Designation of Primary Vortical Structures: (a) Nearly Symmetric State with Two Vortices, (b) Asymmetric State with Three Vortices.

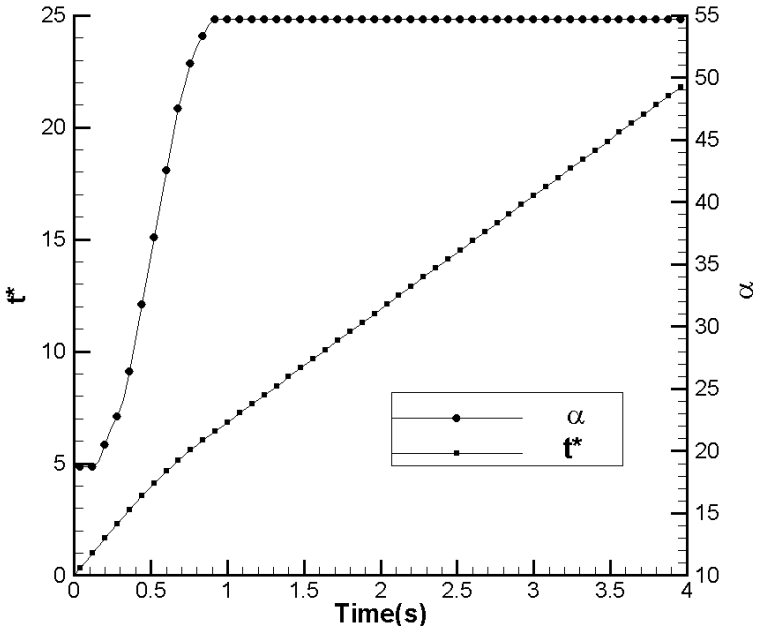

Figure 5.2.5: Dimensionless Time $t^* = \int \frac{U_\infty}{D}(\cos\alpha)dt$ **as a Function of Time. The Model Motion is Included for Comparison.**

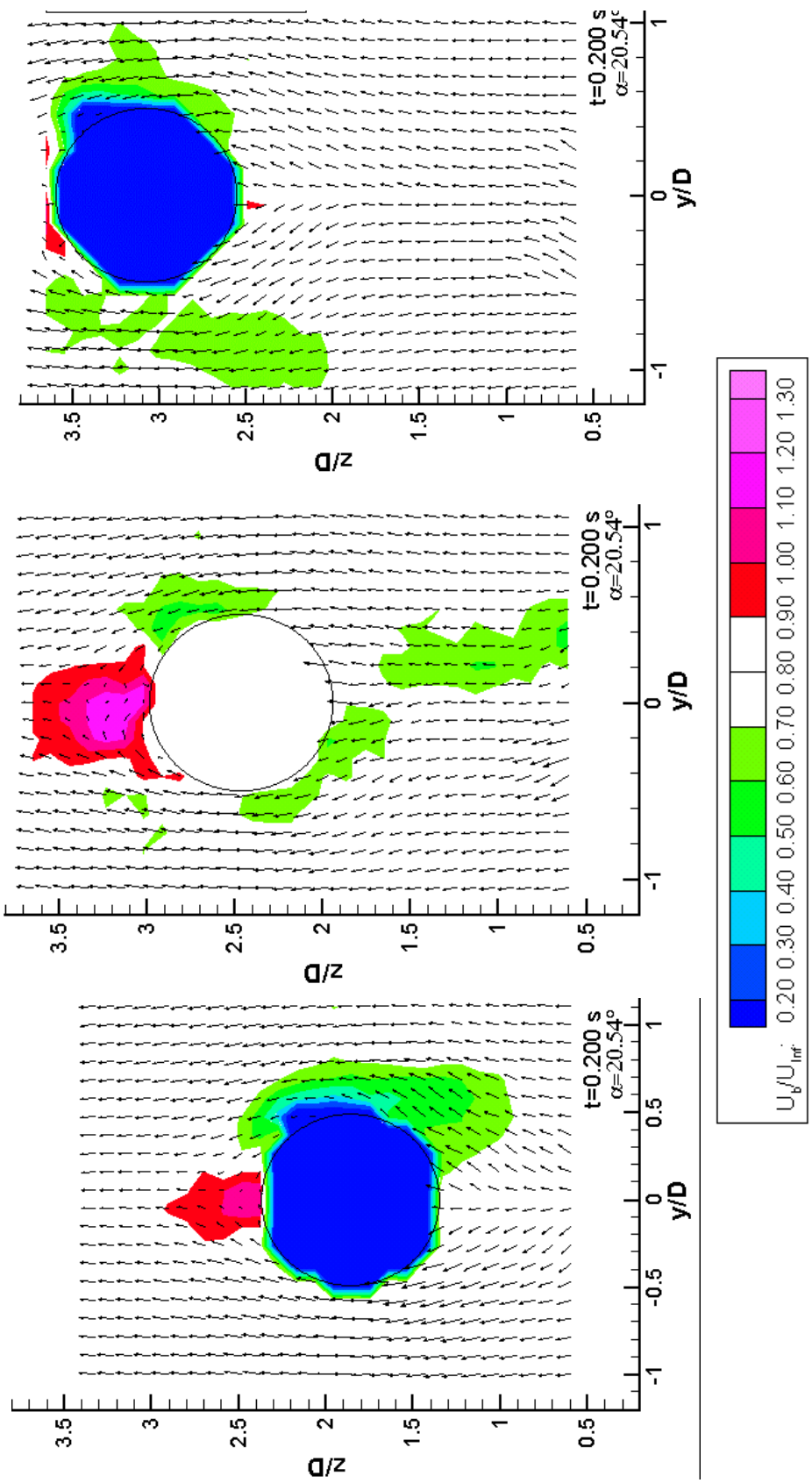

Figure 5.2.6: Three-Dimensional Velocity Fields at $t^* = 0.200$ s, $\alpha = 20.54°$, with $x_p/D = 0$: (a) x/D = 3, (b) x/D = 4, (c) x/D = 5. Contours Represent the Axial Velocity. The Coordinate System is Fixed to the Measurement Plane, which Is Rotated 16.2° from the Crossflow Plane for the Current Measurement.

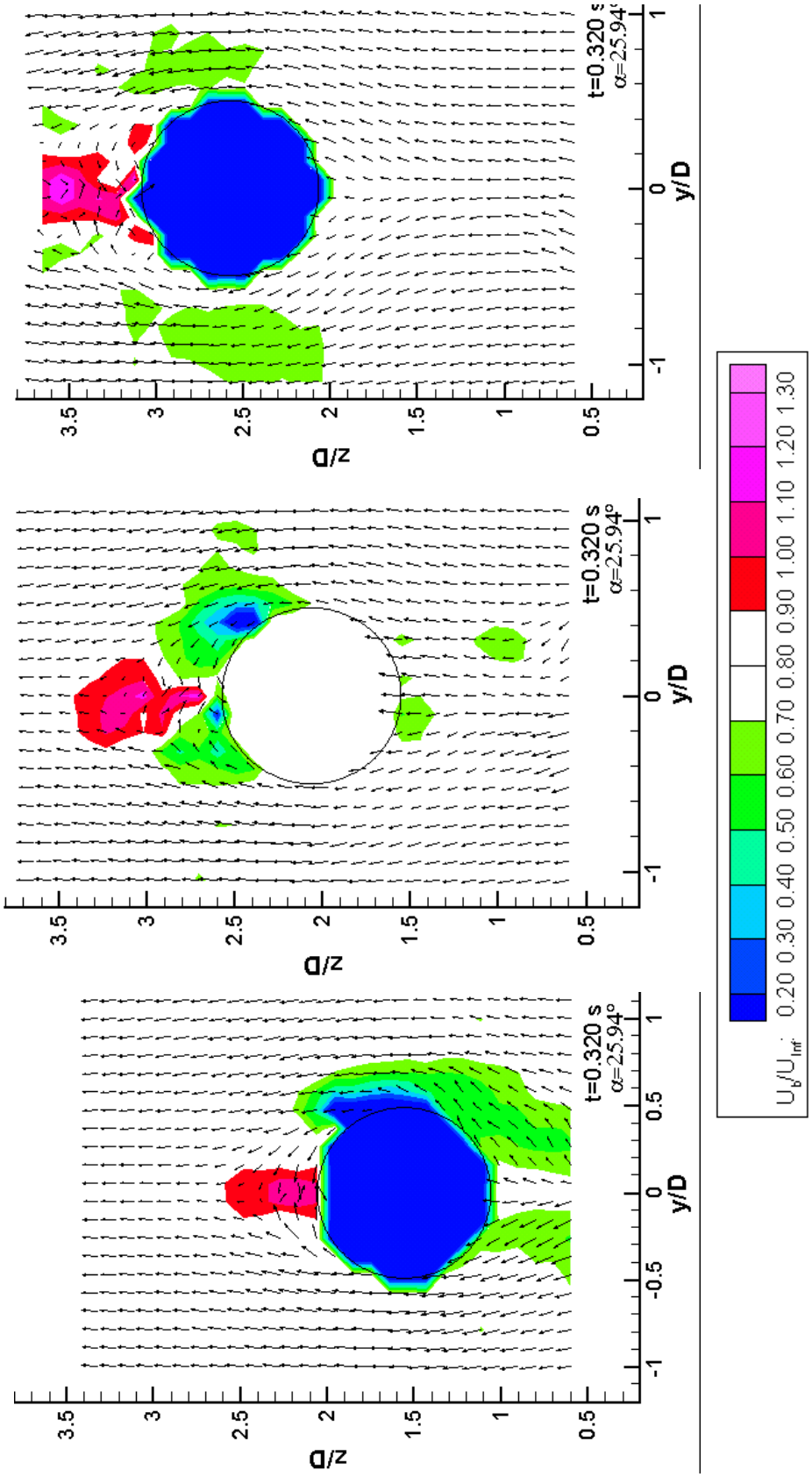

Figure 5.2.7: Three-Dimensional Velocity Fields at t* = 0.320 s, α = 25.94°, with $x_p/D = 0$: (a) x/D = 3, (b) x/D = 4, (c) x/D = 5. Contours Represent the Axial Velocity. The Coordinate System is Fixed to the Measurement Plane, which Is Rotated 10.8° from the Crossflow Plane for the Current Measurement.

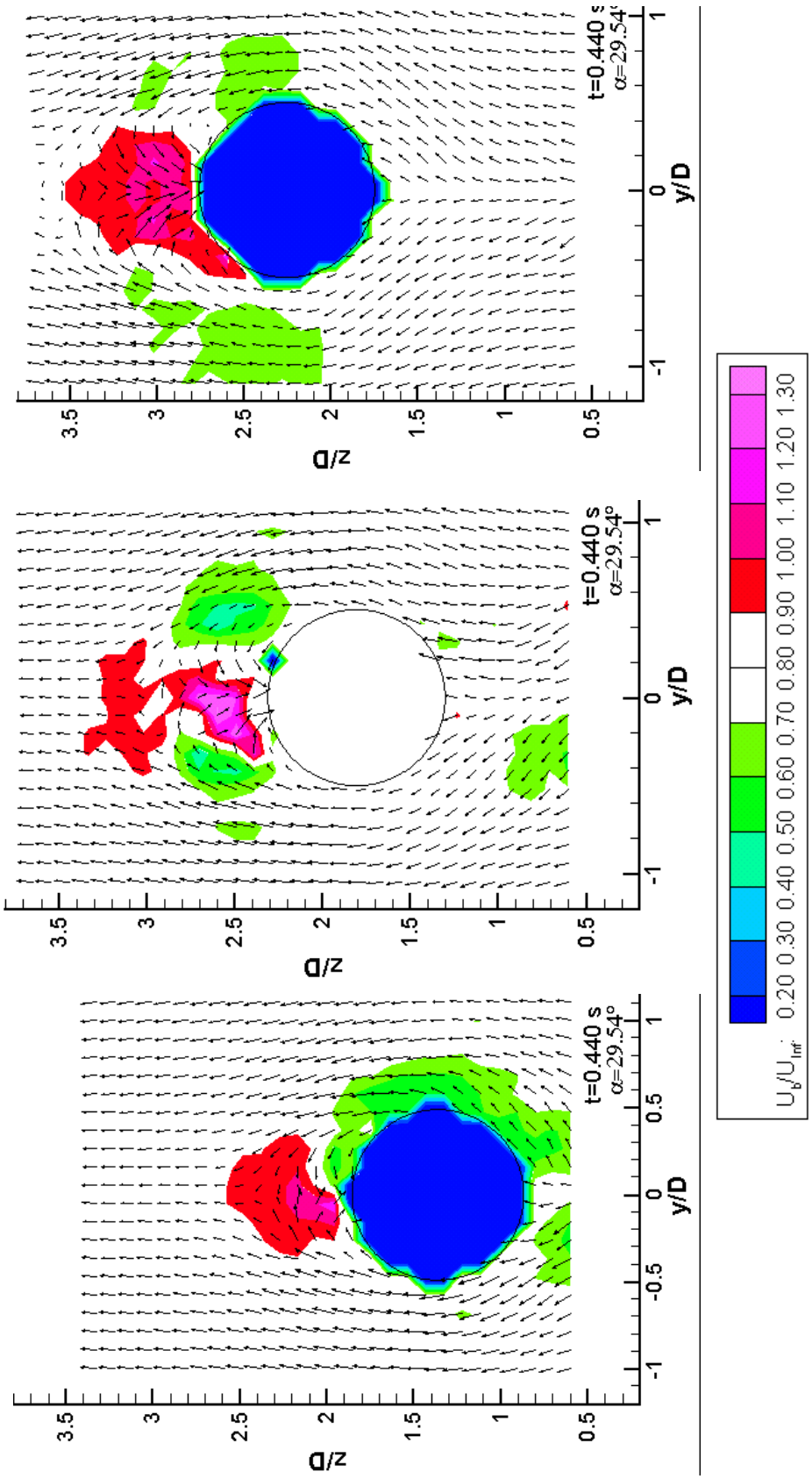

Figure 5.2.8: Three-Dimensional Velocity Fields at $t^* = 0.440$ s, $\alpha = 29.54°$, with $x_p/D = 0$: (a) x/D = 3, (b) x/D = 4, (c) x/D = 5. Contours Represent the Axial Velocity. The Coordinate System is Fixed to the Measurement Plane, which Is Rotated 7.2° from the Crossflow Plane for the Current Measurement.

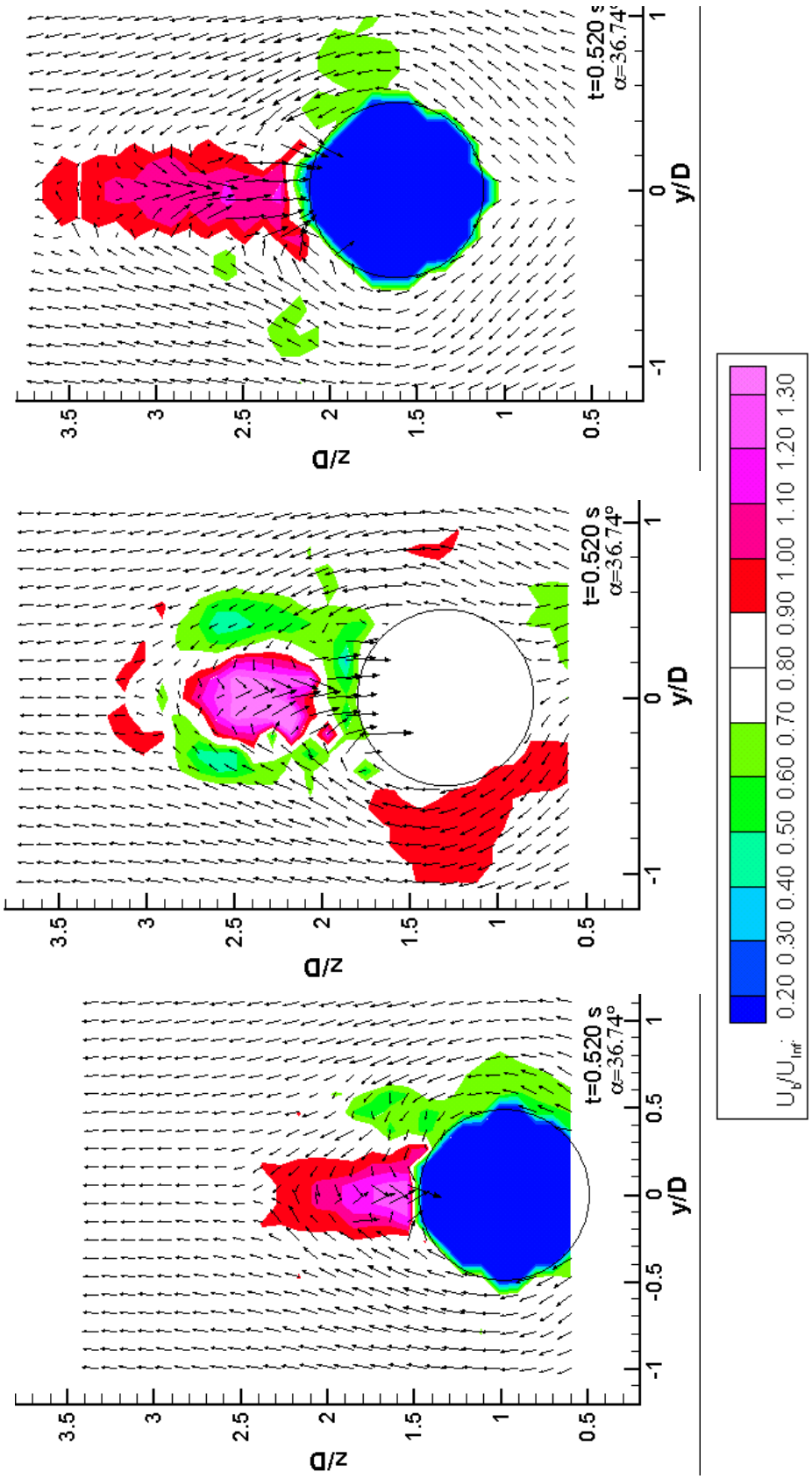

Figure 5.2.9: Three-Dimensional Velocity Fields at t* = 0.520 s, α = 36.74°, with $x_p/D = 0$: (a) x/D = 3, (b) x/D = 4, (c) x/D = 5. Contours Represent the Axial Velocity. The Coordinate System is Fixed to the Measurement Plane, which Is Rotated 0.0° from the Crossflow Plane for the Current Measurement.

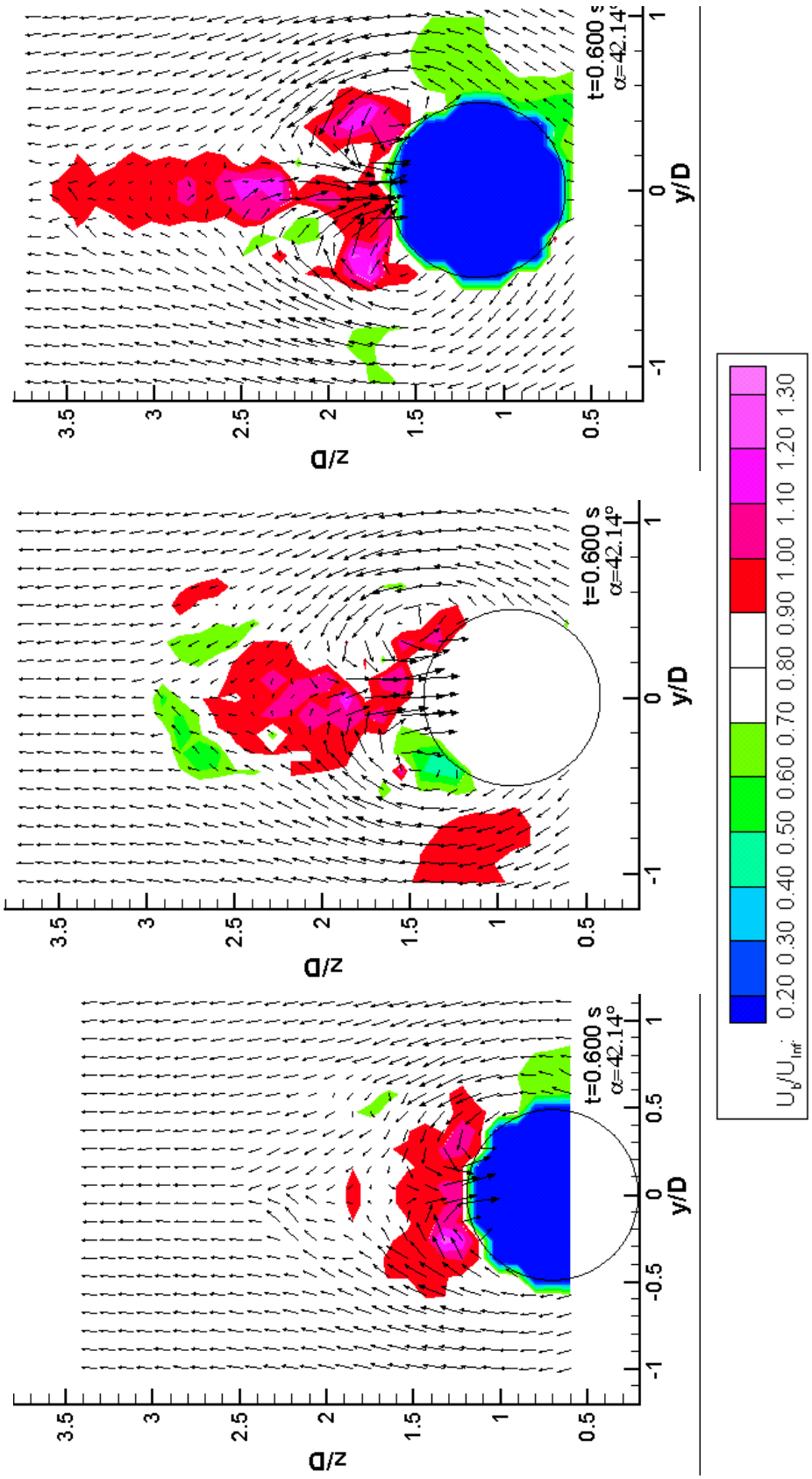

Figure 5.2.10: Three-Dimensional Velocity Fields at $t^* = 0.600$ s, $\alpha = 42.14°$, with $x_p/D = 0$: (a) x/D = 3, (b) x/D = 4, (c) x/D = 5. Contours Represent the Axial Velocity. The Coordinate System is Fixed to the Measurement Plane, which Is Rotated 5.4° from the Crossflow Plane for the Current Measurement.

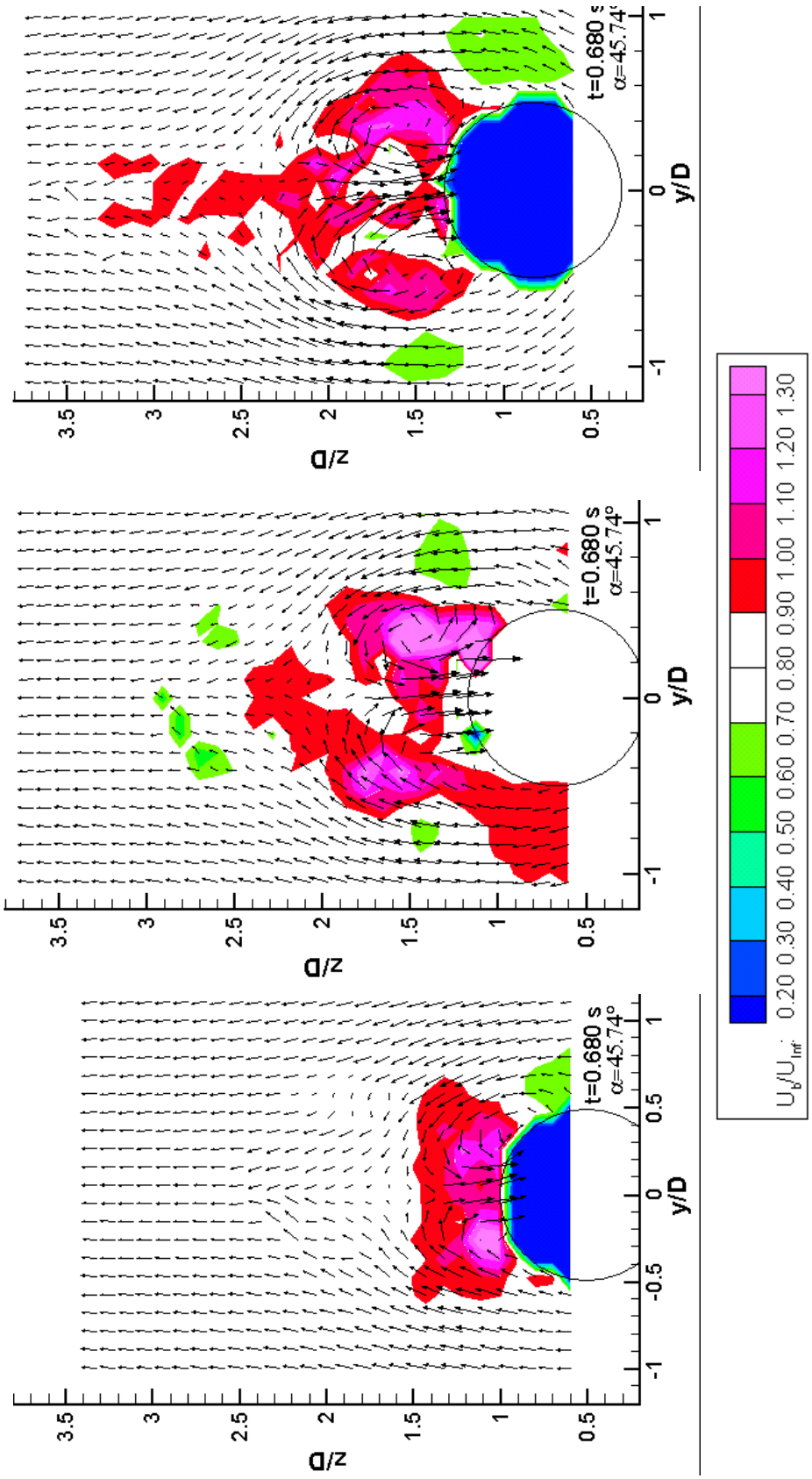

Figure 5.2.11: Three-Dimensional Velocity Fields at $t^* = 0.680$ s, $\alpha = 45.74°$, with $x_p/D = 0$: (a) x/D = 3, (b) x/D = 4, (c) x/D = 5. Contours Represent the Axial Velocity. The Coordinate System is Fixed to the Measurement Plane, which Is Rotated 9.0° from the Crossflow Plane for the Current Measurement.

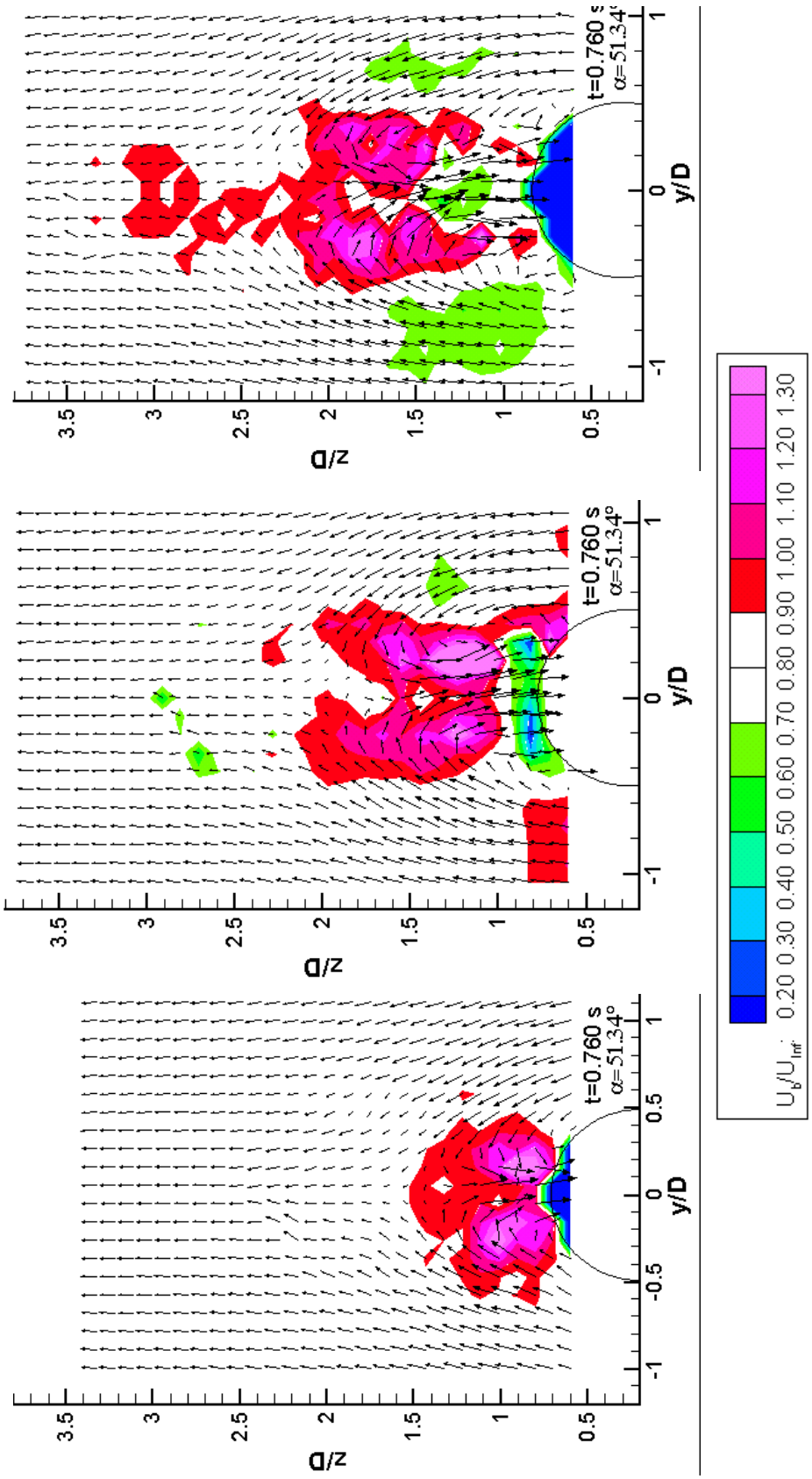

Figure 5.2.12: Three-Dimensional Velocity Fields at $t^* = 0.760$ s, $\alpha = 51.34°$, with $x_p/D = 0$: (a) x/D = 3, (b) x/D = 4, (c) x/D = 5. Contours Represent the Axial Velocity. The Coordinate System is Fixed to the Measurement Plane, which Is Rotated 14.6° from the Crossflow Plane for the Current Measurement.

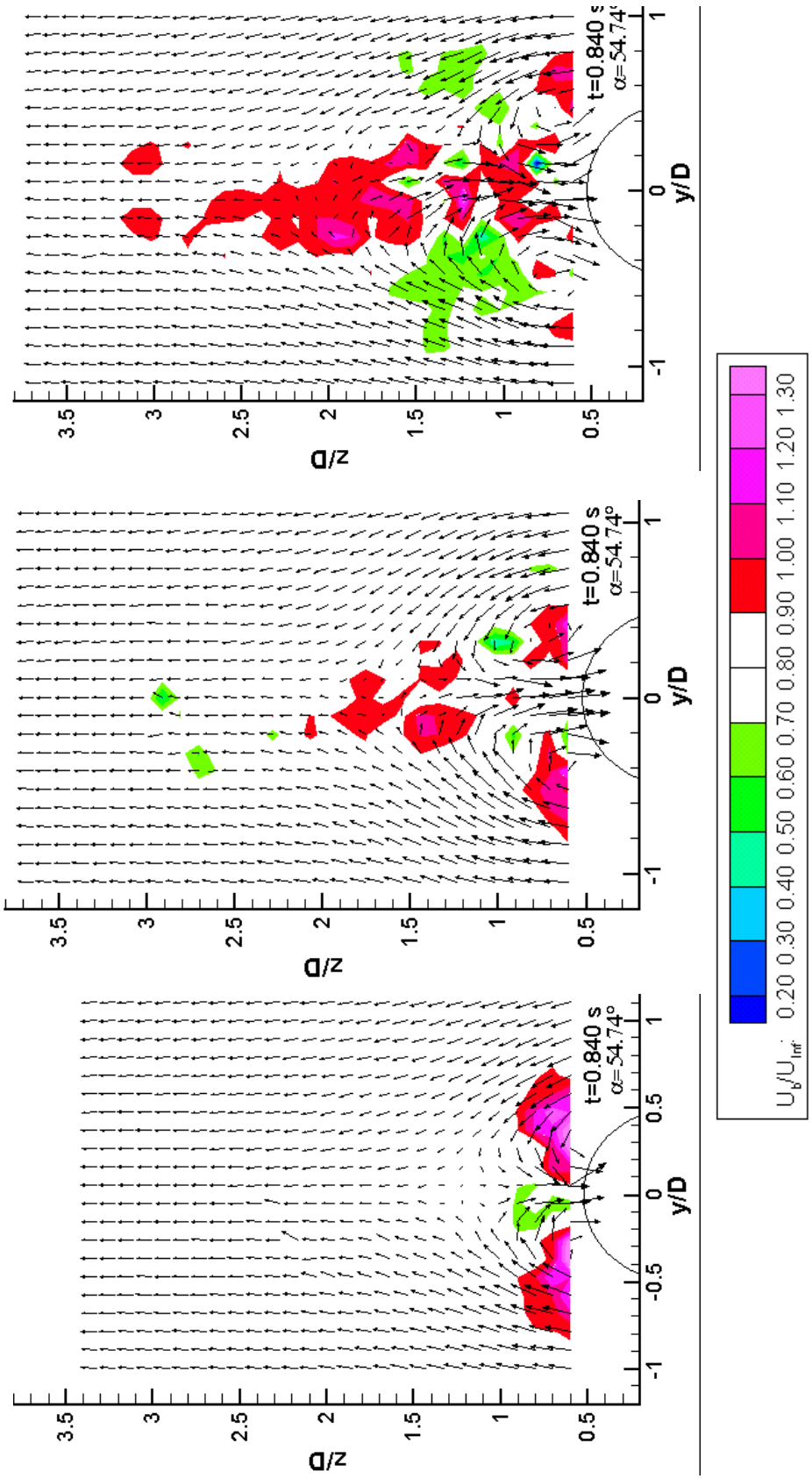

Figure 5.2.13: Three-Dimensional Velocity Fields at $t^* = 0.840$ s, $\alpha = 54.74°$, with $x_p/D = 0$: (a) x/D = 3, (b) x/D = 4, (c) x/D = 5. Contours Represent the Axial Velocity. The Coordinate System is Fixed to the Measurement Plane, which Is Rotated 18.0° from the Crossflow Plane for the Current Measurement.

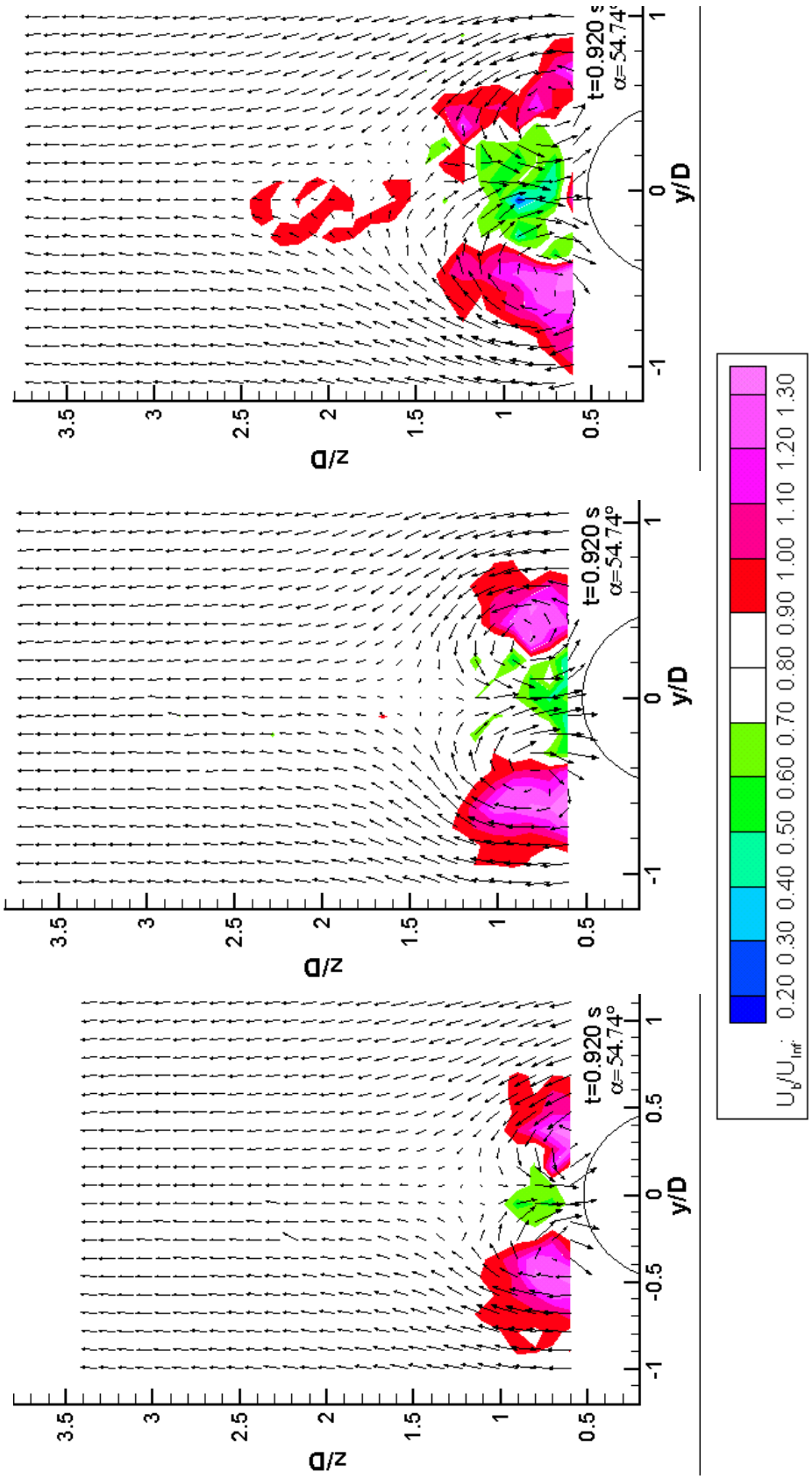

Figure 5.2.14: Three-Dimensional Velocity Fields at $t^* = 0.920$ s, $\alpha = 54.74°$, with $x_p/D = 0$: (a) x/D = 3, (b) x/D = 4, (c) x/D = 5. Contours Represent the Axial Velocity. The Coordinate System is Fixed to the Measurement Plane, which Is Rotated 18.0° from the Crossflow Plane for the Current Measurement.

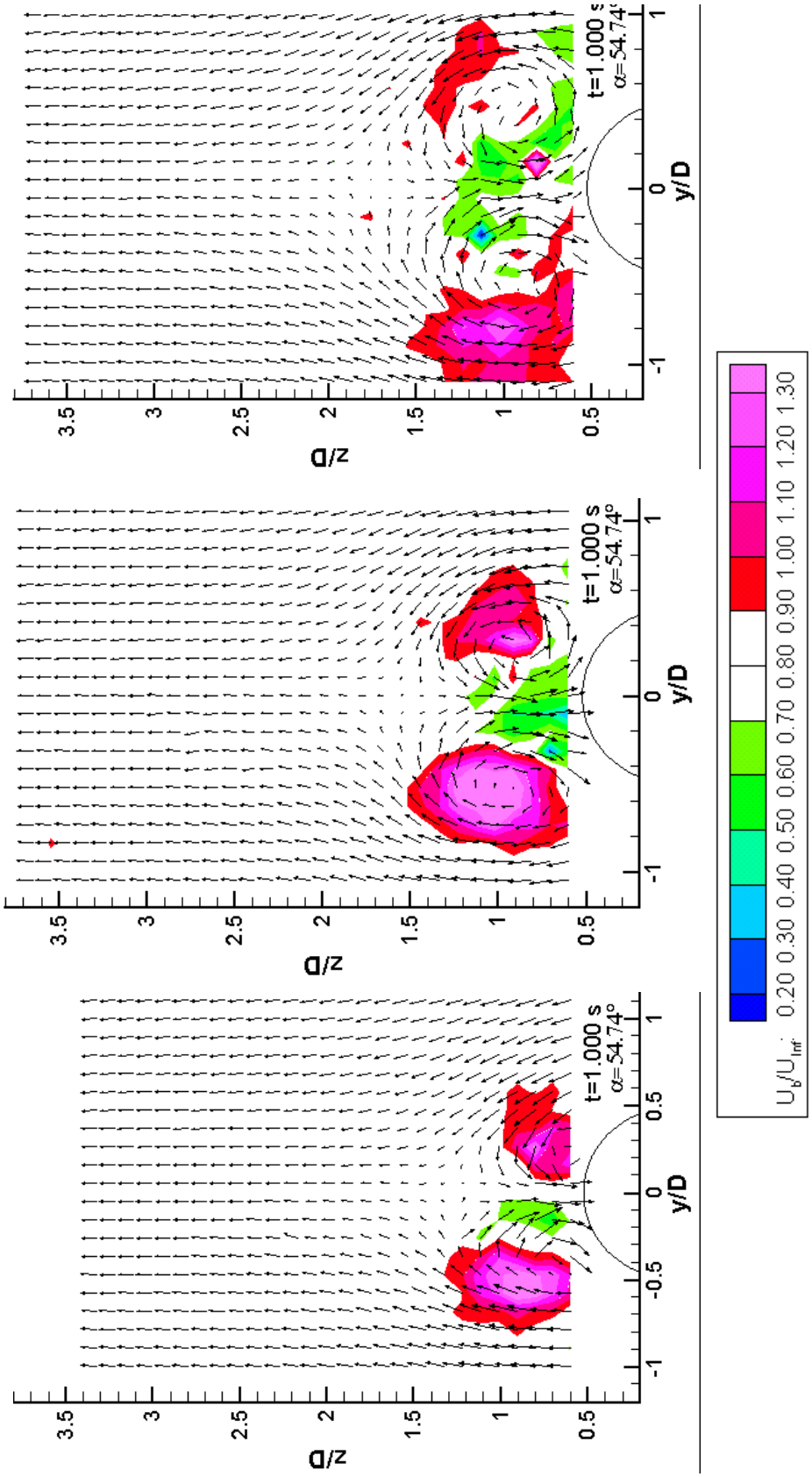

Figure 5.2.15: Three-Dimensional Velocity Fields at $t^* = 1.000$ s, $\alpha = 54.74°$, with $x_p/D = 0$: (a) x/D = 3, (b) x/D = 4, (c) x/D = 5. Contours Represent the Axial Velocity. The Coordinate System is Fixed to the Measurement Plane, which Is Rotated 18.0° from the Crossflow Plane for the Current Measurement.

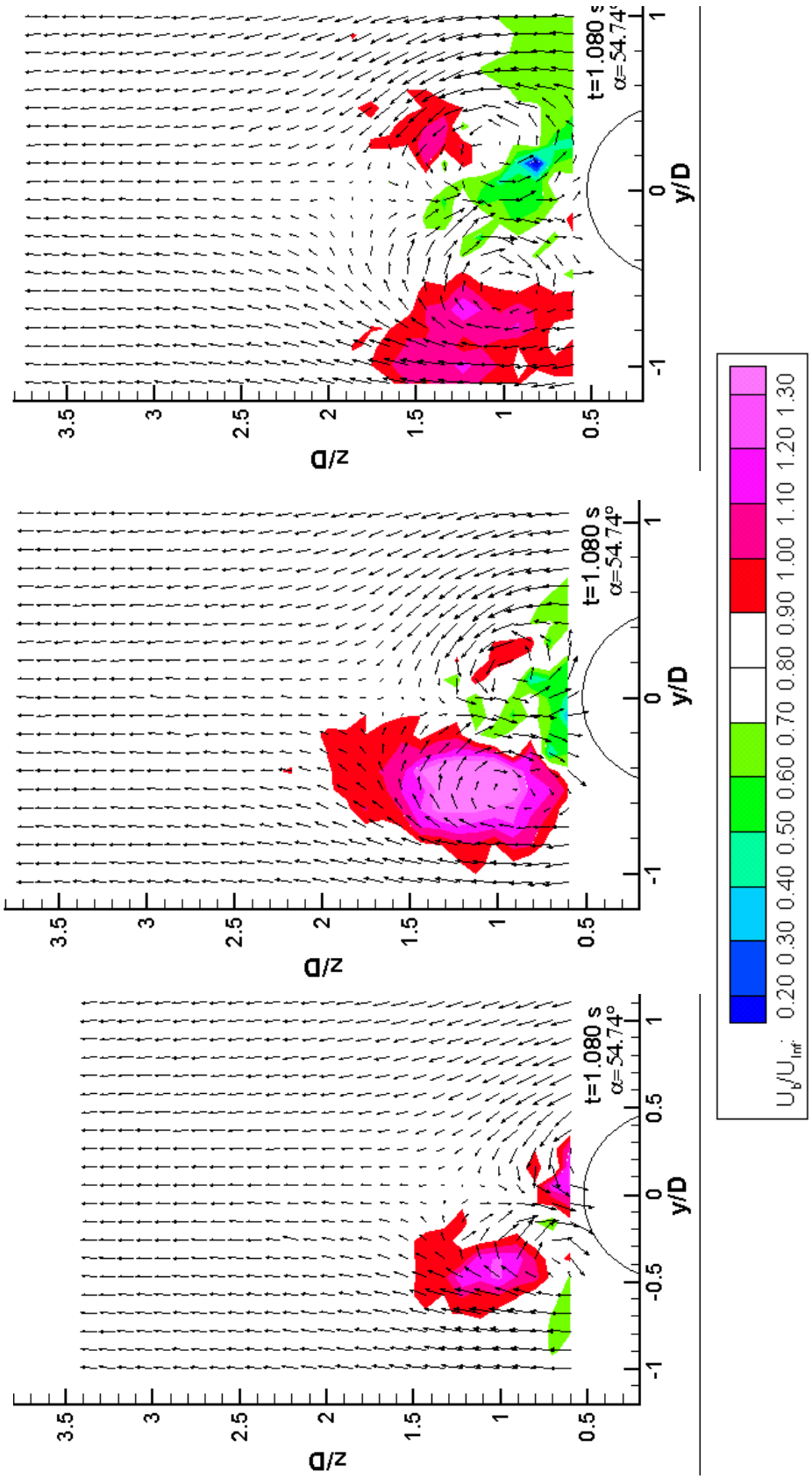

Figure 5.2.16: Three-Dimensional Velocity Fields at $t^* = 1.080$ s, $\alpha = 54.74°$, with $x_p/D = 0$: (a) x/D = 3, (b) x/D = 4, (c) x/D = 5. Contours Represent the Axial Velocity. The Coordinate System is Fixed to the Measurement Plane, which Is Rotated 18.0° from the Crossflow Plane for the Current Measurement.

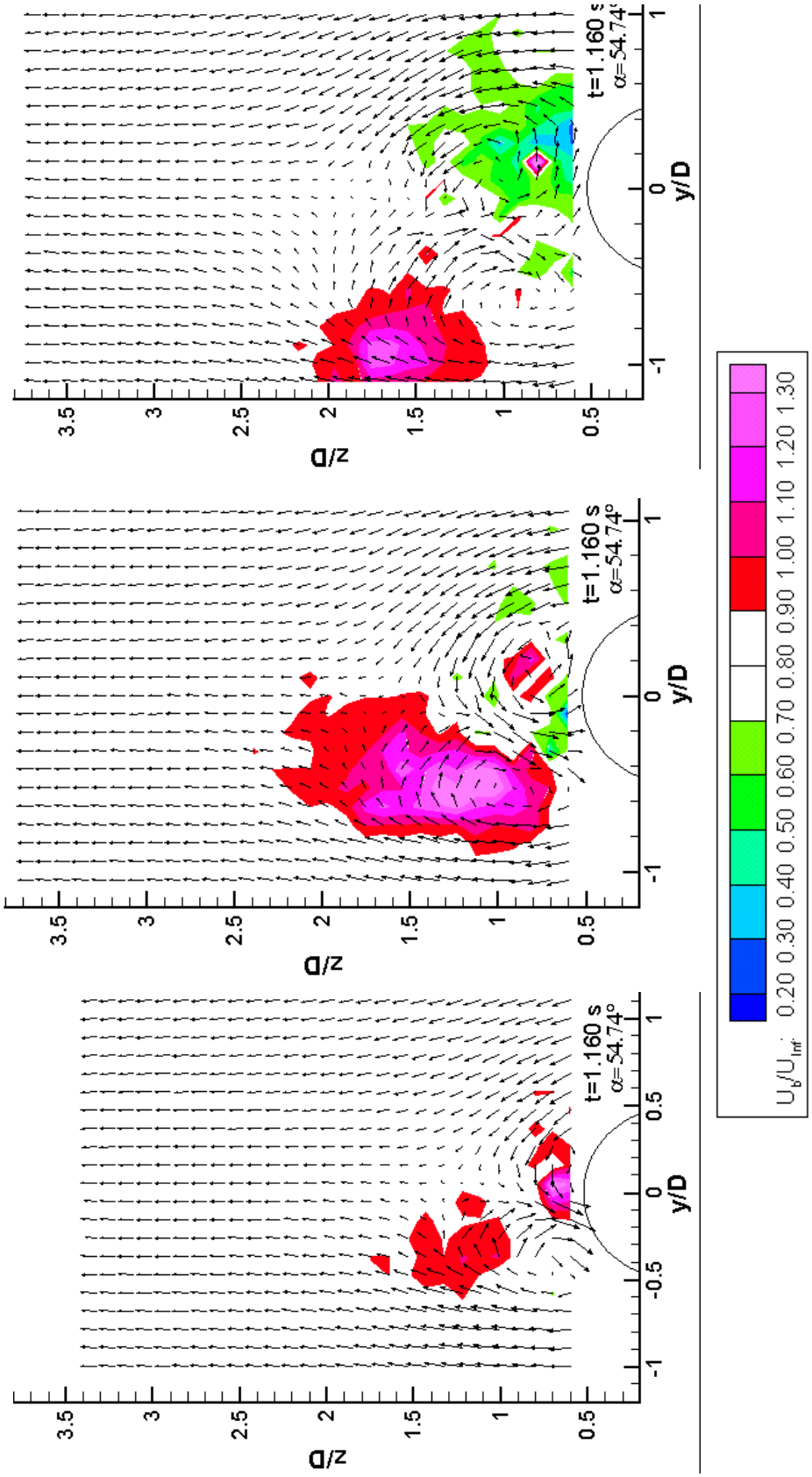

Figure 5.2.17: Three-Dimensional Velocity Fields at $t^* = 1.160$ s, $\alpha = 54.74°$, with $x_p/D = 0$: (a) x/D = 3, (b) x/D = 4, (c) x/D = 5. Contours Represent the Axial Velocity. The Coordinate System is Fixed to the Measurement Plane, which Is Rotated 18.0° from the Crossflow Plane for the Current Measurement.

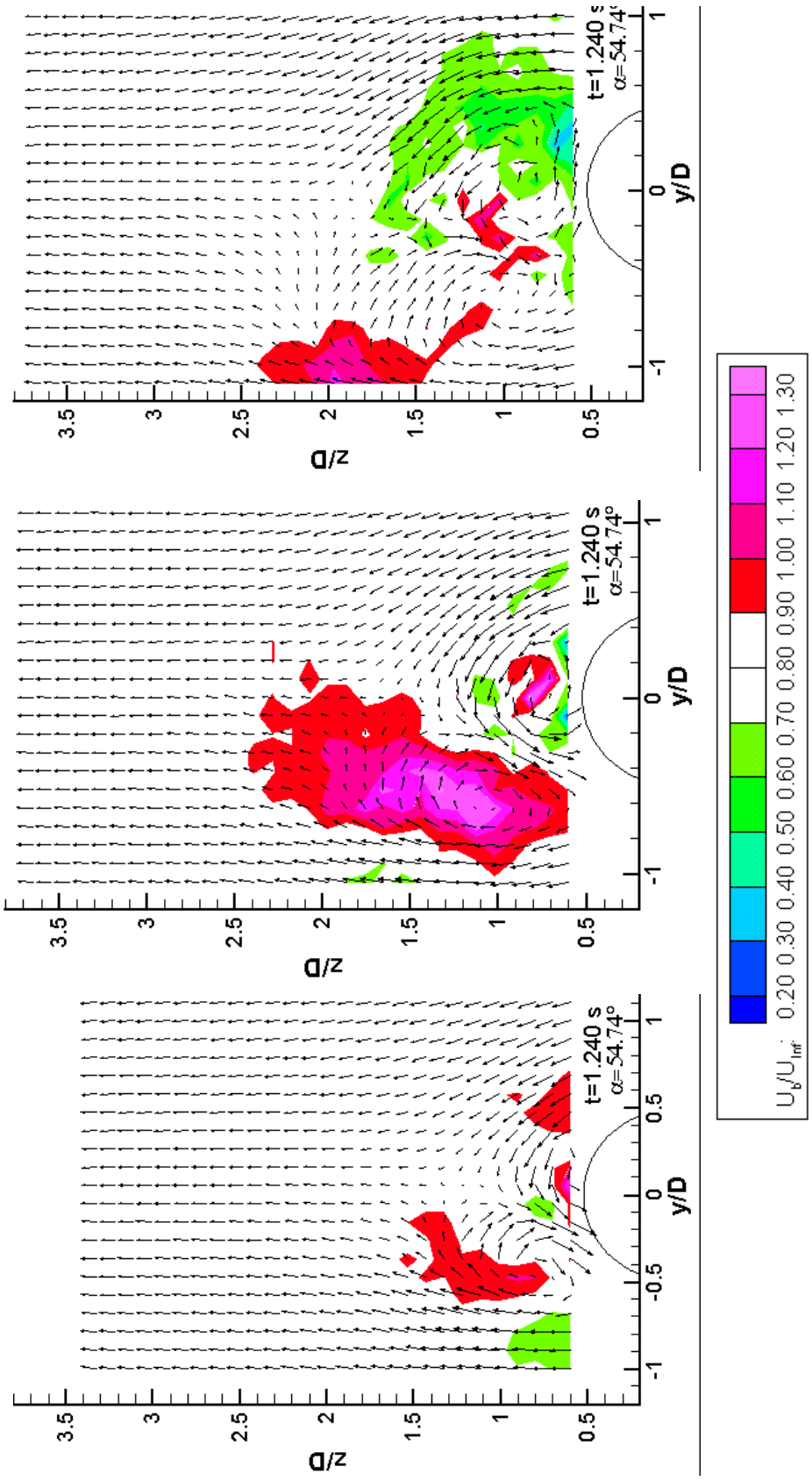

Figure 5.2.18: Three-Dimensional Velocity Fields at $t^* = 1.240$ s, $\alpha = 54.74°$, with $x_p/D = 0$: (a) x/D = 3, (b) x/D = 4, (c) x/D = 5. Contours Represent the Axial Velocity. The Coordinate System is Fixed to the Measurement Plane, which Is Rotated 18.0° from the Crossflow Plane for the Current Measurement.

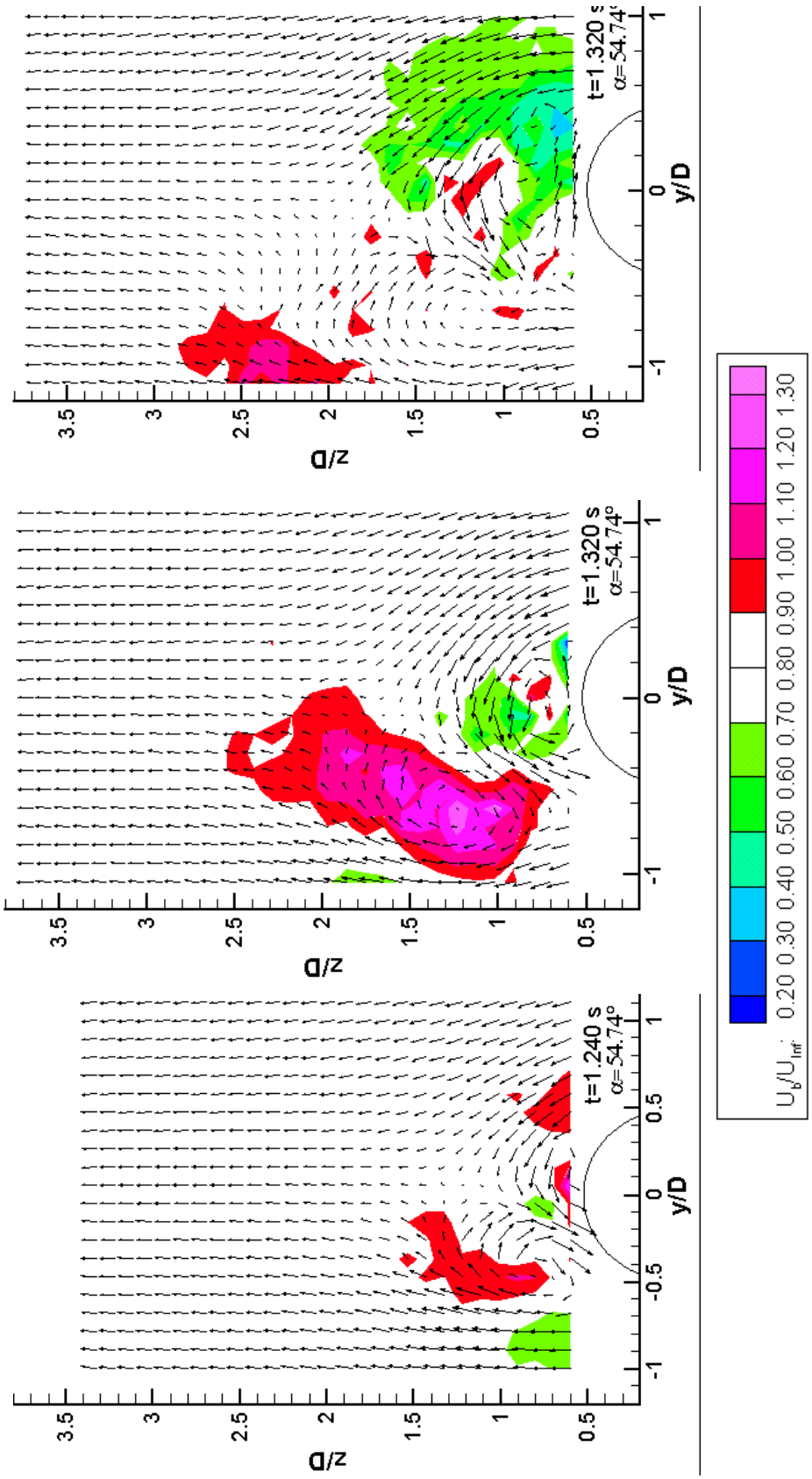

Figure 5.2.19: Three-Dimensional Velocity Fields at $t^* = 1.320$ s, $\alpha = 54.74°$, with $x_p/D = 0$: (a) x/D = 3, (b) x/D = 4, (c) x/D = 5. Contours Represent the Axial Velocity. The Coordinate System is Fixed to the Measurement Plane, which Is Rotated 18.0° from the Crossflow Plane for the Current Measurement.

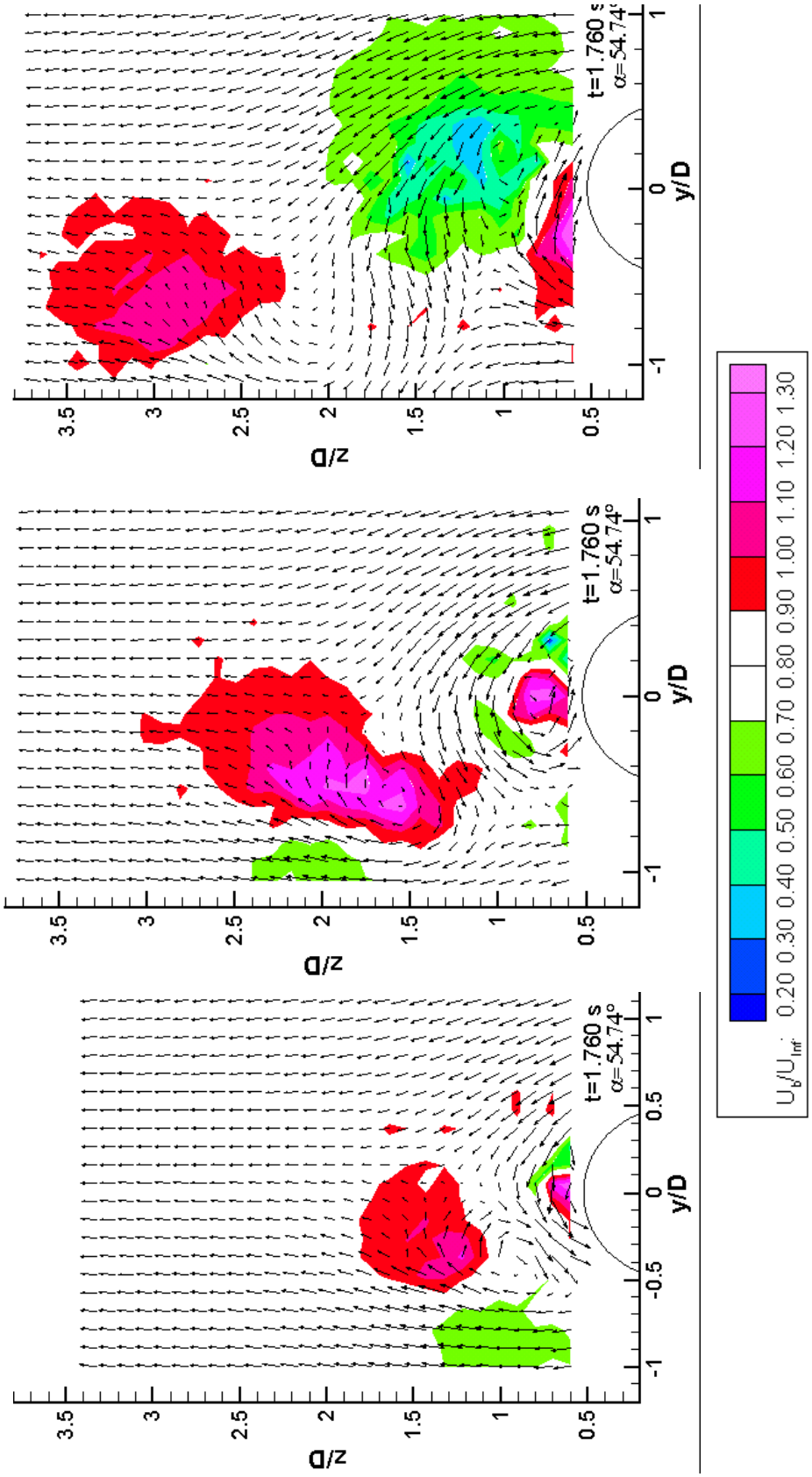

Figure 5.2.20: Three-Dimensional Velocity Fields at $t^* = 1.760$ s, $\alpha = 54.74°$, with $x_p/D = 0$: (a) x/D = 3, (b) x/D = 4, (c) x/D = 5. Contours Represent the Axial Velocity. The Coordinate System is Fixed to the Measurement Plane, which Is Rotated 18.0° from the Crossflow Plane for the Current Measurement.

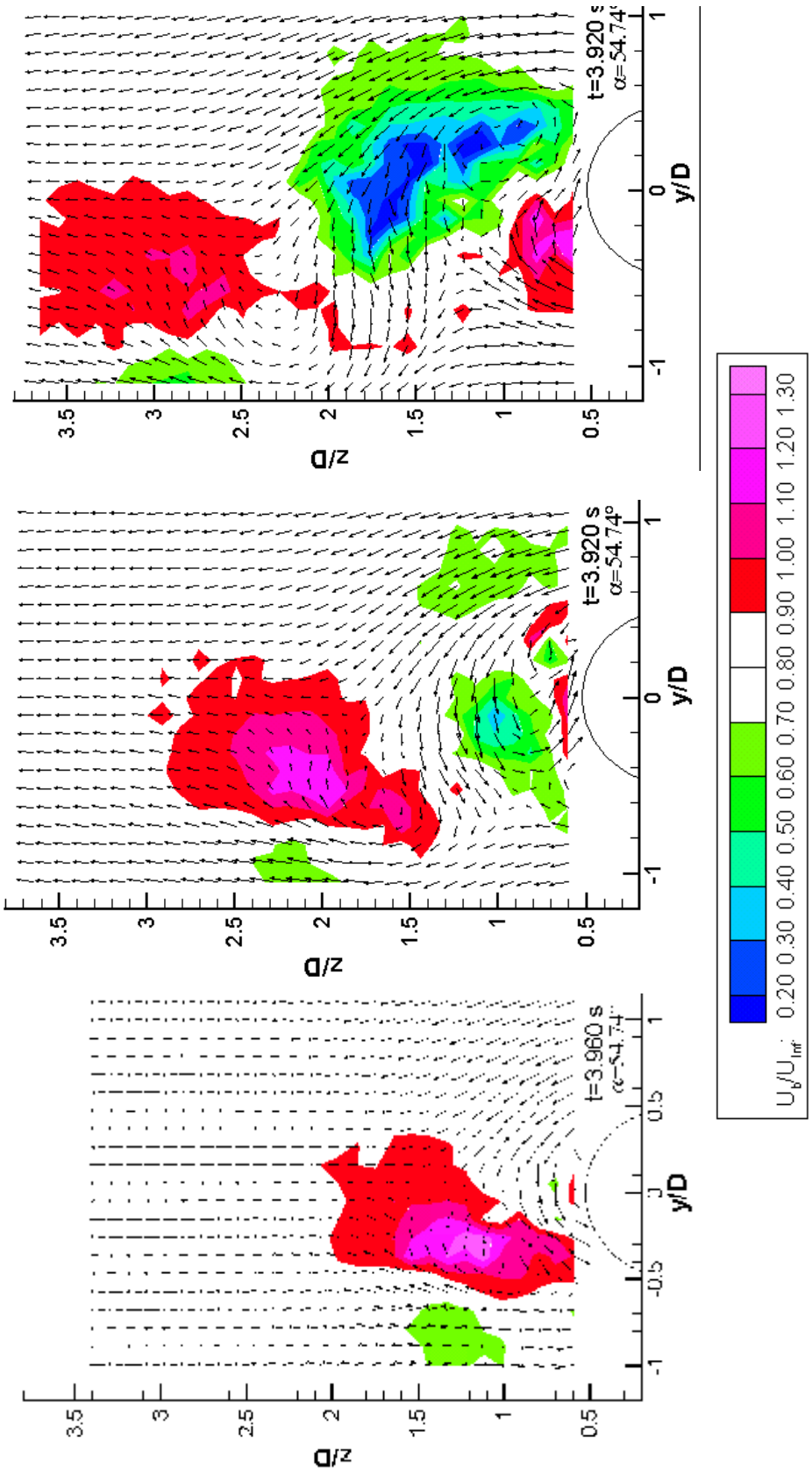

Figure 5.2.21: Three-Dimensional Velocity Fields at $t^* = 3.920$ s, $\alpha = 54.74°$, with $x_p/D = 0$: (a) x/D = 3, (b) x/D = 4, (c) x/D = 5. Contours Represent the Axial Velocity. The Coordinate System is Fixed to the Measurement Plane, which Is Rotated 18.0° from the Crossflow Plane for the Current Measurement.

The three-dimensional flowfields for $x_p/D = 4$ are shown if figures 5.2.22 – 5.2.41. These figures correspond to the same dimensional times as for the sequence where $x_p/D = 0$, with several extra figures. Since the general flow development for this pitch axis is similar to that for $x_p/D = 0$, the discussion will center on the differences between the two flows.

Figures 5.2.22 – 5.2.29 when compared with corresponding plots for $x_p/D = 0$ (figures 5.2.6 – 5.2.13), show an even larger delay in the vortex development for $x_p/D = 4$. When $x/D = 3$ and $x_p/D = 4$, the measurement location is forward of the pitch axis, so the local motion is opposite to the incoming stream. Therefore, the normal pattern of flow separation will be delayed, in a manner similar to that documented by Stanek & Visbal [1991], although not to the same extent because the crossflow velocity due to pitch rate is much less in this case. Therefore, no vortex development occurs over the leeside of the body at this station while the model is in motion. At $x/D = 4$, the pitch axis location and measurement plane coincide. It is expected that the unsteady effects at this location during the motion should be diminished somewhat, since the body does not move normal to its axis.

The development at $x/D = 5$, $x_p/D = 4$ is very similar to that when $x_p/D = 0$. Initially, there is development of symmetric vortices with an increasing wake region exhibiting large values of u. This continues until $t = 0.920$ s (figure 5.2.30), at which time the second vortex is robbed of most of its high core velocity, resulting in an asymmetry in the axial velocity. This is coupled with a slight in-plane asymmetry as well. Note that in all three planes, regions of velocity deficit appear above the body, as seen previously for $x_p/D = 0$. Interestingly, although the second vortex remains a coherent in-plane structure, it never does regain the strong core velocity as it proceeds to breakdown in the manner described previously for $x_p/D = 0$. Based on the characteristics of the u-component of velocity, this process begins much sooner for this pitch-axis location.

A situation involving a reversal of the asymmetry through axial stations is observed in figures 5.2.35 – 5.2.37. In this sequence, the flowfield at $x/D = 3$ is slightly asymmetric, with the second vortex pushing the first to the left and then upwards. At the same instant, as seen in figure 5.2.36, the asymmetry is disposed the opposite way at $x/D = 4$ and $x/D = 5$. Since $t^* = 1.28$ (figure 5.2.35) is the first time that the in-plane flow is observed to be asymmetric at $x/D = 3$, it is not likely that the asymmetry at the more distant axial stations is caused by the convective instability.

As the flow proceeds to the steady state, we again observe the breaking down of vortex two and the emergence of vortex three for x/D = 5. We note that many of the characteristics exhibited by the steady-state second vortex as its development is traced through increasing axial locations is reminiscent of those known to exist during vortex breakdown over delta wings (Schaeffler [1998]), but not to the same degree of severity of the breakdown. As the second vortex moves from a position near the body at x/D = 3, to farther away from the body at x/D = 5, we see that the axial component of velocity decreases drastically, while the area covered by the vortex expands.

There is a small but palpable difference between the steady-state three-dimensional velocity fields for $x_p/D = 0$ and $x_p/D = 4$. The x/D = 5 planes compare slightly better than the other two. There are several possible explanations for this difference. The reader should be familiar with the process used to acquire the data sets, as set forth in sections 2.4 and 2.11. First, it is possible, because of the longevity of the experiment, that the geometric asymmetry used on the tip of the forebody (to ensure constant asymmetry) may have slightly moved or eroded, although. Other than observing the nose of the model before and after the experiments, there was no check done to determine if the asymmetry had changed. It is worthwhile to keep in mind that it has been shown many times that a very small change in the geometric asymmetry can result in large changes in the flow, even to the point of the asymmetry switching directions. Second, it is possible that the planes were not acquired at exactly the same axial positions. Again, other than carefully setting up the experiment and using the same base point on the model to orient the LDV system, the author has no independent check to determine whether this was the case. Third, one could argue that the flow might not have reached the steady state. Although not acquired for this particular experiment, independent steady-state planes of data were acquired in other instances, and the data presented in section 5.2.7 is one such instance. It was found that allowing 3 seconds or more after the motion was sufficient to allow the flow to approach closely to the steady flow. Finally, averaging the results over ten ensembles may not have been sufficient to completely remove flow unsteadiness, especially after an unsteady maneuver. The natural unsteadiness, as outlined in chapter 3, could have been responsible for the discrepancy between the data sets. After careful examination of the data and consideration of the possibilities, it is the author's opinion that a very small change in the asymmetry was responsible for the difference in the flowfields. This could have happened during the handling of the model while the pitch axes were being changed, in that the model could have been aligned slightly differently, giving the asymmetry a slightly different location with respect to the oncoming flow. One way to correct this problem would be to acquire all three components of the velocity simultaneously.

It is hoped that this discussion of possible causes of the differences in the data helps the reader to appreciate the difficulty encountered in experimental investigations on slender forebodies at high angles of attack. If one were to consider delta-wing experiments conducted under the same conditions, it would be recognized that the asymmetry and unsteadiness would not be considerations in data discrepancy, and that the experimenter had control over the number of ensembles and the location of the measurement plane. Accordingly, if the data were wrong, it would be a simple matter to reacquire the data, because the delta-wing flow has repeatable, sharp-edged separation with no gross asymmetries involved. On the other hand, if this occurs during a multi-plane experiment involving a slender forebody, all of the previous data would not be comparable to data taken after the geometric asymmetry had been altered. When changing of the pitch axes occurred, or when the model had to be removed from the tunnel for access, the author always felt quite a bit of consternation because the entire experiment was hanging in the balance. There were at least three or four occasions where only partial data sets were acquired.

5.2.3 The Unsteady Vorticity Fields

The vorticity variable is defined as the curl of the velocity vector. If follows that the x-component of the vorticity is

$$\omega_x = \frac{dw}{dy} - \frac{dv}{dz} \tag{5.2}$$

The details of this applying this calculation to a discrete velocity field are discussed in section 2.11.2. The unsteady vorticity for $x_p/D = 4$ is presented in figures 5.2.42 – 5.2.46 as contours with the in-plane velocity components overlaid. The evolution of the vorticity for $x_p/D = 0$ is similar except for the delay in the onset of asymmetry. The vorticity is nondimensionalized by U_∞/D and values between –2.0 and 2.0 are blanked so that the areas containing vorticity of high magnitude stand out.

Figure 5.2.42, which is just after the maneuver has finished at $\alpha = 54.74°$, shows a pair of symmetric vortices with strong vorticity at each measurement location. The vorticity grows in strength with increasing axial distance. Recall that at this instant, the axial core velocities at x/D = 4 and x/D = 5 are high. The combination of high axial velocity and high vorticity in the core regions of these vortices signifies a strong helical flow, as exhibited by delta-wing vortices. The lower values of vorticity and velocity exhibited here, as compared to the delta wing Schaeffler [1998], are simply due to the difference between body geometry and bluff-body versus sharp-edge separation. The low-pressure regions which would accompany these vortices would serve to increase the normal force on the body, which would

increase both the lift and drag above the equivalent steady-state values. This increase in normal force over a slender forebody was documented by Smith & Nunn [1976].

Figure 5.2.43 and 5.2.44 show the set of flowfields just before the flow at x/D = 3 and x/D = 4 become asymmetric, respectively. Figure 5.2.46 shows the steady-state vorticity. Observing this sequence of figures, it is apparent that the vortices at x/D = 3 are not subject to the effects of breakdown, but only to slight diffusion of vorticity.

The second vortex at x/D = 4 retains its axial vorticity, but recall that the axial velocity in its core is sharply diminished (figure 5.2.41). This vortex still occupies a dominant position, and its diameter equals that of the body. As the first vortex is pushed away from the body by the second vortex, its core vorticity also diminishes.

The vorticity evolution for the second vortex at x/D = 5 clearly shows the occurrence of vortex breakdown. However, the axial vorticity in the core of this vortex remains above 4.0 until after t* = 1.720, long after the axial velocity deficit has appeared there at t* = 1.240 (figure 5.2.34). This loss of axial velocity, followed by the diffusion of vorticity, is exactly the sequence seen by Schaeffler[1998], in the investigation of delta-wing flows. The vorticity in the core of the second vortex at x/D = 5 does not drop below 4.0 until it is lifted from the body by the third vortex. The third vortex maintains a core vorticity with a magnitude above 6.0 and an axial velocity above 1.20, signifying a strong vortex.

We can conclude that the symmetric vortices that develop over a slender body during a pitching maneuver are similar to delta-wing vortices in arrangement and behavior, but not in strength. The displacement of the vortices due to the convective asymmetry leads to severe diffusion of vorticity from the symmetrical arrangement. However, unlike the loss of axial velocity in their cores, which can occur before the vortex symmetry is destroyed, the vortices appear to retain much of their core vorticity until pushed from the body by subsequently developing vortices. It is obvious that changes in axial vorticity do not cause the vortices to become asymmetric, but are instead a result of flowfield development induced by the asymmetry.

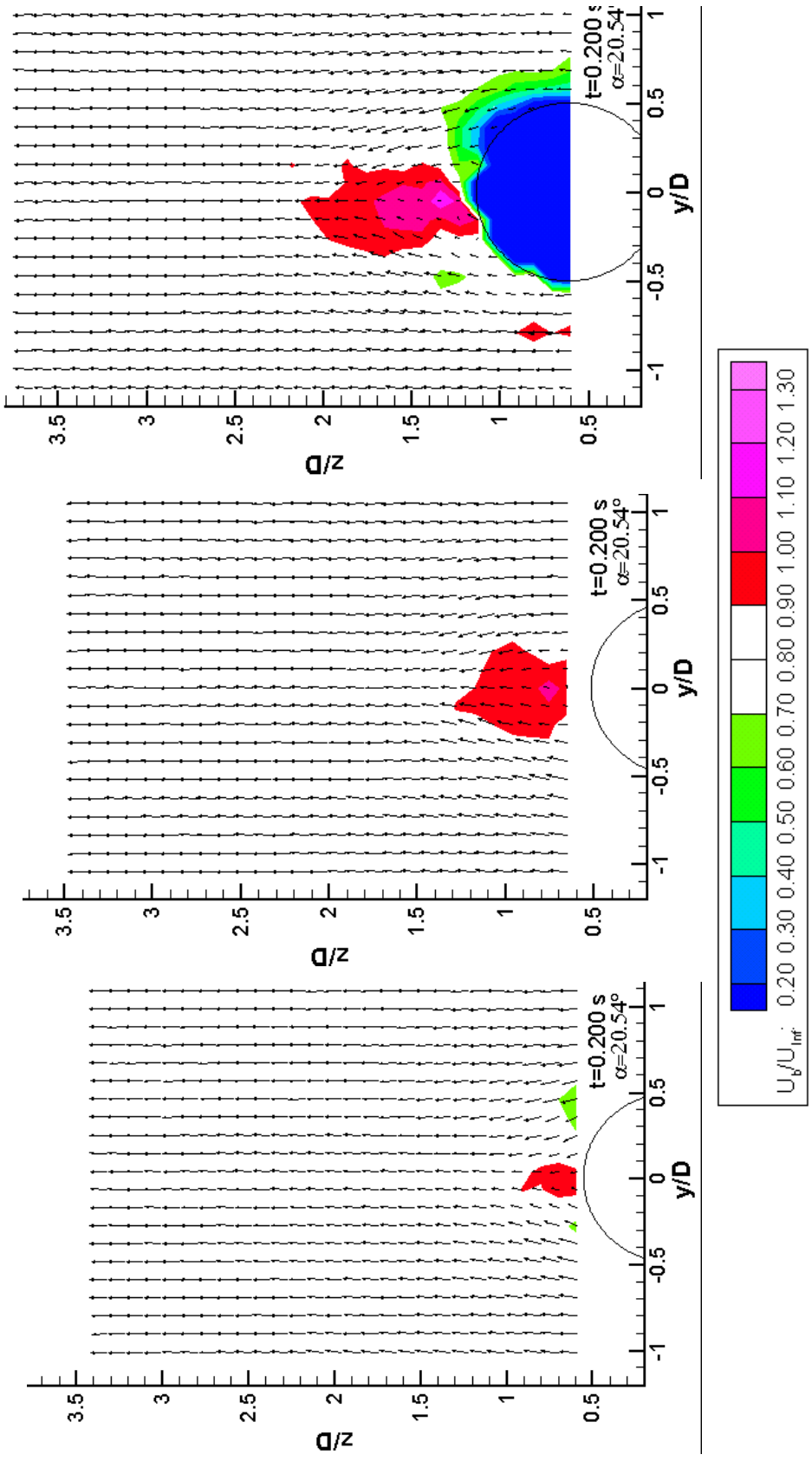

Figure 5.2.22: Three-Dimensional Velocity Fields at $t^* = 0.200$ S, $\alpha = 20.54°$, with $x_p/D = 4$: (a) x/D = 3, (b) x/D = 4, (c) x/D = 5. Contours Represent the Axial Velocity. The Coordinate System is Fixed to the Measurement Plane, which Is Rotated 16.2° from the Crossflow Plane for the Current Measurement.

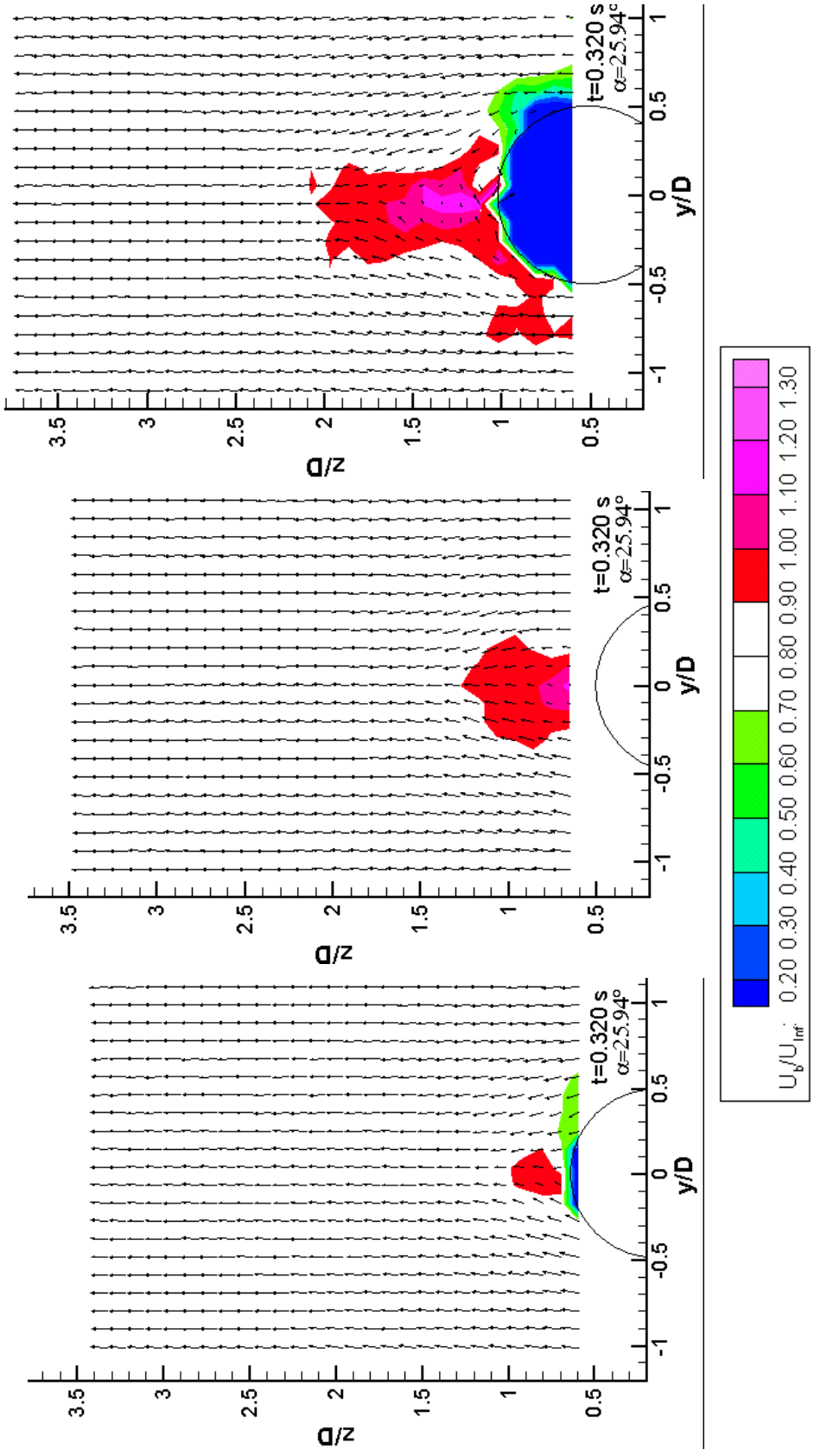

Figure 5.2.23: Three-Dimensional Velocity Fields at $t^* = 0.320$ S, $\alpha = 25.94°$, with $x_p/D = 4$: (a) x/D = 3, (b) x/D = 4, (c) x/D = 5. Contours Represent the Axial Velocity. The Coordinate System is Fixed to the Measurement Plane, which Is Rotated 10.8° from the Crossflow Plane for the Current Measurement.

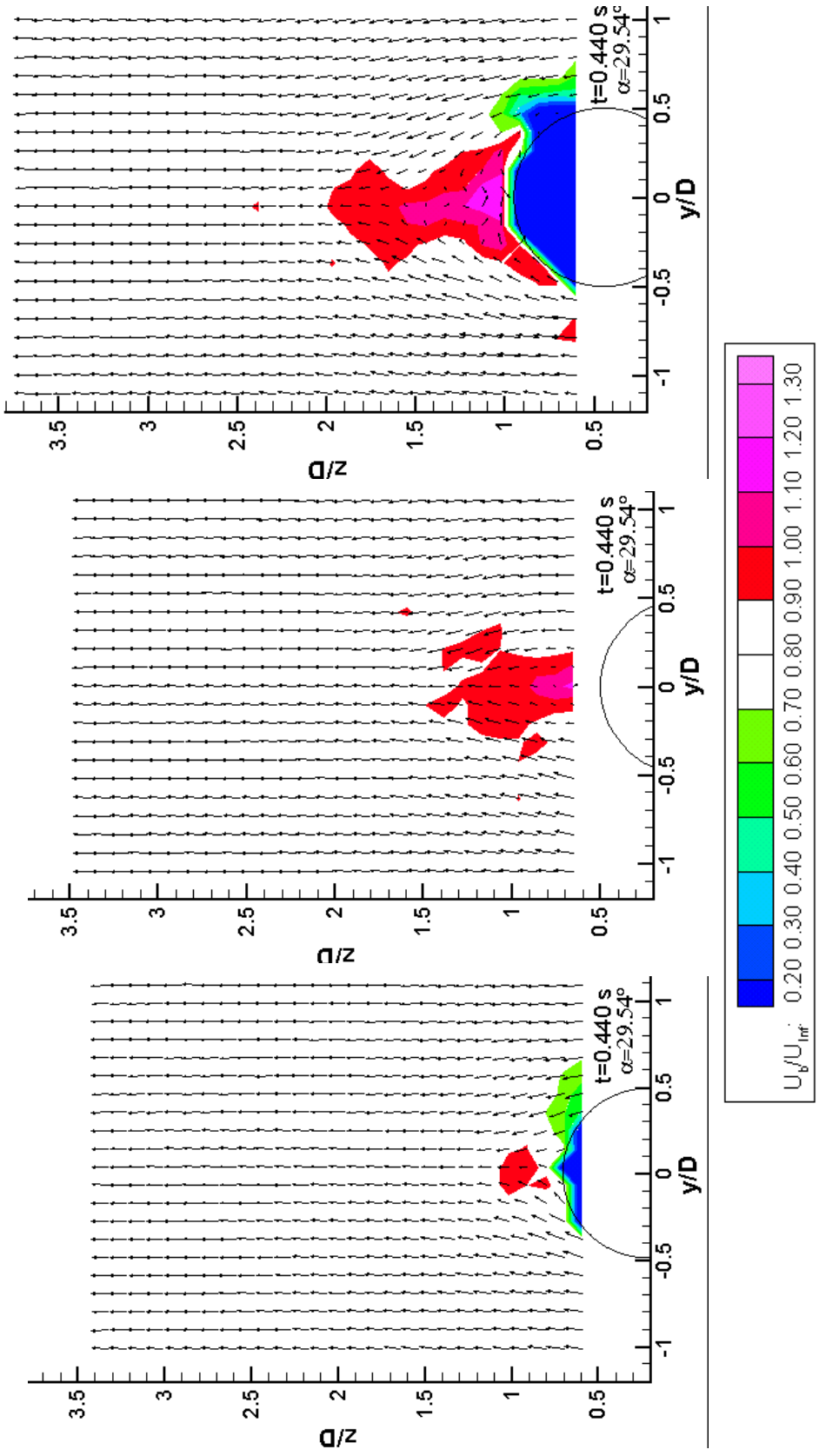

Figure 5.2.24: Three-Dimensional Velocity Fields at t* = 0.440 s, α = 29.54°, with $x_p/D = 4$: (a) x/D = 3, (b) x/D = 4, (c) x/D = 5. Contours Represent the Axial Velocity. The Coordinate System is Fixed to the Measurement Plane, which Is Rotated 7.2° from the Crossflow Plane for the Current Measurement.

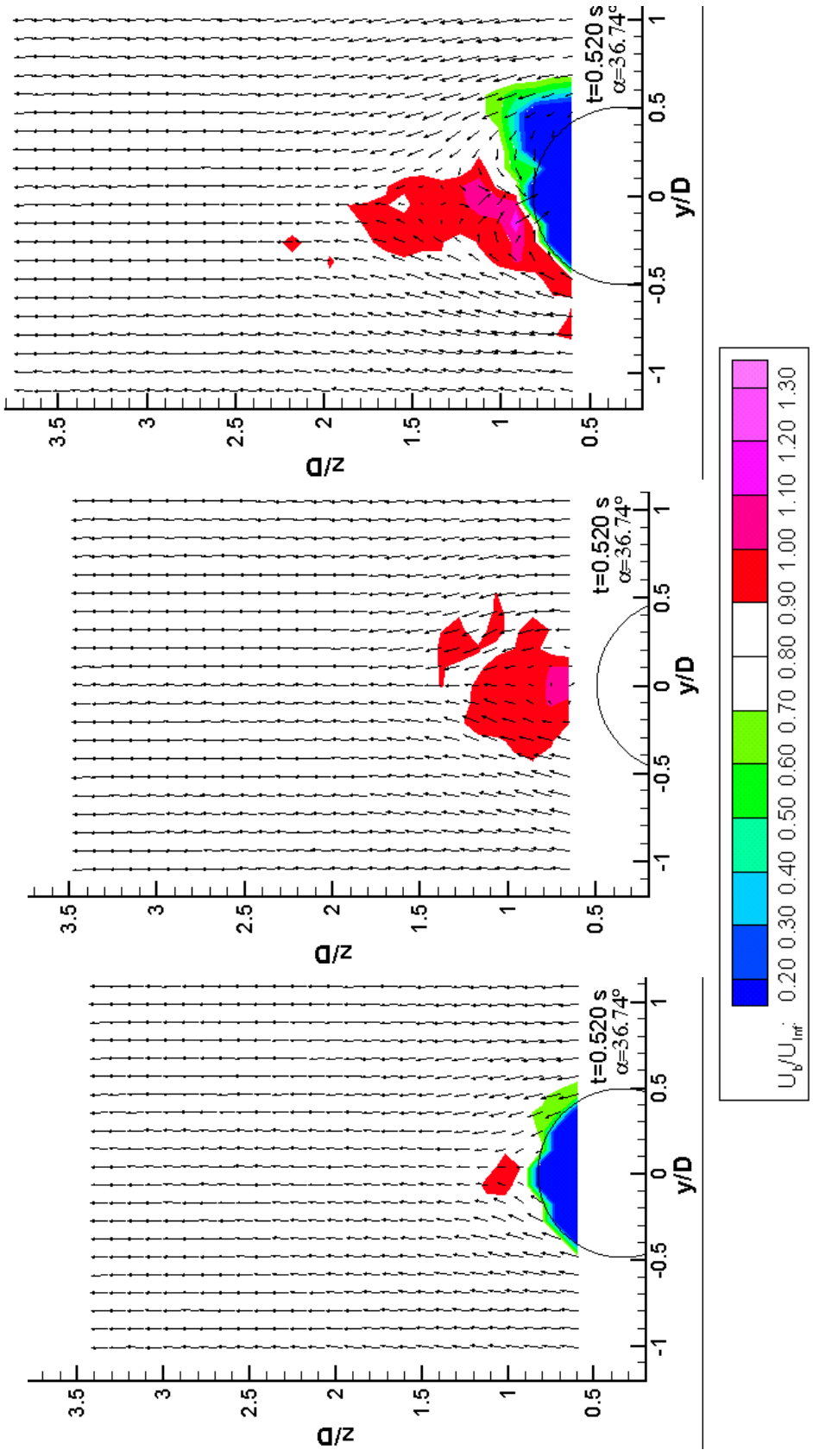

Figure 5.2.25: Three-Dimensional Velocity Fields at $t^* = 0.520$ s, $\alpha = 36.74°$, with $x_p/D = 4$: (a) x/D = 3, (b) x/D = 4, (c) x/D = 5. Contours Represent the Axial Velocity. The Coordinate System is Fixed to the Measurement Plane, which Is Rotated 0.0° from the Crossflow Plane for the Current Measurement.

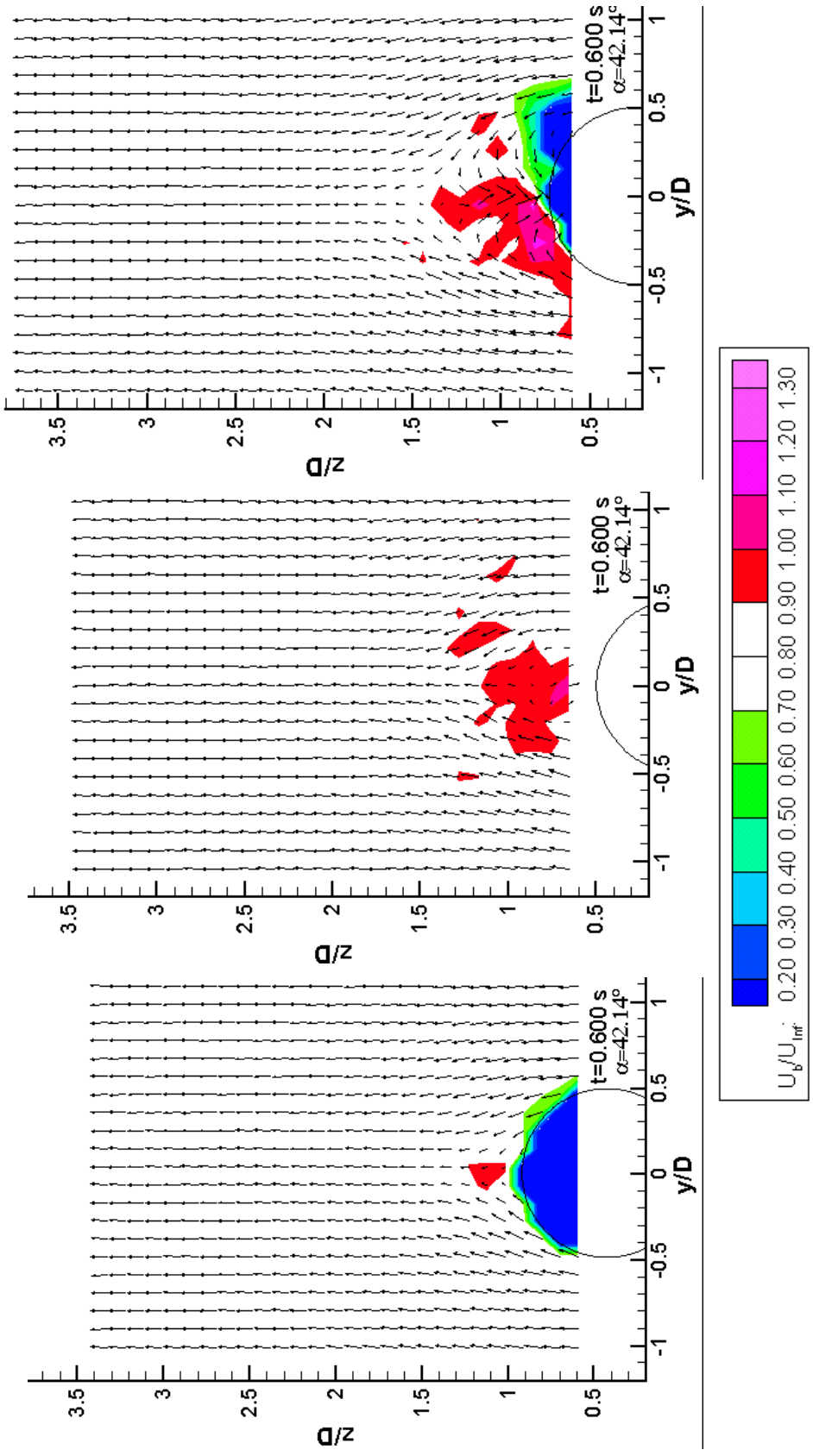

Figure 5.2.26: Three-Dimensional Velocity Fields at t* = 0.600 s, α = 42.14°, with $x_p/D = 4$: (a) x/D = 3, (b) x/D = 4, (c) x/D = 5. Contours Represent the Axial Velocity. The Coordinate System is Fixed to the Measurement Plane, which Is Rotated 5.4° from the Crossflow Plane for the Current Measurement.

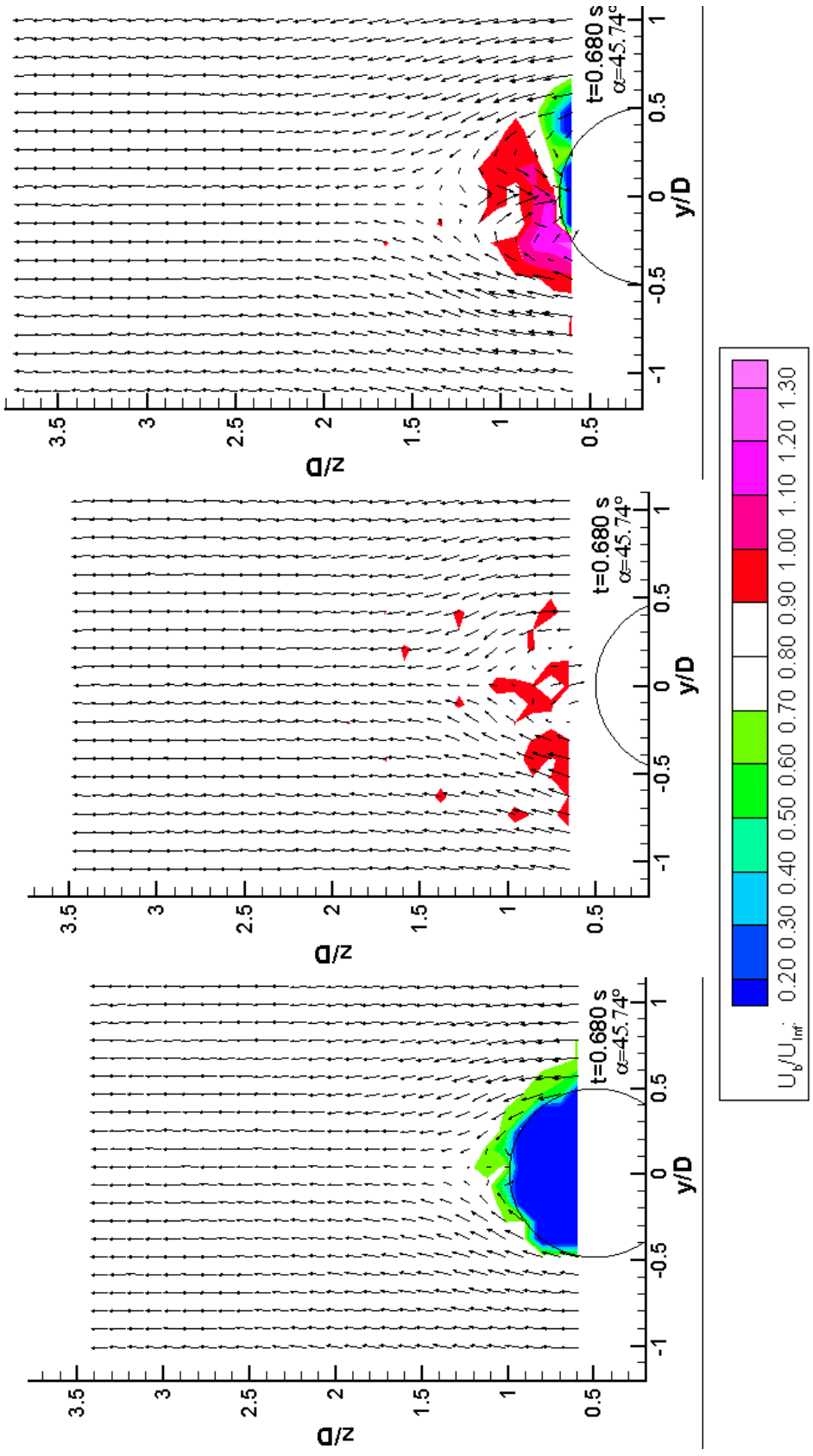

Figure 5.2.27: Three-Dimensional Velocity Fields at t* = 0.680 s, α = 45.74°, with x_p/D = 4: (a) x/D = 3, (b) x/D = 4, (c) x/D = 5. Contours Represent the Axial Velocity. The Coordinate System is Fixed to the Measurement Plane, which Is Rotated 9.0° from the Crossflow Plane for the Current Measurement.

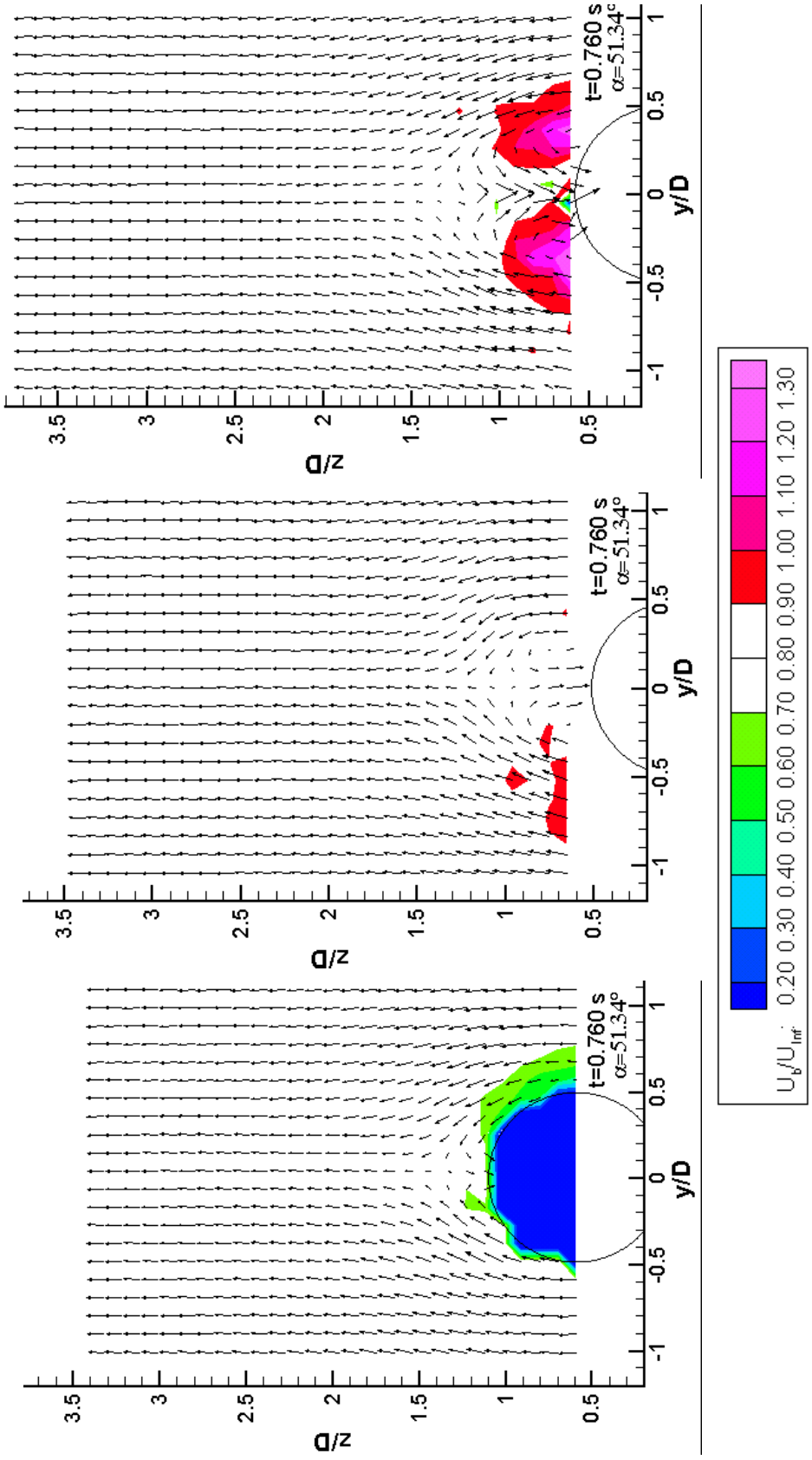

Figure 5.2.28: Three-Dimensional Velocity Fields at $t^* = 0.760$ s, $\alpha = 51.34°$, with $x_p/D = 4$: (a) x/D = 3, (b) x/D = 4, (c) x/D = 5. Contours Represent the Axial Velocity. The Coordinate System is Fixed to the Measurement Plane, which Is Rotated 14.6° from the Crossflow Plane for the Current Measurement.

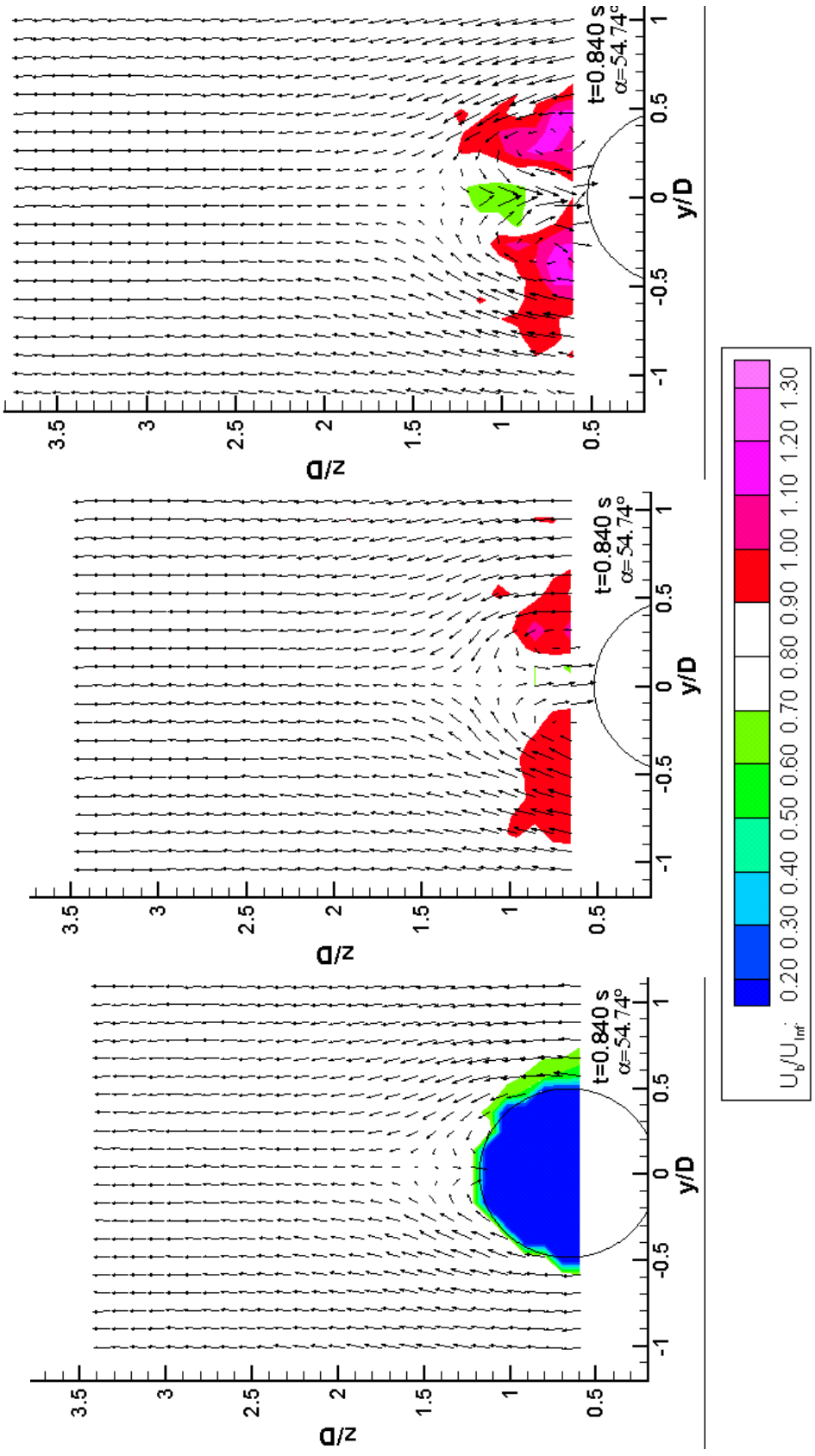

Figure 5.2.29: Three-Dimensional Velocity Fields at $t^* = 0.840$ s, $\alpha = 54.74°$, with $x_p/D = 4$: (a) x/D = 3, (b) x/D = 4, (c) x/D = 5. Contours Represent the Axial Velocity. The Coordinate System is Fixed to the Measurement Plane, which Is Rotated 18.0° from the Crossflow Plane for the Current Measurement.

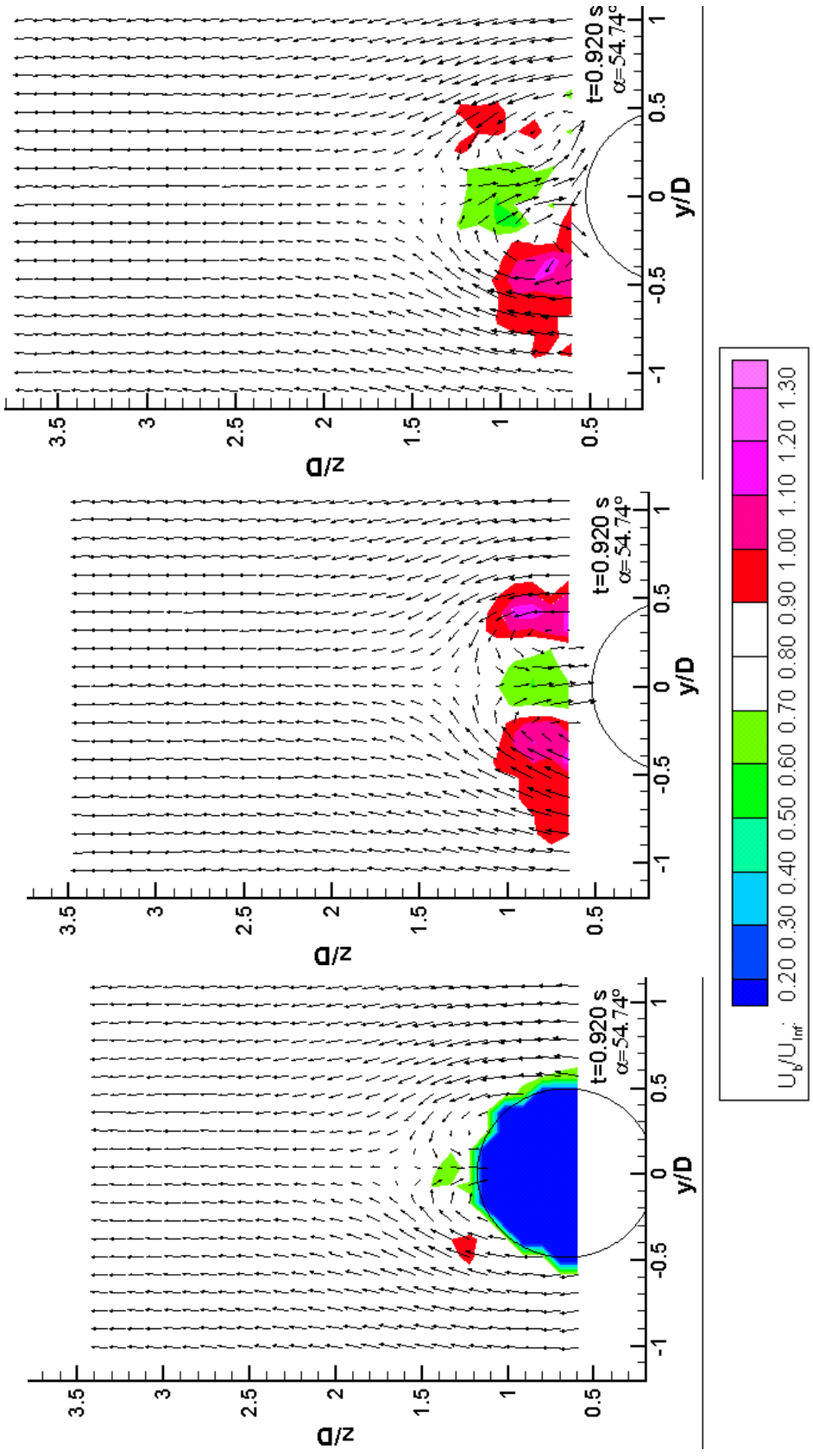

Figure 5.2.30: Three-Dimensional Velocity Fields at $t^* = 0.920$ s, $\alpha = 54.74°$, with $x_p/D = 4$: (a) x/D = 3, (b) x/D = 4, (c) x/D = 5. Contours Represent the Axial Velocity. The Coordinate System is Fixed to the Measurement Plane, which Is Rotated 18.0° from the Crossflow Plane for the Current Measurement.

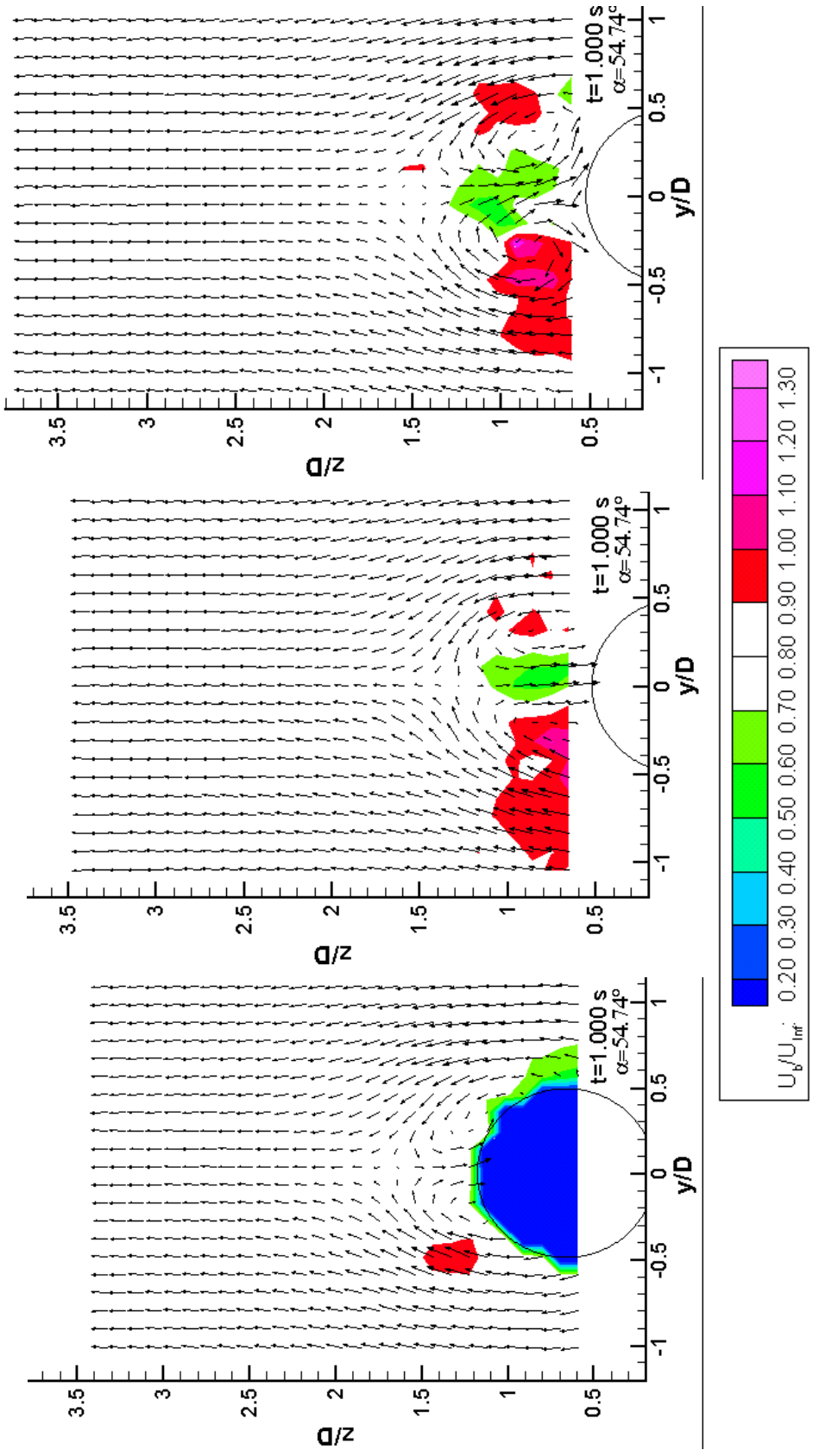

Figure 5.2.31: Three-Dimensional Velocity Fields at $t^* = 1.000$ s, $\alpha = 54.74°$, with $x_p/D = 4$: (a) x/D = 3, (b) x/D = 4, (c) x/D = 5. Contours Represent the Axial Velocity. The Coordinate System is Fixed to the Measurement Plane, which Is Rotated 18.0° from the Crossflow Plane for the Current Measurement.

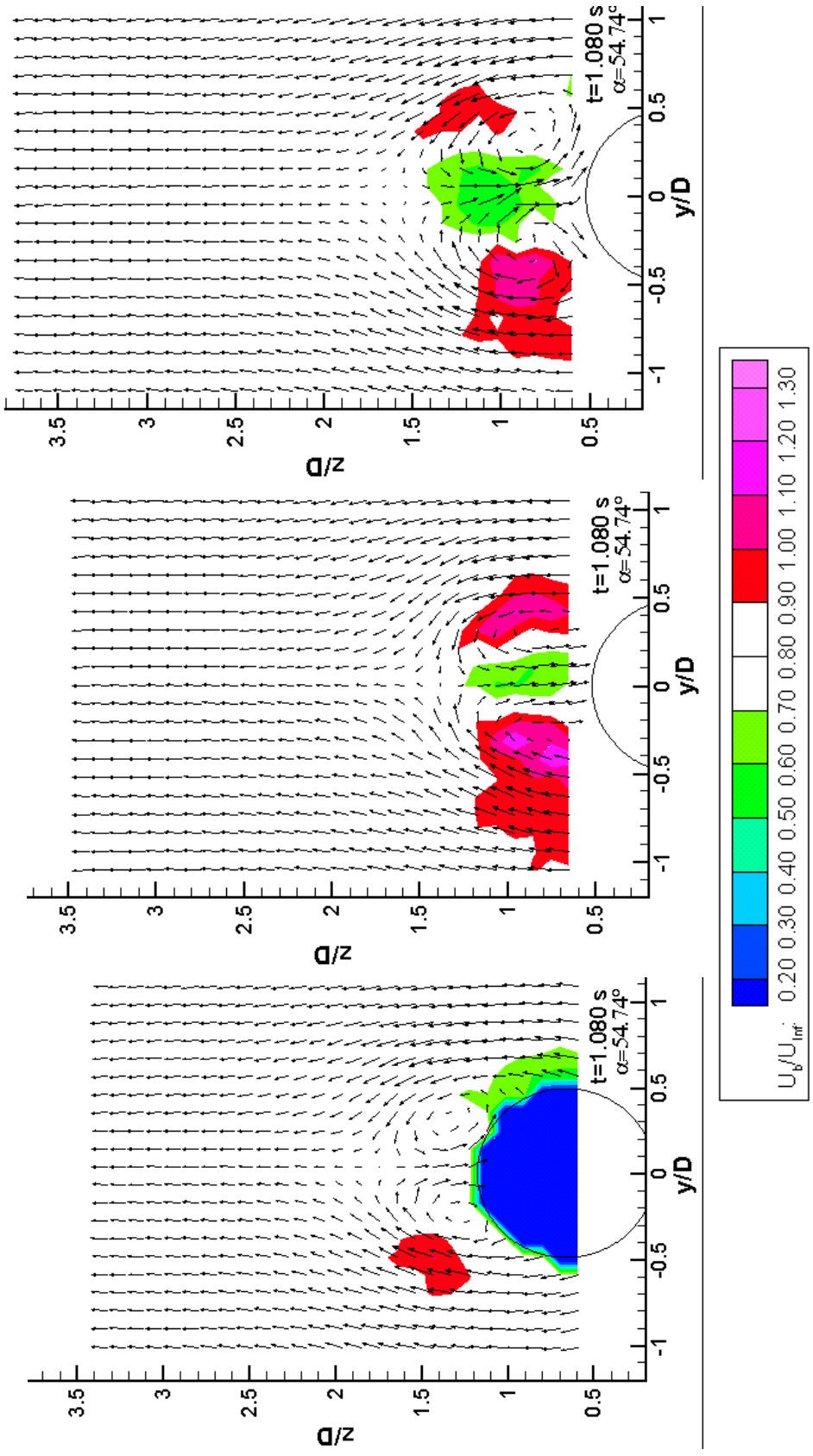

Figure 5.2.32: Three-Dimensional Velocity Fields at $t^* = 1.080$ s, $\alpha = 54.74°$, with $x_p/D = 4$: (a) x/D = 3, (b) x/D = 4, (c) x/D = 5. Contours Represent the Axial Velocity. The Coordinate System is Fixed to the Measurement Plane, which Is Rotated 18.0° from the Crossflow Plane for the Current Measurement.

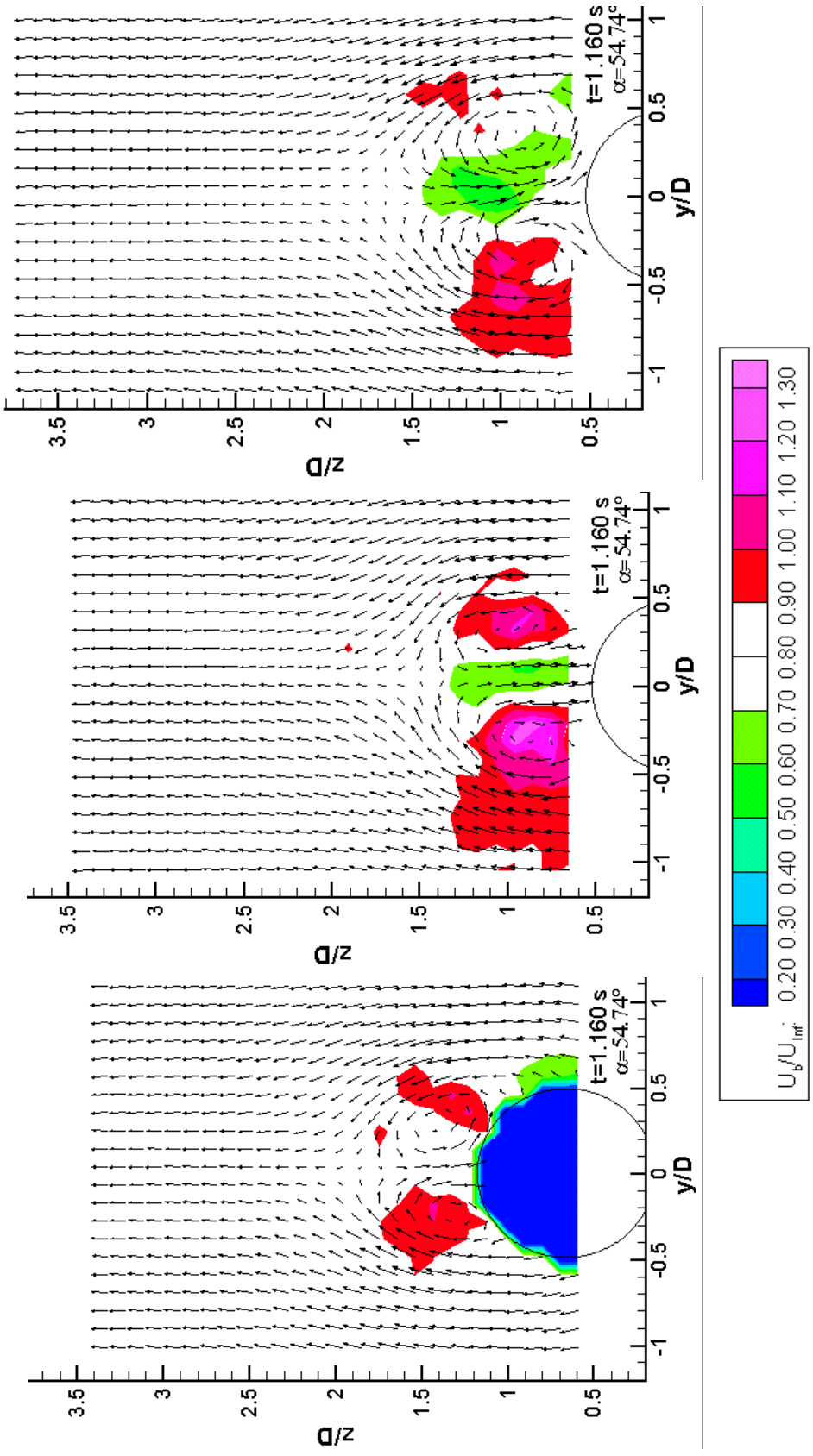

Figure 5.2.33: Three-Dimensional Velocity Fields at $t^* = 1.160$ s, $\alpha = 54.74°$, with $x_p/D = 4$: (a) x/D = 3, (b) x/D = 4, (c) x/D = 5. Contours Represent the Axial Velocity. The Coordinate System is Fixed to the Measurement Plane, which Is Rotated 18.0° from the Crossflow Plane for the Current Measurement.

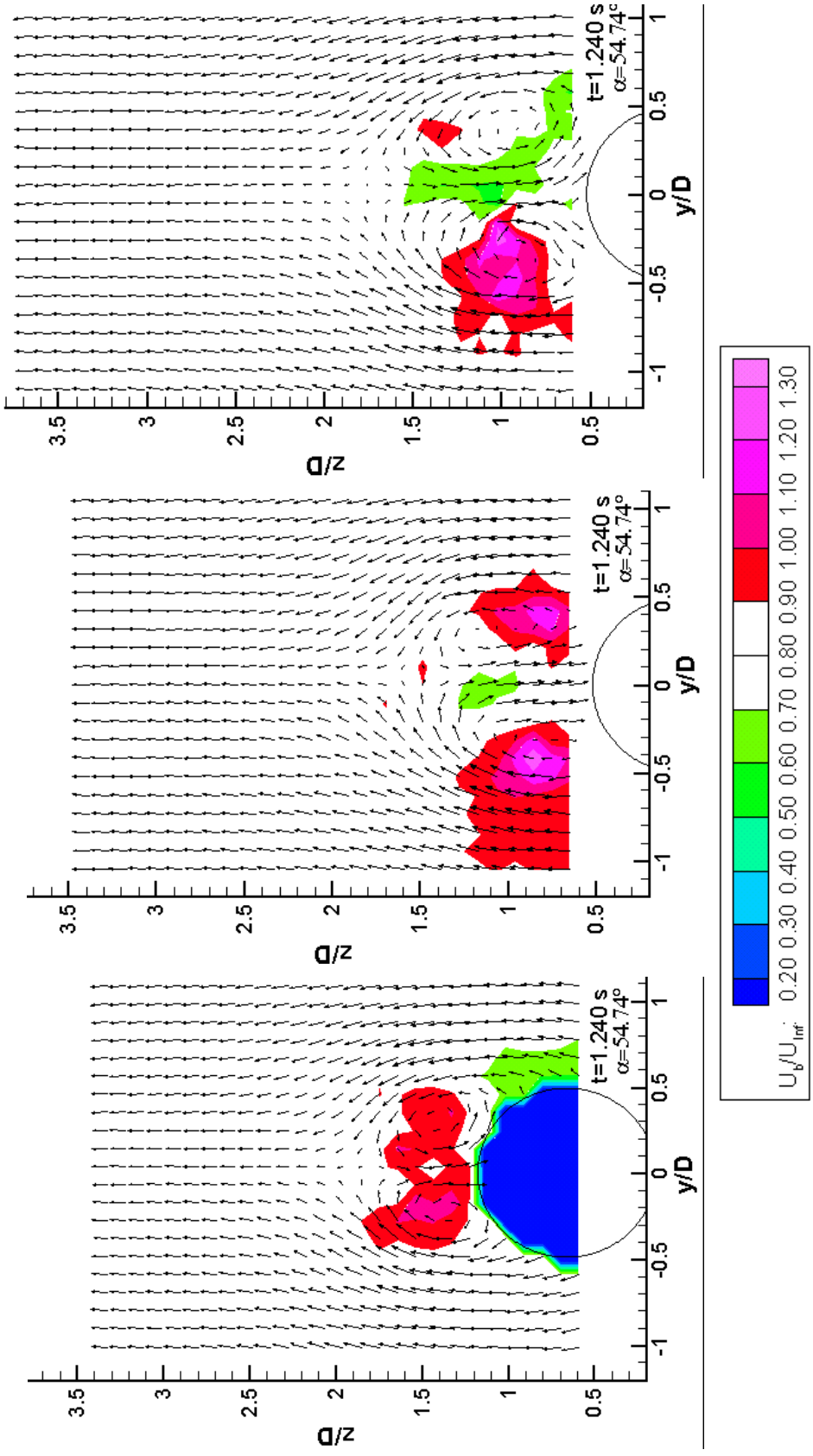

Figure 5.2.34: Three-Dimensional Velocity Fields at $t^* = 1.240$ s, $\alpha = 54.74°$, with $x_p/D = 4$: (a) x/D = 3, (b) x/D = 4, (c) x/D = 5. Contours Represent the Axial Velocity. The Coordinate System is Fixed to the Measurement Plane, which Is Rotated 18.0° from the Crossflow Plane for the Current Measurement.

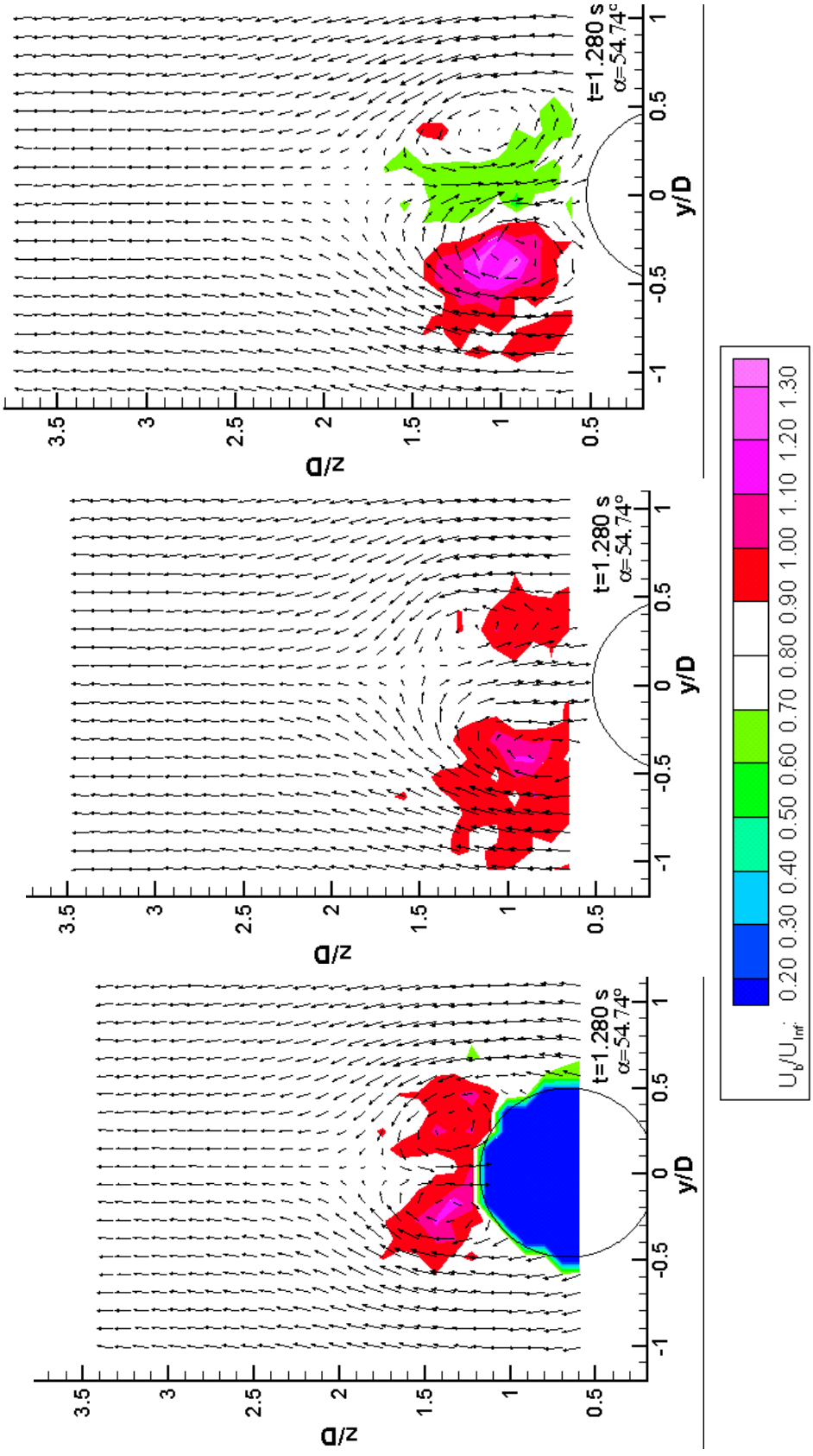

Figure 5.2.35: Three-Dimensional Velocity Fields at $t^* = 1.280$ s, $\alpha = 54.74°$, with $x_p/D = 4$: (a) x/D = 3, (b) x/D = 4, (c) x/D = 5. Contours Represent the Axial Velocity. The Coordinate System is Fixed to the Measurement Plane, which Is Rotated 18.0° from the Crossflow Plane for the Current Measurement.

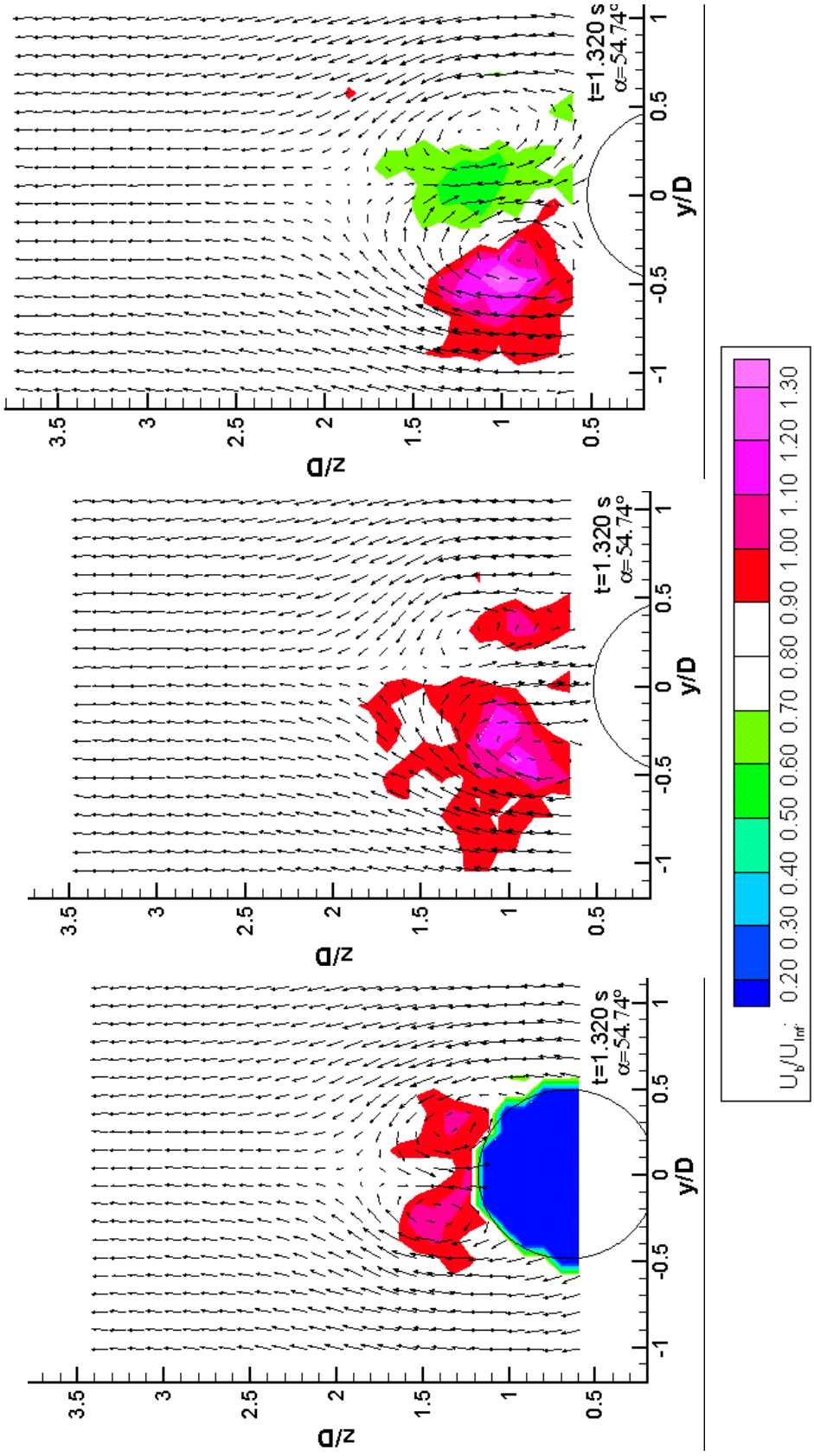

Figure 5.2.36: Three-Dimensional Velocity Fields at $t^* = 1.320$ s, $\alpha = 54.74°$, with $x_p/D = 4$: (a) x/D = 3, (b) x/D = 4, (c) x/D = 5. Contours Represent the Axial Velocity. The Coordinate System is Fixed to the Measurement Plane, which Is Rotated 18.0° from the Crossflow Plane for the Current Measurement.

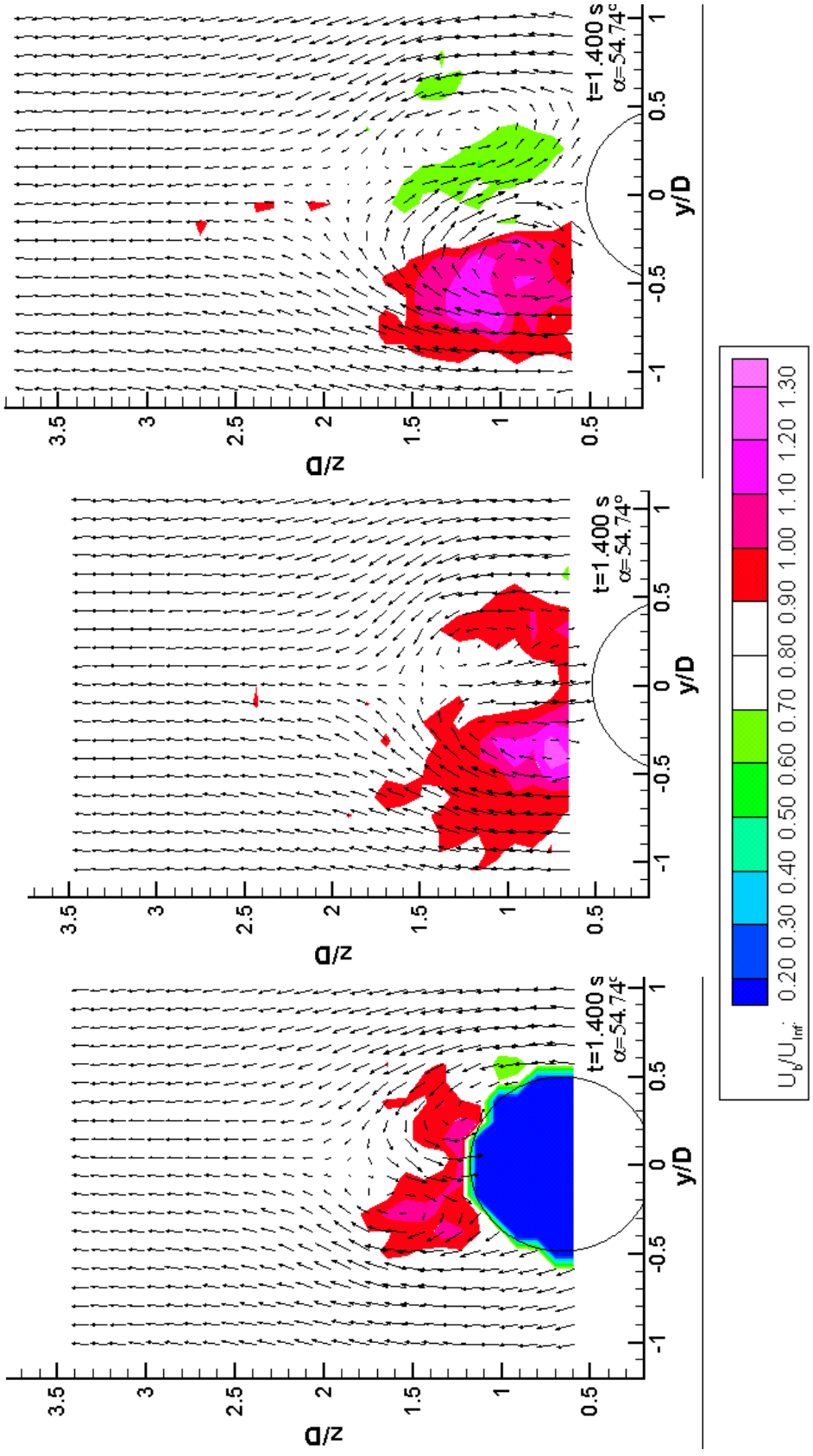

Figure 5.2.37: Three-Dimensional Velocity Fields at $t^* = 1.400$ s, $\alpha = 54.74°$, with $x_p/D = 4$: (a) x/D = 3, (b) x/D = 4, (c) x/D = 5. Contours Represent the Axial Velocity. The Coordinate System is Fixed to the Measurement Plane, which Is Rotated 18.0° from the Crossflow Plane for the Current Measurement.

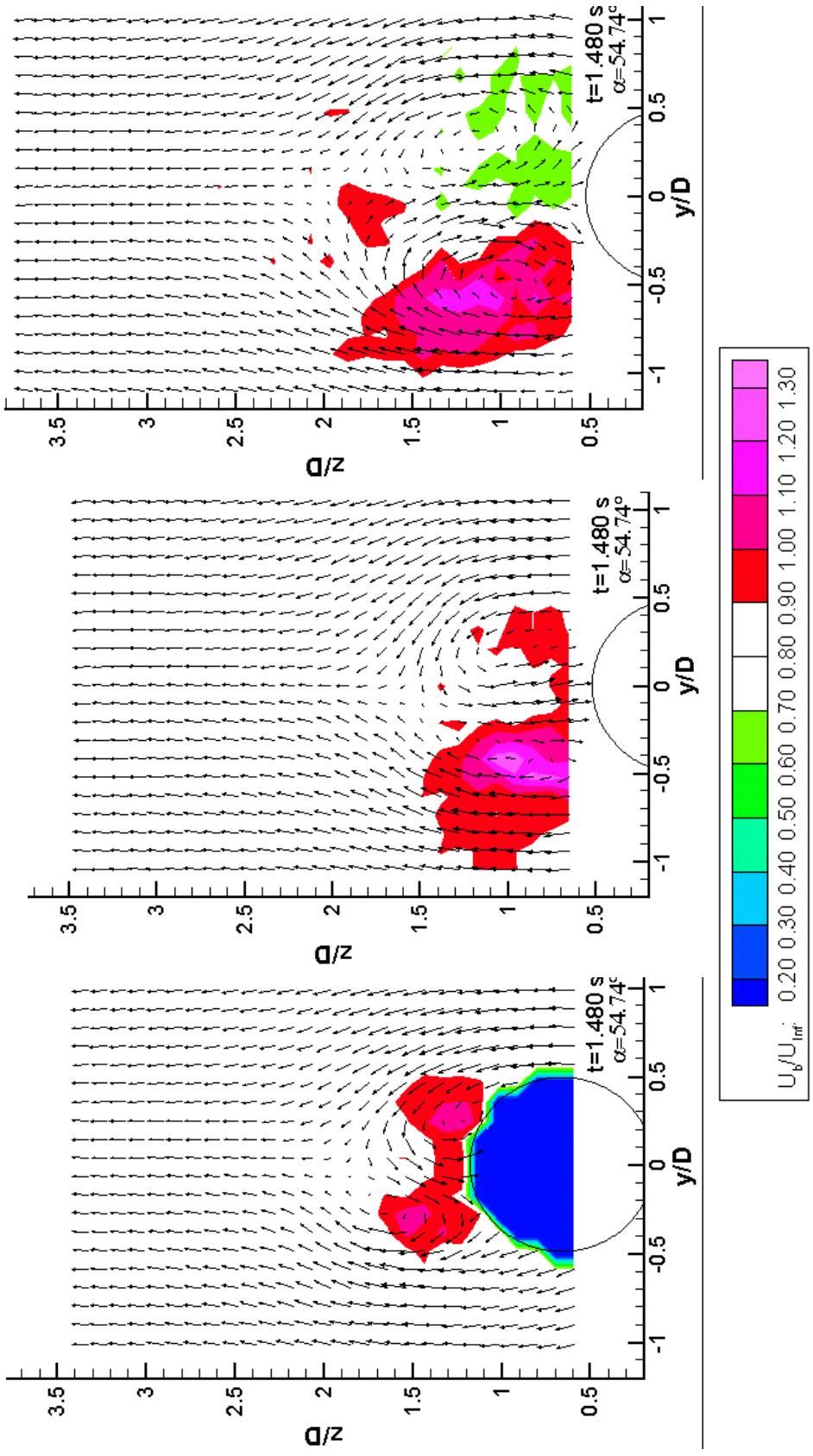

Figure 5.2.38: Three-Dimensional Velocity Fields at $t^* = 1.480$ s, $\alpha = 54.74°$, with $x_p/D = 4$: (a) x/D = 3, (b) x/D = 4, (c) x/D = 5. Contours Represent the Axial Velocity. The Coordinate System is Fixed to the Measurement Plane, which Is Rotated 18.0° from the Crossflow Plane for the Current Measurement.

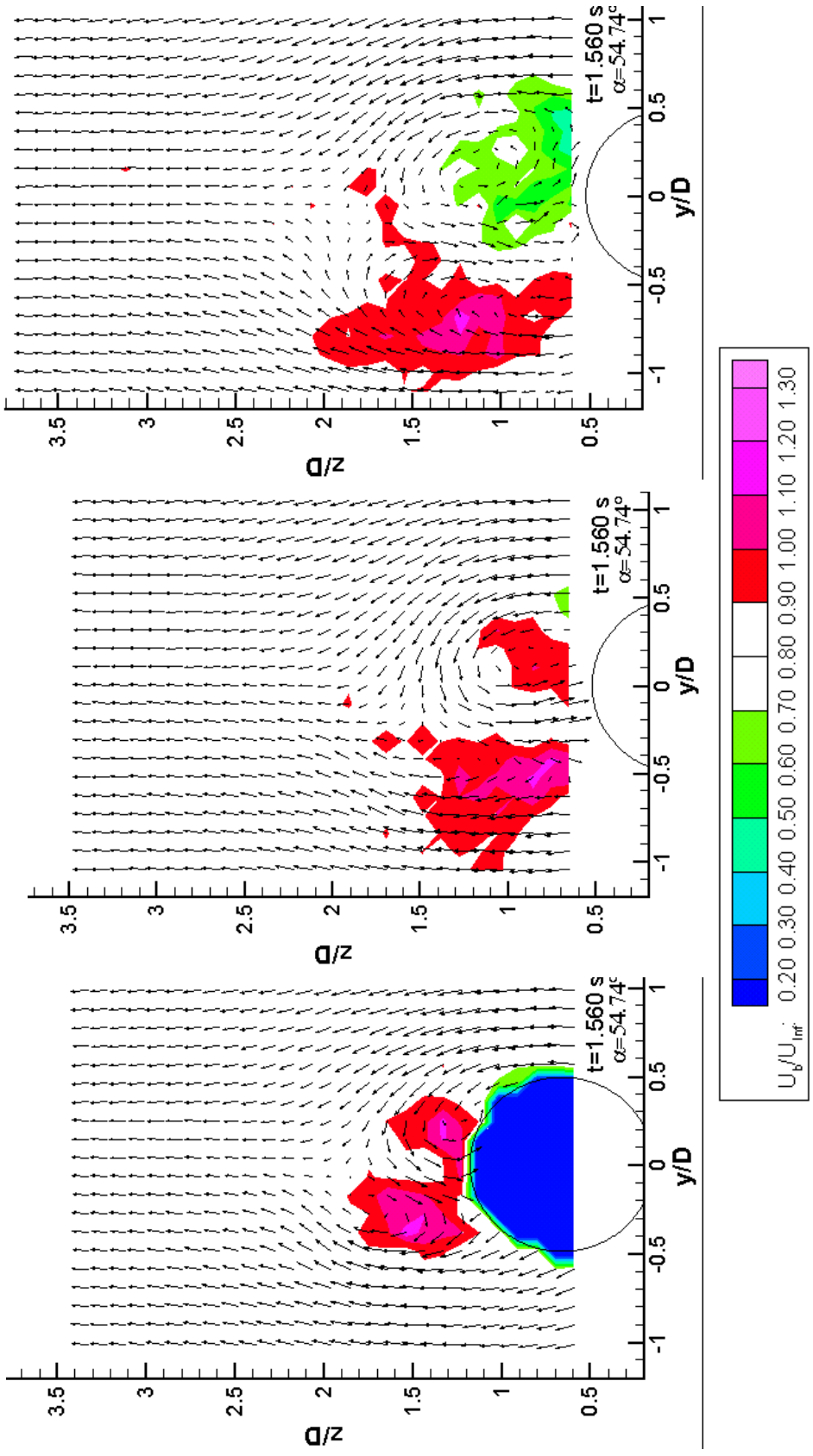

Figure 5.2.39: Three-Dimensional Velocity Fields at $t^* = 1.560$ s, $\alpha = 54.74°$, with $x_p/D = 4$: (a) x/D = 3, (b) x/D = 4, (c) x/D = 5. Contours Represent the Axial Velocity. The Coordinate System is Fixed to the Measurement Plane, which Is Rotated 18.0° from the Crossflow Plane for the Current Measurement.

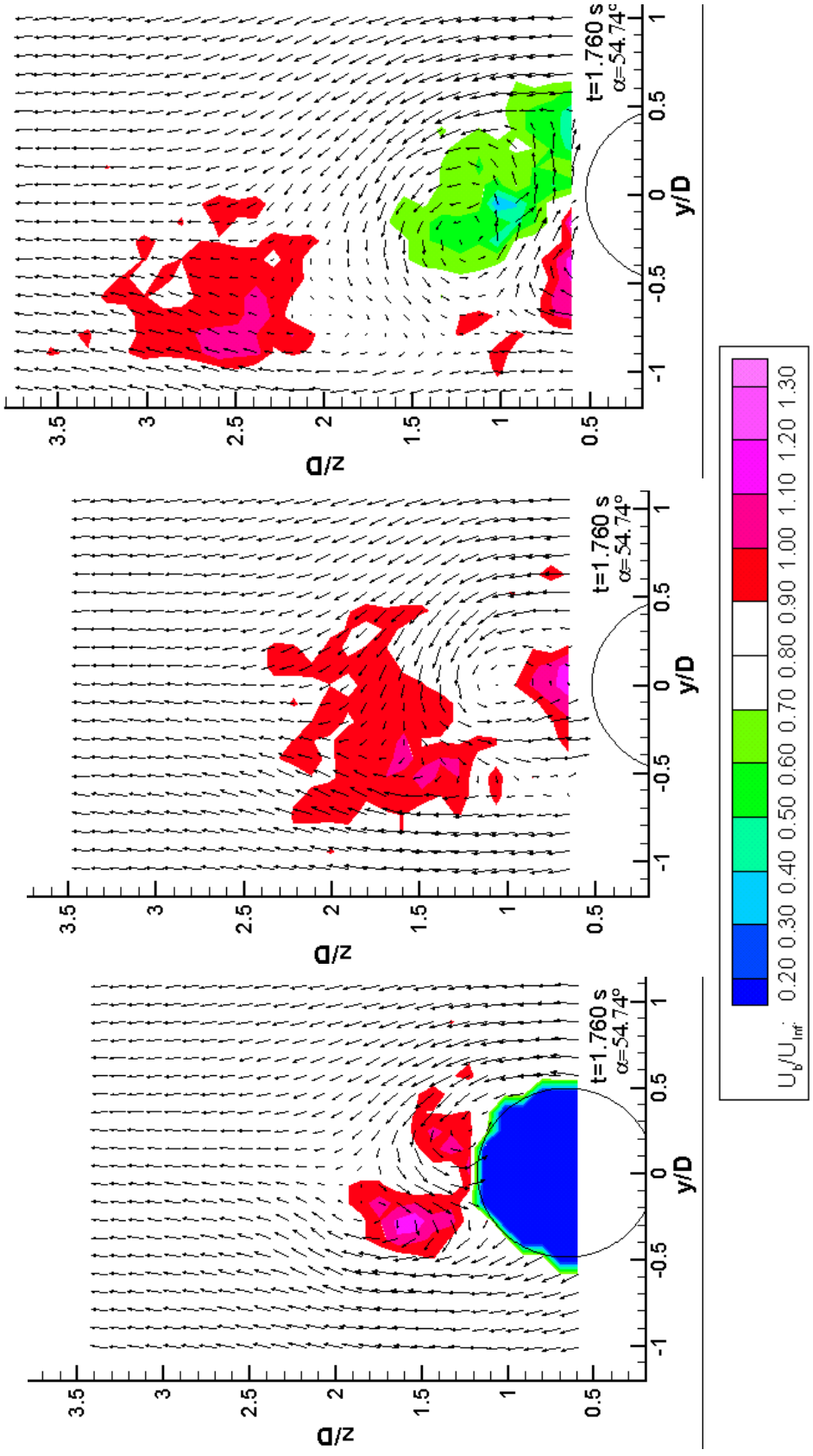

Figure 5.2.40: Three-Dimensional Velocity Fields at $t^* = 1.760$ s, $\alpha = 54.74°$, with $x_p/D = 4$: (a) x/D = 3, (b) x/D = 4, (c) x/D = 5. Contours Represent the Axial Velocity. The Coordinate System is Fixed to the Measurement Plane, which Is Rotated 18.0° from the Crossflow Plane for the Current Measurement.

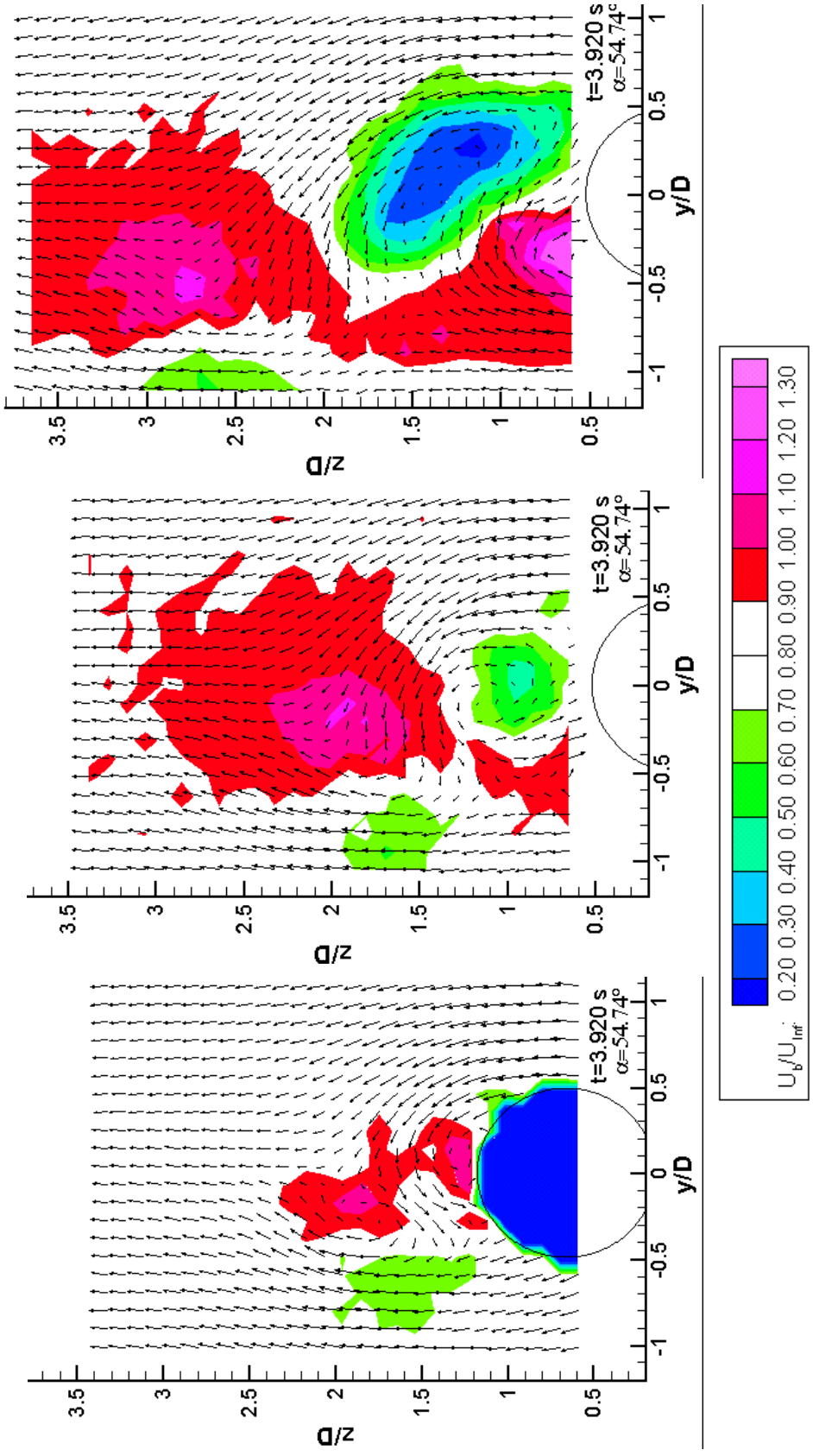

Figure 5.2.41: Three-Dimensional Velocity Fields at $t^* = 3.920$ s, $\alpha = 54.74°$, with $x_p/D = 4$: (a) x/D = 3, (b) x/D = 4, (c) x/D = 5. Contours Represent the Axial Velocity. The Coordinate System is Fixed to the Measurement Plane, which Is Rotated 18.0° from the Crossflow Plane for the Current Measurement.

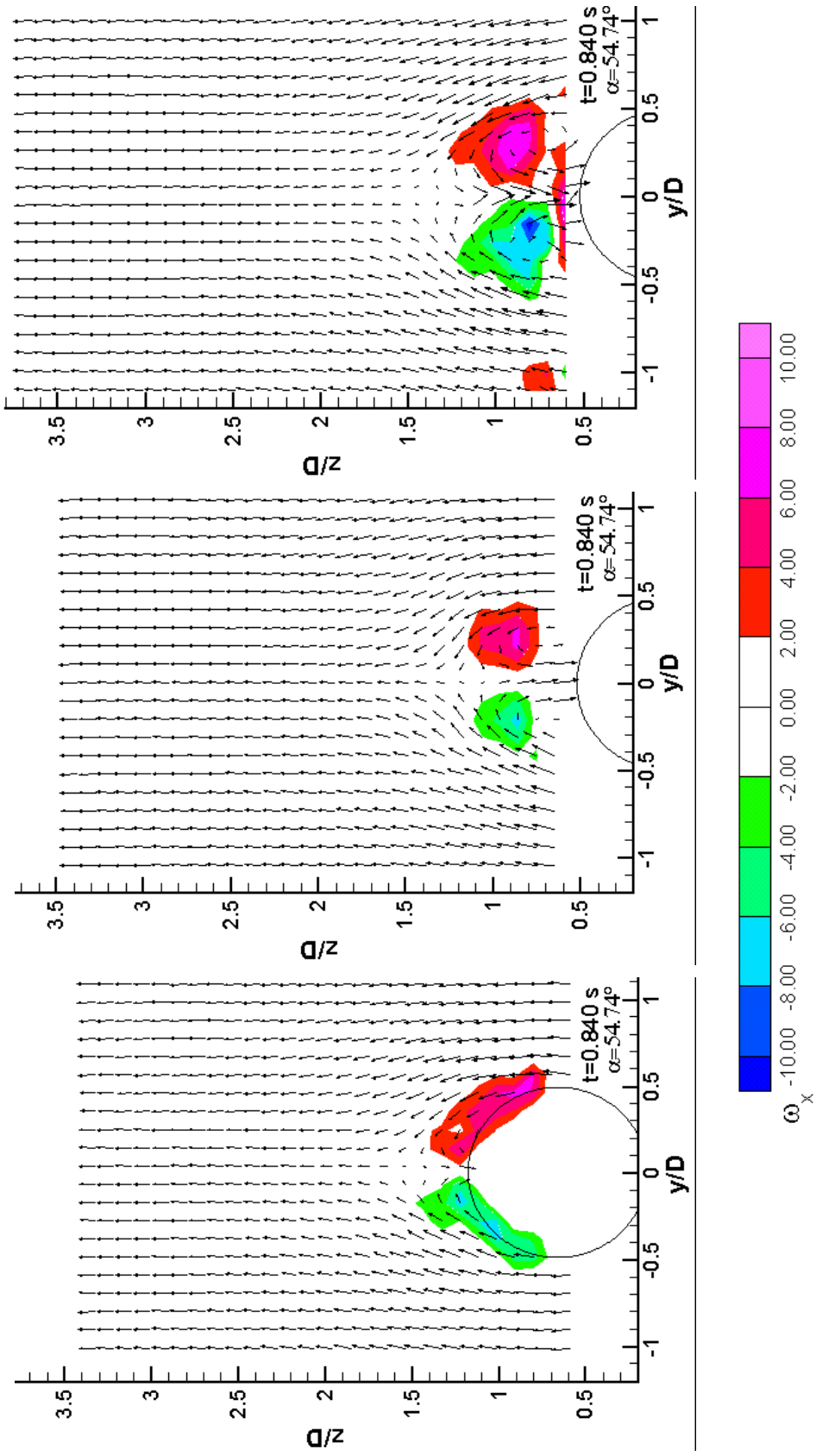

Figure 5.2.42: X-Component of Vorticity and In-Plane Velocity Vector Fields at $t^* = 0.840$ s, $\alpha = 54.74°$, with $x_p/D = 4$: (a) x/D = 3, (b) x/D = 4, (c) x/D = 5. Contours Represent the Axial Vorticity. The Coordinate System is Fixed to the Measurement Plane, which Is Rotated 18.0° from the Crossflow Plane for the Current Measurement.

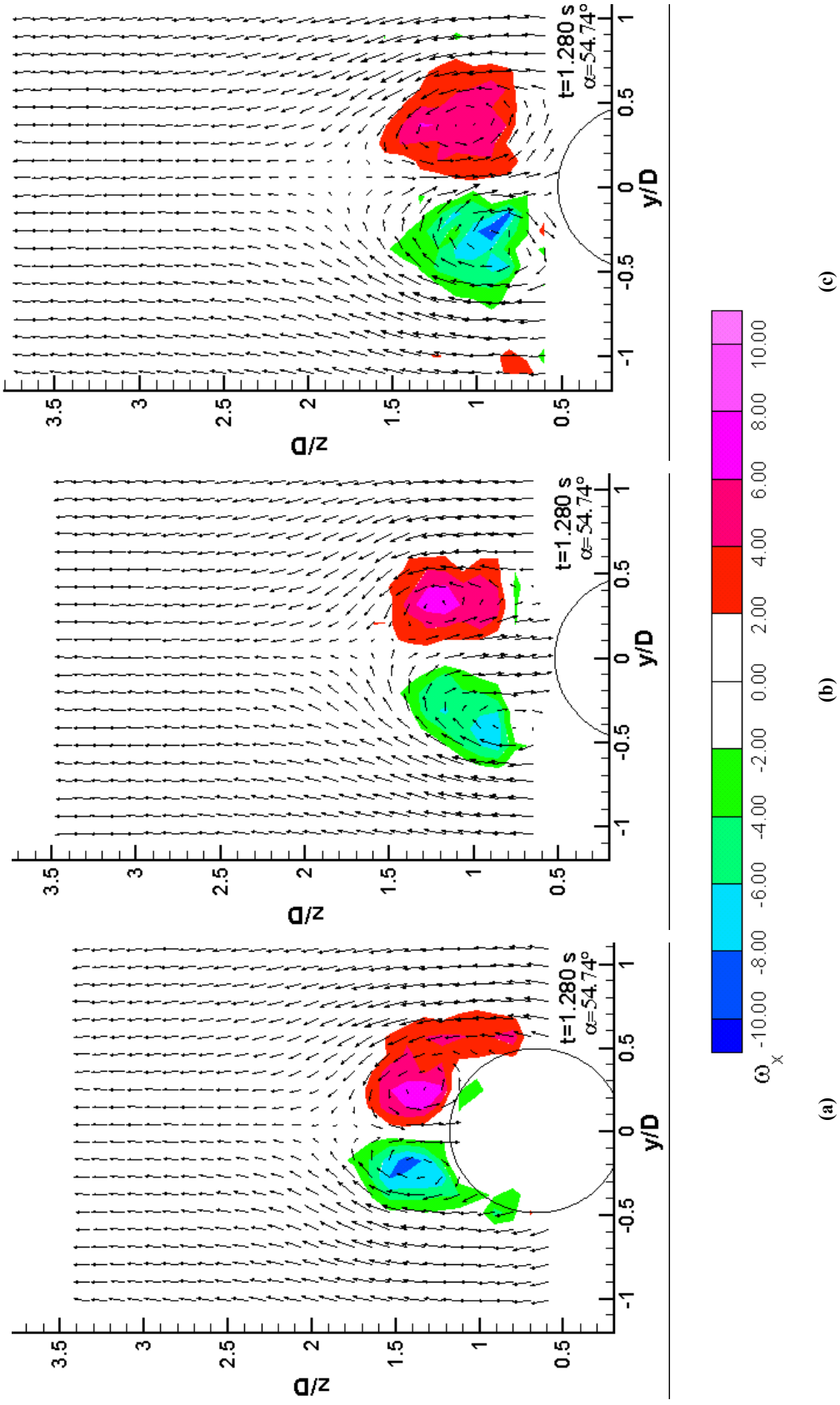

Figure 5.2.43: X-Component of Vorticity and In-Plane Velocity Vector Fields at t* = 1.280 s, α = 54.74°, with $x_p/D = 4$: (a) x/D = 3, (b) x/D = 4, (c) x/D = 5. Contours Represent the Axial Vorticity. The Coordinate System is Fixed to the Measurement Plane, which Is Rotated 18.0° from the Crossflow Plane for the Current Measurement.

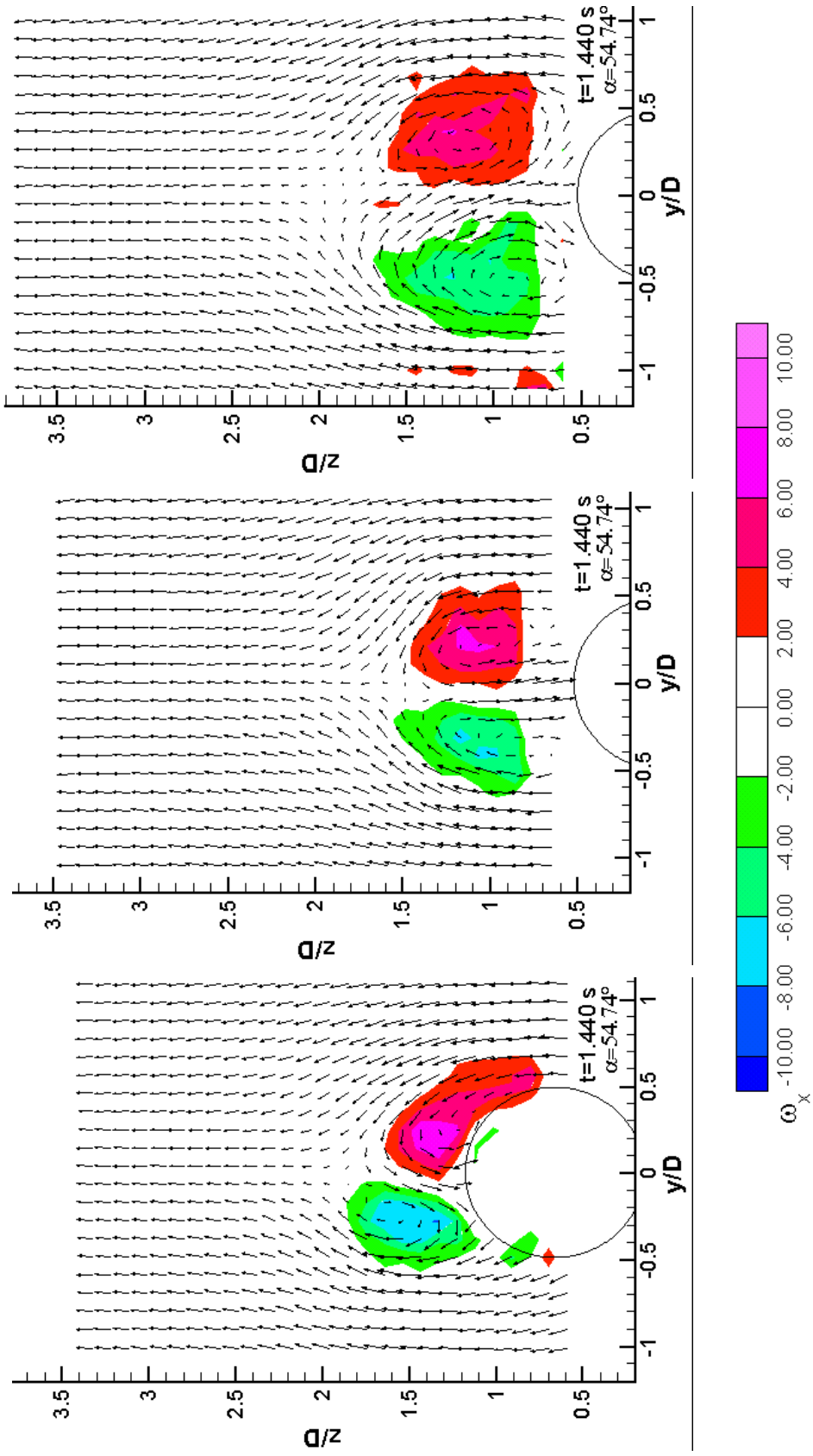

Figure 5.2.44: X-Component of Vorticity and In-Plane Velocity Vector Fields at $t^* = 1.440$ s, $\alpha = 54.74°$, with $x_p/D = 4$: (a) x/D = 3, (b) x/D = 4, (c) x/D = 5. Contours Represent the Axial Vorticity. The Coordinate System is Fixed to the Measurement Plane, which Is Rotated 18.0° from the Crossflow Plane for the Current Measurement.

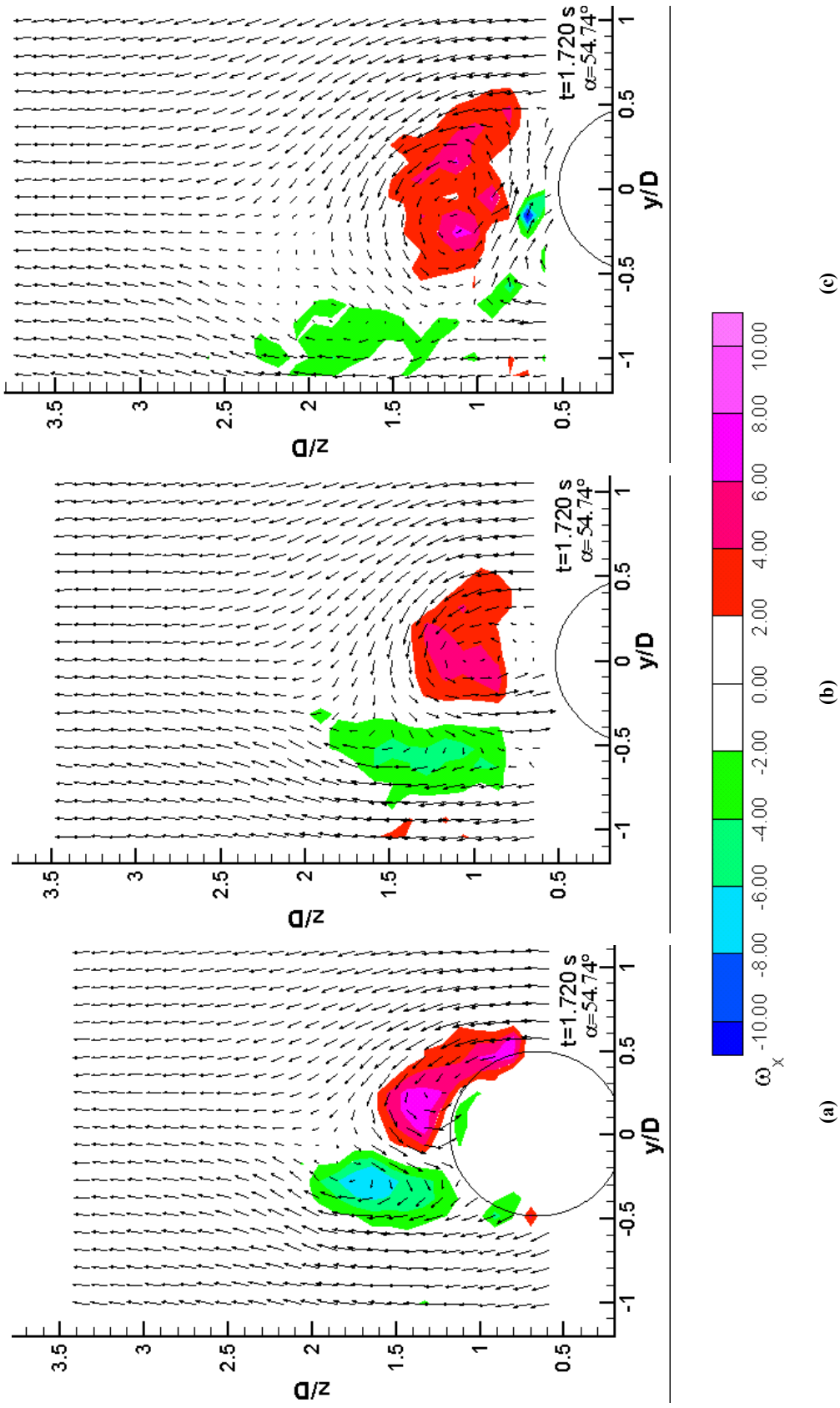

Figure 5.2.45: X-Component of Vorticity and In-Plane Velocity Vector Fields at $t^* = 1.720$ s, $\alpha = 54.74°$, with $x_p/D = 4$: (a) x/D = 3, (b) x/D = 4, (c) x/D = 5. Contours Represent the Axial Vorticity. The Coordinate System is Fixed to the Measurement Plane, which Is Rotated 18.0° from the Crossflow Plane for the Current Measurement.

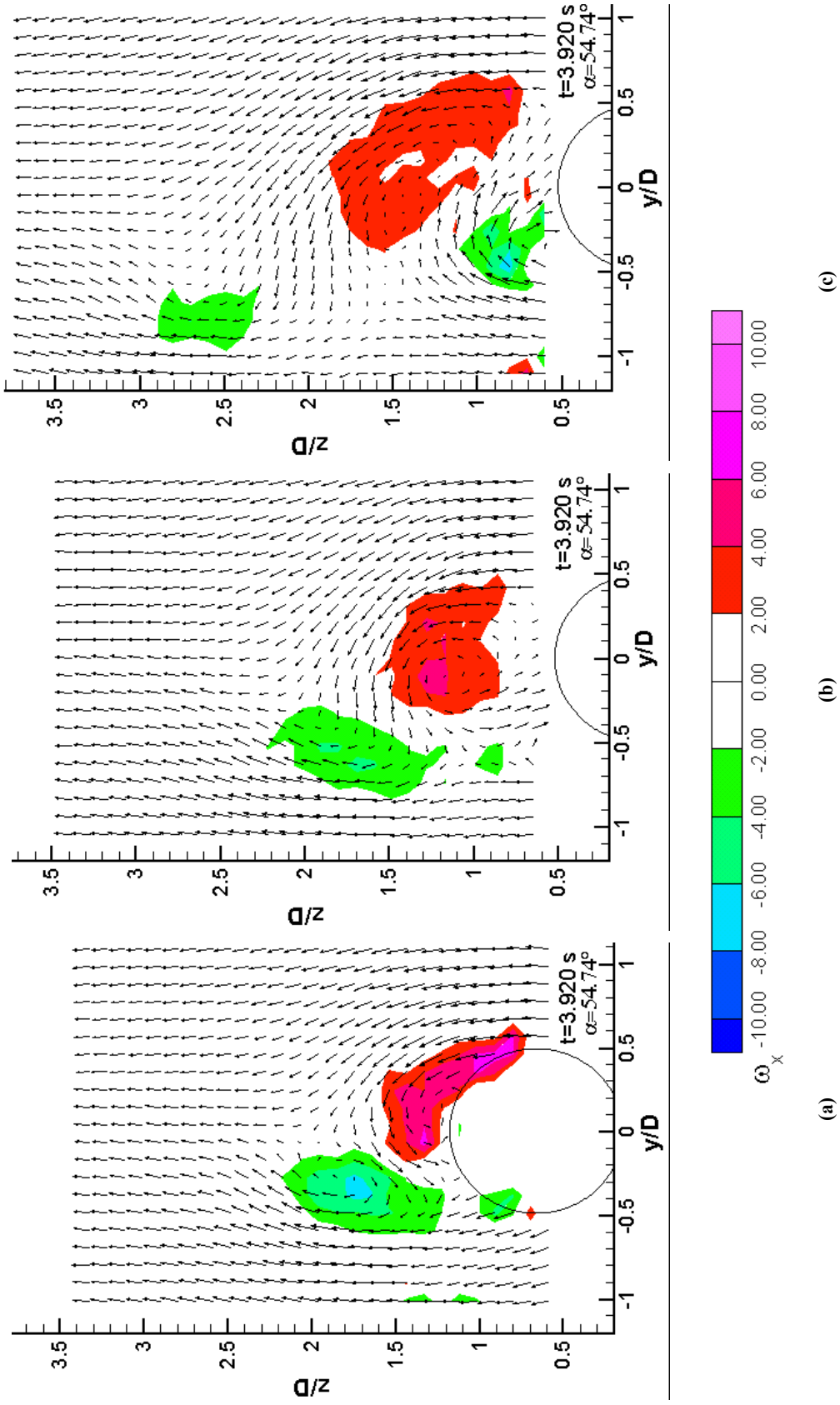

Figure 5.2.46: X-Component of Vorticity and In-Plane Velocity Vector Fields at t* = 3.920 s, α = 54.74°, with x_p/D = 4: (a) x/D = 3, (b) x/D = 4, (c) x/D = 5. Contours Represent the Axial Vorticity. The Coordinate System is Fixed to the Measurement Plane, which Is Rotated 18.0° from the Crossflow Plane for the Current Measurement.

5.2.4 The Mean Turbulent Kinetic Energy (TKE) Fields

As discussed in section 2.11, the ogive cylinder model was pitched ten times at each data location in the ESM Water Tunnel, and the results were ensemble averaged. The standard deviations from the ensemble-averaged velocities were recorded. Since the standard deviations represent the best estimate as to how far any one reading would differ from the mean, they may be taken to represent the average turbulent fluctuations, so that σ_u could represent $\overline{u'}$. We then can define the mean turbulent kinetic energy as

$$TKE = \frac{1}{2}(\overline{u'}^2 + \overline{v'}^2 + \overline{w'}^2) \tag{5.3}$$

The turbulent kinetic energy can be used to make characterizations of the level of unsteadiness in the flow at each point. In the case studied here, the unsteadiness of the vortices may result in fluctuations of the velocity in time and in space, both of which would contribute to the TKE.

Figures 5.2.47 – 5.2.50 present contours of TKE (nondimensionalized by U_∞^2) with the in-plane velocity vectors overlaid. All of these figures have three plots: (a) is for a time before the onset of the asymmetry at that measurement location, (b) is just after the convective asymmetry has passed through the location, and (c) is at the last data acquisition time, very close to the steady state. At low angles, before and just after the motion starts, the TKE resident in the wake flow is low (< 0.05, or 5% of U_∞^2). One exception to this generalization is that the standard deviation (and thus the TKE) is inordinately high for some points near the original model location. At these locations, laser light reflected from the body into the measurement volume skews the measurements not only when the model is at that location, but also for some time after it leaves.

The evolution of the TKE for x/D = 3, x_p/D = 0 is shown in figure 5.2.47. At this location, the turbulent kinetic energy increases to over 0.20 in the vicinity of the symmetric vortex pattern that forms as the model is pitched. The TKE field is more or less symmetric with respect to the angle of attack plane at this instant in time. As the asymmetry moves through the plane (fig. 5.2.47b) and as the flow then progresses toward the steady state (fig. 5.2.47c), the TKE levels remain virtually constant. At x/D = 5, x_p/D = 0, large amounts of TKE build up in the symmetric vortices, as shown in fig. 5.2.48a, where the TKE is greater than 0.40 for large regions of the vortices. The high TKE rapidly diffuses after the asymmetry convects through the plane (fig. 5.2.48b), and at steady state (fig. 5.2.48c), the TKE levels around the vortical regions are as low as those observed at x/D = 3, though distributed across a wider region. The evolution of the TKE at x/D = 4 is much like that at x/D = 5.

When x_p/D is changed to four, the measurement plane at x/D = 3 shows a small increase in TKE before the asymmetry arrives. Recall that the vortices at this station have a large formation delay due to the local effects of the pitch-up motion. However, as the asymmetry convects through the plane, the TKE actually increases (fig. 5.2.49b), and the TKE levels remain high to steady state (fig. 5.2.49c). At x/D = 4, an interesting situation occurs where the TKE associated with the vortices is asymmetric even though the in-plane components are symmetric, as shown in fig. 5.2.50a. This is especially intriguing because this is the only plane for which an asymmetry in TKE appears before the convective asymmetry, and because this is the only station where there is no motion of the cross-section normal to the flow. After the asymmetry passes, the TKE levels increase to above 0.40 in some places (fig. 5.2.50b) before diffusing to the steady-state levels with 0.20 as a maximum value (fig. 5.2.50c). The behavior of the TKE at x/D = 5, $x_p/D = 4$ is much like that of its counterpart when $x_p/D = 0$, and therefore is not shown.

There are some generalizations that appear to be true for the evolution of the turbulent kinetic energy. First, very high levels of TKE in the symmetric vortices are generated at x/D = 4 and x/D =5, for both pitch axes. These levels of TKE are reduced as the symmetry is broken, and the steady-state levels remain reduced with maximum values near 0.20. What is probably occurring is that the body motion causes a highly unsteady wake in which the symmetric vortices form. This unsteadiness can manifest itself in time and space, both contributing to the mean turbulent kinetic energy: First, the vortices will interact with each other and other unsteadiness in the wake, causing location changes from ensemble to ensemble. Second, the cores of the strong, symmetric vortices will be the likely site for flow transition of the free shear layers to turbulence, resulting in more temporal unsteadiness as well.

The ceasing of the motion reduces the strength of the vortices, leading to less temporal unsteadiness. The arrival of the asymmetric flow reduces the level of unsteadiness in the wake because the flow is moving from an inherently unstable state (due to the global hydrodynamic instability, if not the convective, c.f. section 1 of Hoerner [1965] and also Tobak, et al. [1990]) involving the two symmetric vortices to a more stable state with asymmetric vortices.

However, reversed effects occur for x/D = 3, $x_p/D = 4$. In this case, the asymmetric vortices exhibit higher core TKE than before the asymmetry. The cause of this reversal is unknown, and it results in different steady-state TKE when compared with the equivalent flow plane at x/D = 3, $x_p/D = 0$.

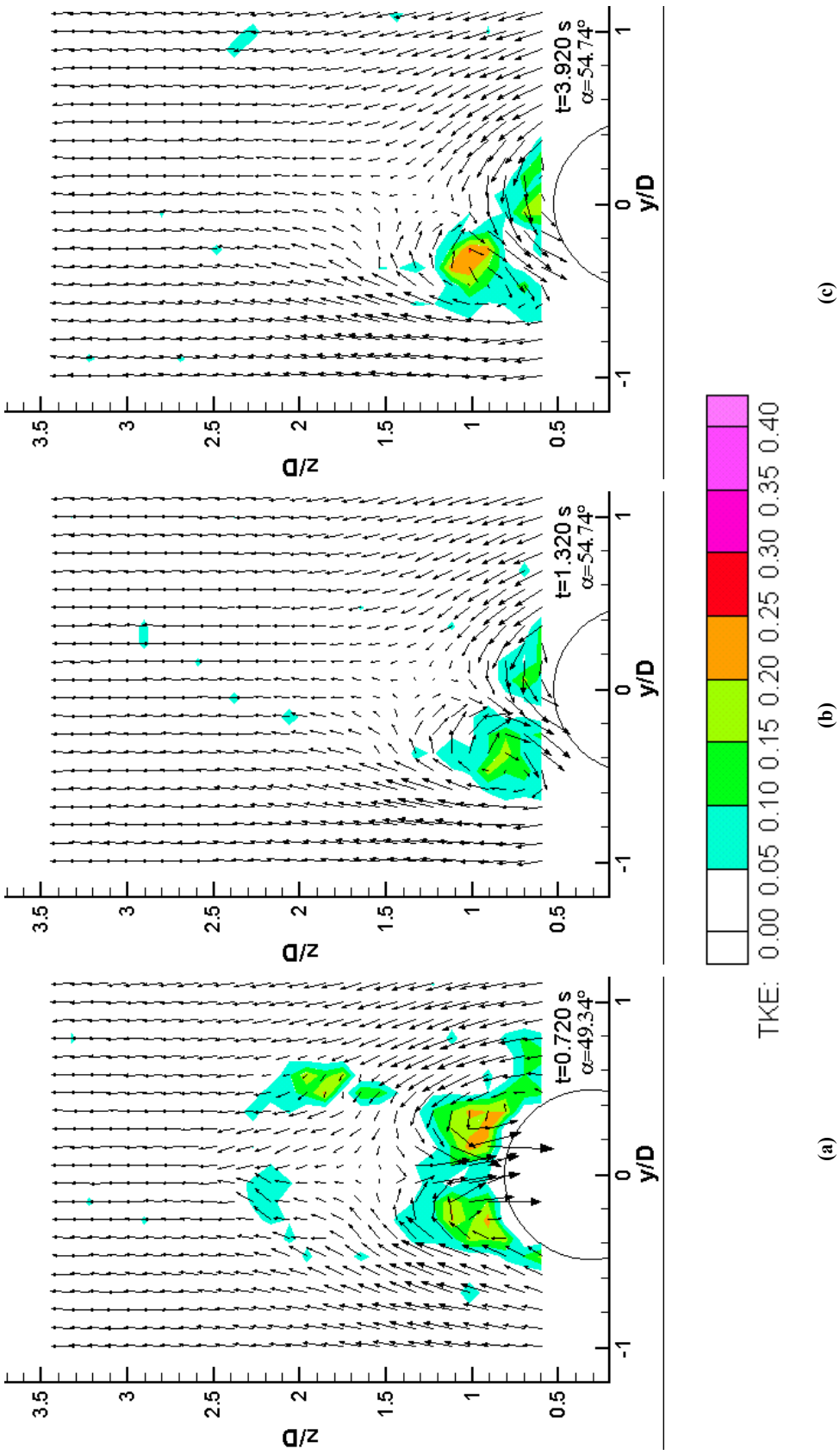

Figure 5.2.47: Nondimensional Turbulent Kinetic Energy Fields with $x_p/D = 0$, x/D = 3: (a) t* = 0.720 s, (b) t* = 1.320 s, (c) t* = 3.920 s. Contours Represent the Turbulent Kinetic Energy, on which the In-Plane Velocity Vectors are Overlaid. The Coordinate System is Fixed to the Measurement Plane, which is Rotated 7.2°, 18° and 18° from the Crossflow Plane, Respectively, for (a), (b) and (c).

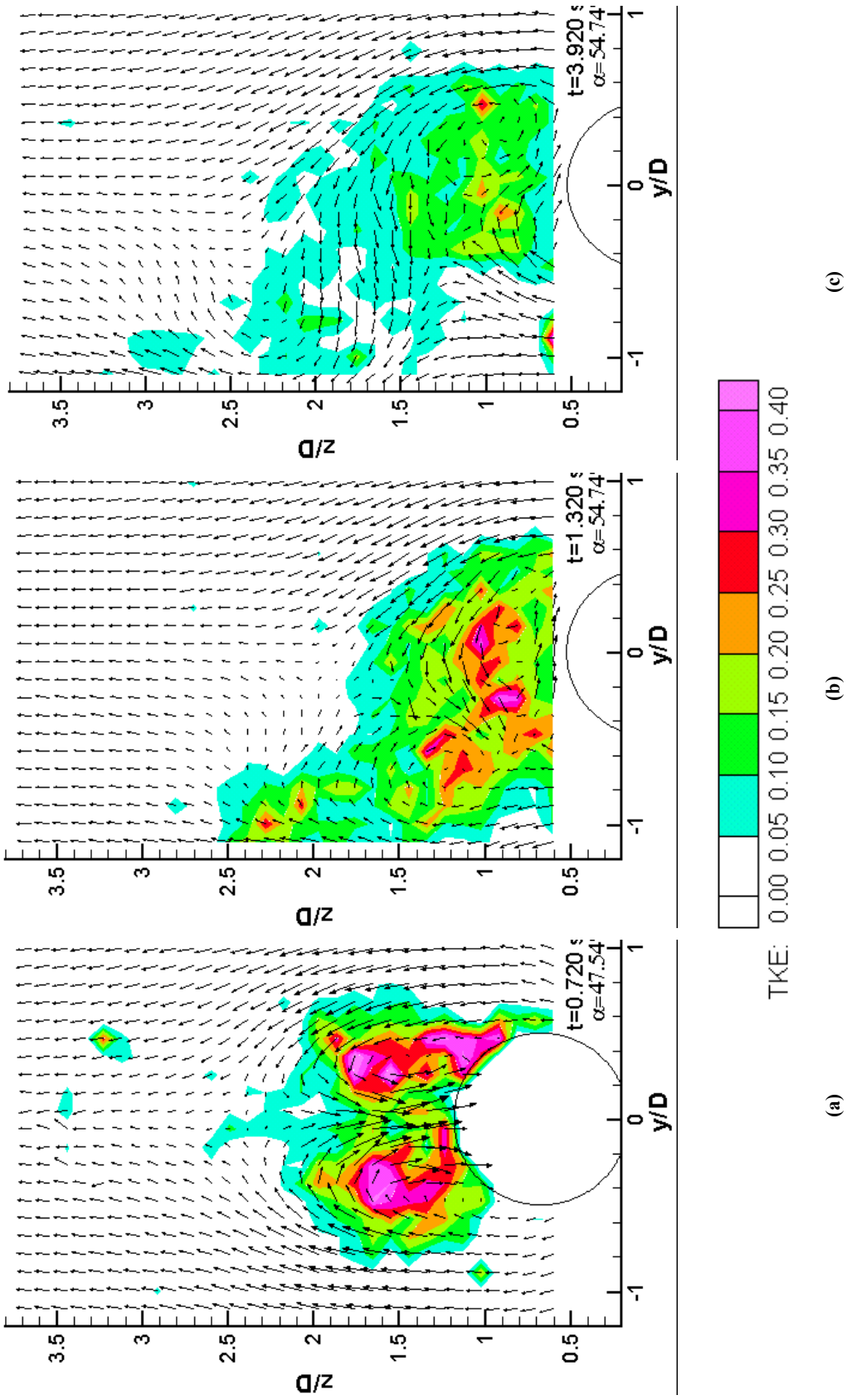

Figure 5.2.48: Nondimensional Turbulent Kinetic Energy Fields with $x_p/D = 0$, x/D = 5: (a) t* = 0.720 s, (b) t* = 1.320 s, (c) t* = 3.920 s. Contours Represent the Turbulent Kinetic Energy, on which the In-Plane Velocity Vectors are Overlaid. The Coordinate System is Fixed to the Measurement Plane, which is Rotated 7.2°, 18° and 18° from the Crossflow Plane, Respectively, for (a), (b) and (c).

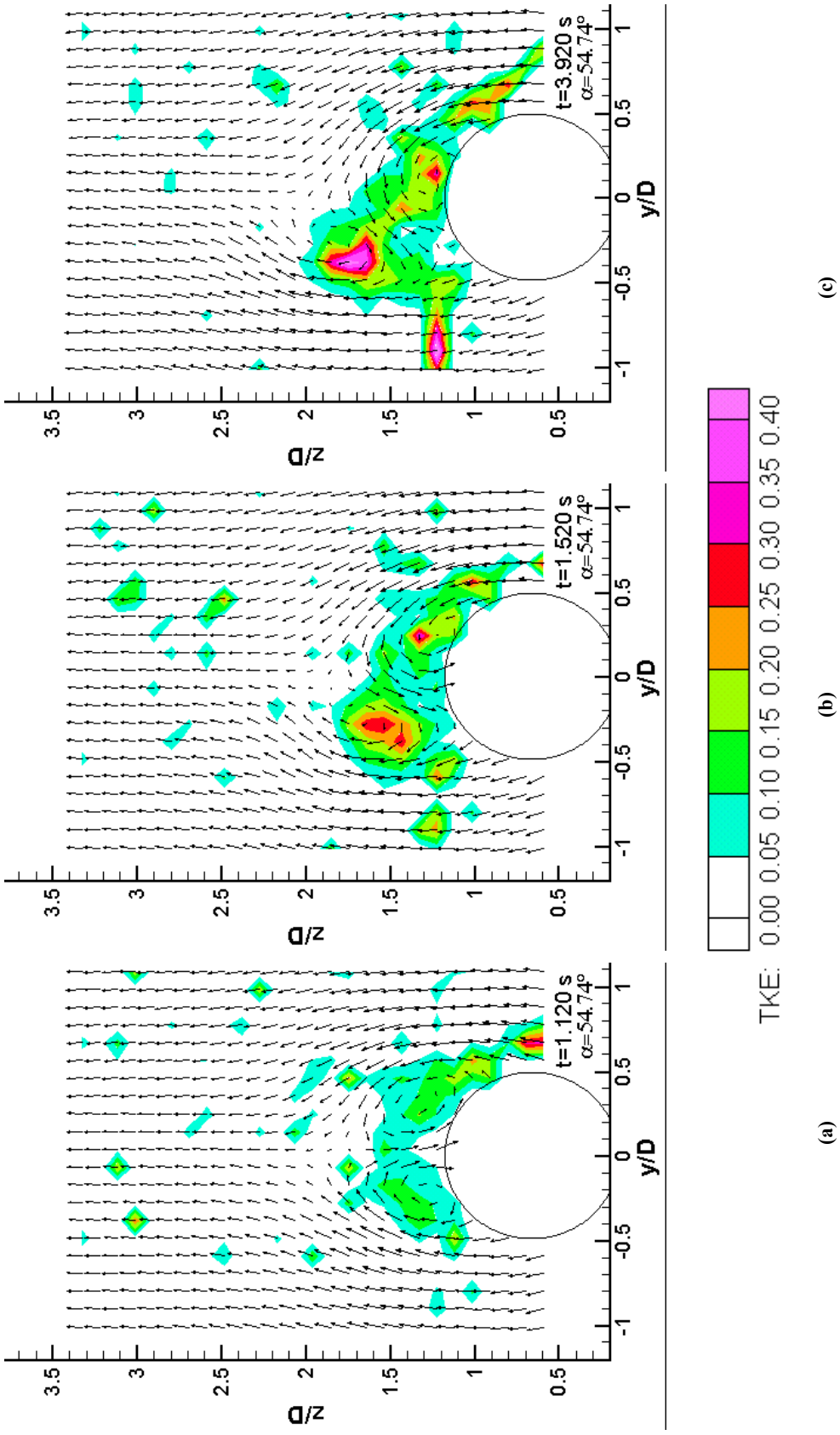

Figure 5.2.49: Nondimensional Turbulent Kinetic Energy Fields with $x_p/D = 4$, x/D = 3: (a) t* = 1.120 s, (b) t* = 1.520 s, (c) t* = 3.920 s. Contours Represent the Turbulent Kinetic Energy, on which the In-Plane Velocity Vectors are Overlaid. The Coordinate System is Fixed to the Measurement Plane, which is Rotated 18° from the Crossflow Plane for All Three Figures.

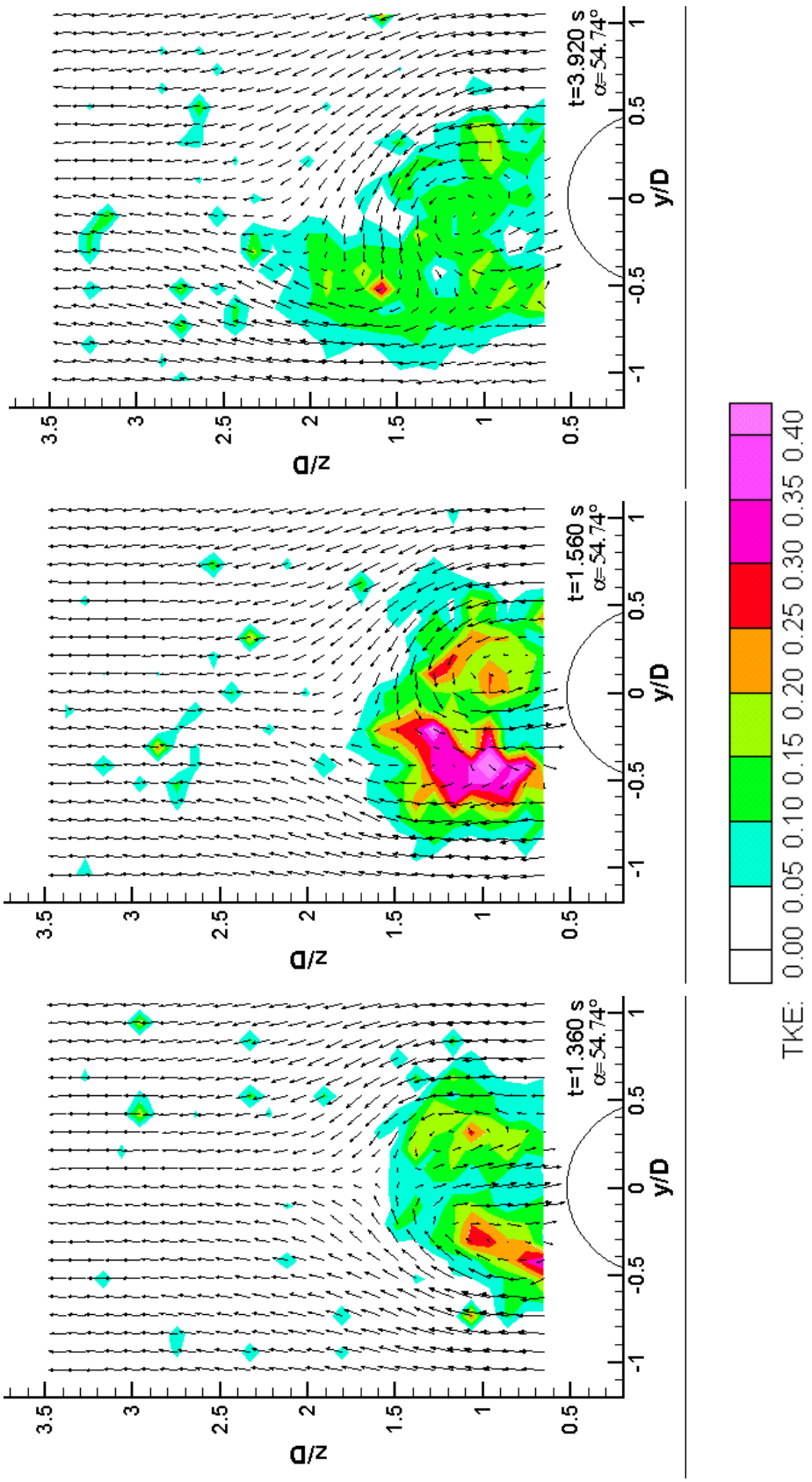

Figure 5.2.50: Nondimensional Turbulent Kinetic Energy Fields with $x_p/D = 4$, x/D = 4: (a) t* = 1.040 s, (b) t* = 1.360 s, (c) t* = 3.920 s. Contours Represent the Turbulent Kinetic Energy, on which the In-Plane Velocity Vectors are Overlaid. The Coordinate System is Fixed to the Measurement Plane, which is Rotated 18° from the Crossflow Plane for All Three Figures.

5.2.5 The Delay in Flow Development and Assessment of the Effect of Pitch-Axis Location

There are three questions that immediately spring to mind when examining the effects of setting the slender forebody in motion. The first is: How does the motion affect the vortex asymmetry? In the case of the pitch-up motion examined here, the relevant question is how does the motion delay the onset of asymmetry. Montividas, et. al. [1989] performed flow visualization over a pitching cone-cylinder for both pitch-up and pitch-down motions and for several different pitch axes. It was determined that the vortex state (symmetric or asymmetric) that existed initially was sustained, even to angles of attack where these states would not normally occur. The delays inherent in the motions were highly dependent upon the location of the pitch axes, and were higher for pitch axes located farther from the forebody tip. Based on these results, it was suggested that the correct reduced frequency for the pitching slender body problem should be $\dot{\alpha}\, x_p/U$. However, we see that for a pitch axis located at the forebody tip, the reduced frequency is zero, regardless of the dimensional value of $\dot{\alpha}$. Therefore, defining the reduced frequency in this fashion neglects local unsteady effects that are a function of the distance of the local plane from the pitch axis, and accounts only for the delay in the asymmetry onset. Ericsson's [1991] later analysis of the visualizations showed that if the asymmetry commenced at the forebody tip when $\alpha_{eff} = 2\delta$ (where $\alpha_{eff} = \alpha + \text{atan}(\dot{\alpha}\, x_p/U)$), and the convective time of the asymmetry was correctly accounted, then the α-regimes of flow symmetry/asymmetry compared more closely with theory. Qualitatively related results regarding flowfield asymmetry delays during pitching maneuvers were recorded by Iwanski [1997] with yaw force measurements, and Panzer, et. al. [1993] with velocity fields over a hemisphere cylinder with asymmetrical flow induced. The delay in the onset of the asymmetry will be mainly an inviscid phenomenon, because it can be described by asymmetry onset delay at the forebody tip and the convection of that asymmetry axially in the outer flow. Viscous effects and boundary-layer state will play minimal roles in these actions.

The second question is one that is usually asked in the case of many ramp-type maneuvers. That is, how long does it take the flow to return to return to the steady state? Unlike the delay in asymmetry onset discussed above, viscous effects will play a major role in this delay. The viscous effects will manifest themselves after the arrival of the asymmetry, as the pressure field generated by the vortical flow affects the separation conditions, which in turn are directly responsible for the vortical flow. This nonlinear interaction is well known (c.f. section 1.2), and is one of the major barriers to theoretical and computational approaches to the slender forebody problem, especially unsteady cases. Because of this

nonlinearity, the flow requires relatively more time to develop a steady state than it does to develop an asymmetric state.

Related to the first two questions is the third: How much does the unsteady flow lag or lead the steady flow at the same (in this case angular) positions? In the case of sectional or overall force measurements (Iwanski [1997]) or separation locations (Wetzel & Simpson [1998]), this question can be answered by direct comparison. In this case, where several planes of the flow are under examination, the variables to compare are less clear. Due to this difficulty, flowfield difference from the steady flow will not be examined in this investigation.

Asymmetry Delay

In an attempt to quantify the asymmetry, it was decided to compare the starboard and port flows for each plane. Two asymmetry variables are defined as

$$A_u = \frac{\sum_{i=1}^{N} \left| u - u_{symm} \right|}{N} \tag{5.5}$$

$$A_{v \cdot w} = \frac{\sum_{i=1}^{N} \sqrt{(v + v_{symm})^2 + (w - w_{symm})^2}}{N} \tag{5.6}$$

where the "symm" subscript refers to the quantity at the symmetric location across the angle-of-attack plane from the location of the non-subscripted value. The A_u and $A_{v \cdot w}$ variables represent the average axial and in-plane asymmetry per point, respectively. An additional advantage of defining the variables in this fashion is the reduction of multiple points of three-dimensional velocities to two variables per plane. These calculations were performed with nondimensional variables.

Figure 5.2.50 shows the variation of A_u and $A_{v \cdot w}$ as a function of time for all six planes of data. By using this asymmetry data in conjunction with plots of three-dimensional velocities, the A_u and $A_{v \cdot w}$ were calculated from the dimensionless three-dimensional velocity data for all x/D and x_p/D locations. The general trend of $A_{v \cdot w}$ is the same for all six planes. Small levels of asymmetry occur during and just after the motion, but the asymmetry levels rise sharply and irrevocably as the asymmetry is convected through the location in question. The time at which A_u levels increase is not as clear-cut, but it is obvious

that A_u increases as the model moves from low to high angles of attack, especially for x/D = 5, the location where asymmetries in the axial velocity were very evident in the three-dimensional velocity fields.

A_u and $A_{v\cdot w}$ were calculated from the dimensionless three-dimensional velocity data for all x/D and x_p/D locations. The resulting data is presented in figure 5.2.50. The general trend of $A_{v\cdot w}$ is the same for all six planes. Small levels of asymmetry occur during and just after the motion, but the asymmetry levels rise sharply and irrevocably as the asymmetry is convected through the location in question. The time at which A_u levels increase is not as clear-cut, but the it is obvious that A_u increases as the model moves from low to high angles of attack, especially for x/D = 5.

Data for each measurement location in figure 5.2.50 contains at least one region of sharply increasing $A_{v\cdot w}$. By observing the three-dimensional velocity fields it was possible to determine visually at what time the in-plane asymmetry arrived. When comparing two times, it was discovered that the onset of the asymmetry corresponded to the point at the base of the sharply increasing region that leads to the largest increase in $A_{v\cdot w}$. Thus, the $A_{v\cdot w}$ values calculated from equation 5.6 capture the degree of physical asymmetry.

The hydrodynamic instability that causes the vortex asymmetry will assert itself at the forebody tip when the angle of attack is approximately equal to 2δ, the included angle at the ogive tip. The geometry of the 3.5-caliber tangent-ogive cylinder (c.f. Appendix D) shows that the half-angle at the tip is 16.3°, so that the asymmetry should become apparent near 32.6° for a sharp forebody tip. Considering the bluntness ratio of the model (R_t/R = 1/50), and results from wind-tunnel testing (not shown), it was determined that the asymmetry onset would occur nearer 34°. When the model is in motion, the effect of the motion of the effective angle of attack at the forebody tip must be considered. The effective angle of attack for the maneuver in question is defined as

$$\alpha_{eff} = \alpha + \text{atan}\left(\frac{-\dot{\alpha} x_p}{U_\infty}\right) \tag{5.7}$$

so that when the angle of attack is increasing and x_p is nonzero, the local effective angle of attack lags the geometric angle, suppressing the hydrodynamic instability. For x_p/D = 0, we see that $\alpha_{eff} = \alpha$. For the motion performed here (figure 5.2.4), the geometric angle of attack at which α_{eff} = 34° is approximately 53°.

We can calculate the theoretical asymmetry arrival time at any station by using the following method. First, determine the dimensionless time at which the $\alpha_{eff} = 34°$. Then, since the dimensionless time was calculated per axial diameter, x/D represents the asymmetry convection time to x. Combining these two times gives the total delay time of the asymmetry for the axial location in question. Using the visual evidence contained in the unsteady three-dimensional velocity, as well as figure 5.2.50, the actual asymmetry arrival times can be ascertained. Table 5.1 lists the expected asymmetry generation times for $x_p/D = 0$ and $x_p/D = 4$, the expected and actual asymmetry arrival times, and the average convection speed to each measurement location. The average convection speed is calculated by dividing the actual arrival time of the asymmetry by x/D.

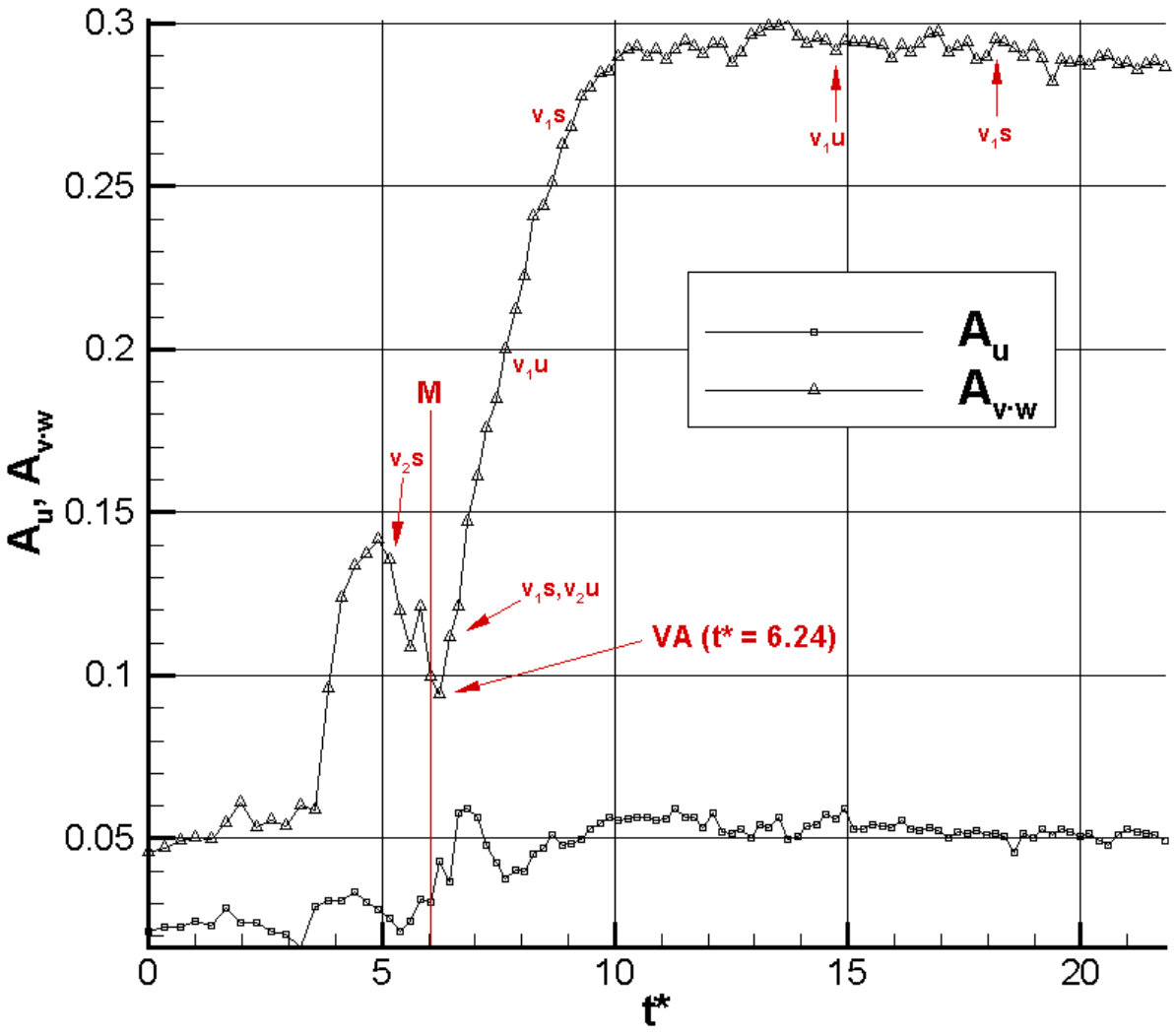

Figure 5.2.51(a): Axial (A_u) and In-plane ($A_{v\cdot w}$) Flowfield Asymmetry as a Function of Time, x/D = 3, x_p/D = 0. M Denotes the End of the Motion ($\alpha = 54.74°$), and VA Denotes the Time at which the Vortex Asymmetry is First Observed in the In-Plane Velocity Field. V_1 and V_2 refer to the First and Second Vortices, Respectively. U and S Denote the Foci Corresponding to the Vortices as Unstable or Stable.

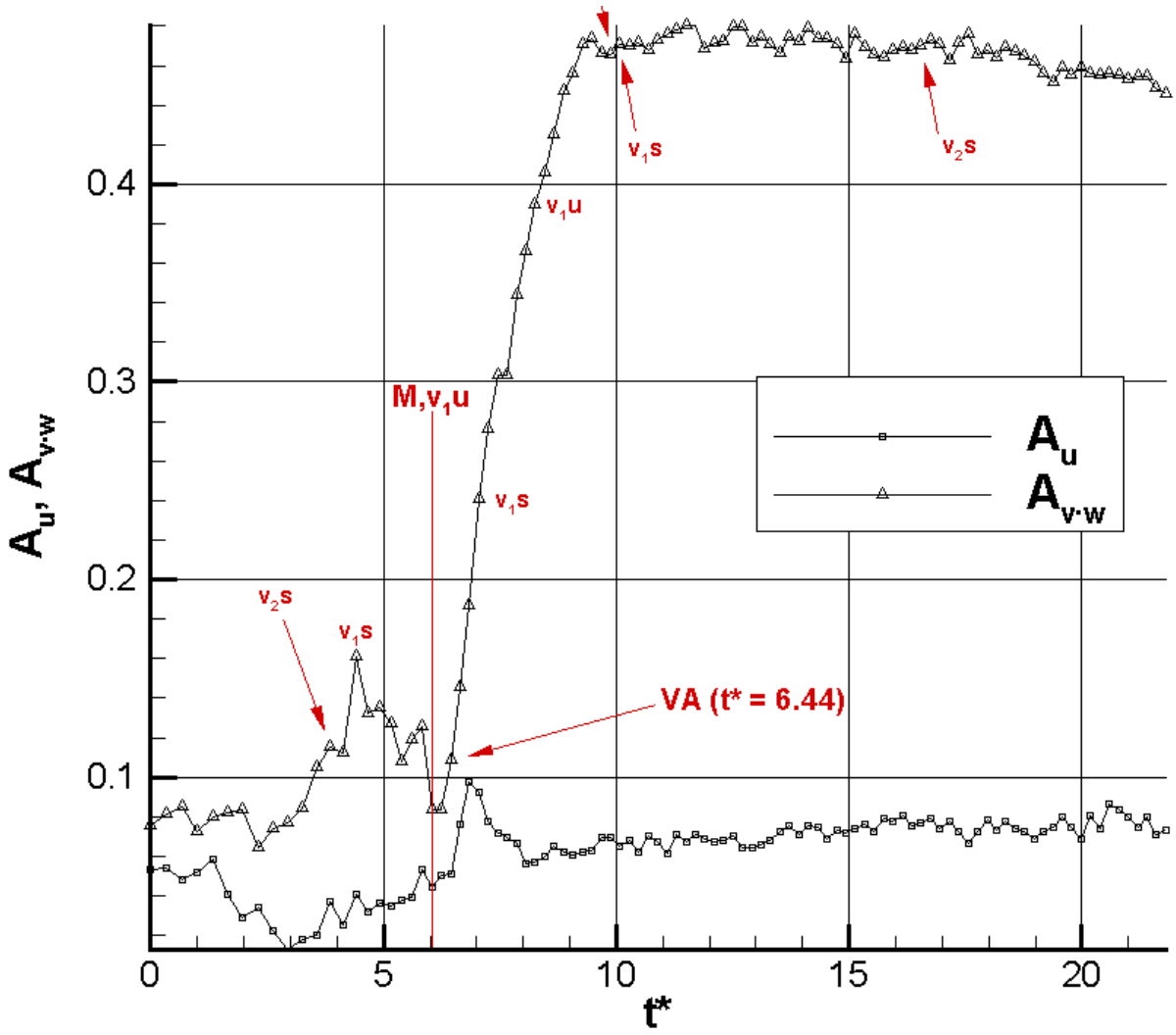

Figure 5.2.51(b): Axial (A_u) and In-plane ($A_{v\cdot w}$) Flowfield Asymmetry as a Function of Time, x/D = 4, x_p/D = 0. M Denotes the End of the Motion (α = 54.74°), and VA Denotes the Time at which the Vortex Asymmetry is First Observed in the In-Plane Velocity Field. V_1 and V_2 refer to the First and Second Vortices, Respectively. U and S Denote the Foci Corresponding to the Vortices as Unstable or Stable.

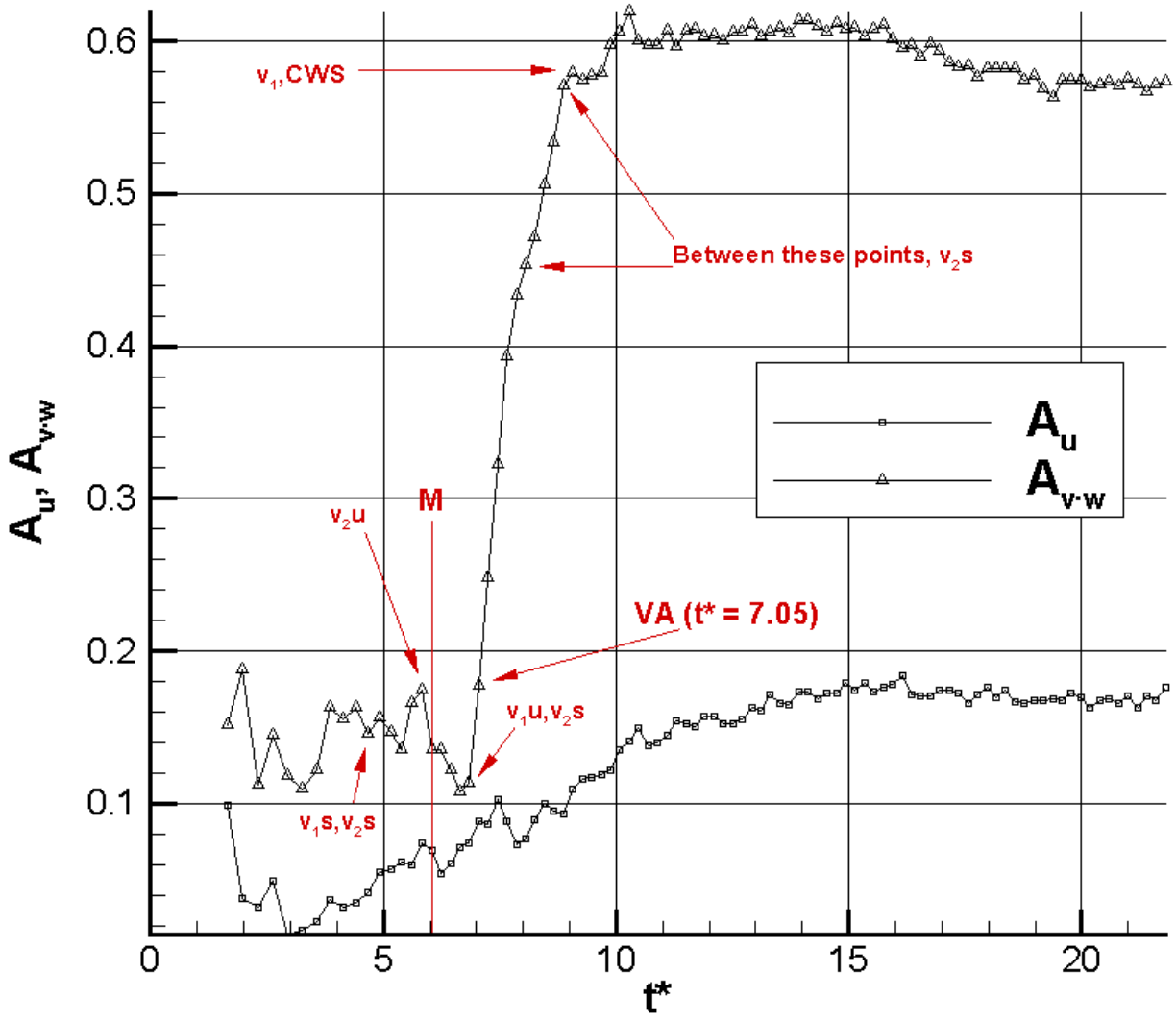

Figure 5.2.51(c): Axial (A_u) and In-plane ($A_{v\cdot w}$) Flowfield Asymmetry as a Function of Time, x/D = 5, x_p/D = 0. M Denotes the End of the Motion (α = 54.74°), and VA Denotes the Time at which the Vortex Asymmetry is First Observed in the In-Plane Velocity Field. V_1 and V_2 refer to the First and Second Vortices, Respectively. U and S Denote the Foci Corresponding to the Vortices as Unstable or Stable. CWS Signifies Combination of a Foci with the Primary Saddle.

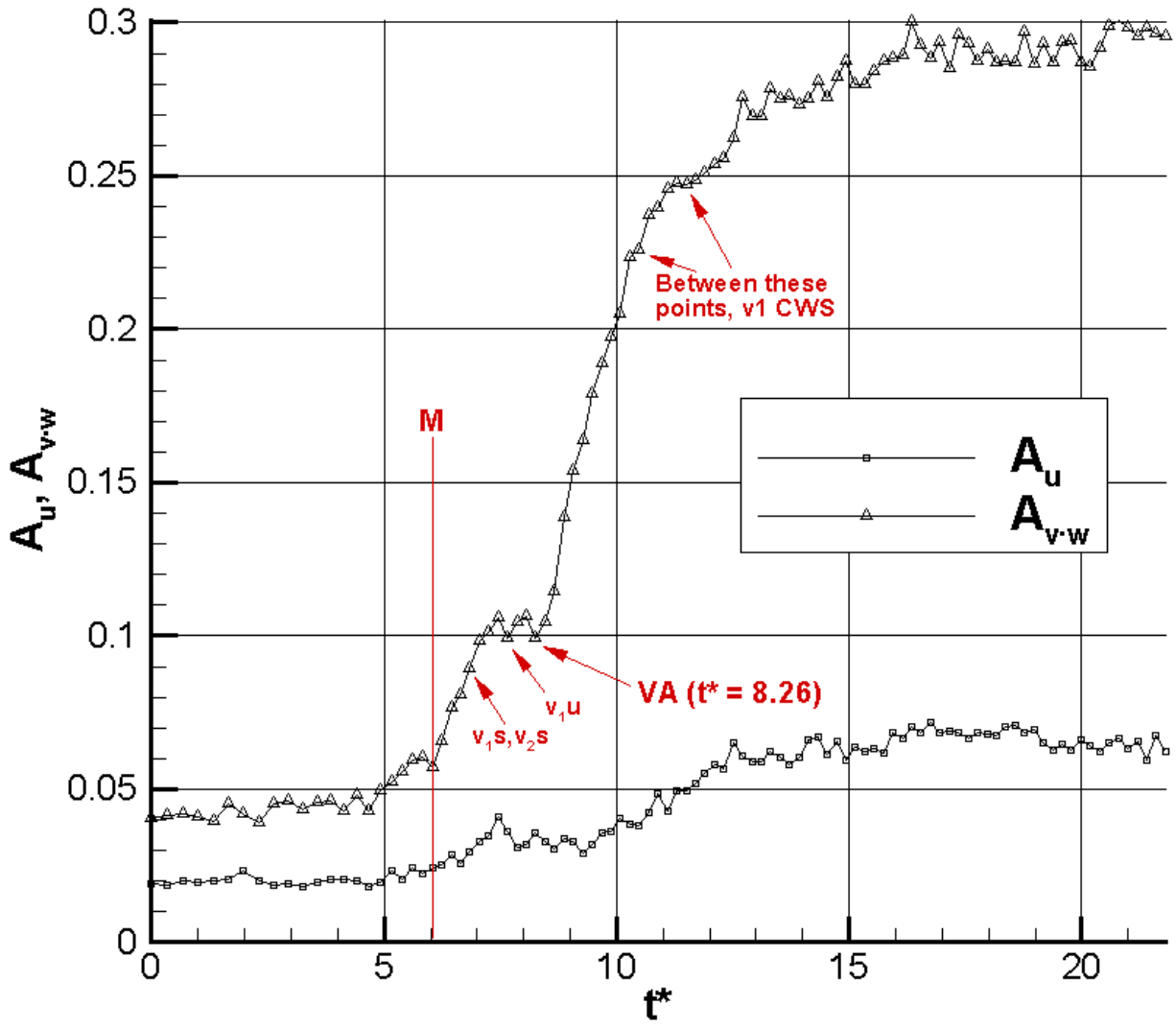

Figure 5.2.51(d): Axial (A_u) and In-plane ($A_{v\cdot w}$) Flowfield Asymmetry as a Function of Time, x/D = 3, x_p/D = 4. M Denotes the End of the Motion (α = 54.74°), and VA Denotes the Time at which the Vortex Asymmetry is First Observed in the In-Plane Velocity Field. V_1 and V_2 refer to the First and Second Vortices, Respectively. U and S Denote the Foci Corresponding to the Vortices as Unstable or Stable. CWS Signifies Combination of a Foci with the Primary Saddle.

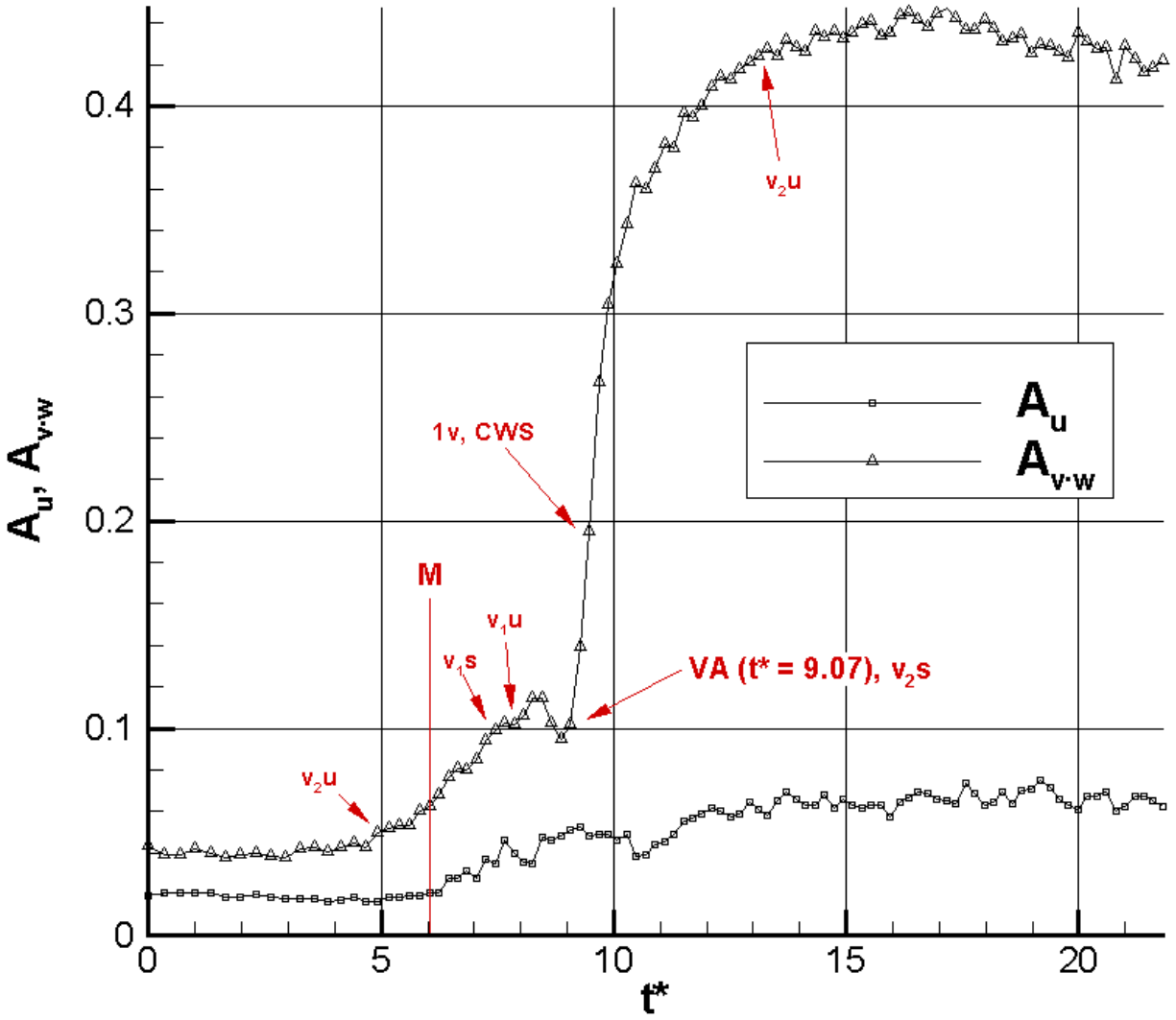

Figure 5.2.51(e): Axial (A_u) and In-plane ($A_{v\cdot w}$) Flowfield Asymmetry as a Function of Time, x/D = 4, x_p/D = 4. M Denotes the End of the Motion ($\alpha = 54.74°$), and VA Denotes the Time at which the Vortex Asymmetry is First Observed in the In-Plane Velocity Field. V_1 and V_2 refer to the First and Second Vortices, Respectively. U and S Denote the Foci Corresponding to the Vortices as Unstable or Stable. CWS Signifies Combination of a Foci with the Primary Saddle.

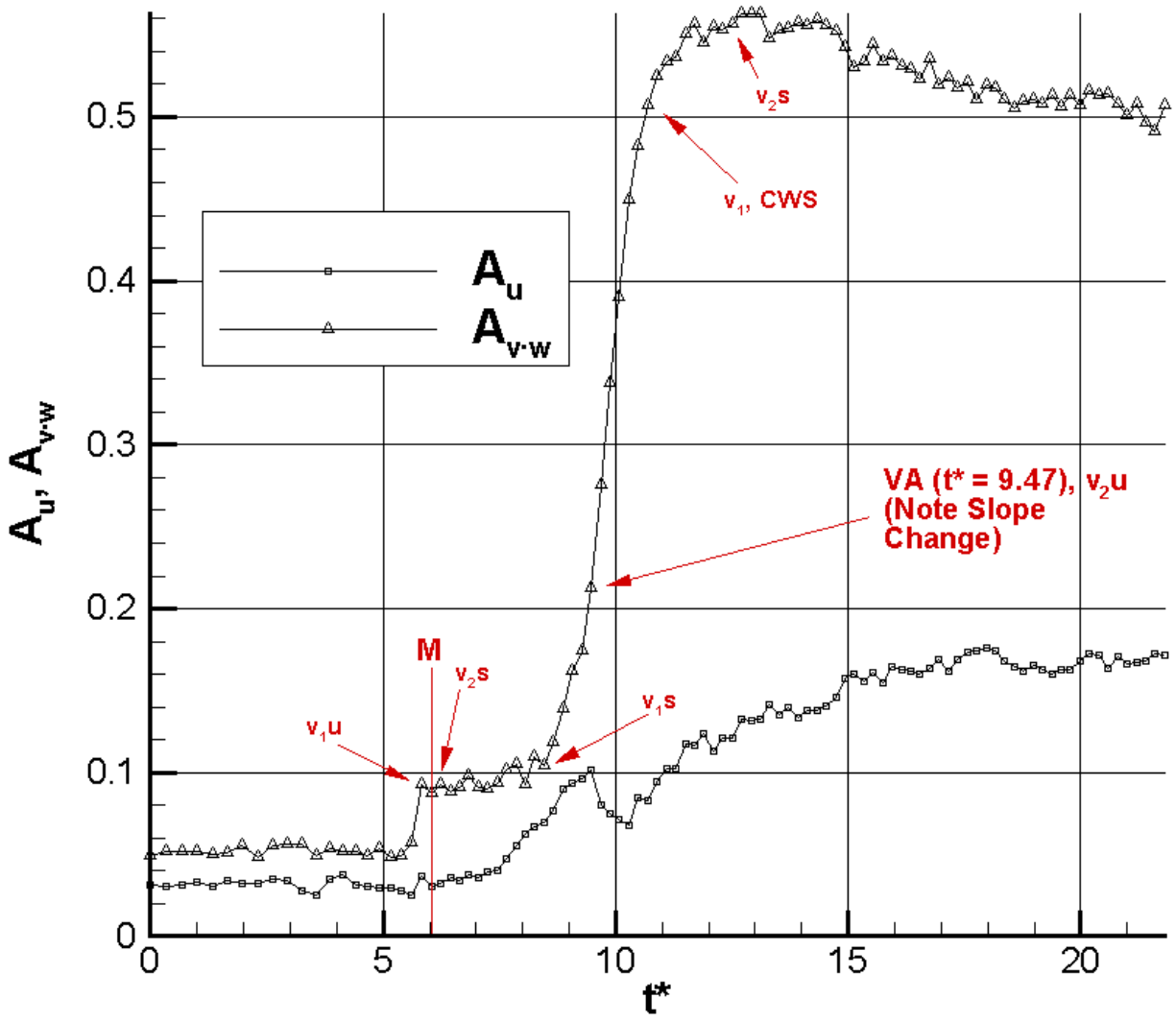

Figure 5.2.51(f): Axial (A_u) and In-plane ($A_{v\cdot w}$) Flowfield Asymmetry as a Function of Time, x/D = 5, x_p/D = 4. M Denotes the End of the Motion (α = 54.74°), and VA Denotes the Time at which the Vortex Asymmetry is First Observed in the In-Plane Velocity Field. V_1 and V_2 refer to the First and Second Vortices, Respectively. U and S Denote the Foci Corresponding to the Vortices as Unstable or Stable. CWS Signifies Combination of a Foci with the Primary Saddle.

Table 5.1 Asymmetry Generation Times, Expected and Actual Asymmetry Arrival Times, Average Axial Convection Speed for the Asymmetry, and Times Required for Flow to Reach Steady State.

	Asymmetry Generation Times: $t_g^* = t^*\,|_{\alpha_{Eff}=34°}$	$x_p/D = 0$: $t_g^* = 3.77$	$x_p/D = 4$: $t_g^* = 5.64$	
	Expected Asymmetry Arrival Time, $t_{eta}^* = t_g^* + x/D$ Location	**Actual Asymmetry Arrival Time, t_{ata}^***	**Average Asymmetry Convection Speed†, $U_{ac} = x/[D\cdot(t_{ata}^* - t_g^*)]$**	**Time to Reach Steady State from Asymmetry Generation‡, $t_{ss}^* - t_g^*$**
$x_p/D = 0$:				
x/D = 3	6.77	6.24	1.21	7.73
x/D = 4	7.77	6.44	1.50	10.55
x/D = 5	8.77	7.05	1.52	12.57
$x_p/D = 4$:				
x/D = 3	8.64	8.26	1.15	7.27
x/D = 4	9.64	9.07	1.17	9.49
x/D = 5	10.64	9.47	1.31	9.90

† The value displayed in this column represents the average dimensionless convection speed as the asymmetry moves from the forebody tip to the location in question. Recall that the dimensionless time is evaluated by integrating the theoretical axial velocity over time: $(U_\infty/D)\int \cos\alpha\cdot dt$. Therefore, if $U_{ac} = 1$, the average convection speed agrees with the assumed theoretical value $U_\infty\cdot\cos\alpha$ over the time period in question. If $U_{ac} > 1$, the actual convection speed is faster than the assumed value, if $U_{ac} < 1$, the convection rate is slower than the assumed value.

‡ The flow is defined to have reached the steady state when the average difference per flowfield point from the final time record (accounting for average flow unsteadiness) is within $0.001\cdot U_\infty$.

In table 5.1, we observe that at x/D = 3, the actual and theoretical asymmetry arrival times agree reasonably well for both pitch-axis locations. However, the actual arrival times diverge from theory for larger axial positions. In fact, at $x_p/D = 0$, the asymmetry convects through all three measurement locations in about 0.8 of a dimensionless time period! The asymmetry arrives at x/D = 5 about 1.75 dimensionless time periods earlier for $x_p/D = 0$ and about 1.2 periods earlier for $x_p/D = 4$.

It is possible to explain some of the time discrepancy by realizing that the theoretical convection speed is assumed to be $U_\infty \cdot \cos\alpha$. The theory will only predict the experimental data correctly if the average convection speeds are comparable. It is reasonable to expect that the asymmetry, once generated, would convect axially through the vortical regions. If this is the case, then the fact that the symmetric vortices tend to entrain axial flow equal to or greater than the component of U_∞ projected onto the measurement plane means that the asymmetry will convect at more rapid rates. Recall that when $x_p/D = 0$, the axial velocity in the cores of the symmetric vortices was higher than if $x_p/D = 4$. Compare, for example, fig. 5.2.12 to fig. 5.2.28, where data were acquired at the same time after motion commencement. This higher velocity could explain the difference between the average convection rates for the two pitch axes. However, even the presence of higher axial velocities cannot explain why the asymmetry convects through the three planes at $x_p/D = 0$ with an average rate of $2.47 \cdot U_\infty \cdot \cos\alpha$. Since this part of the convection occurs when $\alpha = 54.74°$ (the motion is completed), the corresponding dimensional velocity is about $2.0 \cdot U_\infty$. This value is consistent to the highest axial velocities measured, which were in the range of $1.90 \cdot U_\infty$ to $2.0 \cdot U_\infty$, but these were not sustained for longer than a few time records, and almost all of the instances of velocities of this magnitude were measured at x/D = 5.

Progression of Flow to Steady State

In order to determine how quickly the flows over the pitching tangent-ogive cylinder progresses to the steady state, it is necessary to define a variable which relates the flowfield at any time to the steady-state flowfield. Data acquisition proceeded for long enough ($t^* = 16$) past the end of the motion to allow the flow to achieve the steady state. Therefore, we should define a steady-state variable based on the difference between the flowfield at any given time, as compared to the flowfield at the last time record (the steady state flowfield). However, if we are going to make a proper comparison, it should also account for the natural unsteadiness of the flowfield, which can be estimated by using the turbulent kinetic energy (TKE). Therefore we define SS, the steady-state variable as the following:

$$SS = \sum_{k=0}^{k_{max}} \sum_{j=0}^{j_{max}} \left\{ \left[(u_{jk} - u_{ss})^2 + (v_{jk} - v_{ss})^2 + (w_{jk} - w_{ss})^2 \right] - TKE_{ss} \right\} \qquad (5.8)$$

Where j and k are the indices to specify the planar location of the data point and the "ss" subscript indicates evaluation at the steady-state flowfield. TKE is defined as in equation 5.3.

The SS variable is graphed as a function of t* in figure 5.2.52. The first three figures (5.2.52 a, b, c) show the progression to steady state for $x_p/D = 0$, and the last three figures (5.2.52 d, e, f) show the same for $x_p/D = 4$. The time required for the flow to reach steady state may be thought of as a measure of the overall disturbance of the flow. From forcing and moment of inertia considerations, we would expect that a body pitching about its apex ($x_p/D = 0$) would generate more disturbance to the flow than a body pitching about a point closer to its center of mass ($x_p/D = 4$). By examining figure 5.2.52, we see that for $x/D = 3$ and $x/D = 4$, the steady state is reached faster for $x_p/D = 0$. However, for $x_p/D = 5$, the progression to steady state is faster for $x_p/D = 4$. This indicates that for the pitch-axis location does affect not only the delay in the initial appearance of the asymmetry, but in the delay in the appearance of the steady-state flow. We can get another perspective by looking at the difference between the generation of the asymmetry (t^*_g) and the flow reaching steady state (t^*_g). This difference is shown in the last column of Table 5.1. We see that for all measurement axis locations, this difference is lower for $x_p/D = 4$ than for $x_p/D = 0$. The conclusion we can draw from this information is that the pitch axis located near the center of mass of the body (in this case $x_p/D = 4$) promotes a faster progression to steady state, even though the asymmetry onset has a greater delay and the axial flow convection rates are slower for this axis than for pitching about the apex.

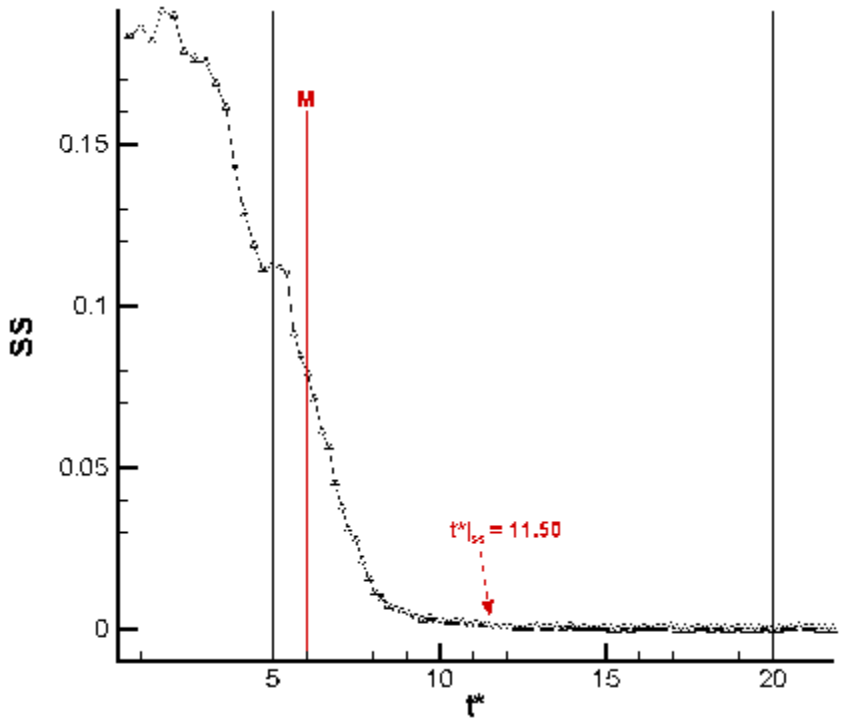

Figure 5.2.52(a): Difference from the Steady State as a Function of t* for x/D = 3, x_p/D = 0. M Denotes the End of the Motion (α = 54.74°), and $t^*|_{ss}$ Denotes When Average Difference per Flowfield Point is Less than 0.1% of U_∞.

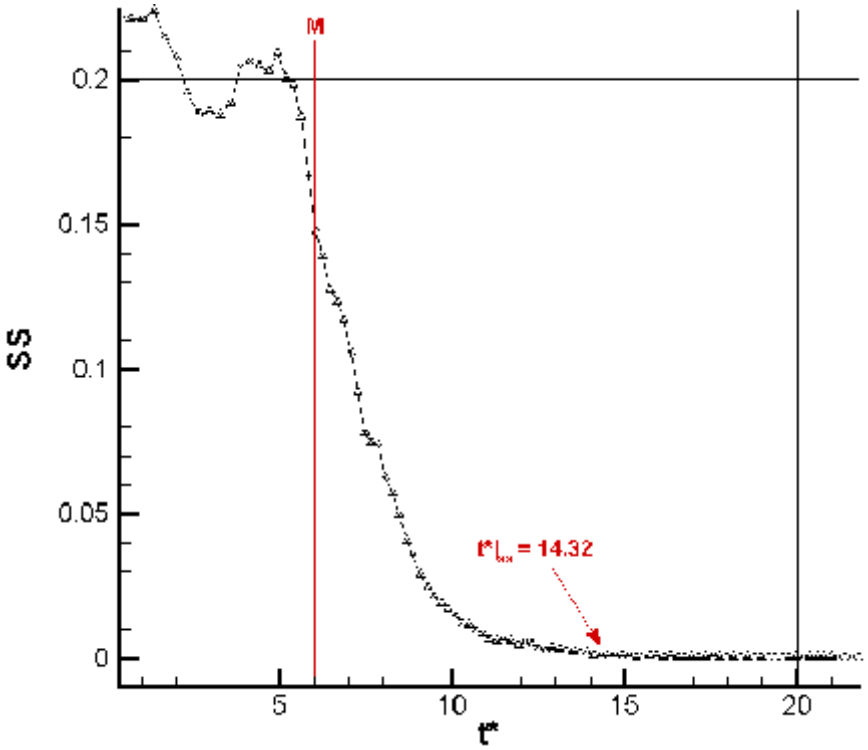

Figure 5.2.52(b): Difference from the Steady State as a Function of t* for x/D = 4, x_p/D = 0. M Denotes the End of the Motion (α = 54.74°), and $t^*|_{ss}$ Denotes When Average Difference per Flowfield Point is Less than 0.1% of U_∞.

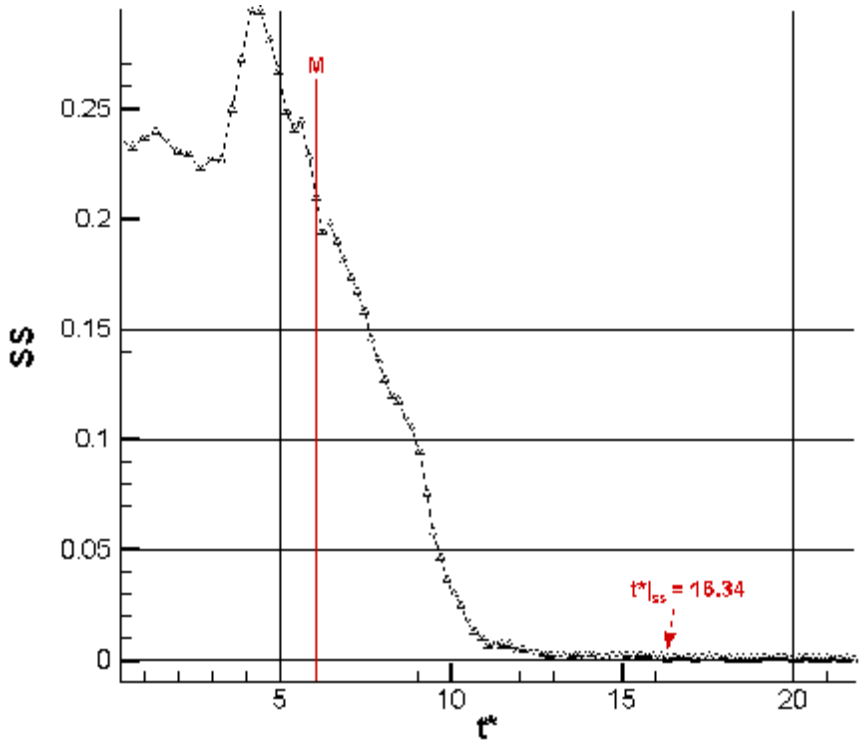

Figure 5.2.52(c): Difference from the Steady State as a Function of t*for x/D = 5, $x_p/D = 0$. M Denotes the End of the Motion ($\alpha = 54.74°$), and $t^*|_{ss}$ Denotes When Average Difference per Flowfield Point is Less than 0.1% of U_∞.

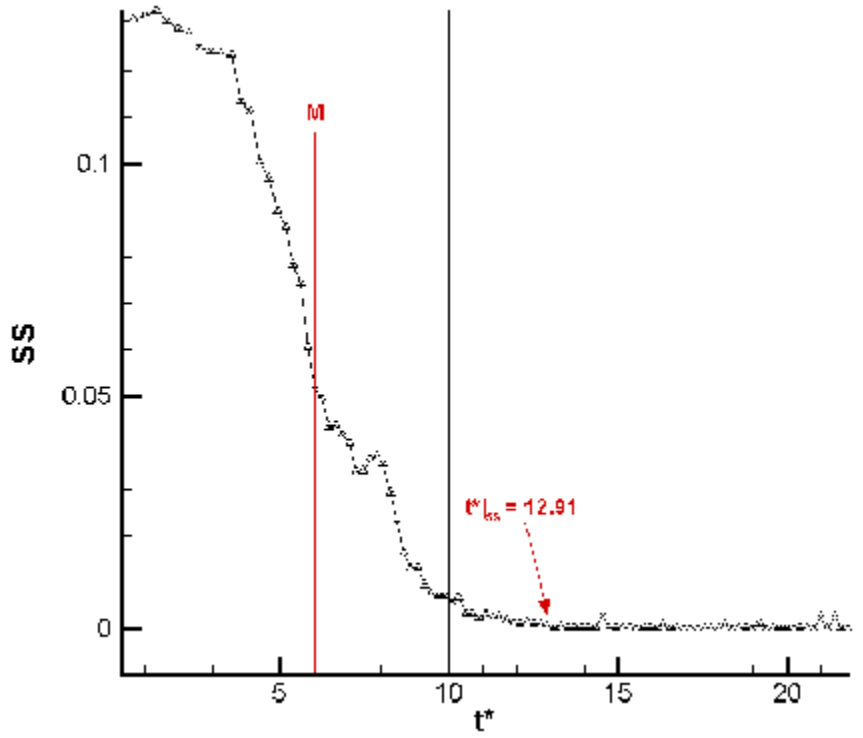

Figure 5.2.52(d): Difference from the Steady State as a Function of t* for x/D = 3, $x_p/D = 4$. M Denotes the End of the Motion ($\alpha = 54.74°$), and $t^*|_{ss}$ Denotes When Average Difference per Flowfield Point is Less than 0.1% of U_∞.

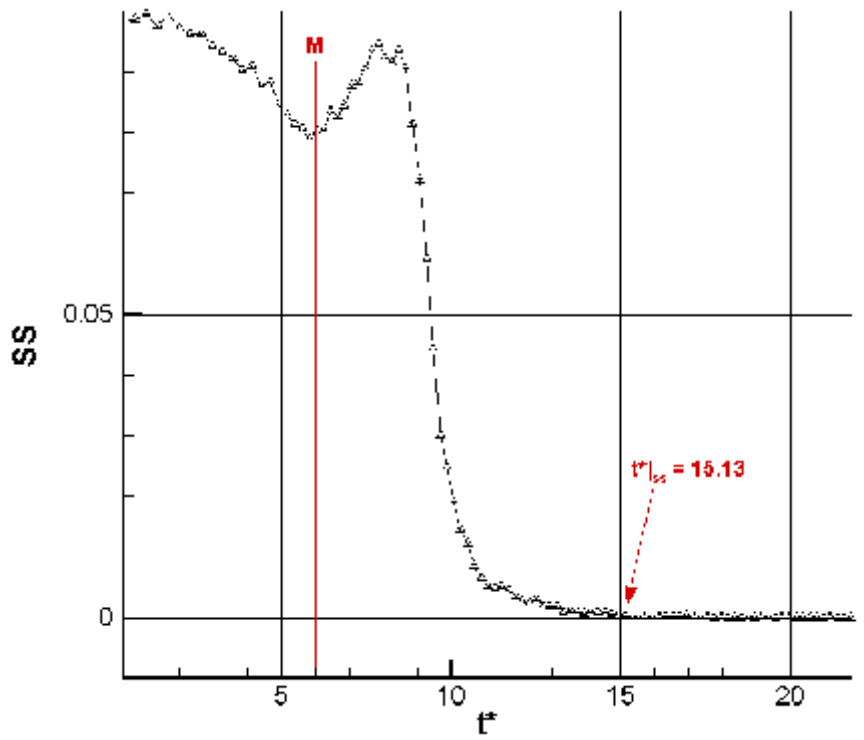

Figure 5.2.52(e): Difference from the Steady State as a Function of t* for x/D = 4, x_p/D = 4. M Denotes the End of the Motion (α = 54.74°), and $t^*|_{ss}$ Denotes When Average Difference per Flowfield Point is Less than 0.1% of U_∞.

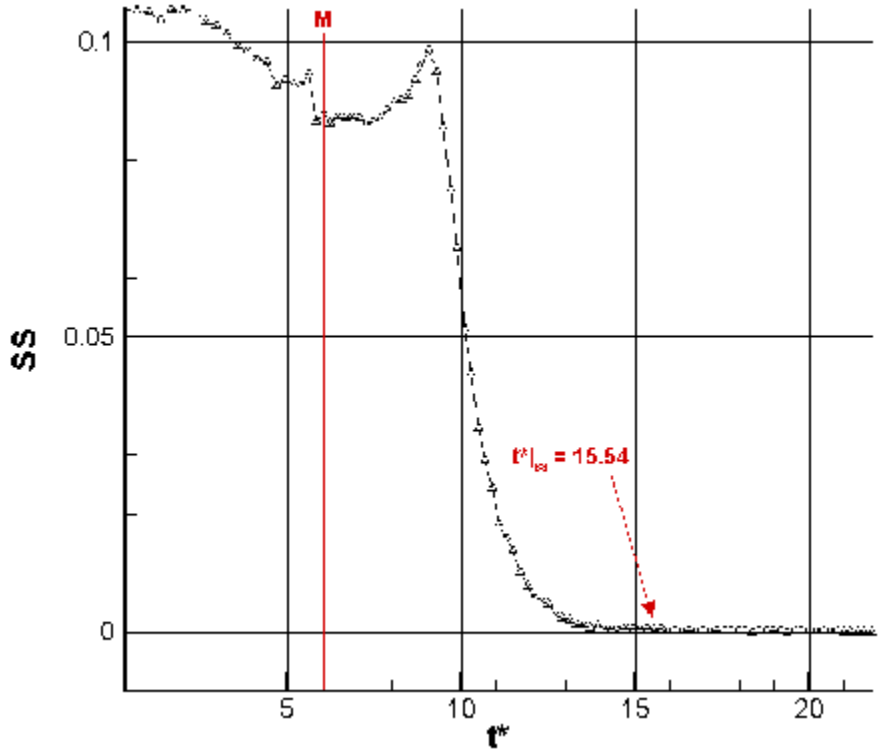

Figure 5.2.52(f): Difference from the Steady State as a Function of t* for x/D = 5, x_p/D = 4. M Denotes the End of the Motion (α = 54.74°), and $t^*|_{ss}$ Denotes When Average Difference per Flowfield Point is Less than 0.1% of U_∞.

Chapter 6 - Conclusions and Recommendations

6.1 Conclusions

6.1.1 Natural Unsteadiness

The natural unsteadiness in the flow over a 3.5 caliber tangent-ogive cylinder at incidence is investigated experimentally at a Reynolds number of 3500. The analysis of the data concentrates on the flow aft of the forebody where oblique shedding occurs and where the flow is roughly equally influenced by the convective and absolute instabilities present in the flow. This results in an unsteady flow that is asymmetric in the mean.

The mean flow nearer the forebody is observed to be highly asymmetric, but the mean-flow asymmetry decreases with downstream location. This is expected, as the flow further downstream is influenced more by the global instability and will thus exhibit periodic shedding of oblique vortices. The asymmetry in this region is not found to be caused by a set of stationary asymmetric vortex structures as exists over the forebody, but rather by an unsteady set of vortical structures with an asymmetric mean position. In addition, the asymmetry is associated with slightly different vorticity-shedding modes, depending on which sign of vorticity is released.

The degree of flow unsteadiness, as shown through the examination of the standard deviation of the mean velocity components is a function of the mean flow asymmetry. This observation agrees with previous results from analysis of surface pressure and flowfield data (Wardlaw and Yanta [1982]). The standard deviations in the v- and w-components of the velocity are found to reach levels in excess of $0.21 \cdot U_\infty$ and $0.16 \cdot U_\infty$, respectively. Regions of the highest σ_v are found to occur in the regions between vortical structures of opposite sign after they have been shed, leading to the conclusion that the releasing of the structures allows the interaction. Regions of large σ_w are observed near the saddle point associated with the upper vortex, showing that a large amount of unsteadiness occurs in this region as the vortical structures move away from the body.

Analysis of the singularities occurring in the streamline patterns corresponding to the mean flow shows that the vortex associated with more unsteadiness in the z-direction is represented by an unstable focus. However, the instantaneous topology is seen to vary widely from the mean topology. Limit cycles are seen in the unsteady topology, and although their presence is not linked to any physical process at this time, it is unlikely that they are associated with vortex breakdown, as in the case of flow over delta wings.

6.1.2 Coning Maneuvers

Coning motions (velocity-vector rolls) were performed in the ESM Wind Tunnel. Time series of circumferential surface pressures were acquired for multiple axial locations and non-dimensionalized into pressure coefficients (C_p). In addition, the C_p were integrated numerically in order to calculate the time series of the section yaw force (C_y). Multiple coning rates and blowing modes were employed to examine the effects of these parameters on the surface pressures. In particular, we are interested in how the inherent vortex asymmetry (which leads to non-zero C_y for $\alpha > 34°$) reacts to the coning motion and forebody blowing.

Conclusions for Coning Maneuvers for $\alpha = 45°$, Laminar Separation :

C_y increases in a direction opposite the motion of the nose of the model. This effect occurs regardless of the position of the measurement station with respect to x_c, to at least the measurement positions examined ($x/D < 5.25$). The magnitude of ΔC_y caused by motion alone increases with increasing distance from the nose. When constant blowing is used during the motion, it is effective at reducing the magnitude of ΔC_y from that seen with no blowing, and in reducing the time required for the flow to recover its initial state after the motion. In the cases where blowing is least effective, it is because its effects on C_y compete with those caused by the motion. However, in many of these cases blowing is still productive. Delayed blowing results in the flow requiring 20-50 flow time constants to achieve steady state.

Conclusions for Coning Maneuvers for $\alpha = 55°$, Laminar Separation :

For maneuvers in flow with laminar separation at $\alpha = 55°$, C_y increases in a direction opposite the motion of the nose of the model, except for $x/D = 5.25$, where it increases in the same direction as the motion. This effect is attributed to the natural tendency of the sectional C_y to switch signs near this

location for $\alpha = 55°$. When constant blowing is used during the motion, it is highly ineffective whenever its effects compete with those of the motion. It appears that for the cases tested, it would be very difficult to augment the motion. Delayed blowing can result in the flow requiring several up to several hundred time constants to achieve steady state.

Additional tests were performed with delayed blowing and no motion. By changing the $C_{\dot{m}}$, the asymmetry at each axial station could be changed. By observing the C_y for the arrival of the changing asymmetry, and knowing the location of the axial station of measurement relative to the forebody tip, the velocity of propagation of the asymmetry onset can be calculated. It was found that for both $\alpha = 45°$ and $\alpha = 55°$, this velocity is nearly equal to $0.8 \cdot U_\infty$. This propagation rate is higher than the convection rate found by simply using the axial component of the freestream $U_\infty \cdot \cos\alpha$ (which is $0.71 \bullet U_\infty$ at $\alpha = 45°$ and $0.57 \bullet U_\infty$ at $\alpha = 55°$).

Conclusions for Coning Maneuvers with a = 50°, Transitional Separation :

Preliminary results from a large dataset involving a maneuvering 3.5 caliber tangent-ogive cylinder at high incidence were discussed in Section 4.3. The testing is done at a Reynolds number of 2.75×10^5, which is in the transitional range. Trip strips were installed on the model, in an effort to ensure that the flow separation be transitional. The main conclusions of this section may be summarized as follows:

- At x/D = 1.25 (close to the ogive tip), coning motions at low reduced frequency result in a reinforcement of the C_y in the direction of motion. Pressure distributions for this case indicate a change in vortex strength in comparison to the pre-motion state.

- At x/D = 1.25, coning motions at high reduced frequency (beyond a threshold value) result in increasing C_y in a direction opposite the motion. Pressure distributions for this case indicate both changes in vortex strength and position with respect to the model, when compared to the pre-motion state.

- Microblowing at $C_{\dot{m}} = 1.35 \times 10^{-4}$ is effective at maintaining the pre-motion C_y, even at locations far from the ogive tip, where the blowing is applied. This is because the microblowing technique leverages the convective instability that causes the vortex asymmetry.

Further analysis of the Virginia Tech Stability Wind Tunnel data and comparison to data gathered at lower Reynolds numbers in the ESM Wind Tunnel will provide a more coherent view of the fluid mechanics involved in the case of the maneuvering slender forebody.

6.1.3 Pitching Maneuvers

We have added to the body of knowledge by obtaining time-series of entire planes of velocity data through which the tangent-ogive forebody/afterbody combination undergoes an unsteady pitching motion to a high angle of attack. Three planes of data each for pitch axis locations at x/D = 0.0 and x/D = 4.0 were acquired and the velocity data were used to calculate the unsteady axial vorticity field. In addition, the rms values of the velocity components were used to calculate the turbulent kinetic energy. This data allows us to not only reproduce the results of prior investigations involving pitching axisymmetric bodies, but also to visualize and quantify the reaction of the flowfield, during and after the pitching motion.

For this investigation, the initial angle of attack was $\alpha = 18.7°$, so that the wake flow of the forebody was symmetric. In this investigation, we discovered the following:

1. A flow asymmetry variable was defined, and this variable accurately portrayed the level of asymmetry in the measured flowfields. The unsteady pitch-up motions delayed the onset of vortex asymmetry to a point in time past when the motion was completed at $\alpha = 54.7°$. This could be expected, based on the results of other investigations (c.f. Montividas [1989]). The dimensionless pitch rate, $k_p = 0.096$ for this investigation, is essentially the ratio of the maximum crossflow velocity induced by the pitch rate on the forebody and the freestream velocity. In this case that ratio was about 10%, but even for this relatively small induced crossflow increment, the effect of the motion on the delayed appearance of the vortex asymmetry was sizable ($\Delta\alpha$ being at least 36°).

2. The delay in the appearance of the flow asymmetry was much greater for a pitch axis located at x/D = 4 than at the forebody tip, by 2-3 convective time constants. This observation, and more generally the first conclusion above, can be explained by the fact that the forebody tip is the location where the hydrodynamic instability acts to generate the asymmetry. Since the asymmetry is generated at approximately $\alpha > 2\delta$, (where is the included forebody tip half-angle, in this investigation $2\delta = 32.6°$, but because the nose is slightly blunted, we use $\alpha = 34°$ as the

asymmetry onset angle of attack), we can expect that if the tip experiences a crossflow that has a relative pitch-down component, that flow will reduce the effective angle of attack of the tip, keeping that angle below $\alpha = 34°$ for a longer time than in a quasi-steady maneuver.

This delay in the appearance of the asymmetry could be considered beneficial if the objective is to keep the flow symmetric into the high-α region, where yaw stability can be a significant problem because of the loss of conventional yaw control force. However, when considering the function of pneumatic vortex control systems (c.f. section 1.3), this symmetry could be a bane, as the control power needed to displace a symmetric vortical arrangement could be considerably greater than for a naturally asymmetrical pattern.

3. The progression of the flow to a steady state at $\alpha = 54.7°$ was delayed by over 9 convective time constants from the end of the motion. It was found that for the motions with a pitch axis at $x_p/D = 4$ delayed the appearance of the asymmetry longer, it actually took the flow a shorter time (by about 1 convective time constant) to reach the steady state, than for the case where $x_p/D = 0$. This was attributed to the fact that pitching about the tip of the forebody, rather than at a point near the center of mass, contributed more overall disturbance to the flow.

4. Axial locations greater than the pitch axis location initially exhibit strong symmetric vortices that tend to entrain a high axial core velocity, while axial locations lower than the pitch axis location have delayed vortex development. It is thought that the higher axial velocity in the vortex cores allows the vortex asymmetry to convect axially faster than the normally accepted $U_\infty \cdot \cos\alpha$, which is an equivalent result to the velocities of propagation found in the wind-tunnel tests with delayed forebody blowing. We have found that the location of the pitch axis will affect the asymmetry convection rate.

5. Calculation of the unsteady axial vorticity fields and comparison with the velocity fields revealed that during the pitching motion there is a high axial vorticity in the cores of the two symmetric vortices. However, the subsequent displacement of the vortices due to the asymmetry convecting from the nose leads to a severe diffusion of vorticity from the symmetrical arrangement. However, unlike the loss of axial velocity in their cores, which can occur before the vortex symmetry is destroyed, the vortices appear to retain much of their core vorticity until pushed from the body by subsequently developing vortices. It is obvious that changes in axial vorticity (from

symmetric to asymmetric state) are not themselves the cause the vortices to become asymmetric, but are instead a result of flowfield development induced by the asymmetry. The vortex breakdown observed in this progression is reminiscient of that experienced by delta-wing vortices during pitching maneuvers. Because additional planes of data with tighter grid spacing in the axial direction would be required to determine if the mechanisms are similar, the ability to do so is beyond the scope of this investigation.

6. The turbulent kinetic energy (TKE) is calculated from the rms values of the measured velocity components. There are two main conclusions regarding the TKE fields during the pitching maneuver. First, the cores of the vortices exhibit the highest TKE values, most likely because the vortical arrangement in the forebody wake is known to be unsteady in time and space (see results of the investigation on natural unsteadiness). This is exacerbated by the fact that the symmetrical vortex arrangement seen at axial stations for which $x > x_p$, because this arrangement becomes unstable at high angles of incidence. Once the vortices become asymmetric, the TKE is seen to decrease.

6.2 Recommendations for Further Research and Experimental Techniques

There are two main types of recommendations that are discussed in this section. First, we discuss further investigations that should be performed as a direct extension of this research. Second, we discuss some of the experimental techniques that we used, and what (if anything) we would have done differently. The latter section may be especially useful for this particular problem of slender forebody flow, where such typically mundane processes such as re-mounting models in a facility can, if not performed properly with forethought, can result in erroneous or inconsistent data.

Further research extending from the investigations documented here should be concentrated in several areas:

1. The effects of the coning and pitching motion on forebody asymmetry need to be determined for flow at high Reynolds number. While the investigations discussed in this document involve data acquired at Reynolds numbers that were in the transitional range, more data needs to be acquired in order to ascertain the effects of motion in the transitional and

turbulent separation regimes. There are only a handful of facilities that allow maneuvering of a large model in high-speed flows. The Virginia Tech Stability Wind Tunnel with the DyPPiR installed is one of these facilities, but the speed limitations of this facility preclude testing in the turbulent separation regime. The goal of these investigations should be to determine the baseline effects of the flow during maneuvering, so that this data can be employed to design forebody vortex control systems for the control of the flow asymmetry. We firmly believe that eliminating the existence of the asymmetric vortices by extreme blunting of the nose, by adding chines/strakes or by changing the cross-sectional shape of the forebody from circular to elliptical (with major axis perpendicular to the pitch plane) as a long-term solution only serves to eliminate a source of super-maneuverability at high incidence. The advent of a robust control system for the forebody vortices could couple with the standard rudder to provide yaw control authority throughout range of angles of attack. The obstacle to this testing is that there are no facilities (to the author's knowledge) that combine the ability to generate high-speed flows to permit testing of the forebody to full-scale Reynolds numbers that also have a dynamic model mount that can maneuver the models at sufficient reduced frequencies in pitching and coning motions.

2. Second, further investigations into the performance of pneumatic vortex control during motion need to be conducted for varying $C_{\dot{m}}$, blowing port location, Reynolds number and Mach number. Building on the data gathered in high-Re flows with maneuvering slender forebodies, these investigations would be critical to designing a control system that will be effective on full-scale aircraft.

3. The PIV data discussed in Chapter 3 can be further analyzed in order to determine the nature of the vortex interaction. In particular, we did not find any evidence of periodic vortex interaction except for that associated with vortex shedding associated with a cylinder in crossflow. Vortex tracking techniques could be used to determine the spatial relationship between the multiple vortices on the leeside of the slender body.

4. The circumferential surface pressure data discussed in Chapter 4 can be further analyzed in order to determine how the time-dependent pressures vary with model motion.

5. The LDV data discussed in Chapter 5 can be further analyzed to show the flow topology as a function of time. This should give more insight into the development of the flow over a pitching slender forebody.

6. Third, given the difficulty in generating consistent experimental data for this problem, it would be extremely beneficial to be able to perform computations for maneuvering forebodies in a reasonable amount of time. Although computing power has increased many times over in the last decade, the obstacle here is still having enough computing power for a problem which is axisymmetic in body geometry, but asymmetric and nonlinear in terms of the flow.

Experimental Techniques for Future Slender Forebody Investigations:

In order to produce consistent data (e.g. between different sets of circumferential pressure ports, planes of LDV data, etc.) investigators should consider how to remove the model from the facility as few times as possible. For instance, if multiple quick disconnects can be used to connect pressure tubing to the sensors, it definitely is worthwhile if it avoids having to move the model. In terms of the LDV data that was acquired and displayed in Chapter 5, it would have been better to have used two mounts and two models in order to avoid having to change the pitch axis location of the model after several sets of data were acquired. This change most likely led to the inconsistencies in the data.

Also in order to produce more consistent data, plan to acquire all data before removing the model from the facility. In the case of the LDV data sets that were acquired to support this document, it would have been better to have been able to use a 3D LDV system rather than a 2D system that required the acquisition of data from two sides of the tunnel.

In order to maintain the level of asymmetry, it would be best to use a 5% blunted model that is well machined. The anodized aluminum model used in the VT Stability Tunnel performed well in this regard. Models that are not blunted are subject to very small changes in the tip, and this is not necessarily predictable in experimental investigations, so sharp forebody tips can easily lead to data inconsistencies.

As a last comment, I feel that this was a very difficult problem because of the complex nature of the slender forebody flow at high incidence angles. However, it was rewarding to be able to develop multiple experimental investigations and see them come to fruition in the wind-tunnel and water-tunnel facilities.

Bibliography

Ahn, S., “An Experimental Study of Flow Over a 6 to 1 Prolate Spheroid at Incidence,” Ph.D. Dissertation, Virginia Polytechnic Institute and State University Aerospace Engineering Department, 1992.

Alexan, K., Hanff, E.S., and Kind, R.J., " Water-Tunnel Investigation of Dynamic Manipulation of Forebody Vortices," AIAA Paper 94-0503, January 1994.

Allan H. J. and Perkins E. W., NACA TM No. 1048, 1951.

Allen, H.J. and Perkins, E.W., "Characteristics of Flow Over Inclined Bodies of Revolution," NACA RM A50L07, 1951.

Almosnino, D. "High Angle-of-Attack Calculations of the Subsonic Vortex Flow on Slender Bodies," AIAA Journal, Volume 23, No. 8, August 1985, pp. 1150 - 1156.

Almosnino, D., and Rom, J., "Calculation of Symmetric Vortex Separation Affecting Subsonic Bodies at High Incidence, " AIAA Journal, Volume 21 No. 3, March 1983, pp. 398 - 406.

Atraghji, E., "A Method for Estimating the Load Distribution on Long Slender Bodies of Revolution at High Angles of Attack in Incompressible Flow, " Paper14, AGARD CP-204, AGARD Symposium on Prediction of Aerodynamic Loading, Ames Research Center, Moffett Field, CA., Sept, 1976.

Ayoub A. and Karamcheti K., “An Experiment on the Flow Past a Finite Circular Cylinder at High Critical and Supercritical Reynolds Numbers”, J. Fluid Mech. 1982 vol. 118, pp-1-26.

Bannik, W.J. and Nebbeling, C., "Measurements of the Supersonic Flow Field Past a Slender Cone at High Angles of Attack", See JFM Vol 87, part 3, Aug. 1978, pp 475-496.

Bauer, S. X. S. and Hemsch, M. J., "Alleviation of Side Force on Tangent-Ogive Forebodies Using Passive Porosity," Journal of Aircraft, Volume 31, No. 2, March - April 1994.

Bernhardt, J.E., and Williams, D.R., "Convective and Global Instability Characteristics of Steady Asymmetric Vortices on a Cone-Cylinder Geometry," Turbulence Structure and Control Conference, April 1990, Columbus OH.

Bernhardt J. and Williams, D., "The Effect of Reynolds Number on Control of Forebody Asymmetry by Suction and Bleed," AIAA Paper 93-3265, July 1993.

Bernhardt, J.E., and Williams, D.R., "The Effect of Reynolds Number on Vortex Asymmetry About Slender Bodies, " Physics Fluids A 5 (2), February, 1993.

Bernhardt, J. and Williams, D., "Closed-Loop Control of Forebody Flow Asymmetry," AIAA Paper 95-0651, January 1995

Bloor M. S. “The Transition to Turbulence in the Wake of a Circular Cylinder”, J. Fluid Mech. Vol 19. 290-304, 1964

Bridges, D.H. and Hornung, H.G., "Effects of Tip Reynolds Number and Tip geometry on the Vertex Wake of an Axisymmetric Body at Angle of Attack", AIAA 30th Aerospace Sciences Meeting, 6-9 January 1992, AIAA Paper No. 92-0406.

Calarese W. “An Experimental Study of Vortex Flow on a Slender Body at Large Incidence” AIAA Journal, vol 20 NO 4 1982.

Celik, Z. Z., Pedreiro, N., and Roberts, L., "Dynamic Roll and Yaw Control by Tangential Forebody Blowing," AIAA Paper 94-1853, June 1994.

Celik, Z. Z. and Roberts, L., "Aircraft Control at High-Alpha by Tangential Blowing," AIAA Paper 92-0021, January 1992.

Chapin, W.G., “Dynamic-Pressure Measurements Using an Electronically Scanned Pressure Module,” NASA TM-84650, 1983.

Clark, W. H., Peoples, J.R., and Briggs, M. M., "Occurrence and Inhibition of Large yawing Moments during High-Incidence Flight of Slender Missile Configurations," J. Spacecraft, Volume 10, No. 8, August 1973, pp. 510-519.

Clarkson, M.H., Malcolm, G.N., and Chapman, G.T., "A Subsonic, High-Angle-of-Attack Flow Investigation at Several Reynolds Numbers," AIAA Journal, Volume16, No 1, January, 1978, pp. 53-60.

Cobleigh, B.R., "High-Angle-of-Attack Yawing Moment Asymmetry of the Aircraft From Flight Test," AIAA Paper 94-1005.

Cornelius, K. C. and Lucius, G. A., "Side Force Augmentation at High Angle of Attack from Pneumatic Vortex Control," Journal of Aircraft, Volume 31, No. 4, July - Aug. 1994, pp. 818- 825.

Costis, C.E., Hoang, N. T., and Telionis, D.P., "Laminar Separating Flow Over a Prolate Spheroid, " J. Aircraft, Volume 26, No. 9, September, 1989, pp. 810-816.

Crowther, W. J. and Wood, N.J., "Tangential Forebody Blowing-Yaw Control at High Alpha," AIAA Paper 93-3406 CP.

Degani, D., "Effect of Splitter Plate on Unsteady Flows Around a Body of Revolution at Incidence," Phys. Fluids A 3 (9), September 1991.

Degani, D., " Effect of Geometrical Disturbance on Vortex Asymmetry," AIAA Journal, Volume 29, No. 4, April 1991, pp. 560-566.

Degani, D. and Levy, Y., "Asymmetric Turbulent Vortical Flows Over Slender Bodies," AIAA Paper 91-3296, September 1991.

Degani, D. and Schiff, L.B., "Numerical Simulation of the Effect of Spatial Disturbance on Vortex Asymmetry," AIAA Journal, Volume 29, No. 3, March 1991, pp. 344-352.

Degani, D. and Tobak, M., "Numerical, Experimental, and Theoretical Study of Convective Instability of Flows Over Pointed Bodies at Incidence," AIAA Paper 91-0291, January 1991.

Degani, D. and Zilliac, G.G., "Experimental Study of Nonsteady Asymmetric Flow Around an Ogive-Cylinder at Incidence," AIAA Journal, Volume 28, No. 4, April 1990, pp. 642-649.

Dunn, E.L., "A Low Speed Experimental Study of Yaw Forces on Bodies of Revolution at Large Angles of Pitch and Zero Angle of Side Slip," U.S. Naval Ordnance Test Station, China Lake, California TM 1588, 1954.

Dyer, D. E., Fiddes, S. P., and Smith, J.H.B., "Asymmetric Vortex Formation From Cones at Incidence - a Simple Inviscid Model," Aeronautical Journal, Vol 33, 1982, pp 293-312. (Also RAE TR 81330)

Ericcson, L.E., "Prediction of Slender Body Coning Characteristics," Journal of Spacecraft, Vol.28, No. 1, Jan.- Feb. 1991.

Ericsson, L. E., "Correlation of Attitude Effects on Slender Vehicle Transition," AIAA Journal, Volume 12, No. 4, April 1974, pp 523-529.

Ericsson, L. E., "Sources of High Alpha Vortex Asymmetry at Zero Sideslip," AIAA Paper 91-1810, 1991.

Ericsson, L. E., "Thoughts on Conical Flow Asymmetry," AIAA Journal, Volume 31, No. 9, September 1993, pp 1563-1568.

Ericsson L. E. "Unsteady Flows" Ch 11, Tactical Missile Aerodynamics: General Topics, Vol 141 Progress in Astronautics and Aeronautics. Publ. by AIAA, 1991.

Ericsson, L. E. and Reding, J.P., "Alleviation of Vortex-Induced Asymmetric Loads," Journal of Spacecraft, Volume 17, No. , Nov. - Dec. 1980.

Ericsson, L.E. and Reding, J.P., "Steady and Unsteady Vortex-Induced Asymmetric Loads on Slender Vehicles," Journal of Spacecraft, Vol. 18, No. 2, March-April, 1981, pp 97-109.

Fiddes, S. P., "A Theory of the Separated Flow Past a Slender Elliptic Cone at Incidence. Computation of Viscous–Inviscid Interactions", Paper 30, AGARD CP291, 1980.

Fiechter, M., “Uber Wirbelsysteme an Schlanken Rotationskorpen und ihren Einfluss auf die Aerodynamischen Beiwerte,” Bericht 10/66, Deutsch-Franzosisches Forchungsinsitut, Saint Louis, France, Dec. 1966.

Fu A. and Lan, C. E., "An Experimental Investigation of the Effect of Leading-Edge Extensions on Directional Stability and the Effectiveness of Forebody Nose Strakes," AIAA Paper 92-2715.

Gad-el-Hak and Ho-Chih-Ming, “Unsteady Flow Around an Ogive Cylinder” Journal of Aircrat Vol. 23 1986 pp 520-528.

Gee, K., Rizk, Y. M., and Schiff, L. B., "Forebody Tangential Slot Blowing on an Aircraft Geometry," Journal of Aircraft, Volume 31, No. 4, July - Aug. 1994, pp. 922-928.

Gittner, N. M. and Chokani, N., "Effects of Nozzle Exit Geometry on Forebody Vortex Control Using Blowing," Journal of Aircraft, Volume 31, No. 3, May - June 1994, pp. 503-509.

Goman, M. and Khrabov, A., “State-Space Representation of Aerodynamic Characteristics of an Aircraft at High Angles of Attack,” Journal of Aircraft, Vol. 31, No.5, 1994, pp 1109-1115.

Graham, J. E. and Hankey, W. L., "Computation of the Asymmetric Vortex Pattern for Bodies of Revolution," AIAA Paper 82-0282, January 1982.

Guyton R.W. and Maerki, G., " X-29 Forebody Jet Blowing," AIAA Paper 92-0017, January 1992.

Hall, R. M., "Influence of Reynolds Number on Forebody Side Forces for 3.5-Diameter Tangent-Ogive Bodies," AIAA Paper 87-2274, August 1987.

Hall, R. M. and Banks, D.W., “Progress in Developing Gritting Techniques for High Angle of Attack Flows," AIAA Paper 94-0169, January 1994.

Hartwich, P. M., Hall, R.M., and Hemsch, M. J., "Navier-Strokes Computation of Vortex Asymmetries Controlled by Small Surface Imperfections," AIAA Journal, Volume 28, No. 2, March 1991,pp 258-264.

Hartwich, P. M., "Symmetry Breaking in Vortical Flows over Cones - Theory and Numerical Experiments," AIAA Journal, volume 32, No. 5, May 1994, pp. 1013-1020.

Hartwich, P. M. and Hall, R.M., "Navier-Strokes Solutions for Vortical Flows over a Tangent-ogive Cylinder," AIAA Journal, Volume 28, No. 7, July 1990, pp. 1171-1179.

Hoang, N. T. and Telionis, D. P., "The Dynamic Character of the Wake of an Axisymmetric Body at an Angle of Attack," AIAA Paper 91-3268, September 1991.

Hoang, N. T., Rediniotis, O. K., and Telionis, D.P., "Separation Over Axisymmetric Bodies at Large Angles of Attack," AIAA Paper 91-0277, January 1991.

Hoang, N. T. and Telionis, D. P., "The Hemisphere-Cylinder at an Angle of Attack," AIAA Paper 90-0050, January 1990.

Hoang, N. T., Wetzel, T.G. and Simpson, R. L., "Unsteady Measurements Over a 6:1 Prolate Spheroid Undergoing a Pitch Up Maneuver," AIAA Paper 94-0197, January 1994.

Hoerner, S.F., "Fluid Dynamic Drag," Hoerner Fluid Dynamics, 1965.

Hunt, B. L. and Dexter, P.C., "Pressure on a Slender Body at High Angle of Attack in a Very Low Turbulence Level Air Stream," Paper 17, AGARD-CP-247, Jan. 1979.

Hunt, B.L., "Asymmetric Vortex Forces and Wakes on Slender Bodies," AIAA Paper 82-1336, August, 1982.

Iosilevskii, G. and Seginer, A., "Asymmetric Vortex Pair in the Wake of a Circular Cylinder," AIAA Journal, Volume 32, No. 10, October 1994, pp. 1999-2003.

Iwanski K., "Aerodynamics of Forebodies Undergoing Longitudinal Motions", AIAA 99-0987, Jan. 1997.

Jenkins J.E. "Nonlinear Aerodynamic Characteristics of a 65 Degree Delta Wing in Rolling Motion: Implications to Testing and Flight Mechanics Analysis", AIAA Paper 97-0742, January 1997

Kandil, O. A., Sharaf El-Din, H. H. and Liu, C. H., "Injection Active Control of Asymmetric Flows Around Slender Pointed Forebodies," First Industry/University Symposium on High Speed Civil Transport Vehicles (HSCTV), Greensboro, NC, December 4-6, 1994, pp. 623-628.

Keener, E.R., "Flow-Separation Patterns on Symmetric Forebodies," NASA TM 86016, January 1986.

Keener, E.R., Chapman, G.T., Cohen, L., and Taleghani, J., "Side Forces on a Tangent-Ogive Forebody with a Fineness Ratio of 3.5 at High Angles of Attack and Mach Numbers from 0.1 to 0.7," NASA TM X-3437, February 1977.

Keener, E.R., Chapman, G.T., Cohen, L., and Taleghani, J., "Side Forces on Forebodies at High Angles of Attack and Mach Numbers From 0.1 to 0.7: Two Tangent Ogives, Paraboloid and Cone," NASA TM X-3438, February, 1977.

Keener, E. R. and Chapman, G.T., "Similarity in Vortex Asymmetries over Slender Bodies and Wings," AIAA Journal, Volume 15, No. 9, September 1977, pp. 1370-1372.

Keener, E.R., Chapman, G.T. and Kruse, R.L., "Effects of Mach Number and Afterbody Length on Onset of Asymmetric Forces on Bodies at Zero Sideslip and High Angles of Attack," AIAA Paper 76-66, Jan. 1976.

Kegelman, J. T. and Roos, F.W., "Influence of Forebody Cross-Section Shape on Vortex Flowfield Structure at High Alpha," AIAA Paper 91-3250, September 1991.

Kiedaisch, J. W. and Acharya, M., "Interaction of Missile Tip Vortices with a Control Surface," AIAA Paper 94-0527, January 1994.

Kline S.J., McClintock F.A. Describing Uncertainties in Single-Sample Experiments. Mech Eng 1:3-8, 1953.

Kramer, B. R., Malcolm, G. N., Suarez, C. J., and James, K.D., "Rotary-Balance and Static Wind Tunnel Tests of Forebody Vortex Control Techniques on an F/A-18," AIAA ICAS- 94-3.4.3, September 1994.

Kramer, B. and Smith, B., "F/A-18 and F-16 Forebody vortex Control, Static and Rotary-Balance Results," 4th NASA High Alpha Conference, Dryden Flight Research Center, July 1994.

Kruse, R.L., Keener, E.R. and Chapman, G.T., "Investigation of the Asymmetric Aerodynamic Characteristics of Cylindrical Bodies of Revolution with Variation in Nose Geometry and Rotational Orientation at angles to 58° and Mach numbers to 2.

Lamont, P. J., "Pressures Around an Inclined Ogive Cylinder with Laminar, Transitional, or Turbulent Separation," AIAA Journal, Volume 20, No. 11, September 1982, pp. 1492-1499.

Lamont, P. J., The Complex Asymmetric Flow Over a 3.50 Ogive Nose and Cylindrical Afterbody at High Angles of Attack," American Institute of Aeronautics and Astronautics, Inc. 1982, 82-0053.

Lamont, P. J., "The Effect of Reynolds Number on Normal and Side Forces on Ogive-Cylinders as High Incidence," AIAA Paper 85-1799.

Lamont, P.J., and Hunt, B.L., "Pressure and Force Distributions on a Sharp-Nosed Circular Cylinder at Large Angles of Inclination to a Uniform Subsonic Stream," J. Fluid Mechanics, v. 76, part 3, pp. 519-559, 1976.

Lanser, W. R. and Meyn, L.A., "Forebody Flow Control on a Full-Scale F/A-18 Aircraft," Journal of Aircraft, Volume 31, No. 6, November - December 1994, pp. 1365-1371.

LeMay, S. P., Sewall, W.G., and Henderson, J. F., " Forebody Vortex Flow Control on the F-16c using Tangential Slot and Jet Nozzle Blowing," AIAA Paper 92-0019, January 1992.

Letko, W., "A Low Speed Experimental Study of the Directional Characteristics of a Sharp Nosed Fuselage Through a Large Angle of Attack at Zero Sideslip," NACA TN 2911, 1953.fs

Levin, D. and Degani, D., "Experimental Investigation of Active Control of Asymmetric Vortex Formation at High Angles of Attack."

Lowson, M. V. and Ponton, A. J. C., "Symmetry Breaking in Vortex Flow on Conical Bodies," AIAA Journal, Volume 30, No. 6, June 1992, pp.1576-1583.

Lowson, M. V. and Ponton, A. J. C., "Symmetric and Asymmetric Vortex Flows at High Angle of Attack," AIAA-91-0276.

Lowson, M. V. and Ponton, A. J. C., "Symmetry Breaking in Vortex Flow on Conical Bodies," AIAA Journal, Volume 30, No. 6, June 1992, pp.1576-1583.

Lou, S. C., Lim, T. T., Lua, K. B., and Chia, H. T., "Flowfield Around Ogive/Elliptic-Tip Cylinder at High Angle of Attack," AIAA Journal, Volume 36, No. 10, October 1998, pp. 1778-1787.

Malcolm G. N. "Forebody Vortex Control", Prog. Aerospace Sci. Vol 28, pp. 171-234, 1991.

Malcolm, G. N. and Ng, T.T., "Aerodynamic Control of Aircraft by Forebody Vortex Manipulation," SAE Paper 892220, February 1990.

Mange, R. L. and Bragg, M.B., "Aerodynamics of a Chined Forebody Oscillatin in Pitch," AIAA Paper 95-1869.

Mange, R. L. and Bragg, M.B. "Unsteady Aerodynamics of a Chined forebody Undergoing Forced Pitch Oscillations ," AIAA Paper 97 2211, June 1997.

Masad, J.A. and Abid, R., "On the Control of Laminar Separation by Suction,"

Mendenhall, M. R. and Lesieutre, D. J., "Prediction of Vortex Shedding from Forebodies with Chines," Journal of Aircraft, Volume 29, No. 3, May - June 1992, pp. 404-412.

Modi, V. J. and Stewart, A. C., "Approach to Side Force Alleviation Through Modification of the Pointed Forebody Geometry," Journal of Aircraft, Volume 29, No. 1, Jan. - Feb. 1992, pp. 123-130.

Modi, V. J., Cheng, C. W., Mak, A., and Yokomizo, T., "Reduction of the Side Force on Pointed Forebodies Through Add-On Tip Devices," AIAA Journal, Volume 30, No. 10, October 1992, pp. 2462-2468.

Montividas R. Reisenthel P. Nagib,H. "The Scaling and Control of Vortex Geometry Behind Pitching Cylinders" AIAA Paper 89-1003, 1989.

Mosbarger, N.A., "Vortex Control with Jet Blowing on a F-16 Forebody," AIAA 94-1830.

Moskovitz, C.A., Hall, R.M., and DeJarnette, F.R., " New Device for Controlling Asymmetric Flowfields on Forebodies at Large Alpha," Journal of Aircraft, Volume 28, No. 7, July 1991, pp. 456-462.

Moskovitz, C. A., Hall, R. M., and DeJarnette, F. R., "Effects of Nose Bluntness, Roughness and Surface Perturbations on the Asymmetric Flow Past Slender Bodies at Large Angles of Attack," AIAA Paper 89-2236, 1989.

Mourtos, N. J., "Control of Vortical Separation on a Circular Cone,"

Munk, Max M., "The Aerodynamic Forces on Airship Hulls," NACA Report 184, 1924.

Ng, T. T. and Malcolm, G. N., "Aerodynamic Control Using Forebody Strakes," AIAA Paper 91-0618, January 1991.

Pagan, D. and Molton, P., "Basic Experiment on a Supersonic Vortex Flow Around a Missile Body," AIAA Paper 91-0287, January 1991.

Panzer E. C Rediniotis O. K. and Telionis D. P. , “The Hemisphere-Cylinder in Dynamic Pitch-Up Motions” AIAA Paper 93-2963, 1993.

Peake, D. J., Owen, F.K., and Johnson, D. A., "Control of Forebody Vortex Orientation to Alleviate Side Forces," AIAA Paper 80-0183, January 1980.

Peake, D. J., Owen, F. K., and Higuchi, H., "Symmetrical and Asymmetrical Separations about a Yawed Cone,"

Pick, G. S., "Investigation of Side Forces on Ogive-Cylinder Bodies at High Angles of Attack in the M = 0.5 to 1.1 Range,"

Poll, D.I.A., "Some Effects of Boundary Layer Transition on Slender Axi-Symmetric Bodies at Incidence in Incompressible Flow," Paper 13, AGARD Symposium on Missile Aerodynamics, Trondheim, Norway, Sept. 1982.

Prandtl, L. “Umber Fluessigkeitsbewegung fei sehz Kleiner Reifung “ III International Congress of Mathematics, Heidelberg, 1904, pp 484-491.

Ralston, J., “Examination of Vortex Control on a Chined Forebody During Manuevering Flight Conditions,” 4th NASA High Angle-of-Attack Project and Technology Conference, Dryden Flight Research Center, July 1994.

Ramberg S. E. “The effects of yaw and finite length upon vortex wakes of stationary and vibrating circular cylinders”, J. Fluid Mech. 1983, vol. 128, pp 81-107.

Rao, D. M. and Sharma, G., "Side-Force Control on a Diamond Forebody at High Angles of Attack," Journal of Aircraft, Volume 31, No. 4, July - Aug. 1994, pp. 915-921.

Rao, D. M., Moskovitz, C., and Murri, D. G., "Forebody Vortex Management for Yaw Control at High Angles of Attack," Paper No. ICAS-86-2.5.2, 1986.

Rao, D. M. and Campbell, J.F., "Vortical Flow Management Techniques," Prog. Aerospace Sci. , Volume 24, pp. 173-224, 1987.

Ravi, R. and Mason, W. H., "Chine-Shaped Forebody Effects on Directional Stability at High-a," Journal of Aircraft, Volume 31, No. 3, May - June 1994.

Rediniotis, O.K., "The Transient Development of Vortices Over a Delta Wing," Ph.D. Dissertation, VPI & SU, Oct. 1992.

Reisenthel P. H. “ Development of a Nonlinear Indicial Model for Maneuvering Fighter Aircraft” AIAA Paper 96-0896, 1996.

Roos, F. W., "Low-Energy Pneumatic Control of Forebody Vortices," Fourth NASA High-Angle-of-Attack Conference, FWR-93-AA13, July 1994.

Roos, F. W., "'Microblowing for High-Angle-of-Attack Vortex Flow Control on a Fighter Aircraft," AIAA Paper 98-0543, January 1996.

Roos, F. W. and Kegelman, J. T., "Aerodynamic Characteristics of Three Generic Forebodies at High Angles of Attack," AIAA Paper 91-0275, January 1991.

Roos, F. W. and Magness, C. L., "Bluntness and Blowing for Flowfield Asymmetry Control on Slender Forebodies," AIAA Paper 93-3409, August 1993.

Roos, F. W. and Manor, D., "An Assessment of Pulsing Effects on Microblowing Management of Forebody Vortex Asymmetry," 37th Israel Conference on Aerospace Science, February 1997.

Sarpkaya, T., "Separated Flow about Lifting Bodies and Impulsive Flow about Cylinders," AIAA Journal, Volume 4, No. 3, March 1966, pp.414-420.

Schaeffler, N.W., "All the King's Horses: Delta Wing Leading-Edge Vortex System Undergoing Vortex Breakdown: A Contribution to its Characterization and Control under Dynamic Conditions," Ph.D. Dissertation, Virginia Polytechnic Institute and State University Engineering Science and Mechanics Department, May 1998.

Schiff, L. B., Degani, D., and Cummings, R. M., "Computation of Three-Dimensional Turbulent Vortical Flows on Bodies at High Incidence," AIAA Journal, Volume 28, No. 11, November 1991, pp. 689-699.

Schiff, L.B. and Tobak, M., "Results form a New Wind-Tunnel Apparatus for Studying Coning and Spinning Motions of Bodies of Revolution," AIAA Journal, Vol. 8, No. 11, November 1970.

Skow, A. M., Titiriga, A., and Moore, W. A., "Forebody/Wing Vortex Interaction and Their Influence on Departure and Spin Resistance," Paper 6, AGARD CP-247, Sept. 1978.

Smith, B.C. , "F-16 Forebody Vortex Control," ICAS-94-4.6.4, 1994.

Smith, L. H. and Nunn, R.H., "Aerodynamic Charicteristiecs of an Axixymmetric Body Undergoing a Uniform Pitching Motion," Journal of Spacecraft, Vol. 13, pp. 8, January 1976

Stahl, W. H. and Asghar, A., "Dependence on Reynolds Number of Onset of Vortex Asymmetry Behind Circular Cone," AIAA Conference, January 1996, Reno, NV, AIAA- 96-0064.

Stanek, M.J. and Visbal, M.R.. "Investigation of Vortex Development on a Pitching Slender Body of Revolution," AIAA Paper 91-3273, September 1991.

Taylor, J.R., "An Introduction to Error Analysis," University Science Books, 1982.

Thomson, K. D. and Morrison, D.F., "The Spacing, Position and Strength of Vortices in the Wake of Slender Cylindrical Bodies at Large Incidence," Journal of Fluid Mech. Volume 50, No.4, 1991, pp. 751-783.

Tobak, M., Degani, D., and Zilliac, G. G., " Analytical Study of the Origin and Behavior of Asymmetric Vortices," NASA Technical Memorandum,1002796, April 1990.

Tobak, M., Schiff L. B., and Peterson, V. L., "Aerodynamics of Bodies of Revolution in Coning Motion," AIAA Journal, Vol 7 No. 1, 1969.

Vanden, K .J. and Belk, D. M., "Numerical Investigation of Subsonic and Supersonic Asymmetric Vortical Flow," AIAA Journal, Volume 31, No. 8, August 1993, pp. 1377-1383.

Van Tuyl, A. H., "Vortex Filament Model of the Wake Behind a Missile at High Angle of Attack," AIAA Journal, Volume 26, No. 3, March 1988, pp. 264-270.

Visbal, M. R., "Crossflow Topology of Vortical Flow," AIAA Journal, Volume 32, No. 5, May 1994, pp. 1085-1087.

Vlachos, P.P., "An Experimental Spatio-Temporal Analysis of Separated Flows over Bluff Bodies Using Quantitative Flow Visualization," Ph.D. Dissertation, Virginia Polytechnic Institute and State University, Engineering Science and Mechanics Department, 2001.

Wardlaw, A. B., and Yanta, W. J., "Multistable Vortex patterns on Slender, Circular Bodies at High Incidence," AIAA Journal, Volume 20, No. 4, April 1982, pp. 509-515.

Wardlaw, A. B. and Yanta, W. J., "Asymmetric Flowfield Development on a Slender Body at High Incidence," AIAA Journal, Volume 22, No. 2, February 1984, pp. 242-249.

Wei T. and Smith C. R. " Secondary Vortices in the wake of circular cylinders" J. Fluid Mech. 1986, vol. 169, pp. 513-533.

Wetzel, T.G. and Simpson, R. L., "Unsteady three-Dimensioal Crossflow Separation Measurements on a Prolate Spheroid Undergoing Time-Dependent Maneuvers," AIAA Paper 97-0618, January 1997.

Wetzel T. G. and Simpson R. L. "Unsteady Crossflow Separation Location Measurements on a Maneuvering 6:1 Prolate Spheroid" AIAA Journal vol. 36 No 11. Nov 1998.

Whitfield, C.C., "Steady and Unsteady Force and Moment Data on a DARPA2 Submarine," M.S. Thesis, Virginia Polytechnic Institute and State University, Aerospace Engineering Department, July, 1999.

Willet, K. A., "Design, Development and Implementation of a Low Cost Slotted Wall Test Section and Race Car Model for Use in Dynamic Wind Tunnel Testing," M.S. Thesis, Virginia Polytechnic Institute and State University, Department of Aerospace and Ocean Engineering, Pending.

Williams, D., "A Review of Forebody Vortex Control Scenarios," AIAA Paper 97-1967, 1997.

Yoshinaga, T, Tate A. and Inoue R., "Coning Motions of Slender Bodies at High Angles of Attack in Low Speed Flow" AIAA 81-1899, 1981.

Zeiger, M.D., Donnelly, M.J. and Telionis, D.P., "An Experimental Investigation of Pitch Axis Effects on Flow Over an Ogive Cylinder," AIAA Paper 96-1955, June 1996.

Zeiger, M.D., Rediniotis, O.K. and Telionis, D.P., "Asymmetric Wakes Over an Axisymmetric Body in Coning Motions," Second International Conference on Experimental Fluid Mechanics. July 1994.

Zeiger, M.D., Rediniotis, D.P., Donnelly, M.J., and Telionis, D.P., "Temporal Evolution of the Flow Field Over a Pitching Tangent-Ogive Cylinder," AIAA Paper 95-0441, January 1995.

Zeiger, M.D. and Telionis, D.P., "Effect of Coning Motion and Blowing on the Asymmetric Side Forces on a Slender Forebody," AIAA Paper 97-0549, January 1997.

Zeiger, M.D. and Telionis, D.P., "Vortex Asymmetry Over Ogive cylinders in Coning and Pitching Motions," AIAA Paper 96-0206, January 1996.

Zeiger, M.D. and Telionis, D.P., Zeiger, P.P., "Unsteady Separated Flows over Three-Dimensional Slender Bodies," Progress in Aerospace Sciences 40, pp 291-320, 2004.

Zeiger, M.D., Vlachos, P.P., Telionis, D.P., "The Dynamic Character of the Vortical Flow over a Slender Axisymmetric Body," AIAA Paper 2001-1036, 2001.

Zilliac, G. G., "Computational/Experimental Study of the Flowfield on a Body of Revolution on Incidence," AIAA Journal, Volume 27, No. 8, August 1989, pp.1008-1016.

Zilliac, G. G., "A Computational/ Experimental Study of the Flow Around a Body of Revolution at Angle of Attack," NASA Technical Memorandum 88329, September 1986.

Appendix A: Summary Table for Flow over Axisymmetric Bodies at High Incidence

This table contains a summary listing of many important experimental, computational and theoretical investigations of the flow over axisymmetric bodies at high angles of attack. In addition, there are some listings that reference review articles that pertain to this subject. For each listing, important variables such as Reynolds number, Mach number, angle of attack, body geometry, and method of investigation are given. The author has also attempted to summarize the most important conclusions of each investigation, as well as cross-reference each listing to other pertinent findings, whether in agreement or disagreement.

In order to make this section independent from the rest of the document, nomenclature and abbreviations used in this table is given below. By doing so, the author hopes to provide a substantial stepping-off point for future investigators of this problem that was not available when the author began work. In the humble opinion of the author, the complexity of the problem has led to a vast amount of available data, including some that have resulted in questionable conclusions when examined in the light of later results. Comments are not the opinion of the author, except to relate the article to others of interest. Important conclusions of the authors are stated, although sometimes (usually when later research seemed to have validated or invalidated a particular point), there are comments on how valid the results were perceived to be.

Nomenclature:

C_b: Blowing Coefficient

M: Mach Number

Re: Reynolds Number

δ: Half-Angle of Forebody Tip

Abbreviations:

CSP: Circumferential Surface Pressures

ASP: Axial Surface Pressures

WFV: Wake Flow Visualization

SFV: Surface Flow Visualization

3D: Three-Dimensional

2D: Two-Dimensional

IFA: 2D Impulsive Flow Analogy

Author(s) & Pub. Date	Investigation Type	Forebody Type (A= Afterbody Present)	Forebody Fineness Ratio (L_N/D)	Angles of Attack (α)	Reynolds Num. (Re_D)	Mach Num. (M)	Investigated Quantities	Conclusions & Comments
Almosnino & Rom 3/1983	Computational (Vortex-Lattice)	Ogive(A) & Cone(A)	O: 2.598, 3 C: 2	0-25° (Symmetric Separation Imposed)	∞	<< 1	C_N, C_m, CSP	Computed C_N compares well with experimental data, while C_m values are comparatively low. CSP do not correctly show effects of secondary vortices.
Almosnino 8/1985	Computational (Vortex-Lattice)	Ogive(A)	3.5	0-25° (Asymm. Separation Allowed)	∞	<< 1	C_N, C_m, C_Y, CSP	Increases number of free vortex filaments from that used by Almosnino (1983). Computed C_N, C_m, C_Y values in very good agreement with experiment at high Re. CSP values still underestimate influence of secondary vortices.
Atraghji 9/1976	Theoretical/Experimental	Ogive(A), Cone(A), Paraboloid(A)	3 & 5	0°- 25°	1.4×10^6	0.5	CSP, C_N, C_Y	Attempts to use the 2D impulsively started crossflow analogy to predict C_N, C_Y. Predicted C_N compares well with experiment. C_Y compares well only qualitatively, poorly quantitatively.
Bannik & Nebbeling	Experimental	Cone	3.8	0° - 34°	45×10^6/m	2.94	CSP, SFV, Wake Pressures & Crossflow Mach #'s	Detailed supersonic wake topology (from experiment). Correlated the CSP to SFV. Embedded shock waves observed for $\alpha > 1.25\delta$, a system of shocks noted for $\alpha > 1.5\delta$. Noted presence of lee shock perpendicular to the symmetry plane. Flow asymmetric for $\alpha > 1.75\delta$.
Bernhardt & Williams 4/1990	Experimental/ Theoretical	Cone(A)	1.93	45°-55°	6300	N/A	C_Y and C_b, Instability Type	Yaw force (C_Y) vs. blowing coefficient (C_b) curves are continuous below α = 50° and show bistable behavior above α=50°. Determination that asymmetric vortices are the result of a spatial instability.
Bernhardt & Williams 2/1993	Experimental	Cone(A)	1.93	55°	2300 - 80.1×10^3	N/A	C_Y and C_b, Instability Type	Re_D affects the instability type (global or convective) that dominates the flow. The bistable state (global instability) is only possible below $Re_D = 1 \times 10^4$. Convective instability exists above $Re_D = 3 \times 10^4$. Intermediate Reynolds numbers result in a two-state flow.

Bridges & Hornung 1991	Experimental	Cone	5.715 (Nominally) w/Various Blunted Tips	60°	Re_t = 889 - 12,200	N/A	WFV, Separation Boundaries	Determined boundaries of regions in the Re_t vs. α plane. However, flow was visually asymmetric for only very high angles. Described a possible mechanism for change from local to global separation patterns. Compared the relation between vortex centers to Foeppl potential flow solution.
Chin, Lan & Gainer 12/1989	Computational (Discrete-Vortex Potential Flow)	Ogive, Cone	O: 5C: 3.58	0° - 40°	∞	N/A	C_Y	Noted that there were two solutions for each location of separation lines, one symmetric and one asymmetric (assuming the separation lines were symmetric). This may provide an alternative method of explaining the existence of asymmetric vortices over slender bodies. The solutions compare well with experimental data up to $\alpha = 32°$.
Degani & Schiff 4/1991	Computational (Thin-Layer Navier Stokes)	Ogive(A)	3.5	40°	$2.6x10^4$, $2x10^5$	0.2	C_N, C_Y, Helicity, Streamlines	One of the first investigations to demonstrate computationally the asymmetric wake characteristics seen experimentally. Computed symmetric flows (α= 40°) are stable to time-varying perturbations. Application of space-fixed, time-fixed perturbation causes flow to become asymmetric.
Degani & Zilliac 4/1990	Experimental	Ogive(A)	3.5	30°-85°	$1.7x10^4$, $2.6x10^4$, $3.5x10^4$	N/A	Surface Pressure Power Spectra, WFV	Flowfield over the model for $\alpha > 30°$ is naturally unsteady to a high degree. Low-frequency von Karman shedding and high frequency shear-layer fluctuations were documented. Moderate frequencies between those mentioned above lead the investigators to surmise that vortex interaction was responsible.
Degani 4/1991	Computational (Thin-Layer Navier Stokes)	Ogive(A)	3.5	20°, 40°	$2.0x10^5$	<<1	CSP, C_N, C_Y, Helicity, Streamlines	Investigation of how minute disturbances near the forebody tip affect the flow. Noted that the asymmetry could become saturated, so that increasing the disturbance level did not increase asymmetry. Flow more sensitive to disturbances near tip. Flow over forebody is less asymmetric than flow over afterbody. Cause of asymmetry is disturbing a convectively unstable symmetric flow.
Degani & Tobak 1/1991	Experimental, Theoretical &Computational (Thin-Layer Navier Stokes)	Ogive(A)	3.5	30°-60°	$1.4x10^4$, $2.3x10^4$, $3.2x10^4$	<<1	C_N, C_Y, Streamlines	Showed that intermediate, nearly symmetric flow states exist for $\alpha > 50°$ and Re = 32,000, further confirming the computational results that convective nature of the instability. Theoretically determined that the presence of natural unsteadiness enables the intermediate mean states. Noted that all changes to flow states by means of a disturbance were reversible.

Dyer, Fiddes & Smith 1981	Theoretical & Computational	Cone	Various	α/δ = 3- 10	∞	<< 1	C_Y, Vortex Position	Computed line vortex positions for an inviscid flow where the separation lines were symmetric & fixed, but the vortices asymmetric. Qualitatively, the results compare well with experiments, but a better method for predicting the vortex/separation interaction is needed, along with the introduction of sheet vortices. Surmised that flow behavior may result from lack of uniqueness in an inviscid flow, because the flows exhibited a bifurcation to asymmetry at a critical α.
Ericsson 9/1993	Review w/Theory	Various Cones						Conical flow asymmetry exists on slender cones where axial flow component is high. Less slender cones cannot produce conical asymmetry, but produce asymmetric flow similar to that on cylindrical afterbodies. Restated that most experimental results support the conclusion that symmetric separation cannot produce asymmetric flow unless symmetric reattachment is prevented.
Ericsson 1991	Review w/Theory	Slender Vehicles						Concluded, from existing experimental results, that vortex asymmetry is not due to hydrodynamic instability (compare later results by Degani (1991) and Williams & Bernhardt). Noted that symmetric separation cannot produce asymmetry unless symmetric reattachment is prevented.
Ericsson 11/1991	Review w/Theory	Slender Vehicles						Responding to the call for testing slender bodies at all roll angles in order to determine the maximum possible side force, Ericsson stresses that this proposition is expensive and perhaps problematic, given that the test results would need to be extrapolated to full-scale aircraft. States that vehicles at high α are usually maneuvering, and thus the moving wall effect will dominate the unreliable effects of nose micro-asymmetries.
Ericsson & Reding 1981	Review	Slender Vehicles						Review of steady and unsteady asymmetric loads on slender bodies. Especially interesting and original is the review of results on maneuvering (coning and pitching) vehicles and rotating nose tips. Stressed that coupling between vehicle motion and vortex generation is very significant.
Fiddes & Smith	Theoretical & Computational(Inviscid Line & Sheet Vortices)	Cone	Various	α/δ = 3- 10	∞	<<1	CSP, C_N, C_Y, Vortex Position	Used line and sheet vortices in conical flow cases (separation occurs at apex) with symmetric and asymmetric separation of vortices. Determined that asymmetric vortices are solutions even with symmetric separation, and that this case makes the best comparison with experimental data. Results showed that it is possible that the asymmetry of the flow may be due to a hydrodynamic instability.

Graham & Hankey 1/1982	Computational (3D Compressible Navier-Stokes)	Cone(A), Ogive(A)	C: 3 O: 3	C: 30° O: 20°	$0.4x10^6$	C: 1.6 O: 1.98	CSP, Total Wake Pressure, Velocity Field	Results compared well with experiment for the ogive-cylinder, but not as well for the cone-cylinder. Discrepancy in the second case was attributed to truncation error, a case of strictly numerical means causing an asymmetric flow. Noted that all cases computed were steady, although time-dependent equations were used.
Hall 8/1987	Experimental	Ogive	3.5	40°, 50°, 60°	$0.2x10^6$, $0.8x10^6$, $3.8x10^6$	Approx .0.25	CSP, SFV	Qualitative comparison of pressure data acquired by Lamont (1982) and SFV done by Keener (1986). Influence of Re on sectional C_Y is very important. Demonstrates that flow with laminar separation compares well with ad hoc IFA. However, correlation fails at high Re due to changes in the boundary layer development.
Hall & Banks 1/1994	Experimental	Ogive(A)	3.5	0°-57°	$0.2x10^6$ - $5.5x10^6$	0.075 - 0.7	CSP, C_Y, C_N	Two gritting techniques, global and two strips 54° from windward were applied in order to determine effectiveness in simulating high Re flow. Global gritting worked the best, except for an excessive increase in C_N, which was attributed to grit drag. Both techniques produce higher C_Y than true high Re data, which was explained by the fact that the gritting does not correctly model the vortex formation near the apex. Standard grit rings near apex are ineffective at high α.
Hartwich, Hall & Hemsch 3/1991	Computational (Thin -Layer Navier- Stokes)	Ogive(A)	3.5	20°, 30°, 40°	$0.8x10^6$	<<1	CSP, Helicity, SFV,C_Y, C_N	Asymmetry was shown to be sensitive to machine accuracy and grid topology (different asymmetric solutions recurred on different machines). Computed data compares well with experimental data for both axisymmetric and elliptic tips. Sectional C_Y and crossflow vortex structure connection analyzed. Maximum sectional C_Y attributed to asymmetric separation. **However, the possibility exists that vortex alignment can affect the nature of separation!**
Hartwich 5/1994 (Also 1/1993)	Theoretical & Computational (Thin-Layer Navier-Stokes)	Cone	11.45, 5.715, 2.836	5° - 30°	Re_L = $0.6x10^6$, $1.2x10^6$, $2.4x10^6$	<<1	CSP, Helicity, SFV, C_Y, C_N	Theoretical application of classical stability analysis showed that the attached or separated flow over a cone is only neutrally stable in regions of decelerating circumferential flow. Reducing slenderness or surface curvature reduced perturbation effects on the stability of the flows, as expected.
Hartwich & Hall 7/1990	Computational (Thin -Layer Navier- Stokes)	Ogive(A)	3.5	0°, 30°	$0.2x10^6$ - $3.0x10^6$	<<1	CSP, SFV, Streamlines, Crossflow Separation	Computational method involved turbulence modeling and modeling of a laminar separation bubble with transition in the free shear layer. Comparison with experimental data is good. Re effects appear to diminish after Re = $1x10^6$.

Hoang & Telionis 9/1991	Experimental	Hemi(A)	0.5	0°-90°	$2.7x10^4$	<<1	Shedding Frequency, Velocity Fields (7HP)	Determined the frequencies of vortex heaving in the wake of a hemisphere cylinder. Determined change in frequencies with angle of attack. Showed that a large disturbance near the nose of the model could cause flow asymmetries similar to those seen in the wake of slender bodies.
Hoang, Rediniotis & Telionis 1/1991	Experimental	Hemi(A)	0.5	20°, 30°	$0.15x10^6$, $0.29x10^6$, $0.42x10^6$	<<1	SFV, ASP, Velocity Fields (LDV, 7HP)	Documented the extent of the separation bubble at low Re. Velocity fields in the crossflow plane presented for both laminar and turbulent separation. Noted discrepancies between 7HP and LDV data, believed to be caused by inserting the 7HP into the flow, perhaps causing a degree of vortex breakdown.
Hoang, Telionis & Jones 1/1990	Experimental	Hemi(A)	0.5	0°, 10°, 20°	$0.29x10^6$ - $1.07x10^6$	<<1	ASP, SFV, Velocity Fields (LDV)	Noted the existence of three distinct regions at $\alpha = 20°$ based on the surface pressures. The region closest to the nose is qualitatively similar to 2D lifting surfaces where there is suction on the lee side. The second is like the 2D yawed cylinder in potential flow. The first two regions are generally inviscid. The third region shows the effects of the lee vortical flow and viscosity.
Hunt & Dexter 1979	Experimental	Ogive(A)	3.0	30° - 90°	$0.4x10^5$ - $1.4x10^5$	<<1	CSP	Freestream unsteadiness and model mount vibration can drastically affect experimental measurements. Meaningful time-averaged data is not likely to be obtained in situations where the freestream turbulence level is high (at least 0.7%). Confirmed that surface pressures were functions of the roll angle. Modifications to the model (nose changes and tape) altered the measured pressures, but not in a consistent or predictable manner.
Hunt 8/1982	Review							Selected Notes: The asymmetry is strongest if it begins as a locally conical flow at the tip of the slender body. Compressible cross flow reduces the magnitude of the yaw force, which becomes negligible for $M_C > 1$. Asymmetry is largest when the boundary layer is laminar or turbulent.
Keener & Chapman 9/1977	Review of Experimental Results, w/Theory	Slender Forebodies and Delta Wings						Show the similarity between vortex asymmetry observed on delta wings to that observed on slender forebodies. Since separation is fixed in the case of the delta wing, but yet asymmetric vortical flow exists, the authors state there exists a distinct possibility that the same mechanism is responsible for vortex asymmetry over forebodies. Hence, they conclude that asymmetric separation is not necessarily a requirement for asymmetric flow. Others, notably Ericsson (1981, 1991) have disputed this fact.

Keener, Chapman, Cohen & Taleghani 2/1977	Experimental	Ogive(A)	3.5	0° - 88° (β also varied from -10° to 30°)	$0.3x10^6$ - $3.8x10^6$ @M=0.25	0.1 - 0.7 @Re_D = $0.8x10^6$	C_A, C_N, C_Y, C_m, C_n	Carefully acquired data show excellent repeatability and very little hysteresis. The maximum C_Y for the forebody can be as high as 1.5 C_N, 1.6 C_N w/afterbody. Maximum normal force occurs at α = 60° (where max C_Y occurs) which indicates that asymmetric vortex formation induces a decrease in the pressure on the lee side of the forebody. Max C_Y decreases with increasing M. Magnitude and direction of yaw force sensitive to boundary layer nature, nose tip geometry (nose boom and strakes). Blunting the nose decreases the asymmetry, strakes can eliminate the asymmetry altogether. Onset angle of C_Y is not affected by M. Addition of an afterbody decreases onset angle, indicating the possibility that initial asymmetry may form on the afterbody. Side forces persist to 80°.
Keener 1/1986	Experimental	Ogive(A), Cone(A),Elliptic Ogive	O: 2.5, 3.5, 5 C: 2.84	0° - 88°	$0.3x10^6$ - $2.0x10^6$	0.1 - 2.0	SFV (Oil, Sublimation), WFV (Schlieren, Vapor-Screen, Vapor-Trail), C_Y, C_N	Extensive and fundamental analysis of the surface flow patterns existing on slender forebodies. Noted that 3D boundary-layer inflectional instabilities occur starting at α = 5° and persist to 55°. A separation bubble exists on the forward part of the forebody to α = 15°- 20°. Identified three types of primary separation that may occur simultaneously along the forebody (due to change in the local diameter with axial distance): Laminar separation (near the nose), transitional (in the midsection) and turbulent (remainder). Noted that the occurrence of vortex asymmetry is not principally dependent on the occurrence of asymmetry in the transitional region of the boundary layer. At α = 40°, the first vortex that detaches quickly diffuses, giving the impression of vortex breakdown. Vortex detachment moves forward with increasing α and occurs at the nose for α = 55°. At very high angles of attack where C_Y typically decreases to zero, a stall-like separation appears on the rearward part of the forebody. At most α, there was little vortex unsteadiness, but at the α where maximum C_Y occurred, some natural unsteadiness was apparent.
Keener, Chapman, Cohen & Taleghani 2/1977	Experimental	Ogive(A), Cone(A), Paraboloid(A) Elliptic Ogive	O: 5, 3.5 C: 2.84 P: 3.5	0° - 88° (β also varied from -10° to 30°)	$0.3x10^6$ - $4.6x10^6$ @M=0.25	0.1 - 0.7 @Re_D = $0.8x10^6$	C_A, C_N, C_Y, C_m, C_n, C_l	All the forebodies experienced C_Y at zero β. C_Y onset angle about 20° (α = 2δ) for cone, 33° for 3.5 ogive, 25° for 5 ogive, and 35° for the paraboloid. The elliptic cross-sections, regardless of orientation, decreased the onset angle. C_Y decreases with M for all bodies **except** for the elliptic ogive with the major axis in the symmetry plane, where C_Y remains large.

Kegelman & Roos 9/1991	Experimental	Ogive (w/Circular, Elliptical & Chined Cross-Sections)	3.5	0° - 60°	Lam. Sep. & Turb. Sep. (w/ B.L. Trips)	<<1	C_Y, C_N, WFV, Velocity Fields (LDV & 7HP)	Tested forebody only, so only two vortices are considered. The detaching vortex is initially stronger than the attached. The detached vortex weakens with axial distance, while the attached vortex strengthens until it bursts. This observation confirms results by Keener (1986). Laminar separation produces stronger vortices than turbulent separation. The elliptical body produces stronger vortices than the circular, while the strongest are generated by the chined forebody, whose vortices are susceptible to vortex bursting similar to those over a delta wing.
Kiedaisch & Acharya 1/1994	Experimental	Ogive(A)	2.5	30° - 45°	$0.6x10^4$, $2x10^4$, $3.4x10^4$	<<1	SP, WFV, C_N (Fin)	A detailed examination of forebody/afterbody vortices interaction with a planar control surface. Interaction is documented for changes in Re, the azimuthal and axial locations of the control surface.
Kruse, Keener & Chapman 9/1979	Experimental	Ogive(A)	0.5, 1.5, 2.5, 3.5	0° - 58°	$0.32x10^6$ $0.43x10^6$, $0.65x10^6$	0.25 - 2.0	C_A, C_N, C_Y, C_m, C_n	Tests over the range of forebody fineness ratios reveal that low fineness ratios (0.5 & 1.5) produce little or no C_Y, while the 3.5 forebody produce higher C_Y. Addition of an afterbody lowers the onset angle of C_Y by 13°-18° for the 3.5 ogive. However, C_Y increases drastically when $\alpha > 30°$ (onset angle for forebody alone), showing that the largest side forces occur as the asymmetry moves onto the forebody. Generally (depending on fineness ratio & α), bluntness increases C_Y for cases where it is small, but decreases C_Y for cases where it is large. Rotating the forebody and forebody tip produce large changes in C_Y. Rotating the afterbody alone also produces changes in C_Y, but to a lesser extent.

Lamont 1982	Experimental	Ogive(A)	2.0	20° - 90°	$0.2x10^6$ - $4.0x10^6$	< 0.3	CSP, C_N, C_Y	Results from a very comprehensive series of tests on ogive-cylinders. **Two basic mechanisms for producing asymmetric flow exist**: Asymmetric wake vortices influence boundary layer development (laminar and turbulent separation regimes) is the more effective of the two at producing C_Y; asymmetric boundary layer states ahead of the primary separation lines (transitional separation regime). The latter mechanism was construed to be the same as that producing nonzero mean side forces in 2D cylinder flow. Noted that tests to determine maximum C_Y or C_N should encompass the entire range of ϕ. In the laminar and turbulent separation regimes, high C_Y was accompanied by low C_N, but high C_Y was accompanied with **low** C_N in the transitional separation regime. **Critical Re boundaries between regions of laminar, transitional and turbulent separation presented.**
Lamont 1982	Experimental	Ogive(A)	3.5	20° - 90°	$0.2x10^6$ - $4.0x10^6$	< 0.3	CSP, C_N, C_Y	Results from a very comprehensive series of tests on ogive-cylinders. Produced 3D pressure plots to show circumferential and axial variation. Confirmed the indications of Lamont (1982) concerning flow mechanisms for producing C_Y. Noted that high fineness ratio forebodies can produce complex flows with "mixed" separation in the transitional separation regime. These flows can produce a wide variety of C_Y. Showed that the maximum C_y occurs in regions of laminar or turbulent separation. Higher fineness ratio forebodies can produce high C_Y at higher Re because laminar separation (rather than transitional) will continue to occur on the forebody.
Lamont 1985	Experimental & Theoretical	Ogive(A)	3.5	20° - 90°	$0.2x10^6$ - $4.0x10^6$	< 0.3	CSP, C_N, C_Y	A majority of the results taken from a very comprehensive series of tests on tangent ogive-cylinders. A detailed exposition of the state of the boundary layers over slender forebodies with afterbodies and a discussion of the effect of the various states on C_Y, C_N. Uses results by Poll (1982) to confirm theories. Notes that **rare exceptions to the rule that the maximum C_Y occurs in the laminar or turbulent separation regimes** involve cases of mixed laminar and transitional separation on long, slender forebodies. Variation of C_Y with axial location may not be cyclical for the transitional regime, as it is for laminar and turbulent regimes. If it is cyclical, the first half-cycle (occurring over the forebody) will be low-amplitude and encompass a short distance axially.

Lamont & Hunt 1976	Experimental	Ogive(A) Cone(A)	O: 1,2,3 C: 2	0° - 90°	$Re_{Dcsc\alpha} = 1.1x10^5$	N/A	CSP, Sectional C_N, C_y	Detailed documentation of CSP for axial locations to 22D for several different forebodies. CSP were integrated to give C_y and these were compared with the theoretical values predicted by IFA. Qualitatively, the experimental data compared to IFA, but there were some major differences: C_y is oscillatory with axial distance, but the amplitude of the oscillation decays to zero after three or four half-cycles; the oscillatory period is affected by α; at very high α, the oscillation is replaced by periodic shedding; very large C_y can occur with the 2 & 3 caliber ogives at moderate α. The last observation is not predicted by IFA, and was attributed to three-dimensional flow development on the forebody. Natural unsteadiness can occur, and can reduce the time-averaged C_y. The amount of natural unsteadiness appears to decrease with until the onset of periodic shedding above = 60°. The level of unsteadiness can vary with ϕ. The freestream turbulence level, which was 0.7%, most likely contributed to the amount of unsteadiness observed in the SP measurements.
Lowson & Ponton 6/1992	Theoretical & Experimental	Circular Cone, Elliptical Cone, Delta Wing	CC: 5.72,11.5 E C: 5.72 DW Sweep Angle: 70°,80°	0° - 90°	$2.0x10^4$ - $3.0x10^6$ (Most results at $3x10^5$)	N/A	Calculation and Visualization of Leeward Vortex Positions	Compared theoretical calculations of critical α for symmetry breaking (onset angle of nonzero C_Y) to experimental observations. Theoretical methods support the existence of conical asymmetries over slender bodies and that the critical angle depends on the ratio of α to δ. The thickness of the body (length parallel to symmetry plane) influences the angle of onset of asymmetry. Experimentally, it is seen that thinner bodies are more resistant to vortex asymmetry, but are susceptible to asymmetries caused by vortex breakdown. Otherwise, slender wings do not support asymmetric flows (any observed due to thickness of apex). The flow states observed over circular cones is described and a mechanism for natural unsteadiness is put forward.
Luo, Lim, Lua, Chia, Goh & Ho 10/1998	Experimental	Ogive, Ogive w/Elliptic Tip	3.5	20° - 80°	$3.5x10^4$	Approx. 0.04	CSP, C_Y, Flow Visualization	Simultaneous CSP and force measurements were performed. CSP $\Delta\theta$ is sparse, so that pinpointing the separation location is difficult. Distributions of C_Y with ϕ are more predictable for the elliptic tip than for the conventional ogive, which was expected.

Moskovitz, Hall & DeJarnette 8/1989	Experimental	Ogive, Cone	O: 3.0 C: 2.84	30° - 60°	$8.4x10^4$, $2.5x10^4$ (Flow Viz)	<<1	CSP, WFV	A fundamental work of investigation into perturbing the flow very near the tip of the forebody and observing the effect on the overall flow. Noted that machining imperfections are significant drivers of flowfield asymmetry over slender bodies, and that small imperfections were many times as good as or better than large imperfections at producing asymmetry. Showed that increasing nose bluntness decreases the amount of asymmetry in the flow, and reasoned that the blunt tips were easier to machine, and thus had fewer imperfections. This has been disputed by theoretical investigations by Hartwich (1994) where a decrease in surface curvature increased the stability of the flow in the region of the tip, thus delaying the onset of an asymmetry due to a hydrodynamic instability. Noted that there was a maximum amount of asymmetry for a given body and freestream conditions, and the amount did not depend on the bluntness of the nose. Substantially confirmed by Hoang & Telionis (1990) and Roos (1991). The most important contribution from the standpoint of control was that $\theta = 135° - 140°$ produced the largest effect on flow asymmetry (Note that this location is well beyond the separation location for laminar flow).
Pagan & Molton 1/1991	Experimental	Ogive(A)	3.0	0°-20°	$0.16x10^6$	2	SFV (Oil Flow), CSP, Velocity Fields (5HP)	Used transition strips to ensure fully turbulent flow, otherwise flow was laminar over the entire body. Greatest difference between the two cases occurred at $\alpha = 5°$, where the laminar flow separates but the turbulent is attached. At $\alpha = 10°$ primary separation is affected by the transition strip, and velocity gradients in wake are smoother for turbulent separation. Results for both cases similar for $\alpha = 10°$ & 20°
Peake, Owen & Higuchi	Experimental	Cone	3.5, 5.72	0°-25°	$R_L = 4.5x10^6 - 13.5x10^6$, $35x10^6$	0.6 - 2.8	CSP, Skin Friction, C_N, C_Y, WFV	Basic investigation into the nature of the boundary layer and free shear flow over cones in compressible flow. When $\alpha/\delta > 2.5$ the vortical flow unsteadiness increases and the flow becomes asymmetric. For M = 0.6, it was discovered that the measured pressure fluctuations decreased to a minimum at the primary separation lines, and increased to a maximum at the reattachment point, which is opposite to the fluctuation behavior in 2D boundary layers. Items of possible interest: The primary separation locations seem to be at greater angles for Mach numbers in the high subsonic to supersonic regimes, even when the separation regimes are equivalent.

Pick	Experimental	Ogive(A)	2.1, 3.1, 4.1	14° - 40°	Re/ft = $2.7x10^6$ - $4.3x10^6$	0.5 - 1.1	SFV, WFV, C_N, C_Y	Note that the results are for quasi-steady tests, as the model was pitched at 2°/s. At all tested Mach numbers, C_Y increased for increasing fineness ratio. Laminar separation lines differed at times by 20°-40° in angular location. C_Y decreased when a boundary trip was installed windward of separation. The author maintains that the boundary layer with the trip was turbulent, but present no verification. It may be that the boundary layers were transitional, which would explain the reduction in side force. It is possible that the author confuses Mach and Reynolds numbers effects, because these parameters could not be varied independently.
Rainbird 12/1968	Experimental	Cone	2.26	12.5° - 25°	$Re_L = 25x10^6$ - $51x10^6$	1.8, 4.25	CSP, Surface Shear	Extensive boundary layer data for a cone at high M and Re. Noted that flow is essentially conical. The symmetric vortices are observed to remain near the cone surface and the symmetry plane.
Roos & Kegelman1/ 1991	Experimental	Ogive (w/ Circular, Elliptical and Chined Cross-Sections)	3.5	0° - 60°	$6.6x10^4$ - $2.25x10^5$	N/A	CSP, SFV, C_Y, C_N	Boundary layer trips used to simulate turbulent separation at transitional Re. Separation state verified by referencing Lamont's high-Re data. Showed that C_N is sensitive to ϕ even at $\alpha = 10°$. A small bump near the forebody tip stabilized the asymmetry, inducing large, repeatable side forces. The chined forebody developed the highest C_N but no C_Y. In addition, sharp-edged separation from the chines eliminated dependence on Re and boundary layer state. Elliptical cross-section (major axis perpendicular to symmetry plane) produced higher C_N than circular. Turbulent separation reduced C_N on circular and elliptical forebodies, C_Y dependence on separation state was unclear.
Sarpkaya 3/1966	Experimental/Theoretical	2D Circular Cylinder	N/A	90°	$0.15x10^5$ - $1.2x10^5$	<<1	SP, WFV	Investigation into C_D and C_N for impulsively started and constantly accelerated 2D cylinders for laminar and turbulent separation states. This experimental information was provided in order that investigations performed on inclined axisymmetric bodies could be compared to the data acquired. Use of the IFA could then be validated or invalidated as a tool to accurately predict the aerodynamic forces on inclined bodies.

Schiff, Degani & Cummings 11/1991	Computational (Thin-Layer Navier-Stokes)	Ogive(A), Secant Ogive(A), F/A-18 Forebody(A)	N/A	4.2, 6.3°, 10.4°, 20°, 25°, 30°	$7.5x10^4$, $2x10^5$, $1.22x10^6$, $5x10^6$, $11.5x10^6$	0.2, 3.0	CSP, SFV, Helicity	Thin-layer Navier-Stokes code used to predict high-α flows over axisymmetric bodies in subsonic and supersonic flow. The turbulence model is that introduced by Degani & Schiff (1991). Computed flowfield is entirely symmetric. Predictions compare well to experimental data. For the most part, this paper is devoted to the computations themselves (grids, turbulence modeling, etc.), and the mechanics of the flow is not a priority. Refer to investigations by Degani (1991), Schiff (1991), Tobak (1990) & Zilliac (1986, 1989) for more discussion of the results of computations of flowfields over axisymmetric bodies at high α.
Skow, Titiriga & Moore 1978	Review of Applications	Various Fighter Forebodies and Delta Wings	Various				WFV, $C_{n\beta}$, $C_{m\beta}$, C_N, C_Y, C_L	A review of Northrop Corp. knowledge and efforts to increase the stability of fighter aircraft at high α. Special interest is given to the development of the forebody and LEX vortices and how these affect the stability of the aircraft. Interactions between the forebody and LEX or wing vortices can either enhance or decrease stability, and careful attention is necessary to ensure the former.
Stahl & Asghar 1/1996	Experimental	Cone	3.558	20° - 40°	$0.5x10^4$ - $2x10^5$	<<1	WFV	Previous investigations by Keener have suggested, at least for the range of Re measured, that the α onset for asymmetric flow does not depend on Re. This investigation clearly shows that (at low Re) the onset angle decreases with increasing Re, approaching the well-known value of 2δ. Surmised that the onset of asymmetry may be characterized by the ratio of vortex strength to separation distance, but more information is necessary to confirm this theory.
Thomson & Morrison 4/1971	Experimental/ Theoretical	Cone(A), Ogive(A)	C: 2.84, 1.87O: 3.0	30° (Main Angle)	Re_C < $2.3x10^4$ - $7.5x10^4$	0.4 - 2.8	WFV (Schlieren), Pressure & Velocity Field (Pitot, Yawmeter), Vortex Strength	Conclude that the wake over a slender, inclined cylinder may be qualitatively modeled by IFA, but the relation is by no means exact. The Strouhal numbers predicted by IFA are the same as those for a 2D circular cylinder and the predicted vortex strengths are higher than that seen experimentally. Vortices that originate near the forebody excepted, the flow behaves as a yawed infinite vortex sheet. Wake flow shows high diffusion of vorticity as axial distance is increased. Vortex paths and strengths are determined through WFV.

Tobak, Degani & Zilliac 4/1990	Analytical	Generic					Analysis of Instabilities of the Flow over Slender Bodies	Noted that the flow over an infinitely long slender body at high α may be separated into three distinct axial regimes. The first regime exists at axial locations far enough from the nose so as to be unaffected by the forebody flow. The flow in the third regime is time-dependent vortex shedding over an inclined cylinder. The instability in this regime, as in the case of the 2D cylinder, is absolute (temporal disturbance required). Near the nose is the third regime, where the flow is dominated by forebody asymmetry, which has been shown (Degani, 1991) to be convective (space-fixed, time-fixed disturbance required). The flow in the first regime is generally steady. The second regime lies between the others axially, and the flow is still affected by the presence of the forebody, so that the vortex shedding is not parallel with the body surface, but inclined to it. Use Ramberg's (1983) WFV to verify the existence of the three regimes. Attribute the existence of the nearly bistable states above a critical angle of attack to the influence of the forebody vortices, which no longer respond to body geometry.
Tuyl 3/1988	Computational(Vortex Filament)	Ogive(A), Hemi(A)	N/A	O: 10° H: 19°	∞	<<1	ASP, Vortex Strengths and Positions	Segmented vortex filaments replace vortex sheets. Leeward surface pressures calculated with this method compared well with thin-layer Navier Stokes results and with experimental results. Windward surface pressures are in good agreement with experimental results.
Vanden & Belk 8/1993	Computational (Thin-Layer Navier-Stokes)	Ogive(A)	5.0	38.5°	$2x10^5$	0.6, 1.4	WFV, Vortex Location	Discovered that with an unsymmetrical numerical method, the numerical error was large enough to induce asymmetry in the flow. For symmetric methods, the flow was symmetric to 12 orders of magnitude, and a bump near the nose was introduced to cause the asymmetry. When the bump was removed, the flow reverted to symmetric state, confirming previous observations (Degani, 1991). Noted that the primary separation vortex interacts with the secondary vortices to a greater extent in subsonic flow, as compared to supersonic.

Wardlaw & Morrison 10/1976	Analytical	Various	Various	Data Available From 0° - 70°	N/A	< 1.2	Prediction Techniques, Based on Experimental Data	The authors use the existing experimental database to discover trends that lead to the prediction of the maximum C_Y, the angle of attack at which max C_Y occurs and the onset angle of asymmetric yaw forces. Note that the IFA can be used to predict the max C_Y to relatively good agreement. The peak side forces occur near defined by IFA to correspond to the shedding of the first vortex. Note that general quantitative conclusions cannot be drawn from a small number of tests, but that a large database is needed. Urge physical understanding of the fluid mechanics in order to develop optimum modeling.
Wardlaw & Yanta 4/1982	Experimental	Ogive(A)	3	35°, 45°, 55°	$1.5x10^5$	N/A	C_y, CSP, Wake Velocity Fields (LDV)	**Combined CSP and flowfield data!** Varying levels of C_y are coupled with changes in the mean vortex pattern, with the highest C_y accompanying the most asymmetric vortex patterns. Fluctuations in CSP were lowest in those cases where C_y was highest. Vortices over the blunted model were of the same strength as over the sharp model, but further removed from the model. Tests performed with turbulence screens installed resulted in only slightly higher levels of measured C_y. Suggest that for a given maximum C_y, there is an associated unique flowfield.
Wardlaw & Yanta 2/1984	Experimental	Ogive(A)	3	45°	$1.5x10^5$	N/A	C_y, CSP, Wake Velocity & Vorticity Fields (LDV)	**Crossflow plane flowfields (fine grid) & topology!** Use of grit trips tends to stabilize flowfield for long tests. Two counter-rotating secondary vortices accompany each primary vortex. Flowfield asymmetries originate from primary saddle. One focus is "captured" by the primary saddle, reverses the direction of its node-saddle connection, and moves leeward from the body. The reversal of direction is unusual, and authors noted that crossflow streamlines may not be representative of 3D flow. Results suggest that at an axial location where the peak side force occurs, the primary saddle and its captured node combine!
Wardlaw 8/1974	Experimental/ Computational (Potential Line Vortices)	Ogive(A)	4.0	0° - 70°	∞	0.5 - 1.1	C_N, C_Y, WFV (Schlieren)	Exposition of a method for predicting forces on slender bodies with separated flows. Especially important is C_Y, because it is much harder to predict than C_N, C_m. Results show that C_N is well predicted over a large range of M and α, but C_Y is only qualitatively correct.

Wardlaw	Review of Existing Predictive Methods & Database	Various	Various					Contains a great number of references and a discussion of the body of knowledge as concerns the missile design community. (As of the late 1970's predictive methods, especially for subsonic flows, depended on experimental data. However, obtaining accurate, repeatable experimental data is difficult due to the nature of the problem. Only a qualitative knowledge of the flow over missiles had been gained to that point.)
Zilliac 9/1989 (Also 9/1986)	Experimental/ Computational (Incomp. Navier-Stokes)	Ogive	3.5	30°, 45°	220, 1.64×10^5	N/A	CSP, Velocity Fields(7HP), WFV, SFV, Vortex Core Power Spectra	Comparison between experimental and computational results was favorable in a validation sense. Noticed Reynolds number effects in onset of asymmetry, foreshadowing the results of Stahl & Ashgar. Hot-wire probes placed in the cores of the vortices showed no significant unsteadiness, and also that the core flow was turbulent. Showed that (in this case of 3D separation) no general correlation exists between the location of separation lines on the body and the value of skin friction.

Appendix B: Summary Table for Flow Control on Axisymmetric Bodies at High Incidence

This table contains a summary listing of many important experimental, computational and theoretical investigations of flow control over axisymmetric bodies at high angles of attack. In addition, there are some listings that reference review articles that pertain to this subject. For each listing, important variables such as Reynolds number, Mach number, angle of attack, body geometry, are given, as well as the methods of investigation and control. The author has also attempted to summarize the most important conclusions of each investigation, as well as cross-reference each listing to other pertinent findings, whether in agreement or disagreement.

In order to make this section independent from the rest of the document, nomenclature and abbreviations used in this table is given below. By providing such a reference, the author hopes to provide a substantial stepping-off point for future investigators of this problem, one that was not available when the author began work. In the humble opinion of the author, the complexity of the problem has led to a vast amount of available data, including some that have resulted in questionable conclusions when examined in the light of later results. In most cases, comments are not the opinion of the author, except to relate the article to others of interest. Important conclusions of the authors are stated, although sometimes (usually when later research seemed to have validated or invalidated a particular point), there are comments on how valid the results were perceived to be.

Nomenclature:

C_b: Blowing Coefficient

M: Mach Number

Re: Reynolds Number

δ: Half-Angle of Forebody Tip

Abbreviations:

CSP: Circumferential Surface Pressures

ASP: Axial Surface Pressures

WFV: Wake Flow Visualization

SFV: Surface Flow Visualization

3D: Three-Dimensional

2D: Two-Dimensional

IFA: 2D Impulsive Flow Analogy (Allen & Perkins, 1951)

Author(s) & Pub. Date	Investigation Type	Method of Control	Forebody Type (A: Afterbody) & Caliber (L_N/D)	Angles of Attack (α)	Reynolds Number (Re_D Unless Otherwise Specified)	Mach No. (M)	Investigated Quantities	Conclusions & Comments
Alexan, Hanff & Kind 1/1994	Experimental	Unsteady Forward Blowing	Parabolic/ Ogive(A): 2.24	10° - 70° (10° Increments)	1200 - 9000	<<1	C_N, C_Y	Control method involved unsteady blowing from forward facing ports similar to those used previously by Ng & Malcolm (1991) and Roos (1996). Blowing oscillated between "on" and "off" states. Various blowing frequencies were employed in order to rapidly oscillate the asymmetric flow between two opposing states. The vortex pattern can be switched at a maximum reduced frequency of $\omega D/U_\infty = 0.16$ by switching the blowing between port and starboard nozzles. It was found that varying the frequency of the blowing could influence the mean loads. Preliminary calculations showed that the response of a full-scale airframe (F/A-18) and the equivalent blowing rates would be acceptable.
Bauer & Hemsch 3/1994	Experimental	Passive Porosity	Ogive(A): 2.5, 5	-5° - 45°	$0.43 \cdot 10^6$, $0.97 \cdot 10^6$, $1.2 \cdot 10^6$	0.2, 0.5, 0.8	CSP, C_N, C_Y	Employed a porous forebody (idea developed by R. M. Wood & Bauer) to reduce C_Y generated by a slender forebody. The normal force coefficients revealed that the porous forebody produced near-turbulent boundary layer conditions. The effect of the porous forebody was to remove C_Y and force the pressure coefficients to be symmetric with respect to the angle of attack plane. Pressure tubes located inside the forebody revealed that the pressure was constant and the velocity very low. The authors note that the flow over the porous forebody is complex, and that the flow physics are not well understood.

Bernhardt & Williams 7/1993	Experimenta	Suction & Blowing (Normal to Surface, θ = ±135°)	Cone (A): 3.798	45°, 55°	6300 – $80.1 \cdot 10^4$	<<1	C_Y vs. Cb, Disturbance Propagation Speed, Velocity Profiles	An investigative effort that is greatly relevant to determining the nature of the instabilities governing slender body flow and the impact of Reynolds number on the instability type (see also Bernhardt & Williams, 1990) For the blowing configuration presented, suction was found to be more efficient than bleed, and the output/input power gain was about 10^8 at $Re_D = 3.0 \cdot 10^4$. The response of the vortex pattern is dependent on the Reynolds dependent, and it appears that at $Re_D < 10^4$, the flow is truly bistable, and governed by a global instability. For $Re_D > 2.4 \cdot 10^4$, symmetric states are achievable. Disturbances to the tip flow propagate through the wake at 0.91 U_∞. Discuss a mechanism by which suction and blowing can alter the flowfield by changing the flux of surface vorticity fed to the vortices.
Bernhardt & Williams 1/1995	Experimental w/ Closed-Loop Feedback Control	Suction (Normal to Surface, θ = ±135°)	2 Ogives(A): 3.5 (One Blunted)	20° - 70° w/ Pitch Rates = 5°/s, 10°/s, 20°/s	$4.0 \cdot 10^4$, $6.0 \cdot 10^4$	<<1	C_Y, C_N, C_n, C_m, Differential Pressure (Error Level) vs. α	An attempt to use feedback control to hold the vortices in a symmetric state during pitching maneuvers. There is no doubt that the control technique is able to influence the vortical flow. At all pitch rates, the flow asymmetry is held to small levels until about α = 40° - 45°. However, at higher angles, the control technique did not perform well. A neural network control algorithm was employed, but did not fare much better. Although not a complete success, this investigation showed the merit of implementing forebody control techniques in an unsteady environment produced during maneuvers.
Celik, Pedreiro & Roberts 6/1994	Experimental	Tangential Slot Blowing	Cone(A): Generic Aircraft Configuration	45° [ϕ = -80°-80°, β = -30°- 30° (ϕ, β varied dynamically)]	$Re_{D\sin\alpha} = 0.3$ $5x10^5$	N/A	C_l, C_n, C_Y, WFV, Wing-Rock Freq. and Amplitude	Investigation demonstrating the use of forebody blowing in the suppression of wing rock for delta wing configurations.

Celik & Roberts 1/1992	Experimental	Tangential Slot Blowing from Wing Leading Edge and Forebody	Ogive(A): Generic Forebody/Delta Wing Configuration	20° - 40°	N/A	<<1	C_Y, C_n, C_l, WFV (Smoke/Laser Sheet)	An investigation into applying tangential slot blowing techniques to a representative aircraft configuration. Flow can be manipulated by blowing from either the forebody or the wing, although blowing from the forebody is more effective at producing changes in C_Y, C_l, C_n, with effectiveness increasing with α. The presence of the forebody reduces the effect of blowing on C_l when blowing from the wing. It was discovered that a model with rounded leading edges could produce larger C_Y than one with sharp leading edges, provided that forebody blowing is used. An increase in forces and moments can be achieved by simultaneously blowing from the wing and forebody.
Clark, Peoples & Briggs 8/1973	Experimental & Computational	Grit Patterns and Vortex Generator Collar	Blunted Ogive(A): N/A	0°-90°	$1.8 \cdot 10^6$, $2.0 \cdot 10^6$	0.4 - 1.2	C_Y, C_n, C_N WFV (Schlieren), SFV (Oil), Vortex Trajectories and Separation Location	Although most testing was performed at high subsonic Mach numbers (approx. 0.8), C_Y is measurable. C_n is sizable, giving credence to the claim that small yaw forces can produce large yaw moments if allowed to act over an afterbody of sufficient fineness ratio. Application of grit collars and strips did less to reduce C_n, while the addition of the vortex generator collar reduced C_n by a factor of 2. SFV allowed the determination of the primary and secondary separation locations. Numerically investigated vortex patterns with three different kinds of asymmetry: strength, radial location, and polar location. Cursory tests to determine the effect of dynamic rotation of the model about its axis appeared to reveal that the Magnus effects are small or nonexistent (compare Ericsson,"Unsteady Flows").
Cornelius & Lucius 8/1994	Experimental	Nozzle Blowing (Various Locations) & Strakes	Generic Fighter Forebody, (Elliptical Cross-Sections)	5° - 60° (β = -20° - 20°)	N/A (Max $U\infty$ = 25 m/s)	<<1	C_Y, C_L, Velocity and Vorticity Fields (7HP)	Nozzle orientation for maximum effect depends on model configuration (straked, unstraked in this case) nozzle configuration. Using a slotted nozzle canted inwards toward the model centerline proved most effective. The straked forebody provides lateral stability with yaw angle, but reduces the ability to create large yaw forces through blowing, especially for large strakes. The nozzles alter the flow by directly affecting the vorticity and velocity fields, as shown by the data acquired by the seven-hole probe. Required blowing rates are acceptable for full-scale application.

Crowther & Wood 1993	Experimental	Tangential Slot Blowing	Ogive(A): 4, (6% Scale Generic Fighter Forebody)	0° - 90°	$4.9 \cdot 10^4$ - $1.1 \cdot 10^5$	N/A	C_l, C_N, C_Y	Tangential slot blowing provides an increase in C_Y in the direction of the blown side (port blowing produces C_Y to port). However, a control reversal can occur which reverses the above effects (also seen by Gee, 1994). Careful placement and design of slot is needed to minimize or eliminate reversal and to make the mass-flow requirements feasible for full-scale application. In general, the amount of C_n available from blowing increases with α. For $\alpha <$ 50°, short slots placed at a forward location are sufficient for control. For control up to $\alpha = 90°$, slots along the entire forebody are required. The jet effect can be best characterized by using C_μ rather than $C_{\dot{m}}$, so that the effects are most likely based upon momentum principles. Increasing the angular location of the slot (θ) increases the amount of C_n available until a critical angular location is reached, and slot stall occurs. Slot stall is characterized by a loss of control C_n and hysteresis in the C_n - α curve.
Degani 9/1991	Experimental/ Computational	Splitter Plate	Ogive(A): 3.5	30°, 40°, 60°, 80°	$2.6 \cdot 10^4$	<<1	SP, WFV, RMS Velocity, Dominant Wake Freq., Helicity	Frequency content of the flow as determined by experimental and numerical techniques compare well. The addition of a splitter plate on the leeward symmetry plane delays or suppresses the formation of asymmetric vortices over the forebody, where a convective instability normally governs the flow. The splitter plate also suppresses or delays the asymmetric vortex shedding that occurs further down the afterbody, where a global instability normally governs the flow. These results led to the conclusion that the splitter plate is suppressing the instabilities inherent in the flow. Although the splitter plate was effective in terms of removing the mean and low-frequency instabilities, high-frequency fluctuations associated with shear-layer instabilities were not suppressed.

Fu, Lan & Shyu 1992	Experimental	Strakes	Generic Fighter Forebody	0°-60°(β = ±5°)	$1.67 \cdot 10^6$/ft	0.2	WFV, C_Y, C_n	An investigation into the effect of LEX's on directional stability. Also includes the effect of nose strakes with and without LEX's present. It was determined that for flow without the LEX's, directional yaw instability was caused by the forebody asymmetry. With the LEX's attached, the yaw instability was still apparent above $\alpha = 25°$. For $\alpha < 50°$, the forebody vortices were suppressed by the stronger LEX vortices, the forebody asymmetry was not apparent, and the directional instability was due to the action of the vertical tail. Because the forebody vortices are dominated by those of the LEX, the addition of strakes did not affect directional stability for $\alpha < 50°$. For $\alpha > 50°$, the forebody asymmetry caused the yaw instability. The yawing moment at $\beta = 0°$ could be eliminated with the addition of large strakes to the forebody. Small nose strakes were generally found ineffective at generating yaw moments.
Gee, Rizk and Schiff 7/1994	Computational	Tangential Slot Blowing	F/A-18 Aircraft Configuration	30.3°	$Re_C = 11.0 \cdot 10^6$	0.243	Helicity, C_n, C_y, Tail Buffet Loads & Freq., Streamlines	The computations compare very well with experimental data. The computations revealed substantial interaction between the LEX and forebody vortices at large axial distances, showing the necessity of modeling the entire aircraft and not just the forebody or forebody/LEX region. Tangential blowing increases the strength of the vortex on the side that blowing occurs. The increased strength leads to earlier than normal occurrence of LEX vortex breakdown on the blowing side. Results show substantial tail buffeting and flow fluctuation in the vicinity of the tail, although the flow over the forebody and LEX's is steady. Tangential slot blowing is found to reduce the dominant frequency of the aerodynamic loads on the tail. Although the frequency was not drastically changed, and tail buffeting still present, these results show the merit of forebody blowing for possible alleviation of tail buffeting.

Gittner & Chokani 5/1994	Experimental	Nozzle Blowing (θ = ±120°)	Ogive(A): 3.0	40°, 50°, 60°	$8.4 \cdot 10^4$	<<1	CSP, C_y, Nozzle Exit Geometry,	Aft nozzle blowing brings the blowing-side vortex closer to the surface and displaces the non-blowing side vortex away from the surface, creating a yaw force to the blowing side. Effectiveness of nozzle blowing depends on nozzle exit geometry. Several nozzles were compared, and the most effective were those nozzles that had broad exits close to the surface rather than thin, vertical exits.
Guyton & Maerki 1/1992	Experimental	Nozzle Blowing (θ = ± 135°, x/D = 0.5, Canted 60° Inboard)	X-29 Aircraft (1/8 Scale Model)	0° - 45° (β = -10°- 5°)	$0.2 - 0.8 \cdot 10^6$	0.3 - 0.5	C_m, C_n, C_l, CN, C_Y, WFV	Angling the nozzles inboard greatly increases their effectiveness. Useful yawing moments due to forebody nozzle blowing generated only for $\alpha > 40°$. Large levels of $C_{\dot{m}}$ observed when blowing at high α. Some Mach number effects were observed for large rates of blowing. Reynolds number effects inconclusive. Presence of vertical tail results in significant changes in total aircraft C_Y when compared with forebody alone characteristics, and substantially more blowing was required when tail was present.
Guyton, Osborn & LeMay	Experimental	Nozzle Blowing (θ = ±135°), Chines, Tangential Slot Blowing	Aircraft Config: 1/8 Scale X-29 1/15 Scale F-15C, Generic Config. w/Chined Forebody	0° - 55° (β = -20°- 20°)	N/A, N/A, $11.5 \cdot 10^3$	0.3, 0.4, <<1	C_m, C_n ,Wing SP, WFV	All of the pneumatic methods of forebody vortex control investigated were able to provide improved maneuverability and directional stability at intermediate to high angles of attack. Required blowing rates are only a fraction of that available through engine bleed. Noted that tangential slot blowing and aft nozzle blowing produce similar effects through different physical mechanisms.
Kandil, Sharaf El-Din & Liu 1994	Computational (Comp. Thin-Layer Navier-Stokes)	Blowing Normal to Surface (From Tip to 0.15LN, β= ±67.5° From Leeward Ray)	Cone: 5.72	40°	$6 \cdot 10^6$	1.4	CSP, Wake Total Pressure Decrement	Normal blowing over small portion of forebody was found to be effective at maintaining symmetric flow at an intermediate angle of attack. Circumferential surface pressures and wake data confirm that the flow is near-symmetric at all axial locations.

Kramer, Malcolm, Suarez & James 9/1994	Experimental	Nozzle Blowing, Slot Blowing, Rotatable Strakes, "Rhino Horn"	6% Scale F/A-18 Aircraft	0° - 60° (β = -10°-0°)	$0.92 \cdot 10^6$/ft	N/A	C_Y, C_n, C_l, CSP	An investigation into the effectiveness of proven forebody control techniques to a maneuvering aircraft configuration. All of the forebody vortex control methods applied in this investigation have been shown to be effective in static conditions where $\alpha > 30°$. Nozzle blowing provided the same levels of control force seen in the static case, at nondimensional rotation rates up to 0.28. Slot blowing was found more effective if applied on the leeward side during rotation. The vertical nose strake ("Rhino Horn") was found to be the effective during rotation, producing the maximum ΔC_n of all tested control techniques. When the blowing commenced, the flow required about two convective time constants to reach equilibrium. When the blowing stopped the flow required about three convective time constants to reach equilibrium.
Lanser & Meyn 11/1994	Experimental	Nozzle (θ = ±135°) & Slot (θ = ±90°) Blowing	Full-Scale F/A-18 Aircraft	25°-50° (β= -15°-15°)	Re_C = 4.5×10^6 - 12×10^6	N/A	C_n, CSP	For $\alpha > 40°$it was discovered that nozzle blowing directly aft produced only slightly larger C_n than that produced by the rudder at max deflection. Nozzle blowing with the nozzles canted inboard by 15° had no effect on C_n. Tangential slot blowing provided the required yaw forces and moments at high α. Interestingly, blowing from 16-in. or 32-in. slots was more effective than from 8-in. or 48-in. slots. This may be due to the interaction of the forebody and LEX vortices. Time delays from commencement and alleviation of blowing to flow equilibrium were 5 and 6.5 convective time constants respectively.
LeMay, Sewall & Henderson 1/1992	Experimental	Nozzle and Tangential Slot Blowing	F-16C Aircraft	0° - 55° (β= -20°-20°)	$2.5 \cdot 10^6$/ft	0.4	Cm, Cn, Cl, CN, C_P,	Neither slot nor nozzle blowing (symmetric or asymmetric) provided enough control to improve the directional stability of the F-16 at high α. For nozzle blowing, nozzle located closer to the forebody tip were more effective. Centers of pressure (CP) of the resultant C_Y due to blowing were in the region of the LEX, leading the authors to conclude that forebody blowing affects the LEX vortices as well as forebody vortices. Blowing symmetrically at small rates from the slots produced large pitch down moments.

Levin & Degani	Experimental	Spinning Nose Section (0 - 3.5x104 RPM)	Ogive(A): 3.5	0° - 55°	1.3·104/cm - 2·104/cm	N/A	C_Y vs. Spin Rate. WFV	Spinning the forebody tip at different rates produced symmetric to very asymmetric flowfields. At high α and low spin rates, the flowfield was unsteady as the vortices switched sides. As the spin rate increased, an asymmetric but steady vortex pattern formed. This method of control has potential to be a practical means of controlling the yaw forces and moments on a slender forebody.
Malcolm & Ng 2/1990	Experimental	Strakes, Aft Nozzle Blowing (θ = ±135°, x/D = 0.5, 1.0, 1.5)	Ogive(A): 4.0(Generic Fighter Configuration: 45° Clipped Delta Wing w/ LEX & Typical Empennage)	0° - 70° (β= -20°-20°)	Re_C = 0.75·106	N/A	Cn, Cm	Nozzle blowing was found to be most effective at x/D = 0.5 (closest to the nose). Proper placement of symmetric strakes can minimize or eliminate asymmetric C_Y, C_n. Blowing from the nozzles (with the strakes) can then alter the flowfield to generate the required control for maneuvering. Blowing normal to the surface not as effective as blowing forward or aft tangent to the surface. Control of the flow through use of forebody blowing alone is much more difficult to achieve than if strakes are used to first establish symmetric condition. Using strakes of the minimum possible size makes it easier for blowing to overcome symmetrically imposed condition. Significant control capability exists to high angles of attack if conventional control surfaces (vertical tail) are augmented by forebody vortex control.
Mendenhall & Lesieutre 5/1992	Numerical Prediction (Potential Flow)	Chines	Ogive-Type Fighter Forebody w/ Chines	10°, 20°, 30° (β= -10°, 0°, 10°)	∞	<<1	CSP, Vortex Strengths & Trajectories, Velocity Fields	Forebody represented by 2D and 3D singularities, and the vortex flow is represented by discrete vortices in crossflow planes. At α = 10° and $\alpha = 20°$, the predicted leeside surface pressures are very close to those measured experimentally, even when $\beta \neq 0$. The method has merit for the prediction of vortex shedding over chined bodies.

Modi & Stewart 1/1992	Experimental	Tip Geometry Modifications, Strakes, Spinning Nose Section (0 - 2000 RPM), Porous Forebody, Nose Booms (9)	Cone(A): 1,2,3 Hemi(A)	0° - 75°	$1 \cdot 10^5$	N/A	CSP, C_Y	Many different methods applied to determine if they are efective at reducing C_Y and C_n. Nose booms reduced the magnitude of max C_y by 50%. Behavior of C_Y vs. ϕ similar to that seen with baseline tip.. The porous tip (20% of L_N), due to several limitations, did not perform as well as expected, but the reduction of C_Y from the baseline case was still 50%, while C_N was not affected (compare Bauer & Hemsch, 1994). Nose strakes reduced the observed C_Y by as much as 88%. All strakes for which LS > 0.02_{LN}were found to have potential for producing a symmetric flow. The maximum reduction of C_Y from spinning the forebody tip was found to be about 75% at 200 RPM. Flow mechanisms for all of these control techniques were not analyzed.
Modi, Cheng, Mak & Yokomizo 10/1992	Experimental	Strakes, Porosity, Nose Booms	Cone(A):	±50°	$1 \cdot 10^5$	N/A	C_Y	Delta strakes can eliminate the yaw force almost completely (96%) for $\alpha < 50°$. Minimum reduction by delta strakes was 50%. The porous tip reduced C_Y by as much as 86%. It was suggested that a microscopically porous tip might be better suited to this application. Nose booms of appropriate length can reduce the yaw force when added to a standard conic tip, but the boom must be aligned precisely with the nose. A porous forebody used in addition to the nose boom or delta strake provided no improvement. Authors note the amount of innovation that is possible in this field.
Mosbarger 1994	Experimental	Nozzle Blowing (Multiple Nozzle Locations)	6% Scale F-16 Forebody, Three Generic Elliptical Forebodies	15° - 35°	Re_C = $0.6 \cdot 10^6$, $1.3 \cdot 10^6$, $2.4 \cdot 10^6$ ft-1	0.4, 0.5, 0.6	C_Y	The blowing coefficient $C\mu$, based on the momentum flux through the nozzle, effectively scales the blowing effects across large ranges of M and Re. The best axial location for the nozzles was at the most upstream location, showing that disturbances near the nose tend to have more leverage in controlling the flow. Optimal direction to point nozzle is 60° inboard from directly aft. This pointing direction has been shown to be optimal for the F-16, X-29 and F/A-18. the results of this investigation and others confirm that the optimal pointing location is not a function of freestream conditions or model orientation.

Moskovitz, Hall & DeJarnette 7/1991	Experimental	Elliptic-Circular Blend Forebody Tip	Ogive(A): 3.0, Cone(A): 1.37	30°, 40°, 50°, 60°	$2.4 \cdot 10^4$, $8.4 \cdot 10^4$	N/A	C_y, CSP	Mainly an investigation into the behavior of C_y with ϕ for several different tip geometries. Specifically, evaluation of a new elliptic/circular tip for flowfield control is examined. Regular repeatable and predictable variations in the C_y distribution result from application of the new tip. The elliptical tip ensures the availability of large amplitude yaw forces and has potential for use as a control device at moderate to high α.
Mourtos 6/1990	Theoretical (Inviscid Outer Flow Matched to Viscous Boundary Layer)	Tangential Blowing	Cone: 5.715	0° - 32°	Applied to Both Laminar & Turbulent B.L.	N/A	CSP, CL, Primary and Secondary Separation Locations	A von Karman/Pohlhausen technique is used to solve the crossflow momentum equations, and predicted separation lines agree well with experiment. The use of 2D separation criteria is justified by the conicality of the flow (it would be interesting to determine the flow in this manner for an ogive forebody, where the flow is not conical, except at the tip). Vortex strength, position and surface pressures are not predicted as well by this theory. Tangential slot blowing displaces the primary separation lines affecting the strength of the vortices and amount of asymmetry.
Ng & Malcolm 1/1991	Experimental	Rotatable Nose-Tip Strakes	Truncated 6% Scale F/A-18 Aircraft	15° - 65° (β = -20-20°)	0.7·103/cm	<<1	Cn, WFV	Control of the vortical flow over the F/A-18 model through the use of rotatable nose strakes is exceptional to 65° (maximum angle tested). Comparison with previous studies involving a single strake (Hall/Erickson/Straka/Peters/etc, Degani(Origin of... 1990), Zilliac/Degani/Tobak Asymmetric Vortices... 1990), Moskovitz/Hall/DeJarnette (...New Device...1990)) revealed that the second strake allows a continuous and relatively smooth variation in C_n with rotation of the strakes. Note that more control could be gained by altering the angle between the strakes (it was fixed in this investigation). In essence, the strakes alter the shape of the nose, providing large and controllable micro-asymmetries. The strakes are thought to be too small to influence the vortical flow by means of injecting additional vorticity. the rotatable strakes were also effective for the entire range of β tested. It was noted that the characteristics of the control depend strongly on the vortical flow normally present at a particular α and model orientation, so that the key to control is to be flexible in application.

Peake, Owen, & Johnson 1/1980	Experimental	Normal, Forward & Aft Nozzle Blowing	Cone: 5.715 give: (16° Semi-Angle)	Approx. 0° - 70°	Re_{LN} = $13.5 \cdot 10^6$ (Cone), $5.3 \cdot 10^6$ (Ogive)	0.6	C_Y, C_N, C_n, C_m, C_l, CSP, CDP, Mean & Fluctuating Heat Transfer, SFV (Oil Dot), WFV, Velocity Fields (LDV), Skin Friction	An extensive experimental investigation into the effects of nozzle blowing on slender forebody vortical flow and accompanying forces and moments. Drawing on the findings of Mishicka and Sato, the authors suggest that the leeward enclosing saddle point is the location at which the amplification of the hydrodynamic instability (which leads to the vortex asymmetry) first occurs, and provide some supporting evidence (see Wardlaw & Yanta, 1984). The authors also postulate that the shedding of vortices may be attributed to the amplification of instabilities at an interior saddle point. Thus, it makes sense to attempt flow control by blowing near the primary and secondary saddle points. It was discovered that small blowing rate are required to change the flow in a global manner. The vortex structure from the blowing jet does not entrain or mix with the primary vortex, but remains separate and identifiable. **The authors discover that blowing normal to the surface appears to be more effective than tangential blowing, a view soon to be reversed when more optimal nozzle configurations and locations are examined.**
Peake & Owen 5/1979	Experimental							
Rao & Sharma 7/1994	Experimental	Diamond Forebody w/Retractable Strakes	Diamond Cross-Section	0° - 70°(β=-20°-20°)	Re_{LN} = $0.5 \cdot 10^6$	N/A	C_Y, C_N, C_n, CSP, WFV, SFV (Oil Flow)	A preliminary investigation into vortex control over bodies of diamond cross-section. By deploying strakes normal to the windward facets of a diamond-shaped forebody, the vortical flow over the forebody is effectively controlled. Deploying two strakes in tandem on opposite sides of the body results in zero net side force. Strake deployment increases suction on the windward side and decreases the windward side suction, so that up to 30% reduction in the normal force can be achieved at high α.

Rao, Mosko vitz & Murri 1986	Experimental	Asymmetrically Deployed Strakes	Cone(A): 3.16 eneric Fighter Configuration	30° - 80°	$4.1 \cdot 10^4$ - $1.9 \cdot 10^5$	N/A	C_n, C_l, C_n, CSP, WFV	Deploying a single strake generated slightly more C_n as that generated by a rudder at max deflection at $\alpha = 25°$. For the locations considered, the single strake had considerable control power when located at $\theta = 105° - 120°$. Two strakes deployed asymmetrically did not generate as much Cn as the single strake. In addition, two strakes deployed symmetrically at $\theta = \pm 120°$ did not generate symmetric flow.
Ravi & Mason 5/1994	Computational (Euler)	Chines	Ogive: 0.805, 2.07	20° - 40°($\beta = 0°$-5°)	$Re_L = 1.02 \cdot 10^6$	0.2	C_β, C_y	In general, chined forebodies that are flat in the crossflow direction have better directional stability. Ideally, C_β should be positive, but forebody contributions are susceptible to becoming too large at high α, which can result in poor yaw-damping characteristics. The included angle of the chines was found to be irrelevant unless the chine angle was large. This result points to the possible existence of a critical chine angle. As Roos & Magness (1993) have seen experimentally, the forebody contribution to yaw characteristics is stabilizing. the largest contribution from the forebody comes from the aft part, where the chine leading edge sweep is nearly 90°.

Roos & Magness 8/1993	Experimental	Nose Bluntness (20%), Microblowing ($\theta = \pm 135°$)	Ogive: 3.5	0° - 90°	$7.0 \cdot 10^4$, $1.6 \cdot 10^5$, $2.2 \cdot 10^5$ (Turbulent Separation Induced by Gritting Techniques)	N/A	C_Y, C_N vs. C_{mdot}	Demonstrated that a 20% blunted 3.5 caliber tangent-ogive forebody developed no yaw force for $\alpha < 60°$ with both laminar and turbulent separation. Forward blowing near the tip was found to be ineffective for $\alpha < 35°$. Blowing on the right side of the forebody produced a yaw force to the left, and vice versa. Slight blowing through nozzle orifices near the forebody tip enabled proportional control of the flow through a range of $C_{\dot{m}}$. For larger blowing rates, the amount of generated yaw force saturated. The maximum force generated was affected by α, nose bluntness and nature of boundary-layer separation. Blowing effectiveness for this forward blowing configuration was shown to scale with mass flow rate and insensitive to Re variation. Since the effectiveness scales with the mass flow and not the momentum of the jet, it seems likely that the jets use a displacement effect (much like a material perturbation) to manipulate the flow. Reducing the bluntness of the body increased the amount of control C_Y able to be generated by blowing.
Roos & Magness 1/1994	Experimental	Chines	Ogive: 3.5	0° - 60°(β = -15°-0°)	Low-Speed	<<1	WFV, C_Y, C_N, SP	At $\alpha < 15°$ (pre-separation), chined forebody directionally unstable due to crossflow drag. For $15° < \alpha < 45°$, forebody is stable because upwind vortex has increased suction, while the downwind vortex is pushed away from the forebody. The combined effect is a vortex-induced restoring force. For $\alpha > 45°$, the upwind vortex bursts prematurely, causing directional instability.
Roos 1/1996	Experimental	Microblowing (x/D = 0.1, $\theta = \pm 135°$)	10% Scale F-15 Aircraft	0° - 80° (β=-20°-20°)	N/A (U_∞ = 80 ft/s)	N/A	C_n	As with the tangent-ogive forebody, microblowing was ineffective for $\alpha < 35°$. However, for $\alpha > 50°$, microblowing was found to be very effective, generating C_n levels comparable to other proven nozzle blowing configurations (Iwanski and Rourke), but with 1/100 the mass flow rate. Maximum effect of microblowing on C_n occurred at $\alpha = 60°$

Roos 6/1996	Experimental	Microblowing (x/D = 0.3, $\theta = \pm 135°$)	Hemi(A)	0° - 60°	$1.6x10^5$	N/A	C_N, C_Y, WFV, SFV	As expected, the hemisphere cylinder did not generate any asymmetric C_Y at high α. Application of slight blowing on the hemisphere surface was sufficient to enable proportional control of the flowfield and C_Y in the same manner as previous techniques on blunted tangent-ogive forebodies. Microblowing was shown to have an amplification factor over 1400 times that of an equivalent reaction control jet thrust.
Roos & Manor 2/1997	Experimental	Pulsed Microblowing (x/D = 0.1, $\theta = \pm 135°$)	Ogive: 3.5 (Blunted 20%)	30° - 90°	N/A	N/A	C_Y	An investigation into the effect of pulsing the mass flow rate for the previously proven microblowing configuration. Results indicate that within the rage of pulsing frequencies tested, there is no additional benefit derived from pulsed microblowing.
Roos 6/1994	Experimental	Nose Bluntness, Microblowing (x/D = 0.1, $\theta = \pm 105°$, $\pm 135°$)	Ogive: 3.5	0° - 60° (β=-15°-15°)	$1.6x10^5$	N/A	C_Y	A presentation of results from microblowing investigations. New results include an investigation into the effects of microblowing on a sharp-nosed tangent-ogive forebody. The sharp-nosed body develops a higher control C_Y than the blunted forebodies, but the region of proportional control is minimal, at least for the laminar separation cases studied. Demonstrated the potential of using a two-point pressure difference as input for a control system centered on forebody blowing techniques.
Smith 9/1994	Experimental	Forebody Geometry Modifications, Strakes, Chines, Nozzle ($\theta = \pm 150°$) & Slot Blowing	10% Scale F-16	0° - 60°	N/A (Dynamic Pressure = 20 psf)	N/A	Cn	The standard F-16 forebody is statically unstable in yaw for > 30°. Addition of chines (stable) or substituting the shark-nose geometry (neutral or stable) gives characteristics that are more acceptable. Both of these modifications also reduce C_n from the standard configuration. Both tangential-slot and nozzle blowing were effective, with nozzles canted inboard and slots positioned more forward showing the most promise. Slots required more mass flow to develop the same Cn. Nozzle blowing was able to produce C_n on the same order as conventional control surfaces, but at high α, where conventional controls are typically compromised. Nose boom strakes are effective for > 40°, producing Cn levels equal to that from the rudder. Axial position of the strakes had a large effect on Cn control. The strakes were found ineffective with the chined forebody.

Suarez, Malcolm & Ng 1/1992	Experimental	Rotatable Nose-Boom Strakes	F-16 Aircraft & F-16 Forebody, X-29A Forebody	15° - 60°	Re_C = 0.47 - 0.94x105/m (Water), 3.3x106/m (Air)	<<1 (Water), 0.3 (Air)	WFV, Separation Location, Cn,	**F-16:** The nose-boom wake tends to dominate the other sources of forebody asymmetry for moderate to high α. The small, rotatable nose-boom strakes were found to be an efficient method of vortex manipulation between α = 45° - 60°, but the control was found to depend strongly on strake position and planform. Strakes inefficient at low α. **X-29:** Forebody strakes make highly asymmetric flow nearly symmetric. Rotation of single strakes was found to be effective in yaw control. Larger strakes generally supply larger Cn, however there are cases where a smaller strake is better because it can impact the flow in a location that affords more leverage. Dual strakes provide more flexibility in control because they act in tandem. The effectiveness of the nose-boom strakes is greatly reduced when forebody strakes are present.
Tang, Graham & Peraire 6/1996	Analytical	w/Optimum control	2D Cylinder					
Williams & Bernhardt 6/1990	Experimental	Dynamic Normal Blowing (θ = ±135°)	Cone(A): 10.7	0° - 90°	6300	<<1	C_Y, CSP, WFV, Velocity Fields	At α = 45°proportional control of the flow asymmetry is achieved for a range of blowing coefficients (which are based on mass flow), with saturation eventually being reached (compare Roos, 1996). The authors suggest that nonlinear effects are responsible for the saturation in response as the blowing coefficient is increased further. As the angle of attack is increased to 55°, proportional control was no longer achievable because of the existence of a bistable vortical pattern (which truly exists here because of the low Re). It is possible that proportional control could be achieved at α > 50° if the control actuator has sufficiently fine control (see Degani/Schiff, 1991) and if the Reynolds number is higher.

Appendix C: Summary Table for Natural and Forced Unsteady Flow over Axisymmetric Bodies at High Incidence

This table contains a summary listing of many important experimental, computational and theoretical investigations of the unsteady flow over axisymmetric bodies at high angles of attack for investigations pertaining to natural and forced unsteadiness. In addition, there are some listings that reference review articles that pertain to this subject. For each listing, important variables such as Reynolds number, Mach number, angle of attack, body geometry, and method of investigation are given, as well as the type and characteristics of the motion. The author has also attempted to summarize the most important conclusions of each investigation, as well as cross-reference each listing to other pertinent findings, whether in agreement or disagreement.

In order to make this section independent from the rest of the document, nomenclature and abbreviations used in this table is given below. By doing so, the author hopes to provide a substantial stepping-off point for future investigators of this problem that was not available when the author began work. In the humble opinion of the author, the complexity of the problem has led to a vast amount of available data, including some that have resulted in questionable conclusions when examined in the light of later results. In most cases, comments are not the opinion of the author, except to relate the article to others of interest. Important conclusions of the authors are stated, although sometimes (usually when later research seemed to have validated or invalidated a particular point), there are comments on how valid the results were perceived to be.

Nomenclature:

C_b: Blowing Coefficient

M: Mach Number

Re: Reynolds Number

δ: Half-Angle of Forebody Tip

Abbreviations:

CSP: Circumferential Surface Pressures

ASP: Axial Surface Pressures

WFV: Wake Flow Visualization

SFV: Surface Flow Visualization

3D: Three-Dimensional

2D: Two-Dimensional

IFA: 2D Impulsive Flow Analogy (Allen & Perkins, 1951)

Author(s) & Pub. Date	Investigation Type	Forebody Type (A=Afterbody) & Fineness Ratio (L_N/D)	Type of Unsteadiness, Motion or Maneuver	Range and Rate of Motion or Maneuver	Reduced Frequency	Reynolds No./Mach No. (M)	Investigated Quantities	Conclusions & Comments
Bernhardt & Williams 1/1995 & 5/2000	Experimental w/ Closed-Loop Feedback Control	Suction (Normal to Surface, $\theta = \pm 135°$)	2 Ogives(A): 3.5 (One Blunted)	α =20° - 70° w/ Pitch Rates = 5°/s, 10°/s, 20°/s	N/A	<<1	C_Y, C_N, C_n, C_m, Differential Pressure (Error Level) vs. α	An attempt to use feedback control to hold the vortices in a symmetric state during pitching maneuvers. There is no doubt that the control technique is able to influence the vortical flow. At all pitch rates, the flow asymmetry is held to small levels until about 40° - 45°. However, at higher angles, the control technique did not perform well. A neural network control algorithm was employed, but did not fare much better. Although not a complete success, this investigation showed the merit of implementing forebody control techniques in an unsteady environment produced during maneuvers.
Calarese 4/1982	Experimental	Ogive(A): 3.0	Natural Unsteadiness $\alpha = 45°$	N/A	N/A	Re: $7x10^6$/m M: 0.6, 0.7	Wake Power Spectra, Turb. Intensity, WFV, SP	Flow visualization showed that vortices are asymmetric and generally steady at α = 45°.Power spectra obtained (M = 0.6) from hot-film measurements showed definite resonant peaks near 800 Hz. Power spectra inside the vortices showed high turbulence levels and another peak in the power spectrum (near 2700 Hz) occurs in the axial direction. The 800 Hz frequency was attributed to a Rayleigh instability, but the 2700 Hz resonance was not classified on the basis that it may have come from extraneous (non-flow) sources.
Cobleigh 1/1994	Calculations From Flight-Test Data	X-31 Forebody(A)	Various Maneuvers	α = 35°-75°	N/A	Re_D: Full-Scale Flight Testing M: N/A	C_n	Calculations of C_n revealed yaw asymmetries at all α for maneuvering. Envelope reduction occurred because of saturation of thrust vector vane displacement. Strakes and transition strips reduced the asymmetry. Calculated flight-test data at full-scale Reynolds numbers did not compare well to wind tunnel data.
Degani & Zilliac 4/1990	Experimental	Ogive(A): 3.5	Natural Unsteadiness, α = 30°-85°	N/A	N/A	Re_D: $1.7x10^4$, $2.6x10^4$, $3.5x10^4$ M: N/A	SP Power Spectra, WFV	Flowfield over the model for $\alpha > 30°$ is naturally unsteady to a high degree. Low-frequency von Karman shedding and high frequency shear-layer fluctuations were documented. Moderate frequencies between those mentioned above lead the investigators to surmise that some type of vortex interaction was present.

Ericsson 1/1991	Theoretical, Based on Analysis of Experimental Data	Cone(A):	Coning	Free Coning (360°+)	$k = \omega L/2U_\infty$ Varied	Re: About 10^5 M: N/A	Steady Rotation Rate as a Function of α U_∞ and Model Geometry	Since the experimental models showed little preference in direction of rotation, even though the steady yaw moment is biased to one side, Ericsson made the important conclusion that the **effects of body motion must overcome the initial asymmetry**. Assumed that in the coning motion of slender bodies, the driving moment was generated by vortex asymmetry on the forebody only. For steady coning rates, the driving moment would be balanced by a moment due to cylinder drag from all parts of the body. Used the experimental data from Yoshinaga, et al. (1981) to compare with the derived prediction. The theoretical calculations succeeded mainly in the prediction of the slope of the coning rate vs. U_∞ curves, but only for $U_\infty < 10$ m/s. Possible reasons for the differences between experiment and theory were suggested. Mechanisms of oscillatory coning were discussed.
Ericsson & Reding 3/1981	Review	Various	Vortex-Induced Loads on Slender Vehicles	Pitching and Coning				In addition to reviewing static results, the authors also look at how pitch rate and coning rate affect the vortex formation and aerodynamic forces and moments on slender bodies. At the time of this paper, only the unsteady results from Tobak et al. (1990), Schiff & Tobak(1970), and Smith & Nunn (1976) were available. Calculated that the negative pitch damping contribution due to pitch rate could be up to two orders of magnitude larger than the body-alone positive damping.

Gad-el-Hak & Ho 6/1986	Experimental	Ogive(A): 3	Oscillatory Pitching About Mean α	$\Delta\alpha = \pm 5°$, $\pm 10°$, $\pm 15°$ About α = 10°, 15° (Pitch Axis at x/L = 0.5)	$k = \pi fD/U_\infty = \omega D/2U_\infty$= 0.04-0.75	Re_D: $2.0x10^3$ - $1.2x10^3$ M: <<1	WFV, Vortex Position	Employed fluorescent dye in a towing-tank experiment to visualize the leeside vortices over a tangent-ogive cylinder executing a sinusoidal pitching motion. Longitudinal and transverse laser sheets were used to illuminate the dye as the model was towed. Effects of reduced frequency, Reynolds number (within the laminar range), and pitching amplitude were investigated. The body vortices were observed to be symmetric at all times. Noted that there were two distinct pairs of vortices, one pair emanating from the afterbody during the downstroke (α increasing) and the other from the forebody during the upstroke (α decreasing). It is not surprising to see the afterbody generate the initial vortices as the body pitches up, since the effective angle of attack aft of the pitching center is higher than the geometric angle of attack due to the pitching motion. The streamwise growth of the forebody vortices was observed to be linear or conical in nature. The circumferential position of the vortices was highly dependent on the reduced frequency, with low reduced frequencies causing the vortices to remain almost directly to the lee of the body, while high reduced frequencies caused the vortices to move away from the leeward symmetry plane. The interaction between the two pairs of vortices was visually documented.
Hoang, Wetzel & Simpson 1/1994	Experimental	Prolate Spheroid: 6	Ramp Pitching Pitch Axis: x/L = 0.5	α = 0° - 30° $d\alpha/dt$ = 90°	$k = \omega L/U_\infty$ = 0.016	$Re_L = 4.2x10^6$	CSP	In part, this paper stands as a validation of the capabilities of the Dynamic Plunge, Pitch and Roll Model Mount (DyPPiR) installed in the Virginia Polytechnic Institute and State University Stability Tunnel. The DyPPiR was shown to be capable of large-amplitude, high-frequency preprogrammed motions, even with models as large as 150 lb. The pressure distributions on the lee side of the prolate spheroid showed that the wake is highly unsteady. In addition, it was shown that dynamic lift can be achieved with an axisymmetric body in a pitch-up maneuver, due to the strong leeside vortices which develop.

Iwanski & Nelson 1/1999	Experimental	Ogive: 3.5 Circular and Chined Cross-Sections	Oscillatory Pitching Pitch Axis: x/D = 3.5 (Forebody Base)	$\alpha = 0° - 45°, 0° - 90°$(Pitch Axis at Forebody Base)	$k = \omega L/U_\infty$ 0.042	Re_D: 76.3 $x10^3$ M:N/A	C_N, C_Y	As could be expected, the chined forebody develops about 22% more normal force and substantially less yaw force than the round forebody. **Round Cross-Section , 0°-90° Motion:** C_N is less than the static case during the upstroke of the pitching motion, but slightly more than the static case during the downstroke. The onset of C_Y is not delayed by the upstroke of the pitching motion ($\alpha_A = 30°$ for static and dynamic cases), but the magnitude of C_Y is lower than the static case until $\alpha = 50°$. However, the maximum C_Y is about 25% higher in the dynamic case, where it occurs at $\alpha = 57°$, compared to $\alpha = 45°$ for the static case. **Chined Cross-Section, 0°-90° Motion:** C_N is just barely higher than the static case during the upstroke, but there is a noticeable difference in the downstroke, where C_N decreases from the static case. **0°-45° Motion:** For both models, the dynamic data is not very different from the static data.
Kramer, Malcolm, Suarez & James 9/1994	Experimental	6% Scale F/A-18 Aircraft w/ Nozzle Blowing, Slot Blowing, Rotatable Strakes, "Rhino Horn"		$\alpha = 0° - 60°$ ($\beta = -10° - 0°$)		Re_D: $0.92x10^6$/ft M: N/A	C_Y, C_n, C_l, CSP	An investigation into the effectiveness of proven forebody control techniques to a maneuvering aircraft configuration. All of the forebody vortex control methods applied in this investigation have been shown to be effective in static conditions where $\alpha > 30°$. Nozzle blowing provided the same levels of control force seen in the static case, at nondimensional rotation rates up to 0.28. Slot blowing was found more effective if applied on the leeward side during rotation. The vertical nose strake ("Rhino Horn") was found to be the effective during rotation, producing the maximum ΔCn of all tested control techniques. When the blowing commenced, the flow required about two convective time constants to reach equilibrium. When the blowing stopped the flow required about three convective time constants to reach equilibrium.

Kramer & Smith 7/1994	Experimental	F/A-18 & F-16 Forebody w/ Nozzle Blowing, Slot Blowing, Rotatable Strakes, "Rhino Horn"	Steady Coning & Flight Testing Coning Axis: N/A	$\omega < 200$ RPM $\alpha = 0° - 60°$	$k=\omega b/2U_\infty$, $k_{max} = 0.175$	Re_D: 0.56 - 0.92x106/ft M: N/A	C_n, Time Lag Associated with Vortex Control	Testing on the NASA Rotary Rig showed that all FVC methods could be effective for $\alpha > 30°$. Jet blowing is not greatly affected by a rotary flow field. Slot blowing effectiveness is reduced if rotation places the slot on the windward side of the forebody, but slot effectiveness is increased if rotation places the slot to the leeward side of the forebody. The single rotating tip strake (when positioned on the leeward plane of symmetry) and the "Rhino Horn" increased the anti-spin tendency of the F/A-18. The time lag associated with blowing is about 2-3 convective time units, or on the order of conventional control deflection times. FVC used on an F-16 during flight testing expanded the performance envelope and increased the maneuverability of the aircraft. There was a palpable pilot preference for the FVC-equipped aircraft (active control) rather than one equipped with just passive chines (stable, but not maneuverable at high α).
Lowson & Ponton 6/1992	Theoretical & Experimental	Circular Cone: 5.72, 11.5; Elliptical Cone: 5.72; Delta Wing Sweep Angles: 70°, 80°	Natural Unsteadiness, $\alpha = 0° - 90°$	N/A	N/A	Re_D: $2.0x10^4$ - $3.0x10^6$ (Most results at $3x10^5$) M: N/A	Calculation and Visualization of Leeward Vortex Positions	Compared theoretical calculations of critical α for symmetry breaking (onset angle of nonzero C_Y) to experimental observations. Theoretical methods support the existence of conical asymmetries over slender bodies and that the critical angle depends on the ratio of α to δ. The thickness of the body (length parallel to symmetry plane) influences the angle of onset of asymmetry. Experimentally, it is seen that thinner bodies are more resistant to vortex asymmetry, but are susceptible to asymmetries caused by vortex breakdown. Otherwise, slender wings do not support asymmetric flows (any observed due to thickness of apex). The flow states observed over circular cones is described and a mechanism for natural unsteadiness is put forward.

Mange & Bragg 6/1995	Experimental	Chined Ogive: 3.5	Oscillatory Pitching Pitch Axis: x/D = 4.92 – 5.45	$0 < \omega < 2\pi$ rad/s	$k=\omega L/2U_\infty$ (L = Model Length = 10.5") $0.0027 < k < 0.0137$	Re_D: $1.4x10^5$ – $2.8x10^5$ (WFV at Re_D = $2.8x10^4$)	SP, SFV, WFV, C_m, C_N	Measured SP were integrated to overall forces and moments. Unsteady WFV was done, but not presented. SFV done for steady cases. In steady cases, the secondary vortex, a product of viscous separation, is a dominant feature of the flow over a chined body. During pitch-up motion, the primary vortex remains closer to the body and further inboard than the steady case at equivalent α. During the upstroke (pitch-down) the primary vortices were further removed from the body as compared to the steady case. C_N increases more quickly during the upstroke and unloads faster during the downstroke as compared to the steady case. Increasing the reduced frequency resulted in an increase in CN during the upstroke and decrease during the downstroke, an almost uniform decrease in SP across the span and an increase in the effect of Re_D. It appears that the center of pressure is unaffected by pitch rate, so that its position does not change during the motion. The chines prevent the existence of C_Y at any α.
Mange & Bragg 6/1997	Experimental	Chined Ogive: 3.5	Oscillatory Pitching Pitch Axis: x/D = 4.92 – 5.45	$0 < \omega < 2\pi$ rad/s	$k=\omega L/2U_\infty$ (L = Model Length = 10.5") $0.0027 < k < 0.0137$	Re_D: $2.1x10^5$ – $2.8x10^5$ (WFV at Re_D = $2.8x10^4$	SP, SFV, WFV, C_m, C_N , Vortex Position, Burst Points	Essentially an updated and revised version of the authors' 1995 paper on the same subject, this paper adds some interesting insight. Compared calculated forces and moments (from integrated SP) to existing data for the forebody (Roos & Kegelman, 1991), with little error. Vortex positions were tracked, and it was found that the lag during the upstroke in the position of the primary vortex relative the forebody is coupled with a similar lag in the position o the secondary vortex. The authors attribute this effect to the inability of the secondary vortex to displace the primary vortex, which has added strength due to the pitching motion. In addition to lower leeward SP, higher windward SP were noted. Vortex bursting (primary vortex burst leads immediately to secondary breakdown) was delayed during pitch-up motion and induced during pitch-down motion. 3D plots of SP are presented.

Montividas, Reisenthel & Nagib 3/1989	Experimental	Cone(A): 2.51, Varying Bluntness & Overall Fineness Ratios w/Passive Vortex Control	Ramp Pitching Pitch Axis: N/A	$0° < \alpha < 90°$, $50°/s < \lvert d\alpha/dt \rvert < 300°/s$	$k = \omega L/U_\infty$, $\lvert k \rvert < 0.35$	Re_D: 2700 – $11x10^3$ M: << 1	WFV, Vortex Shedding Location, Wake Velocity Fields (LDV)	Used flow visualization to determine vortex separation locations for various models and pitch rates. The boundaries between the flow regimes (symmetric, asymmetric, and unsteady) were found to be insensitive to Reynolds number for the range of pitch rates and Reynolds numbers investigated. It was discovered that the use of the nondimensional pitch $k = \omega L/U_\infty$ (L being the distance from the apex to the pitch axis), rather than $k = \omega D/U_\infty$ is the proper scaling parameter for this type of flow, collapsing the flow regime maps for a given L/D ratio. Attempted to predict the flowfield development with a quasi-steady approach and concluded that the quasi-steady approximation is not realized, and is only valid for a small range on pitch rates. Used both large and small wing-like devices to maintain flow symmetry to higher angles of attack than for the basic body, for both maneuvering and non-maneuvering conditions.
Panzer, Rediniotis & Telionis 7/1993	Experimental	Hemi(A)	Ramp Pitching Pitch Axis: x/D = 0	$15° < \alpha < 30°$ $\omega = 2.5°/s$, 15°/s (approx)	$k = \omega L/U_\infty$ = 0.0004, 0.0014, 0.0065, 0.01	Re_D : $1.5x10^4$, $2.8x10^4$ M: N/A	Wake Velocity Fields (7HP, LDV)	A tip disturbance created an asymmetric flow over a hemisphere cylinder. Velocity fields acquired downstream of the model showed delay in the development of the steady asymmetric flowfield for reduced frequencies above 0.006. As the pitching motion initiates, two symmetric counter-rotating vortices appear on the leeside of the model. For k = 0.0014, the vortices contain more vorticity at the same α as compared to the steady case. As the motion progresses further, the size of the high-vorticity regions grow as the flow moves to steady state.
Ralston 7/1994	Experimental	F-16 Chined Forebody w/Nozzle and Slot Blowing	Coning Coning Axis: N/A	$10° < \alpha < 60°$	$k=\omega b/2U_\infty$ $-0.3 < k < 0.3$	N/A	C_n	The vortices produced by a chined forebody are more difficult to manipulate than forebodies of conventional cross-section. However, nozzle and slot blowing can still be effective on a chined forebody, even in maneuvering conditions or in sideslip, as long as the actuators are located effectively. The slotted jet is more effective at maintaining yawing moment in maneuvering conditions than the normal slot, although the normal slot can generate a higher yawing moment in static conditions.

Smith & Nunn 1/1976	Experimental	Ogive(A): 3.0 (L/D = 15)	Ramp Pitching Pitch Axis: x/D = 8.179	$0° < \alpha < 90°$ $10.8°/s < d\alpha/dt < 281.3°/s$	$k = \omega D/U_\infty = 2.7x10^{-3}$ Plus Others	Re_D: $5x10^4$ & $8x10^4$ M: N/A	C_N, C_m, C_P Location, WFV	The results show that there is an increment of C_N directly caused by the pitching motion. There is an increment in C_m to about $\alpha = 70°$. At higher angles of attack, C_m is lower than for the static case. Also, there appears to be a reduced frequency which results in a (locally) maximum increment of C_m or C_N. Increasing the pitch rate from this point results in less increment in C_N or C_m. The authors believe that this may be a result of the C_N/C_m increment being closely coupled to the Reynolds number. They submit that any apparent increment in C_N/C_m would result when the motion changes the crossflow Reynolds number so that a change in separation angle, boundary layer transition or wake vortex configuration would result. It is interesting to note that while the maximum velocity change induced by the pitching motion was only 3 ft/s. However, the net effect of this increment near the apex of the ogive could be very great, because the flow near the tip dictates the global flow at high α due to the presence of the convective hydrodynamic instability.
Schiff & Tobak 11/1970	Theoretical & Experimental	Cone: 2.836 (10° Half Angle)	Coning Coning Axis: @ C.G. of Cone	$(d\phi/dt)_{max}$ = 600 rpm	N/A	Re: 1.0 – $3.5x10^6$/ft M: 1.4, 2	C_m, C_n, C_Y, C_N, WFV	C_N and C_m are not functions of the coning rate. Also, C_Y and C_n are not functions of the spin rate of the body about its axis. This latter observation may be due to the high Mach numbers at which the tests were run. C_Y and C_n were found to be linear functions of the coning rate. $C_n(d\phi/dt)$ and $C_Y(d\phi/dt)$ were found to be linear functions of α as long as α was small, nonlinear functions at high α, due to the appearance and asymmetric displacement of vortices over the model. The vortices are displaced (swept) opposite to the direction of rotation of the nose. The direction of displacement is consistent for the entire length of the body, regardless of the local position relative to the coning axis (opposite to the results of Yoshinaga et al., 1981). The vortical angle of displacement from the leeside plane of symmetry was found to be = tan-1 $[(d\phi/dt)x_{cg}/U_\infty]$.

Tobak, Schiff & Peterson 1/1969	Theoretical & Experimental	Ogive(A): N/A	Coning Coning Axis: x/D = 12	$d\phi/dt$ = 200, 400, 600 rpm $10° < \alpha < 40°$	N/A	Re: 1.0 – 3.5×10^6/ft M: 1.4	WFV, C_n	Noted that the linear formulation of the aerodynamic moment equations lack possible coupling between the longitudinal and lateral directions. This shortcoming was resolved by using nonlinear indicial response methodology to formulate an expression for the nonlinear coupling, which required the knowledge of the term $C_{n(d\phi/dt)}$, which is the change in yaw moment caused by a change in coning rate. The authors conducted a coning experiment in which they determined that the variation of C_n with $d\phi/dt$ is essentially linear, within uncertainty. In addition, WFV showed that the vortices over the slender body will displace at a constant angle with respect to the original angle-of-attack plane. Because C_n is not constant with $d\phi/dt$ at high angles of attack, the effect of the displaced vortices could cause large-amplitude circular limit motions.

Stanek & Visbal 9/1991	Computational	Ogive(A): 3.5	Ramp Pitching Pitch Axis: x/D = 5.84, 17	$0° < \alpha < 20°$, $d\alpha/dt$ = 54°/s, 90°/s	$k = \omega L/U_\infty$ = 0.5, 1.5	Re_D: $2x10^4$ M: N/A	CSP, Vorticity Fields, Crossflow Streamlines, C_N, Sectional C_N, Surface Shear	Validates the full unsteady, three-dimensional compressible Navier-Stokes code by comparing to Lamont's pressure data (1982) and the computations of Hartwich (1990) And Degani (1991). For the pitching case where k = 1.5, the location of the pitch axis at x/D = 17 causes vortices to appear on the *windward* side of the forebody. The strong deceleration of the body causes the formation of a shear layer that rolls up into vortical structures reminiscent of dynamic stall of airfoils. The presence of the stall-like vortices induces regions of high suction on the lee side of the body, which results in a large increment of C_N from the static case. In fact, sectional C_N as high as seven times the static value were observed. The other pitching case, where k = 0.5 caused much weaker shear layers to appear over the forebody, and vortex formation first appears over the aft section of the body (as Gad-el-Hak/Ho, 1986 and Zeiger, 1996). The plots of surface topology and vorticity contours are especially illuminating, as the strong stall-like vortices interact with the body surface and ejection of vorticity occurs. No vortex asymmetry was observed at any time. **The author emphasizes that "detailed unsteady experimental measurements are required to provide additional insight into these complex maneuvering body flowfields."**

Wetzel & Simpson 1/1997, 11/1998	Experimental	Prolate Spheroid: 6	Ramp Pitching Pitch Axis: x/L = 0.5	$0° < \alpha < 30°$, $d\alpha/dt$ = 54°/s, 90°/s	$k = \omega L/U_\infty$ = 0.047	Re_L: $4.2x10^6$ M: N/A	Minimum Wall Shear & Crossflow Separation Locations (Hot-Film Sensors)	Hot-film sensors are used with constant-temperature anemometers to measure the unsteady wall shear over the surface of a maneuvering 6:1 prolate spheroid. Minima in the wall shear correspond to crossflow separation locations. Separation can be delayed by as much as 10° angle of attack as compared to the steady case. The separation structure during the unsteady maneuvers lags the steady data by as much as 1.5-3.5 convective time units. The authors note that the time-lag models used by Montividas et al. (1989) did not properly describe the unsteady effects that were observed in this flow. Using a method established by Goman and Khrabov (1994), a first-order time-lag model is fit to the data, and the results are reasonably good. The time lags obtained from this model indicate that the convective speed of the disturbances produced by the maneuvers is slower than the freestream. The authors contend that the slower convective velocity in the boundary layer might well be responsible for the slower convection rates. The VPI&SU DyPPiR model mount is employed to maneuver the model (see Hoang, Wetzel and Simpson, 1994).

Yoshinaga, Tate & Inoue 8/1981	Experimental	Various Cones(A): Included Tip Angles of 20°, 30°, 40° Sharp and Blunted	Coning Coning Axis: C.G. or Near C.G., Which Varied With Model	Free Coning (360°+) $45° < \alpha < 135°$	$k = \omega L/2U_\infty$ Varied	Re: About 10^5 M: N/A	Steady Rotation Rate as a Function of α U_∞ and Model Geometry, WFV	Observed the steady-state coning rates of cone-cylinder models of different geometries. Noted that although the initial yaw moment was biased (as expected from static tests) the model would rotate readily in either direction, only needing a light push to be started. The steady-state rotation rates are not dependent on rotation direction for moderate angles of attack $45° < \alpha < 55°$. The steady rotation rates of the sharp-nosed cone-cylinder depended on rotation direction more than for the blunted cone-cylinder. In fact, the rotation rates of the sharp-nosed model showed some dependence on roll angle. The steady-state rotation rate increases with increasing U_∞, reaches a maximum rate, then begins to decrease with further increases in U_∞. The maximum observed rotation rate decreases with α, for $\alpha > 45°$. At $\alpha = 90°$, very little rotation was observed. Cylinders with no forebody and cone-cylinders (for > 90°) were observed to have periodic yawing rotations. Wake flow visualization showed that the vortices forward of the rotation center shift in a direction opposite to the direction of rotation of the nose. Aft of the rotation center, the vortices shift opposite to the local direction of rotation (i.e. opposite to the shift on the forebody). Note that the latter observation is opposite to that of Schiff & Tobak (1970) who saw that the vortices aft of the rotation center shifted in the same direction as those forward.

Appendix D: The Tangent - Ogive Geometry

"What's an ogive?" – S. L. Hendricks, at the Dissertation Proposal

A tangent-ogive body is generated by the revolution of a circular arc about an axis, such that one end of the arc is tangent to a line parallel to the axis and the other terminates on the axis as shown in figure A.1. The caliber of an ogive is defined as the ratio *L/D*.

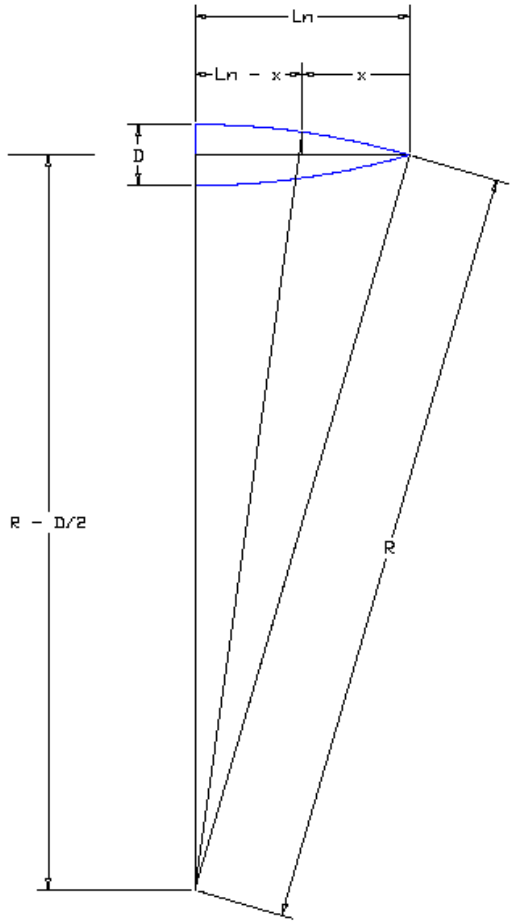

Figure D.1: Tangent-Ogive Cylinder Geometry

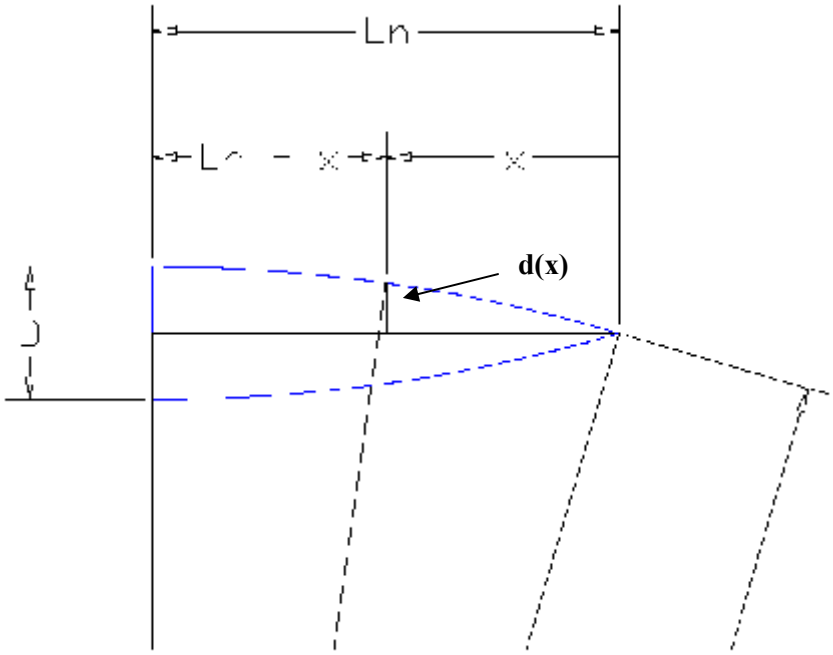

Figure D.2: Detail of Tangent-Ogive Geometry

The radius of the circular arc, R is related to the diameter of the body at its base, D and the forebody length L by

$$R^2 = (R - D/2)^2 + L^2 \qquad [D1]$$

where

L = cD, c being the caliber of the tangent ogive.

Substituting L = cD (c being the caliber of the tangent ogive), and c = 7/2 (3.5 caliber), D1 reduces to

$$R = \frac{25}{2} D \qquad [D2]$$

The included angle of the nose for the 3.5-caliber ogive becomes:

$$\omega s\gamma = 3.5 \text{ D/R}, \ \gamma = 73.74^\circ \qquad [D3]$$

In order to determine the diameter of the tangent-ogive as a function of x, we note that:

$$R^2 = (L - x)^2 + (R - D/2 + d)^2 \qquad [D4]$$

$$R^2 - \left(\frac{7D}{2} - x\right)^2 = (R - D/2 + d)^2 \qquad [D5]$$

and thus

$$d = \left[R^2 - \frac{4gD^2}{4} + 7Dx - x^2\right]^{1/2} + \frac{D}{2} - R \qquad [D6]$$

which reduces to

$$d(x) = -12D + \left[144D^2 + 7Dx - x^2\right]^{1/2} \qquad [D7]$$

Since d(x) is essentially the cross-sectional radius at any location x, we can define the D(x), the cross-sectional diameter:

$$D(x) = 2d(x) = -24D + 2\sqrt{144D^2 + 7Dx - x^2} \qquad [D8]$$

The analysis performed below was done in order to determine the following:

1. Tangent point of the ogive shape with a 5% blunted hemispherical tip. This was required in order to design models for the ESM Wind Tunnel and the VT Stability Tunnel.

2. The planform area of the 3.5 caliber tangent-ogive forebody, which was required to non-dimensionalize the mass flow coefficients used in the ESM Wind Tunnel and VT Stability Tunnel investigations that used pneumatic flow control actuators.

3. The center of mass of the forebody, which was used to plan DyPPiR motions and design the model for the VT Stability Tunnel. The location of the center of mass is necessary in order to properly calculate the model stresses during the maneuvers.

```
In[1]:= f = 625 * Diameter^2 / 4 - 7 * Diameter * x + x^2
```

$$\text{Out[1]}= \frac{625\ \text{Diameter}^2}{4} - 7\ \text{Diameter}\ x + x^2$$

```
In[2]:= l = Sqrt[f]
        z = 25 * Diameter / 2 - l - 0.125
        zz = z /. {Diameter -> 5}
```

$\rightarrow \ell(x)$

$z = R - \ell(x) - .125$ to find where tangent pt for spherical nose meets ogive for 5% blunted forebody

$$\text{Out[2]}= \sqrt{\frac{625\ \text{Diameter}^2}{4} - 7\ \text{Diameter}\ x + x^2}$$

$$\text{Out[3]}= -0.125 + \frac{25\ \text{Diameter}}{2} - \sqrt{\frac{625\ \text{Diameter}^2}{4} - 7\ \text{Diameter}\ x + x^2}$$

$$\text{Out[4]}= 62.375 - \sqrt{\frac{15625}{4} - 35\ x + x^2}$$

```
In[5]:= Plot[zz, {x, 0.4, 0.6}]
```

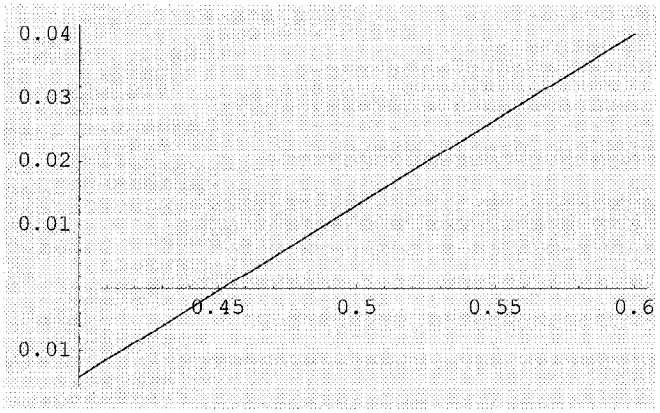


```
Out[5]= - Graphics -
```

```
In[6]:= FindRoot[zz == 0, {x, .4, .5}]
```

```
Out[6]= {x → 0.451815}
```

$= x_*$ (center of rounded tip)

```
In[7]:= dX1 = -12 * Diameter
        dX2 = Sqrt[144 * Diameter^2 + 7 * Diameter * x - x^2]
        dX = dX1 + dX2
```

$$\text{Out[7]}= -12\ \text{Diameter}$$

$$\text{Out[8]}= \sqrt{144\ \text{Diameter}^2 + 7\ \text{Diameter}\ x - x^2}$$

$$\text{Out[9]}= -12\ \text{Diameter} + \sqrt{144\ \text{Diameter}^2 + 7\ \text{Diameter}\ x - x^2}$$

In[10]:= **ddd = dX /. {Diameter -> 5, x -> 0.451815}** → d(.451815) for D = 5"

Out[10]= 0.129938

In[11]:= **DD = -24*Diameter + 2*Sqrt[144*Diameter^2 + 7*Diameter*x - x^2]**

Out[11]= $-24\,\text{Diameter} + 2\sqrt{144\,\text{Diameter}^2 + 7\,\text{Diameter}\,x - x^2}$

Finding Planform Area

In[12]:= **Dint = Integrate[DD, x]**

Out[12]= $-24\,\text{Diameter}\,x + \left(-\frac{7\,\text{Diameter}}{2} + x\right)\sqrt{144\,\text{Diameter}^2 + 7\,\text{Diameter}\,x - x^2} - \frac{625}{4}\,\text{Diameter}^2\,\text{ArcTan}\left[\frac{(-7\,\text{Diameter} + 2\,x)\sqrt{144\,\text{Diameter}^2 + 7\,\text{Diameter}\,x - x^2}}{2\,(-144\,\text{Diameter}^2 - 7\,\text{Diameter}\,x + x^2)}\right]$

In[16]:= **D1 = Dint /. {x -> 7, Diameter -> 2}**
D2 = Dint /. {x -> 0, Diameter -> 2}
Area = D1 - D2

Out[16]= -336

Out[17]= $-168 - 625\,\text{ArcTan}\left[\frac{7}{24}\right]$

Out[18]= $-168 + 625\,\text{ArcTan}\left[\frac{7}{24}\right]$

In[19]:= **N[%]**

★ Out[19]= 9.37132 in.^{2} (2" = D)

In[20]:= **D1 = Dint /. {x -> 17.5, Diameter -> 5}**
D2 = Dint /. {x -> 0, Diameter -> 5}
Area = D1 - D2

Out[20]= -2100.

Out[21]= $-1050 - \frac{15625}{4}\,\text{ArcTan}\left[\frac{7}{24}\right]$

★ Out[22]= 58.5707 in^2 (D = 5")

Planform Areas

In[26]:= **Dint2 = Integrate[x*DD, x]**

Out[26]= $-12\,\text{Diameter}\,x^2 + \sqrt{144\,\text{Diameter}^2 + 7\,\text{Diameter}\,x - x^2}\left(-\frac{433\,\text{Diameter}^2}{4} - \frac{7\,\text{Diameter}\,x}{6} + \frac{2\,x^2}{3}\right) - \frac{4375}{8}\,\text{Diameter}^3\,\text{ArcTan}\left[\frac{(-7\,\text{Diameter} + 2\,x)\sqrt{144\,\text{Diameter}^2 + 7\,\text{Diameter}\,x - x^2}}{2\,(-144\,\text{Diameter}^2 - 7\,\text{Diameter}\,x + x^2)}\right]$

Finding $x_{c.g.}$

```
In[27]:= D3 = Dint2 /. {x -> 17.5, Diameter -> 5}
         D4 = Dint2 /. {x -> 0, Diameter -> 5}
         Moment = D3 - D4

Out[27]= -181135.
```

$$\text{Out[28]= } -162375 - \frac{546875}{8}\,\text{ArcTan}\left[\frac{7}{24}\right]$$

```
Out[29]= 639.571

In[33]:= D3 = Dint2 /. {x -> 7, Diameter -> 2}
         D4 = Dint2 /. {x -> 0, Diameter -> 2}
         Moment = D3 - D4
```

$$\text{Out[33]= } -\frac{34778}{3}$$

$$\text{Out[34]= } -10392 - 4375\,\text{ArcTan}\left[\frac{7}{24}\right]$$

$$\text{Out[35]= } -\frac{3602}{3} + 4375\,\text{ArcTan}\left[\frac{7}{24}\right]$$

```
In[36]:= N[%]

Out[36]= 40.9326
```

$$x_{c.g.} = \frac{\text{Moment}}{\text{Area}} = \underline{2.184\,D}$$